NASA/TM—2008–215465

Advanced Materials for Exploration Task Research Results

Compiled by
M.B. Cook
Marshall Space Flight Center, Marshall Space Flight Center, Alabama

K.L. Murphy
Jacobs Engineering Group, Huntsville, Alabama

T. Schneider
Integrated Concepts and Research Corporation, Huntsville, Alabama

July 2008

The NASA STI Program…in Profile

Since its founding, NASA has been dedicated to the advancement of aeronautics and space science. The NASA Scientific and Technical Information (STI) Program Office plays a key part in helping NASA maintain this important role.

The NASA STI program operates under the auspices of the Agency Chief Information Officer. It collects, organizes, provides for archiving, and disseminates NASA's STI. The NASA STI program provides access to the NASA Aeronautics and Space Database and its public interface, the NASA Technical Report Server, thus providing one of the largest collections of aeronautical and space science STI in the world. Results are published in both non-NASA channels and by NASA in the NASA STI Report Series, which includes the following report types:

- TECHNICAL PUBLICATION. Reports of completed research or a major significant phase of research that present the results of NASA programs and include extensive data or theoretical analysis. Includes compilations of significant scientific and technical data and information deemed to be of continuing reference value. NASA's counterpart of peer-reviewed formal professional papers but has less stringent limitations on manuscript length and extent of graphic presentations.

- TECHNICAL MEMORANDUM. Scientific and technical findings that are preliminary or of specialized interest, e.g., quick release reports, working papers, and bibliographies that contain minimal annotation. Does not contain extensive analysis.

- CONTRACTOR REPORT. Scientific and technical findings by NASA-sponsored contractors and grantees.

- CONFERENCE PUBLICATION. Collected papers from scientific and technical conferences, symposia, seminars, or other meetings sponsored or cosponsored by NASA.

- SPECIAL PUBLICATION. Scientific, technical, or historical information from NASA programs, projects, and missions, often concerned with subjects having substantial public interest.

- TECHNICAL TRANSLATION. English-language translations of foreign scientific and technical material pertinent to NASA's mission.

Specialized services also include creating custom thesauri, building customized databases, and organizing and publishing research results.

For more information about the NASA STI program, see the following:

- Access the NASA STI program home page at <http://www.sti.nasa.gov>

- E-mail your question via the Internet to <help@sti.nasa.gov>

- Fax your question to the NASA STI Help Desk at 301–621–0134

- Phone the NASA STI Help Desk at 301–621–0390

- Write to:
  NASA STI Help Desk
  NASA Center for AeroSpace Information
  7115 Standard Drive
  Hanover, MD 21076–1320

NASA/TM—2008–215465

Advanced Materials for Exploration Task Research Results

Compiled by
M.B. Cook
Marshall Space Flight Center, Marshall Space Flight Center, Alabama

K.L. Murphy
Jacobs Engineering Group, Huntsville, Alabama

T. Schneider
Integrated Concepts and Research Corporation, Huntsville, Alabama

National Aeronautics and
Space Administration

Marshall Space Flight Center • MSFC, Alabama 35812

July 2008

Acknowledgments

The Advanced Materials for Exploration Program has been able to produce the results identified within this Technical Memorandum thanks to the hard work of many individuals. A particular note of recognition and appreciation is due to the many Principal Investigators who did such a great job over the past 4 years in providing new and interesting technology advancements to the materials community. Gratitude is also warranted for the many who managed to keep the program on schedule, in budget, and within scope—namely David Chafee, Sandy Cothren, Tracy McMahan, Karen Murphy, Janet Salverson, Twila Schneider, and Charlotte Shea.

TRADEMARKS

Available from:

NASA Center for AeroSpace Information
7115 Standard Drive
Hanover, MD 21076–1320
301–621–0390

This report is also available in electronic form at
<https://www2.sti.nasa.gov>

TABLE OF CONTENTS

TABLE OF CONTENTS (Continued)

LIST OF FIGURES

LIST OF FIGURES (Continued)

LIST OF FIGURES (Continued)

LIST OF FIGURES (Continued)

LIST OF FIGURES (Continued)

LIST OF FIGURES (Continued)

LIST OF FIGURES (Continued)

LIST OF FIGURES (Continued)

LIST OF FIGURES (Continued)

LIST OF FIGURES (Continued)

LIST OF FIGURES (Continued)

LIST OF FIGURES (Continued)

LIST OF FIGURES (Continued)

LIST OF FIGURES (Continued)

LIST OF FIGURES (Continued)

LIST OF TABLES

LIST OF TABLES (Continued)

LIST OF ACRONYMS

AEDL	aerocapture, entry, descent, and landing
AFM	atomic force microscopy
AFRL	Air Force Research Laboratory
AME	Advanced Materials for Exploration
AO	atomic oxygen
AO/VUV	atomic oxygen/vacuum ultraviolet
APS	advanced photon source
ARC	Ames Research Center
ASOA	advanced state of the art
ASTM	American Society for Testing and Materials
ASTP	Advanced Space Transportation Program
ASTRA	Advanced Systems, Technologies, Research and Analysis
ATK	Alliant Techsystems
AWG	American wire gauge
AXF–5Q	high-strength graphite
BAE	British Aerospace
BRI	Boeing rigid insulation
CAIB	Columbia accident investigation board
CaLV	cargo launch vehicle
CC	ceramic core
C–C	carbon-carbon
CCD	charge coupled device
CDDF	Center Director's Discretionary Fund
CERMET	ceramic metallic

LIST OF ACRONYMS (Continued)

CEV	crew exploration vehicle
CLV	crew launch vehicle
CMC	ceramic matrix composite
CME	coronal mass ejection
Co-PI	Co-Principal Investigator
COTR	contracting officer's technical representative
CP	colorless polyimide
CRAI	capabilities and requirements analysis and integration
CRSC	ceramic reaction sintered coating
CRL	capability readiness level
C-SiC	carbon-silicon carbide
CT	computed tomography
CTE	coefficient of thermal expansion
CVD	chemical vapor deposition
DARPA	Defense Advanced Research Projects Agency
DIII–D	a magnetic confinement device in San Diego used for fusion research
DoE	Department of Energy
DMA	dynamic mechanical analysis
DSC	differential scanning calorimetry
DU	depleted uranium
EBTPS	electronically biased thermal protection system
EB–PVD	electron beam physical vapor deposition
ED	Engineering Directorate
ED	electrodynamic
EDS	energy dispersive spectroscopy

LIST OF ACRONYMS (Continued)

EDX	energy dispersive x-ray
EI	entry interface
EMC	electromagnetic compatibility
EMI	electromagnetic interference
EMPA	electron microprobe analyzer
EOIM	evaluation of oxygen interaction with materials
EPA	Environmental Protection Agency
ESL	electrostatic levitation
ET	external tank
EVA	extravehicular activity
FGM	functionally gradient material
FLUENT	software program for computational fluid dynamics
FTIR	Fourier transform infrared
FY	fiscal year
GA	General Atomics
GER	gaining electrons is reduction
GFRC	graphite fiber reinforced composite
GRC	Glenn Research Center
HETC	high-efficiency tantalum-based ceramic
HIP	hot isostatic pressing
HIPPO	high-pressure preferred orientation
HiTEMS	high-temperature emissivity measurement system
HIVHAC	high-voltage Hall accelerator
HM	high modulus
H–O	hydrogen-oxygen

LIST OF ACRONYMS (Continued)

HPFTP	high-pressure fuel turbopump
HT	high tensile
HTT	high-heat treatment
IHT	intermediate heat treatment
IL	ionic liquid
ILPI	ionic liquid-based material developed at MSFC
IM	intermediate modulus
IPP	Innovative Partnership Program
IR	infrared
IRAD	Independent Research and Development
IR&D	Internal Research and Development
ISS	International Space Station
JIMO	Jupiter Icy Moons Mission
JSC	Johnson Space Center
JSC–1	lunar mare simulant developed at Johnson Space Center
JUTEM	Japan Ultrahigh Temperature Materials Laboratory
K	Kelvin
KSC	Kennedy Space Center
LANSCE	Los Alamos Neutron Science Center
LaRC	Langley Research Center
LCF	low-cycle fatigue
LEAP	lightweight exoatmospheric projectile
LED	light emitting diode
LEO	low-Earth orbit losing electrons is oxidation

LIST OF ACRONYMS (Continued)

LHMEL	Laser Hardened Materials Evaluation Laboratory
LNTPMTP	Lightweight Nonmetallic Thermal Protection Materials Technology Project
LOS	loss of signals
LPIR	laboratory portable infrared reflectometer
LPSR	laboratory portable spectroreflectometer
MAPTIS	Materials and Processes Technical Information System
MCC	main combustion chamber
MCP	master change proposal
MISSE	Materials on International Space Station Experiment
MLI	multilayer insulation
MMC	metal matrix composites
MSFC	Marshall Space Flight Center
NaK	sodium-potassium
NASA	National Aeronautics and Space Administration
NBS	National Bureau of Standards
NDE	nondestructive evaluation
NERVA	nuclear engineer for rocket vehicle application
NGLT	Next Generation Launch Technology
NIST	National Institute of Standards and Testing
NOAX	nonoxide adhesive experimental (polymer sealant)
NRC	Nuclear Research Council
NSWC	Naval Surface Warfare Center
NTR	nuclear thermal rocket
OMS	orbital maneuvering system
OOI	Occean Optics, Inc.

LIST OF ACRONYMS (Continued)

PAN	polyacrilonitrile
PBO	phenylenebenzobisoxazole
PBZ	polybenzoxazine resin
PFOA	perfluorooctanoate acid
PI	Principal Investigator
PICA	phenolic impregnated carbon ablator
P/M	powder metallurgy
PMC	polymer matrix composites
PMTI	Pittsburgh Materials Technology, Inc.
PPI	Plasma Process, Inc.
PRL	Propulsion Research Laboratory
PTTB	plasma torch test bed
PVD	physical vapor deposition
R&D	research and development
RCC	reinforced carbon-carbon
RCG	reaction cured glass
RF	radio frequency
RFP	request for proposals
RIBA	reactive ion beam assisted
ROVER	remotely operated video enhanced receiver
RSRM	reusable solid rocket motor
RT	room temperature
RTF	Return to Flight
RTV	room temperature vulcanized
SDI	Strategic Defense Initiative

LIST OF ACRONYMS (Continued)

SDOS	Systems Development and Operations Contract
SEM	scanning electron microscopy
SEP	solar electric propulsion
SHT	superhigh tensile
SIMS	secondary ion mass spectroscopy
SLA	super lightweight ablator
SLI	Space Launch Inititative
SSME	Space Shuttle main engine
SoA	state-of-the-art
TBE	Teledyne Brown Engineering
TC	thermal conductivity
TEM	transmission electron microscopy
TFSI	bis(trifluromethylsulfonyl)imide anion
TiTIG	tungsten inert gas
TPS	thermal protection system
TRL	technology readiness level
UHM	ultrahigh modulus
UM	University of Michigan
UMass	University of Massachusettes,
USM	University of Southern Mississippi
UT	University of Tennessee
UTS	ultimate tensile strength
UTTR	Utah Test and Training Range
UV	ultraviolet
VOC	volatile organic compound

LIST OF ACRONYMS (Continued)

VPS	vacuum plasma spray
VUV	vacuum ultraviolet
W	tungsten
WPAFB	Wright Patterson Air Force Base
X–33	subscale technology generator for reusable launch vehicles
XACCT	x-aerogel insulated composite cryotank technology
YS	yield strength

NOMENCLATURE

A	surface area
a	location of the thermocouple adjacent to the heating element
Al	aluminum
Al-Li	aluminum-lithium
Ar	argon
Au	gold
b	within the outer shell where the metal overlaps and forms a pocket for the thermocouple
BN	boron nitride
B_4C	boron carbide
C	carbon
Cr	chromium
Cu	copper
e	emissivity
HfB	hafnium boron
HfC	hafnium carbide
HfB_2	hafnium diboride
HfO	hafnium oxygen
HfO_2	hafnium dioxide
Li	lithium
N	nitrogen
Nb	niobium
Ni	nickel
O	oxygen
P	power
Pd	palladium
Pt	platinum
q	unit length of cylinder

NOMENCLATURE

Q_{bar}	dynamic pressure
S	solid of one composition
Si	silicon
SiC	silicon carbide
Sn	tin
T	object temperature
T_a	temperature of the thermocouple adjacent to the heating element
T_b	temperature within the outer shell
T_c	cooler background temperature
T_g	curing exotherm
Ti	titanium
U	uranium
V	transformation rate
Zr	zirconium
α	solar absorptance
ε	IR emittance
a_i	constant
θ	latitude
$r(\theta)$	radius at a specific latitude
σ	Stefan-Boltzman constant
λ	spacing thermal conductivity
λbar	average TC

TECHNICAL MEMORANDUM

ADVANCED MATERIALS FOR EXPLORATION TASK RESEARCH RESULTS

1. INTRODUCTION

The pursuit of long-term space exploration will yield new technical materials challenges in spacecraft and propulsion that will require innovative solutions. The Advanced Materials for Exploration (AME) activity in Marshall Space Flight Center's (MSFC) Exploration Science and Technology Directorate coordinated activities from 2001 to 2006 to support in-space propulsion technologies for future missions. Working together, materials scientists and mission planners identified material shortfalls that are limiting the performance of long-term missions. Selected materials must operate beyond the thresholds of today's materials capabilities. In the harsh environment of space, materials must retain their properties or adjust in a desired way to optimize performance. These materials must have reduced mass, increased strength, and an increased temperature operating range.[1]

Leveraging a history of materials development and characterization for high-temperature furnaces, materials solidification processes, analysis and effects, and microstructural investigation of materials behavior, MSFC aligned its materials research program to address the specific space propulsion needs identified by NASA's in-space program offices.

This AME activity relied on existing program offices to identify current material limitations associated with the propulsion aspect of their missions. Customer focused workshops, held in 2001 and 2003, identified materials needs associated with next generation nuclear propulsion technologies and in-space propulsion technologies. Using these forums, customers such as the In-Space Propulsion Program and the High-Energy Propulsion System Office identified high-priority propulsion materials research needs. Materials scientists and engineers then surveyed the community to identify state-of-the-art materials available to respond to those needs. The deltas were identified as technology gaps that needed to be addressed through materials research activities. Appropriate materials development opportunities were identified and became the scope for the AME activity.

Critical materials technology gaps were identified in high-temperature materials for propulsion systems, environmentally protective and resistant materials and coatings, lightweight structural materials, nonintrusive monitoring and diagnostic materials, materials for increased heat management efficiency (in radiators and heat pipes), and materials characterization at elevated temperatures and in simulated environments. Beginning with funding in 2004, a focused programmatic activity was established to develop a road map coordinated with customer needs. This road map, shown in figure 1, identified targeted research areas and was the foundation of awarded and directed research within the project. As validation of this selection of critical technologies, the gaps identified by AME correlated well with

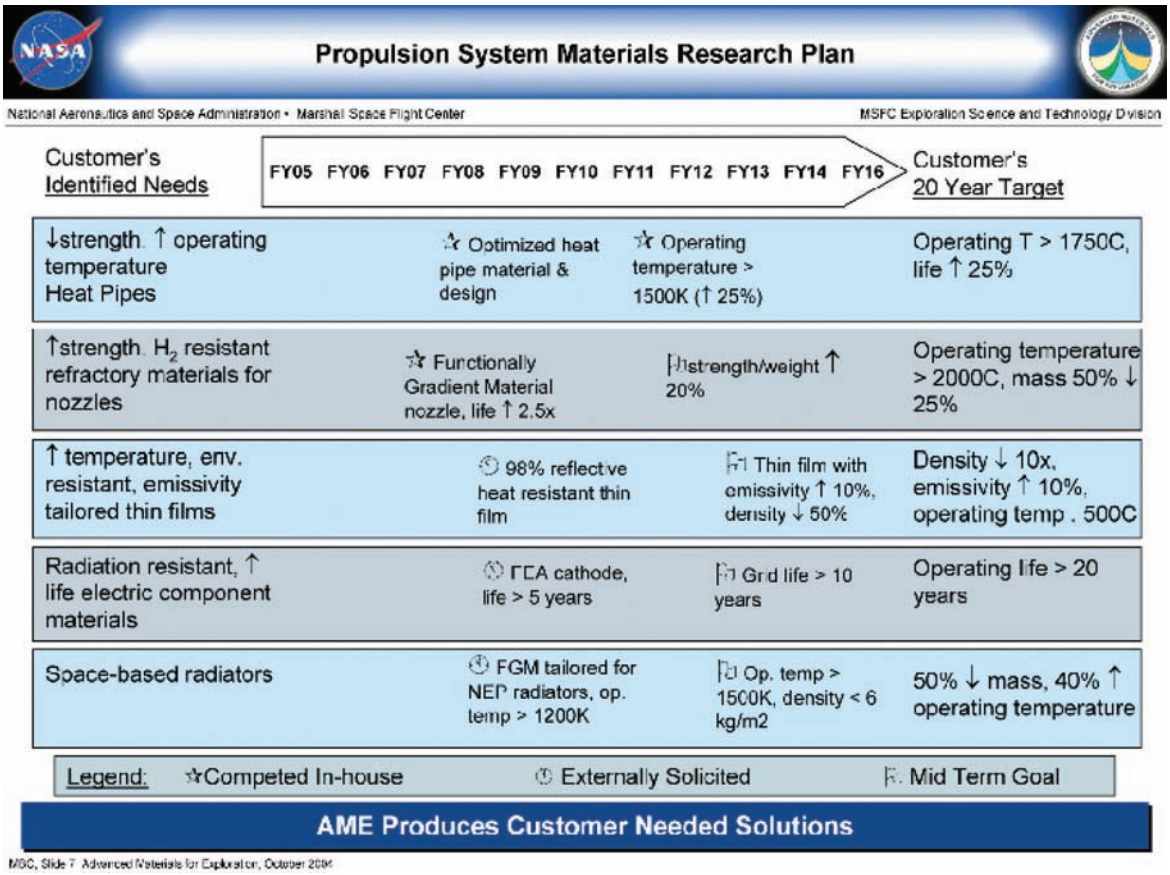

Figure 1. 2004 AME Propulsion Systems road map.

the Advanced Systems, Technologies, Research, and Analysis (ASTRA) work breakdown structure on materials, shown in figure 2. These independent activities have identified similar materials issues that must be resolved to expand our capabilities for NASA's Vision for Space Exploration.

The AME materials requirements were used as a foundational element to the capabilities and requirements analysis and integration (CRAI) road mapping activity relating to materials. This architectural review of Advanced Materials and Structures, presented in August of 2003, prioritized the materials gaps identified above with gaps identified through the Next Generation Launch Technology (NGLT), In-Space Propulsion Office, and Air Force space programs. CRAI also assessed the cost associated with responding to these issues. According to this CRAI assessment, an estimated $1.5 billion is needed in dedicated research from FY 2005 to FY 2014 to adequately address the identified issues with structural materials, radiation shielding, thermal protection system (TPS) and leading edges, propulsion materials, thin films, and radiators and heat pipes.

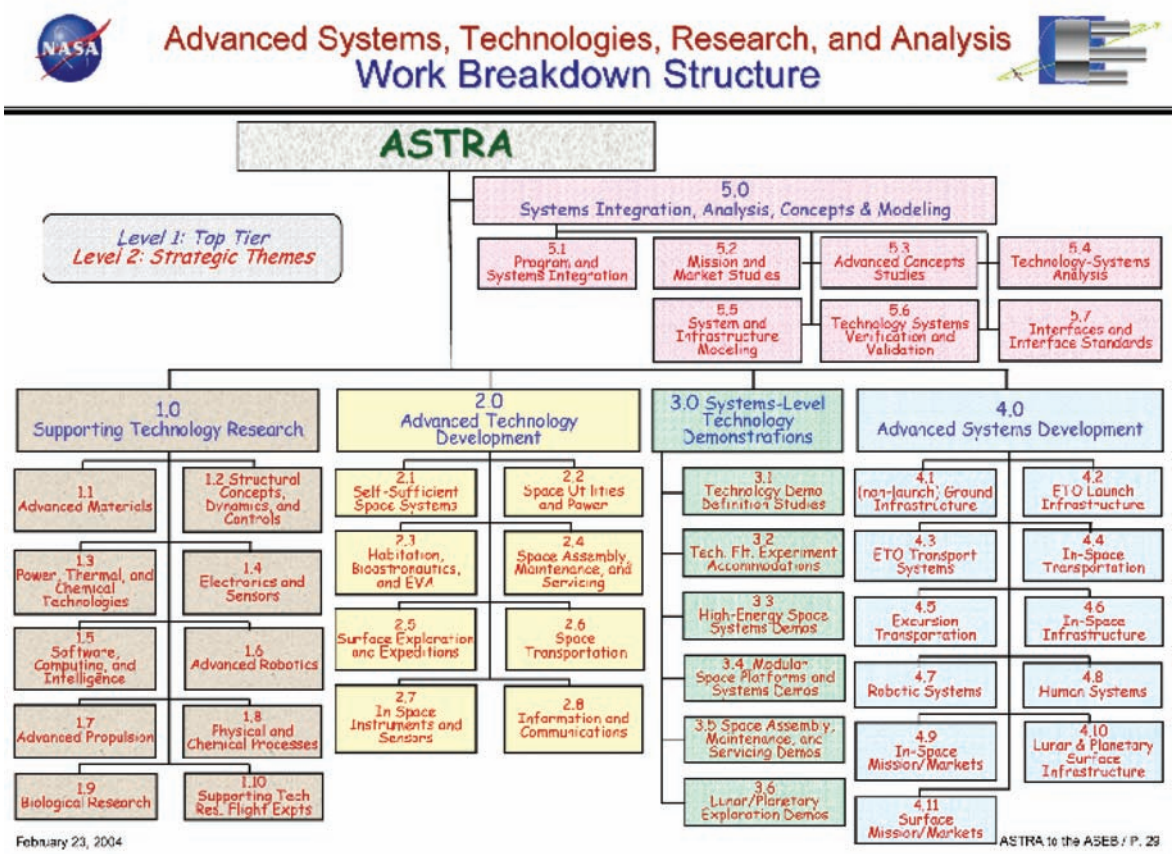

Figure 2. Presentation entitled "Advanced Systems, Technologies, Research, and Analysis to Enable Future Space Flight Capabilities and Realize the U.S. Vision for Space Exploration," given by John C. Mankins, Director of NASA's Human and Robotic Technology Development Programs Office, at the *Stepping Stones to the Future of Space Workshop* of the National Academies, February 23, 2004.

The scope of materials research needed to address the many issues is larger than any one organization—Federal or commercial. The work load must be shared among many organizations in a cooperative fashion if progress is expected in a suitable timeline to benefit the goals of NASA's Vision for Space Exploration. The Air Force Research Laboratory (AFRL), the Department of Energy (DoE), Defense Advanced Research Projects Agency (DARPA), and several private companies are working in targeted areas that will lead to the needed advancements in materials development.[2]

The goal of the AME project was to deliver improved materials in targeted areas to meet technology development milestones of NASA's dedicated exploration activities such as the Science Mission Directorate's In-Space Propulsion Project. To achieve this goal, directed tasks capitalized on Center infrastructure and core competencies uniquely suited for solving critical materials issues. Peer-reviewed research contributed additional expertise for the development of performance enhancing deliverables. The selected tasks within this project delivered the initial stages of material advancements that can be staggered across multiple years such that handoffs would be available each year in support of customer road maps.

Materials research tasks were targeted in five areas: Thermal management materials, propulsion materials, materials characterization, vehicle health monitoring materials, and structural materials. Selected tasks were scheduled for completion so that these new materials could be incorporated into customer development plans.[3]

The focus of AME was to identify gaps not being addressed by current efforts and to move technology forward in those areas. AME supported conceptual and lab-scale projects that demonstrated feasibility of a new material or material application. As these tasks mature innovative ideas to reality, the concepts will be handed over to engineering organizations to begin the task of advancing the manufacturability of these materials and incorporating them into production processes. The initial tasks within AME were as follows:

- Heat pipe/radiator design.
- Refractory functionally gradient material (FGM).
- Electronically biased TPS.
- Carbon fiber thermal conductivity (TC).
- Tether wire development.
- Solar sail contouring.
- Phase contrast x-ray imaging.
- High-temperature creep measurements.
- Large-scale superconducting magnets.
- Radiation-resistant electronics.
- Titanium (Ti) matrix TPS.

The AME activity continued to interact with program managers leading missions in all aspects of exploration. Through more detailed discussions and focused reviews of aerocapture and nuclear programs, materials issues were refined. Many materials issues were refined in support of the aeroassist community. Over a 2-mo period, AME interviewed, researched, and explored limitations associated with aeroassist technologies. Needed research was identified in thermal protection systems, leading edges, thin films, sensing technologies, and adhesives. These specific needs were integrated into the overall AME road map and addressed with later work. In another 2-mo effort, materials issues were identified in the nuclear community and as a result, several tasks were identified for immediate response:

- High-temperature emissivity measurements.
- Molybdenum-rhenium process comparison.

- Heat-pipe degradation.
- Tether materials development.
- Composite aerogel tanks.
- Thrust chamber liners.

Additional work in the form of nine new tasks was added in November 2005. Top experts were challenged to address the following materials issues with initial evaluations by September 2006:

- Stardust materials analysis.
- MISSE–6 materials selection.
- Hot-hydrogen materials testing.
- Chemical propulsion high-temperature materials.
- Adhesives/bonding agents for aerocapture.
- Ti- and Zirconium (Zr)-based wires.
- Novel nanolaminates.
- High-performance ablative composites.
- Reaction sintered coatings.

An additional area targeted by the AME activity was advanced life support technologies. Again, AME conducted a focused review of the program to refine the understanding of materials limitations associated with the technologies. Studies were conducted to determine state-of-the-art (SoA) and the next steps in several critical life support areas. Through this activity, specific research needs were identified by the customer and added to the AME road map to be addressed in later solicitations.[2]

References

1. AME Web site.

2. Clinton, R.; and Whitaker, A.: "Materials Requirements for Advanced Propulsion Systems," *AIAA–2005–1441*, NASA MSFC, Huntsville, AL, 43rd AIAA Aerospace Sciences Meeting and Exhibit, Reno, NV, January 10–13, 2005.

3. AME Project Plan.

2. RESEARCH RESULTS

The research results presented in this Technical Memorandum (TM) were provided by the Principal Investigators (PIs) and Co-Investigators (Co-Is) noted in each report. They are organized by discipline and include the fact sheets developed by AME to highlight their achievements. Tasks without final reports at the time of publication are represented only by their fact sheets, all of which are included in appendix B.

3. MATERIALS CHARACTERIZATION

3.1 Materials Analysis of Returned Hardware From Stardust

PI—Miria Finckenor, NASA MSFC Environmental Effects Branch, Materials and Processes Laboratory.

Objectives

The Materials Analysis of Returned Hardware from Stardust AME task received funding to perform nondestructive analyses of the nonprimary science hardware components of the Stardust sample return capsule. The following components were analyzed to determine the materials' durability in the space environment:

- Blunt body reentry heat shield encased in phenolic impregnated carbon ablator (PICA).
- Backshell of superlightweight ablator 561 (SLA–561) material handpacked into phenolic Flexcore and coated with CV–1100 silicone.
- Rope seal between the heat shield and backshell.
- Internal multilayer insulation (MLI) blankets.
- Parts of the Kevlar® straps left attached to the backshell.

The goals of the task were to determine how the various materials from which the components were built weathered the extreme temperatures and harsh space environment during the capsule'used to build the components weathered the extreme temperatures and harsh space environment during the capsule's nearly 7-yr voyage to and from its rendezvous with Comet Wild 2 and provide lessons learned data for designers of future missions. In addition, this task complements the AME materials characterization goals.

Description of Research

While the Stardust mission's primary science goal was to capture and return cometary and interstellar dust particles in aerogel collectors, the sample return capsule and science hardware themselves also returned critical information about how the materials out of which they were constructed performed during the mission. Scientists can learn how materials properties were affected by ultraviolet radiation (UV), charged particle radiation, high vacuum, and extreme temperatures experienced in space. During the Stardust mission, the capsule's components were exposed to the combined effects of these conditions, an environment that cannot be fully simulated on Earth. AME funding afforded a unique opportunity for materials engineers to analyze returned space hardware with the fourth longest space exposure.

Research Method

The PI traveled to Johnson Space Center's (JSC's) Stardust curation site to conduct nondestructive evaluation (NDE) measurements on Stardust nonprimary science hardware (heat shield, backshell, seals, parachute cords, and thermal blankets) to assess their durability in the space environment. Focus was on the ablative materials that protected the blunt body capsule and its payload from the heat of reentry. The PI had asked for access to other flight components such as the avionics box, thermal control surfaces, and deployment/retraction mechanisms but that access was denied.

The specific NDE techniques were selected to gather data on changes in solar absorptance (α) and infrared (IR) emittance (ε) caused by exposure to the space environment and reentry heating. Data collected from these nondestructive tests are compared to existing data for the materials. A detailed technical report with lessons learned will be prepared. Postflight materials data will be archived in the NASA Materials and Processes technical information system databases.

Rationale

The PI planned the following NDE methods to analyze the Stardust hardware:

- Torque measurements on fasteners.
  - Breakaway and running torque data, when compared with preflight values, may indicate galling or reveal other mechanism failures. While these measurements have been made by JSC personnel, the data have not yet been released to MSFC.
- Visual and photographic observations of material conditions, particularly the aeroshell.
  - These data indicate how well the spacecraft's trajectory and its aeroshell heat shield protected the sample return canister.
- Black light illumination (Spectroline UV lamp model B–14F).
  - This analysis reveals particulate and molecular contamination, which can then be identified later using Fourier transform infrared (FTIR) diffuse reflectance measurements (SOC–400 FTIR spectrophotometer).
- Solar absorptance measurements using an AZ Technology laboratory portable spectroreflectometer (LPSR).
  - The LPSR measures total normal hemispherical reflectance from 250 to 2,800 nm.
- IR reflectance measurements by AZ Technology Temp 2000A IR Reflectometer.
  - IR reflectance measurements by AZ Technology laboratory portable IR reflectometer (LPIR) were added later. The TEMP instrument gives an integrated emittance measurement by ASTM–E–408, test method B, while the LPIR measures IR reflectance from 2 to 20 microns using a prism monochromator. Solar absorptance and IR reflectance/emittance measurements are used by thermal engineers in modeling ascent and reentry heating and energy absorption.

Schedule

This AME task was funded for 10 mo (December 2005–September 2006). The Stardust sample return capsule parachuted to its soft landing in the Utah desert in January 2006. Access to the capsule components of interest was delayed for 6 mo, however, related to circumstances beyond the PI's control. In mid-July 2006, the PI was granted access to the hardware at JSC, and has focused on data analysis since returning to MSFC in late July.

Results

Data. When the Stardust return capsule landed at the Utah Test and Training Range (UTTR), it bounced several times, leaving some char material on the dirt as it rolled, as shown in figure 3. Measurements of the heat shield and backshell are presented with the acknowledgment that uneven amounts of char and pyrolized material were measured. All data presented in this TM are from areas without dirt, although to assist other Stardust hardware investigations, some measurements were made of areas that clearly contained Utah dirt.

Figure 3. Stardust spacecraft immediately after landing at UTTR. Note the roll track in the dirt.

Heat Shield. NASA developed PICA specifically for reentry thermal protection when the heat flux is greater than 400 W/cm^2.[1] Stardust was a good candidate for the first PICA flight test, and ablative material was an appropriate choice since the sample return capsule was not intended for reuse, as is the Space Shuttle. Also, PICA is much lighter than the FM5055 carbon-phenolic ablator used on the Pioneer Venus and Galileo missions. Figures 4 and 5 compare the solar absorptance and IR reflectance, respectively, of typical postflight heat shield to samples of pristine PICA and a sample from arc jet testing at Ames Research Center (ARC). All comparison samples were measured on the same equipment as the Stardust heat shield. Reflectance in the UV to near-IR wavelengths matched well between the arc jet tested sample and the heat shield. The IR reflectance measurements of the rim of the heat shield were different than those of the majority of the blunt body. The IR reflectance of the arc jet test sample was closer to that of the rim than to those of the rest of the heat shield.

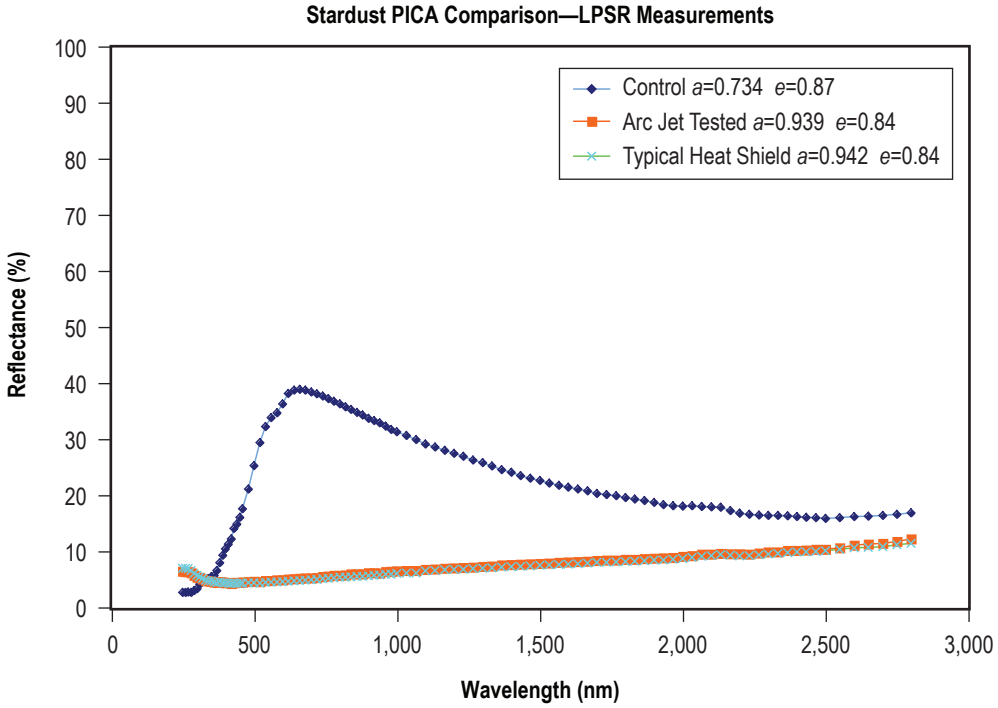

Figure 4. Comparison of solar absorptance of postflight Stardust heat shield samples to pristine and ground-tested PICA samples.

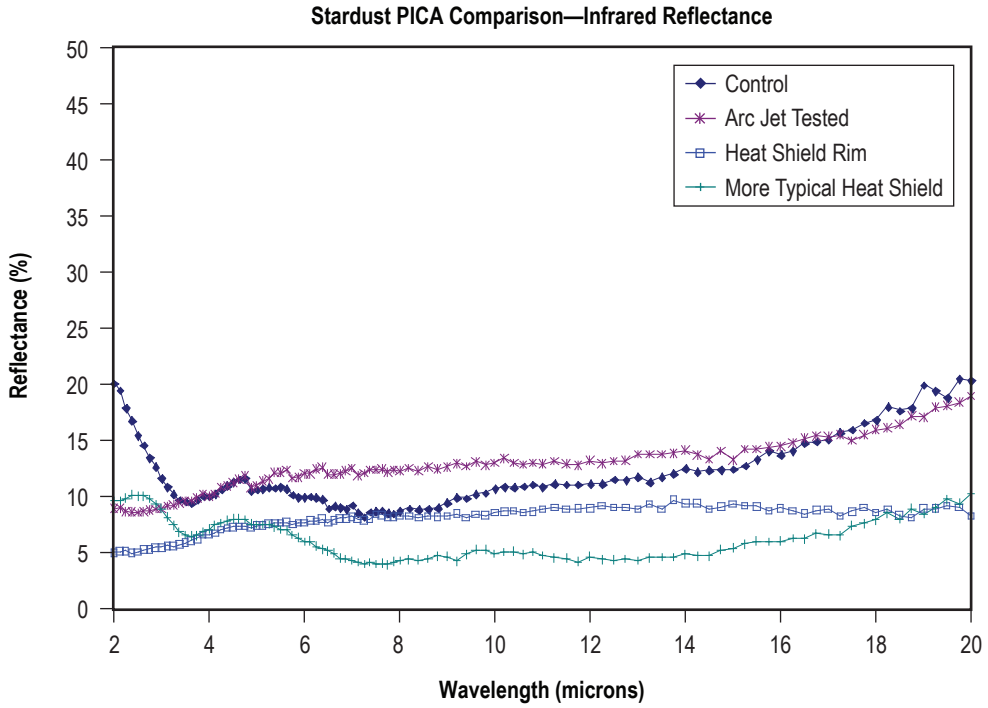

Figure 5. Comparison of IR reflectance of postflight Stardust heat shield samples to pristine and ground-tested PICA samples.

The rim of the heat shield, shown in figure 6, appeared to be more affected by reentry heating than the nose, figure 7, but this may be related to the removal of the char layer. The initial impact site, figure 8, shows the visibly darker area of the PICA's pyrolysis zone as compared to the rest of the heat shield. The Utah dirt and the residual Z93 paint are also visible.

Figure 6. Stardust heat shield rim.

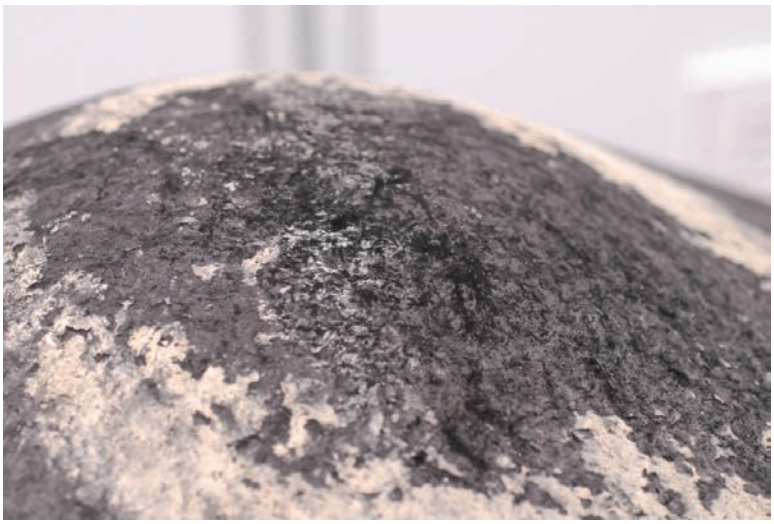

Figure 7. Stardust heat shield nose.

Figure 8. Stardust initial impact site.

For postflight analysis reference, the heat shield was mounted on a stand with circumference points marked. The center point between the hinges was 0° and the initial impact point was 75–90°. Measurements were made every 30° around the heat shield at approximately the same distance from the rim, as seen in figure 9. The measurements indicate some variation in the material response across the heat shield, with 30–60° being the most reflective and 120–150° the most absorptive.

Originally the PICA had been coated with Z93 zinc oxide/potassium silicate thermal control coating. Z93 is a fairly common spacecraft coating, so even though a control sample was not available for measurements, solar absorptance data were readily obtained. As shown in figure 10, the absorption band at 1,933 nm and the cutoff at 400 nm are present; however, these bands are not present in the optical measurements of areas containing the Utah dirt.

Backshell. The backshell was coated with SLA–561V handpacked into phenolic Flexcore and then coated with CV–1100 silicone. SLA–561V is the same thermal protection material used on the Viking missions. It should not be confused with the SLA–561 handpacked insulation used on the Space Shuttle's external tank (ET). SLA–561 hand pack, used on the ET, is gray in color from the addition of carbon black to improve its performance at cryogenic temperatures.[2]

The odor of the backshell, even after 6 mo in atmosphere, was quite noticeable. The backshell had a very strong burnt charcoal smell, much more than did the heat shield. It had more brownish tones in the char and also carried some of the Utah mud from the landing. The backshell was not mounted on a stand as was the heat shield, so, as shown in figure 11, circumference was noted with 0° being centered between the hinge points. By these markings, the darker areas seem to be between 180–240° (fig. 12).

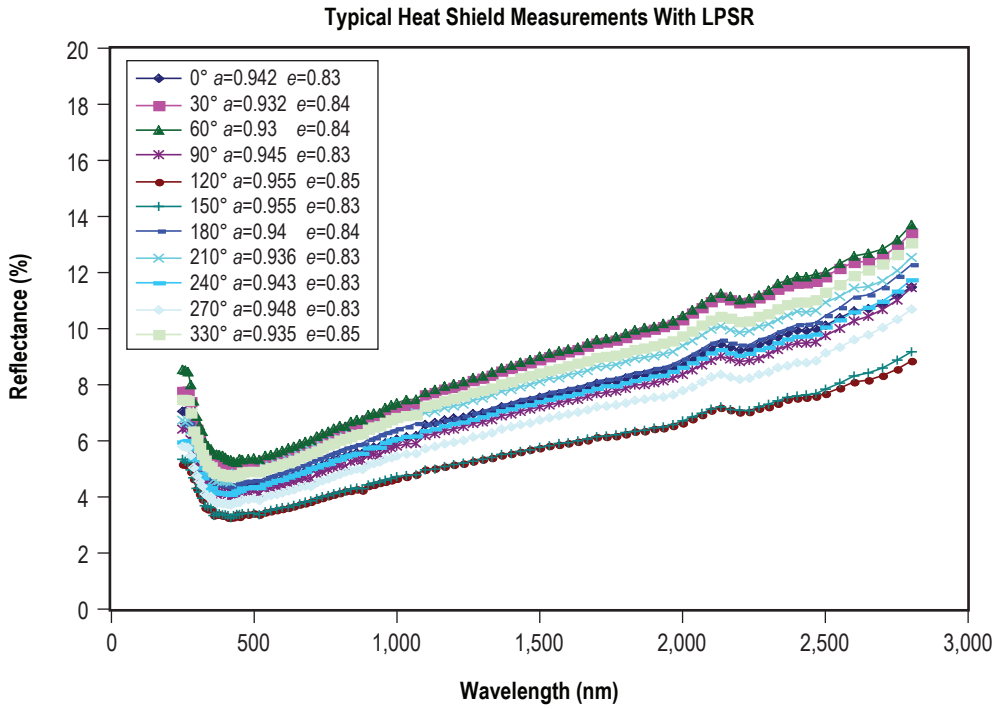

Figure 9. Variations in heat shield reflectance.

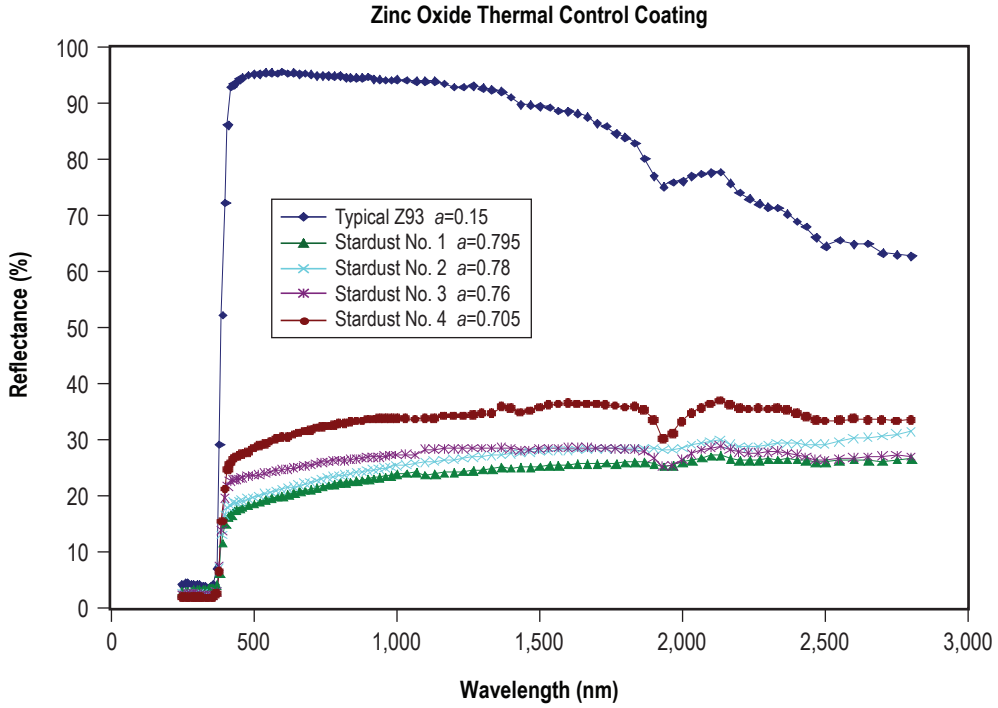

Figure 10. Z93 reflectance comparison.

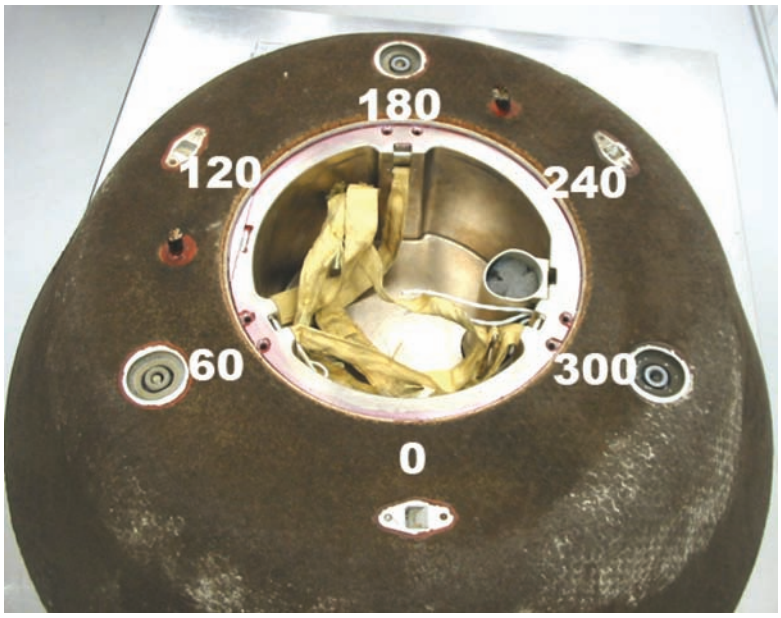

Figure 11. Backshell circumference references.

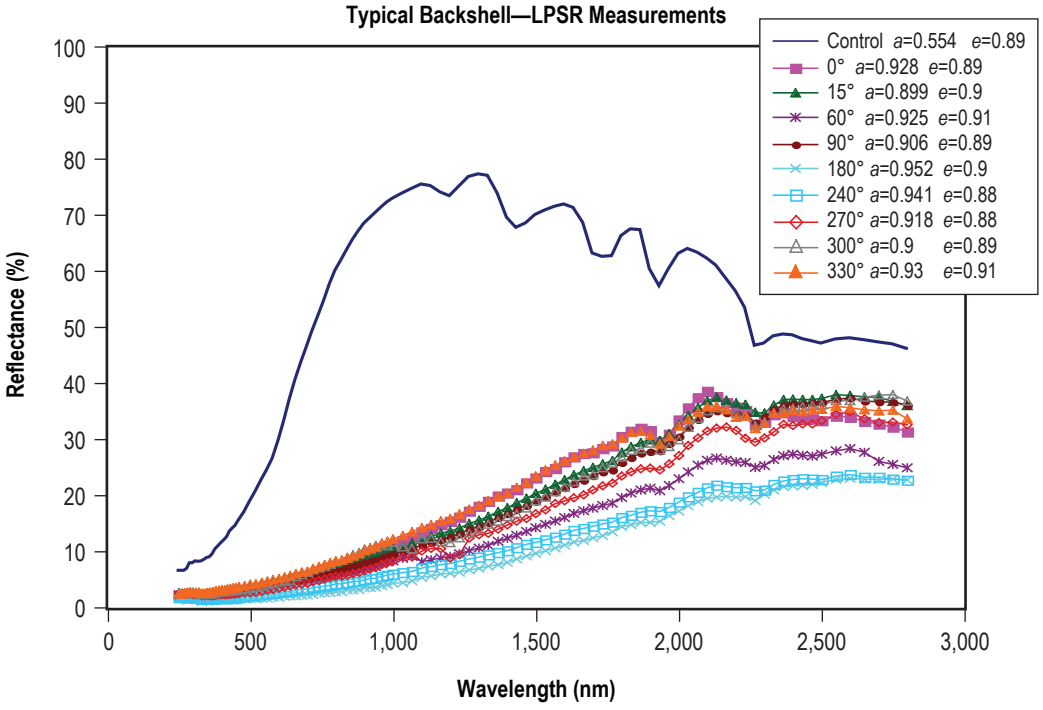

Figure 12. Backshell reflectance measurements.

Although backshell solar absorptance measurements varied somewhat, based on the distance from the heat shield rim, there was no distinctive pattern, as shown in figures 13 and 14.

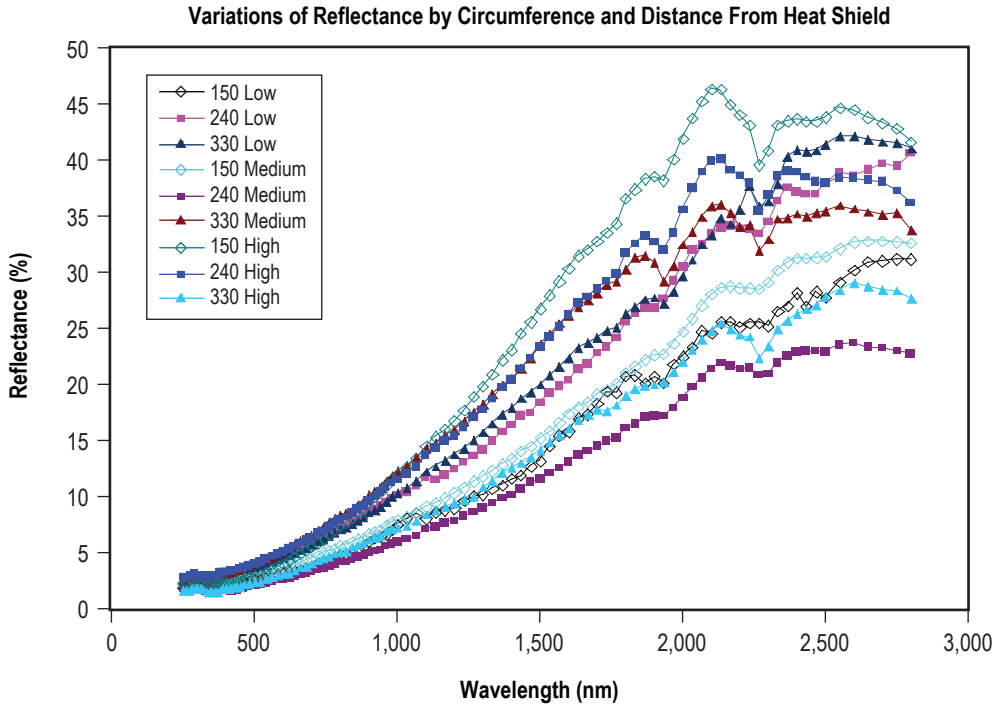

Figure 13. Backshell reflectance variations.

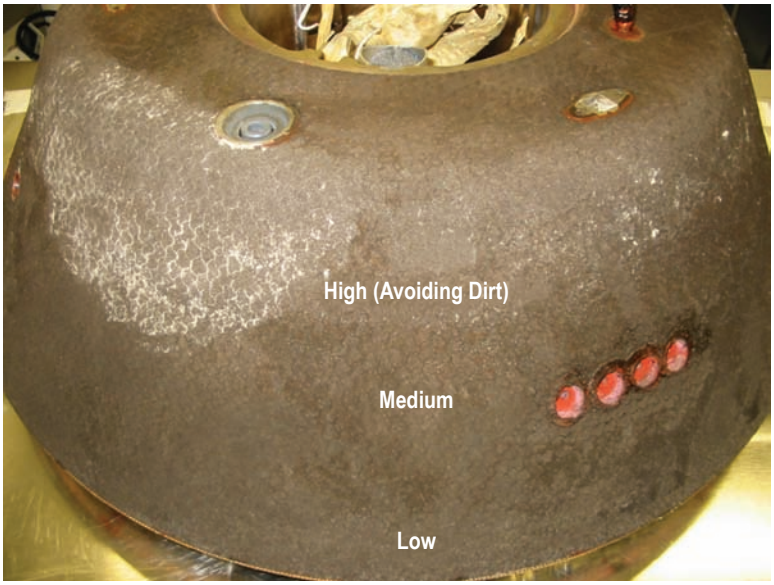

Figure 14. Areas of reflectance measurements of the backshell at 240° (see legend, figure 13).

The LPIR measurements were fairly consistent across the backshell. Figure 15 shows the change in reflectance from the original SLA–561.

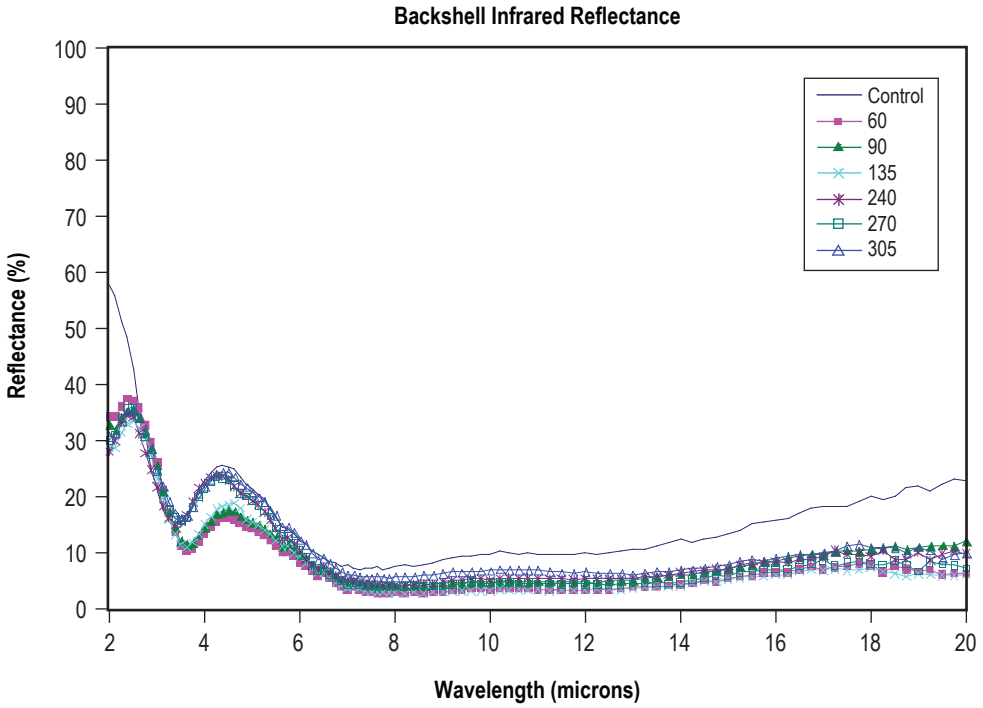

Figure 15. Change in SLA–561 reflectance.

Black light observations indicated outgassing from the room-temperature vulcanized (RTV) materials used during assembly, figure 16. Seams in the Flexcore were also visible under black light (fig. 17).

Figure 16. Plugs (located at ≈240°) surrounding blue-green areas indicate outgassing from RTV materials.

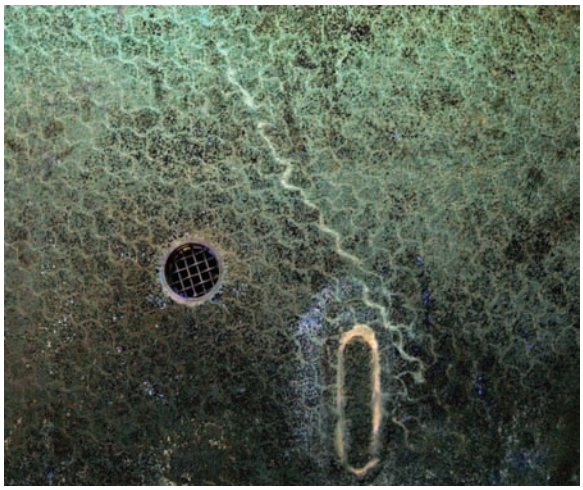

Figure 17. Visible Flexcore seam (≈150°) running lower right to upper left.

Rope Seal. No optical property measurements were made on the backshell rope seal, but visual observations, shown in figures 18–20, indicate no catastrophic failure of the seal. Some areas were darker than others, but this may be caused by particles from the heat shield or char contamination.

Figure 18. Typical area of rope seal.

Figure 19. Outer rope-seal joint.

Figure 20. Inner rope-seal joint.

MLI Blankets. Molecular contaminant deposition was observed on the MLI blankets on both the heat shield and the backshell. The heat shield was bolted onto a stand that blocked optical property measurements of the MLI blankets. Contamination was clearly visible in several locations as shown in figure 21.

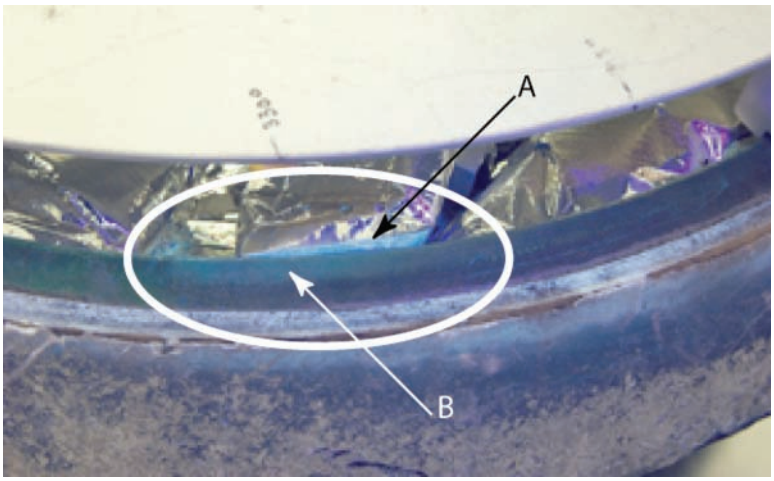

Figure 21. Black light photograph of MLI blankets (a) Outgassing from MLI and (b) also appears on the outer edge of the sealing ring.

Solar absorptance and IR emittance measurements were made on the MLI blankets attached to the backshell, as shown in figure 22. These MLI blankets appeared to be composed of aluminized, perforated, reinforced Kapton® film and aluminized Kapton tape, though this has not been confirmed. In general, MLI aluminized films have solar absorptance ranging from 0.08 to 0.14 and IR emittance of 0.02–0.04. Nomex® reinforced Kapton may have α and ε values around 0.3 and control samples of these materials were not available.[3] Typical aluminized Kapton data are presented with the Stardust data in figure 23.

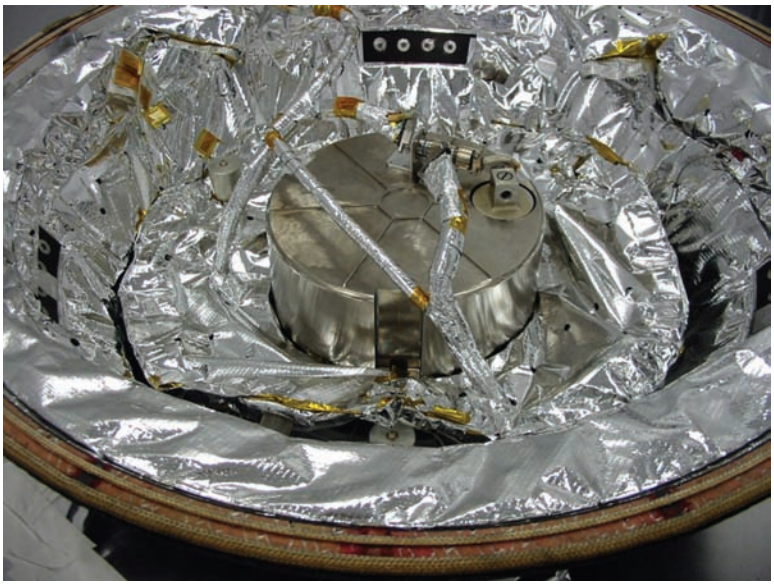

Figure 22. MLI blankets on Stardust backshell.

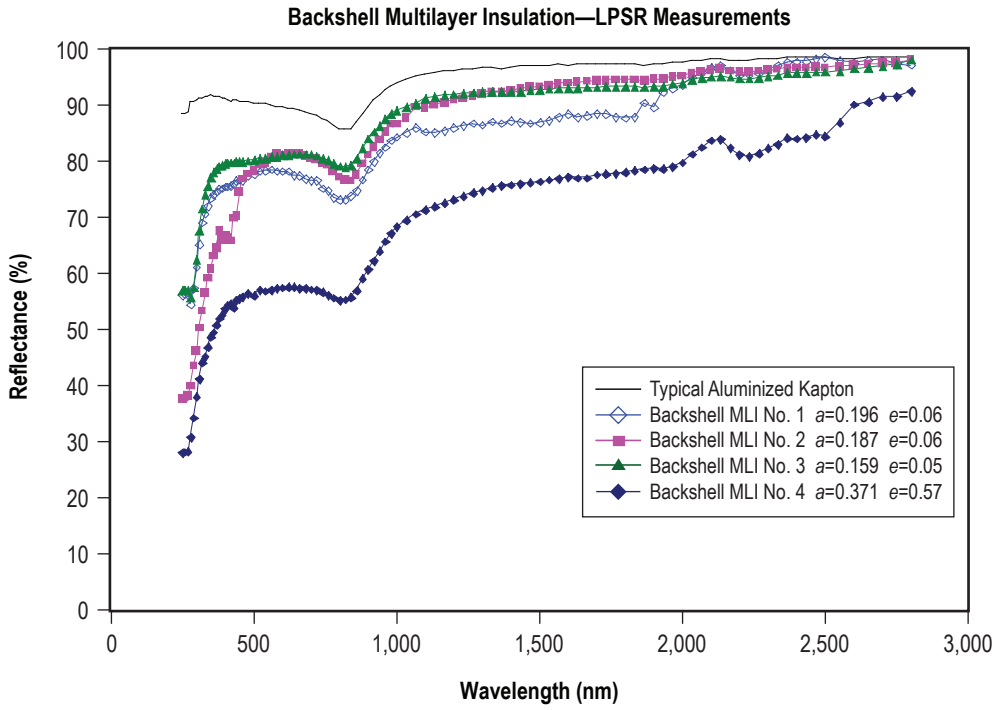

Figure 23. Stardust MLI blanket reflectance compared to typical Kapton reflectance.

The IR emittance of the aluminized film varied from 0.05 to 0.14, with most measurements being around 0.06. This change in emittance, along with the increase in solar absorptance, is more likely related to contamination than to space exposure. Areas with higher IR emittance measurements had brighter fluorescence under black light illumination. Examples of this contamination are shown in figures 24–26.

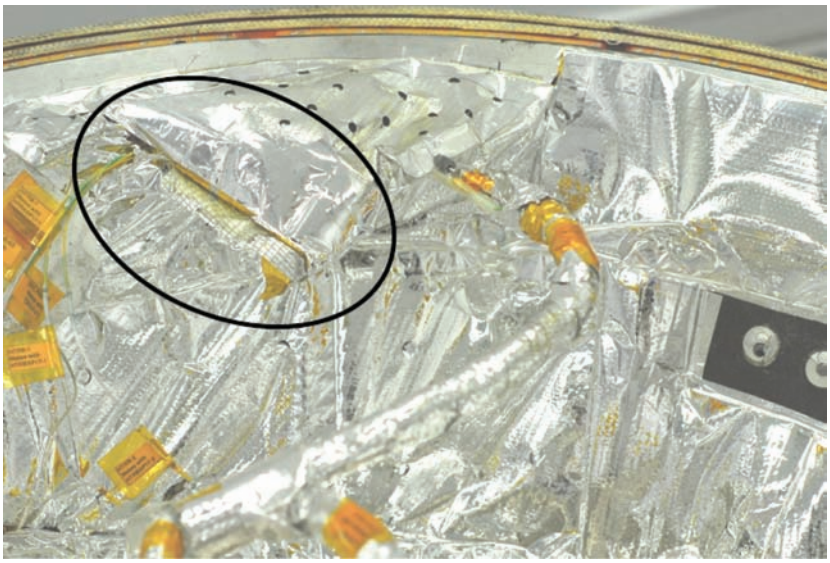

Figure 24. Contamination visible in normal light on backshell MLI; circled area is shown again in figure 25.

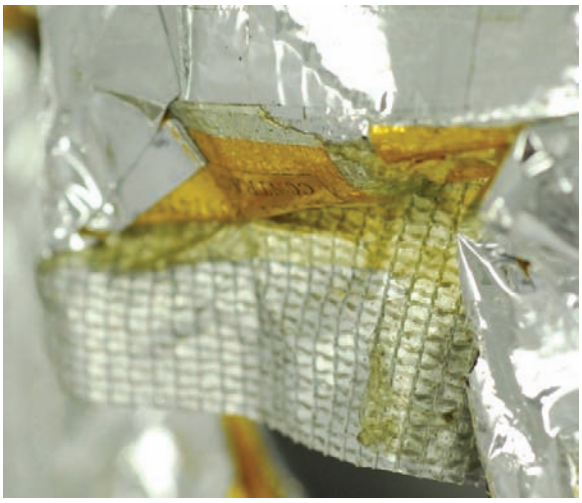

Figure 25. Circled area of contamination in figure 24 from different angle.

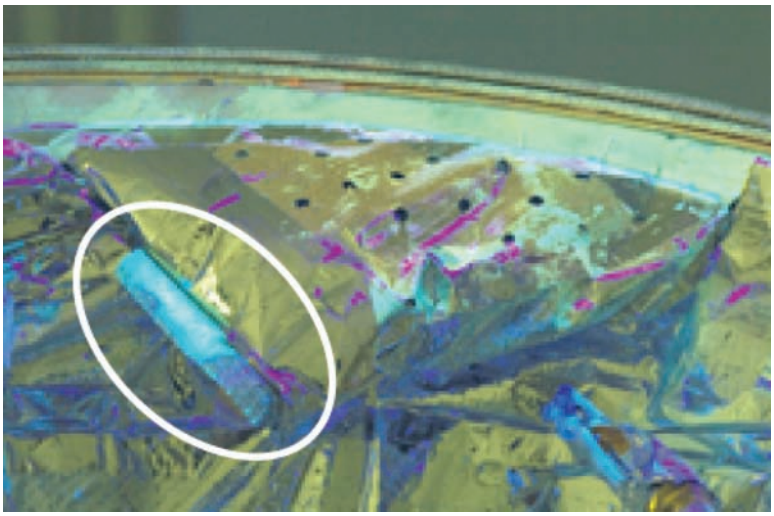

Figure 26. Same area under black light.

Kevlar Straps. Kevlar straps attached to the backshell are visible in figure 11. They are somewhat stained by char particles but are in excellent shape otherwise. LPSR measurements of two of the straps are shown in figure 27.

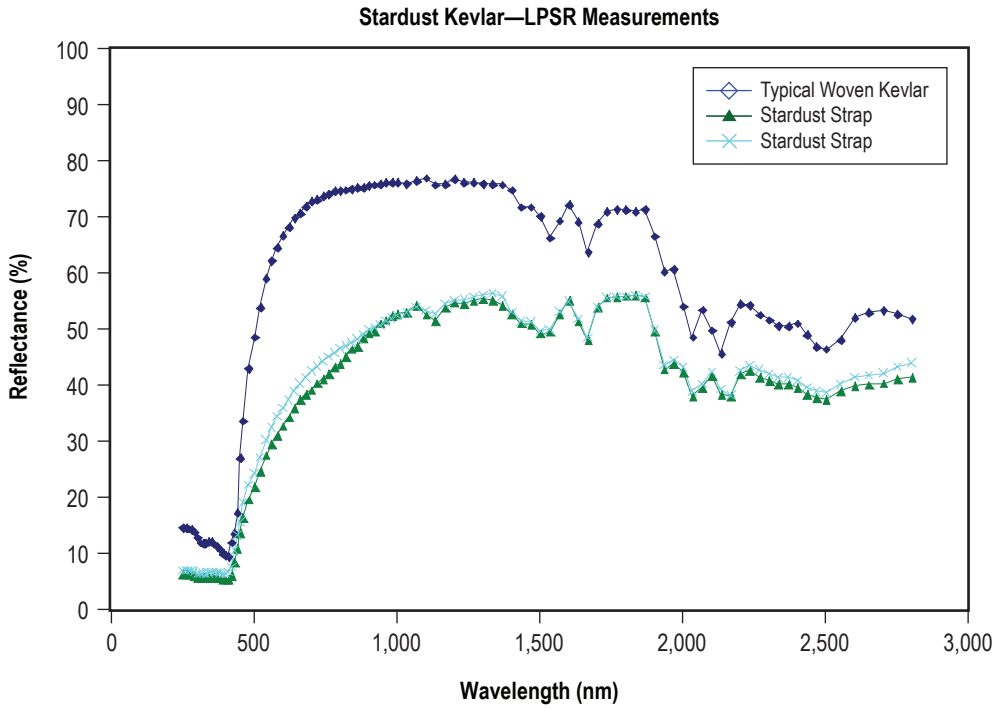

Figure 27. LPSR measurements of two Kevlar straps.

Implication for AME Goals. This AME task analyzed subsystem-level flight hardware, confirms the capability readiness level (CRL) of 7 for these materials, and has provided safety and reliability data that prove the materials' performance. What has been learned about material behavior and property changes during long-term operation and exposure in space can be directly applied to materials selection and design of future robotic and human missions, and can improve ground simulations of the space environment.

Possible Future Research

Next Steps. Additional disassembly of the Stardust capsule is planned, as well as coring of the heat shield and backshell to determine pyrolysis zone depth. PICA was one of the ablative materials irradiated in the Lightweight Nonmetallic Thermal Protection Materials Technology Project (LNTPMTP) at MSFC. Comparing the ground-tested PICA to the flight cored PICA, particularly with FTIR analysis, would be helpful in studying the radiation effects and determining the accuracy of ground simulations and dose-depth profiling. Further investigations into contaminant film on the MLI blankets are needed to determine the extent and composition of contamination and its effect on optical properties. This effort may be especially important for Stardust scientists, as the presence of silicone may interfere with identifying organic materials in the cometary impacts. In addition, the techniques and data used for this NDE postflight assessment of materials properties can be used for the analysis of hardware returned from the Moon and other planets.

Value of Next Steps. Investigation of the contamination of the MLI blankets may not only help the science team members who are analyzing organic compounds in the cometary and interstellar material, but it may also help with Genesis investigations. A brown discoloration was found on the Genesis Al canister shield, only on surfaces exposed to the Sun and solar wind hydrogen.[4] X-ray photoelectron spectroscopy analysis of this contaminant indicates the presence of hydrocarbon, fluorine, and silicon contaminants, likely polymerized by the UV exposure. There may be one or more common materials used in the Stardust and Genesis sample return canisters that are clearly contraindicated for spacecraft use where contamination control is desired.

While each returned mission will have its own lessons and opportunities for future experiments, comparing data from several missions will reveal how the harsh environmental conditions in space erode material, component, and system performance. This knowledge will assist scientists, materials engineers, and designers in developing improved materials or material protection systems for future spacecraft, including those that carry humans far from Earth.

Future Research

Validation of the PICA is especially important for design of the crew exploration vehicle (CEV), because the TPS ablator used on Apollo (Avcoat 5026–39/HC–G) is no longer available.[5] Researchers will also gain insight into new uses for the analyses techniques and develop new protocols that may improve analysis sensitivity.

Additional Information

The PI will publish a NASA technical paper detailing the spacecraft materials' conditions, measurements performed, evaluation of durability in the space environment, and recommendations for further testing.

References

1. Laub, B.: "Development of New Ablative Thermal Protection Systems," http://asm.arc.nasa.gov/materials.html.

2. Private communication with Preston Landry, Staff Engineer, Lockheed Martin Michoud Operations, August 21, 2006.

3. *Sheldahl Red Book: Aerospace Thermal Control Materials and Films*, Northfield, MN, May 2006, http://www.sheldahl.com/Product/bulletins/Redbook.pdf

4. Burnett, D.S.; McNamara, K.M.; Jurewicz, A.; and Woolum, D.: "Molecular Contamination on Anodized Al Components of the Genesis Science Canister," Lunar and Planetary Science, Vol. 36, Houston, TX, 2005.

5. "Aerocapture, Entry, Descent, and Landing (AEDL) Human Planetary Landing Systems, Section 10, AEDL Analysis, Test, and Validation Infrastructure," Capabilities Road Map Briefings to the National Research Council, presented by J. O. Arnold, 2005.

Acknowledgments

- Carlton Allen, Michael Zolensky, and Karen McNamara of the JSC Astromaterials Acquisition and Curation Office for access to Stardust.

- Carol Schwarz, Norma Ramirez, Ron Bastien, and Tom See, engineering support contractors, for their assistance while the PI was at JSC.

- Robert Markowitz (JSC) for black light photography.

- Dean Kontinos (ARC), Betsy Pugel (Goddard Research Center (GRC)), Joe Vellinga (Lockheed Martin), and Preston Landry (Lockheed Martin) for information on the Stardust materials.

- Beth Cook (MSFC AME Project Lead), Bonnie James, Bryan Barley, and Dennon Clardy (MSFC), and Twila Schneider (ICRC), for their support at MSFC

- Charlotte Shea, Qualis Corporation, for assistance with this TM.

3.2 Aerocapture and In-Space Propulsion Materials on the International Space Station Experiment 6

PI—Miria Finckenor, NASA MSFC Environmental Effects Branch, Materials and Processes Laboratory.

Objective

Spacecraft and other space equipment needed for the Vision for Space Exploration require the best possible materials for their structures, radiation protection, thermal control and other systems. These materials must be able to withstand the rigors of the space environment including UV radiation, vacuum, atomic oxygen (AO), thermal cycling, and meteroid impacts and must to maintain their mechanical integrity and thermooptical properties. While ground-based testing provides critical information leading to the characterization of materials for space-based use, no simulator on Earth can reproduce the effect of the combined exposure environment actually experienced in space. To this end, MSFC has partnered with Langley Research Center (LaRC); GRC; ARC; AFRL; The Boeing Company; Physical Sciences, Inc.; Ball Aerospace Corporation; and a number of universities to build a flight experiment—Materials on International Space Station Experiment (MISSE). This AME effort funded the contribution of a number of material samples for passive exposure on MISSE–6 to be flown aboard the International Space Station (ISS) for 1 yr.

Description of Research

MISSE–1 and MISSE–2, the suitcaselike trays (fig. 28) containing the samples, were passively exposed on the ISS from August 2001 to July 2005. These first two packages were scheduled for 1 yr of exposure, but the Columbia accident and subsequent grounding of the Space Shuttle fleet extended the mission. Some of the polymeric film samples were lost because of the longer exposure, and the UV radiation monitors were saturated. Most samples, however, yielded significant data on the long-term effects of the space environment. Valuable data were gathered about the ISS thermal cycles, radiation environment, contamination deposition, and shielding effects of ISS hardware. MISSE–5, shown in figure 29, was delivered to the ISS in July 2005 and scheduled for return in September 2006, it focused on solar cell technology, with over 200 thin material samples attached to a thermal blanket. MISSE–3 and MISSE–4, similar to MISSE–1 and MISSE–2 and shown in figure 30, are suitcaselike containers with a large variety of passively exposed samples and some environmental monitors. These samples were delivered to the ISS in July 2006, deployed by extravehicular activity (EVA) on August 3, and will be exposed for approximately 1 yr.

MISSE–6 consists of two suitcases—6A and 6B—that contain both active and passive experiments. MSFC was initially granted space for two passive trays, one on the ram face and one on the wake face of MISSE–6. The MSFC payload also includes a scale ballute module box and two smaller passive trays that will be attached to the MISSE–6 baseplate. Each 6B tray (figures 31 and 32) holds 46 samples, while the module and smaller trays hold a total of 9 samples. The major categories of MSFC experiments are ballute material, aluminum-lithium (Al-Li) alloys, thermal protection materials, radiation shielding materials, crack repair materials, and thin films. Each of these categories, their significance, and specific samples are fully described in the Rationale and Results section.

(a)

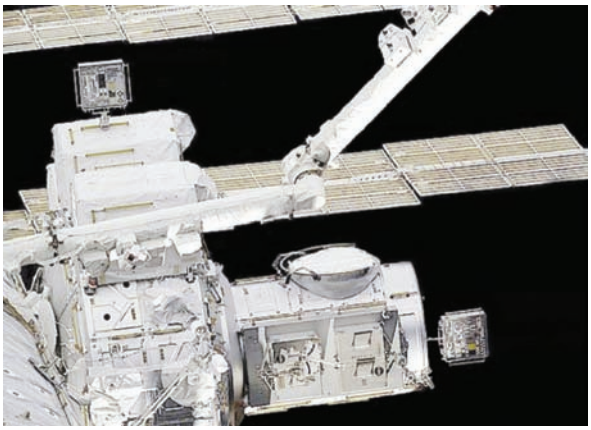

(b)

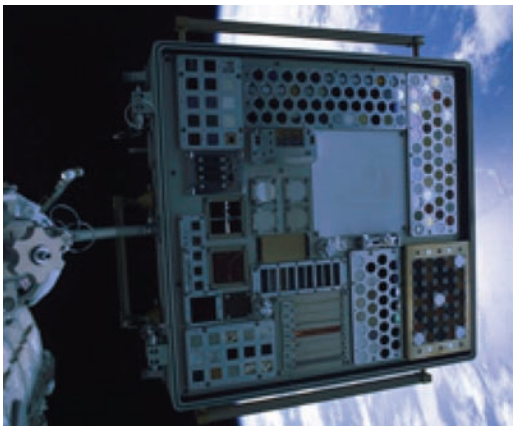

Figure 28. MISSE–2 (a) and closeup of MISSE–1 (b) on the ISS.

Figure 29. MISSE–5 mounted outside on the ISS.

(a)

(b)

Figure 30. MISSE–3 (a) and MISSE–4 (b) mounted outside on the ISS.

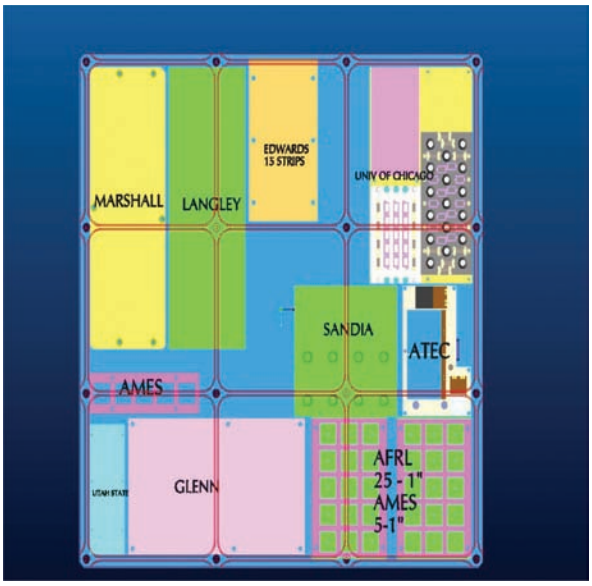

Figure 31. MISSE–6B sample layout for wake-face tray, UV only.

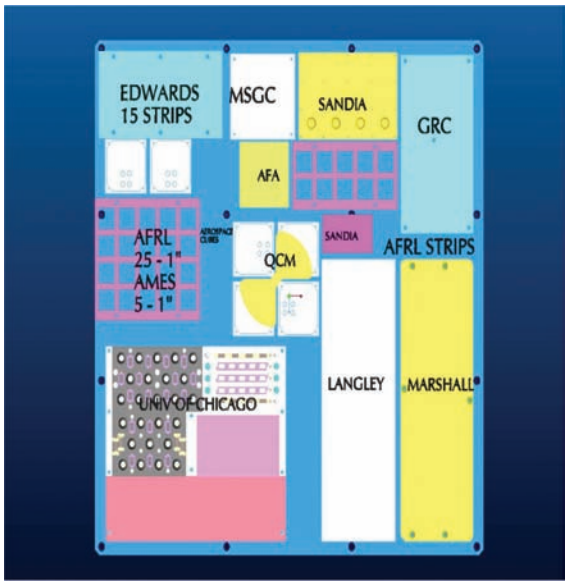

Figure 32. MISSE–6B sample layout for ram-face tray, AO plus UV.

Research Method Description. The MSFC PI identified the candidate materials with input from materials experts from both industry and Government. She worked with the Exploration Science and Technology Division to ensure desired materials were selected. Some materials were selected because of past results in flight/ground exposure experiments. Once the candidate materials samples were secured or fabricated, they were baked in a thermal vacuum to minimize outgassing. Some of the newer materials were tested for flight qualification in accordance with NASA–STD–6001 testing, including flammability, toxicity, and thermal vacuum stability. Next, the individual samples in their trays will be delivered to LaRC for integration into the MISSE–6 payload.

Research Method Rationale. The PI used research methods, sample preparation, and loading procedures that had proven successful on earlier MISSE flights for which she served as the MSFC MISSE PI to select candidate materials and integrate them into the MISSE–6 trays. She also consulted with materials experts and scientists and engineers working on NASA's new exploration spacecraft. She used the standard NASA procedures and NASA–STD–6001 tests to qualify materials for spaceflight. For cost effectiveness, all testing was performed in MSFC Materials and Processes Laboratory facilities.

Schedule. The original schedule for this effort has been met and most tasks have been accomplished, as shown in table 1. The scale model ballute remains to be packed in its box and some backup materials samples are being prepared. Also remaining is the delivery of flight hardware to LaRC. MSFC has completed thermal vacuum bakeout of individual samples to ensure minimal outgassing. LaRC has taken responsibility for the final thermal vacuum bakeout. Hardware delivery will likely take place in October 2006 rather than September. This delay is for two reasons: (1) Some of the experiments on MISSE–6 required more time to complete flight qualification tests and (2) STS–115 was launched on September 9, 2006 and returned to Earth September 21 with the MISSE–5 experiment. Since many of the same people are on both the MISSE–5 and MISSE–6 teams, travel funds can be used most efficiently by deintegrating MISSE–5 at the same time MISSE–6 is integrated.

Table 1. FY 2006 schedule.

Task	D	J	F	M	A	M	J	J	A	S
Candidate material selection	■	■								
Sample fabrication			■	■	■					
Sample characterization				■	■	■				
NASA STD–6001 tests						■	■			
Final assembly								■		
Thermal vacuum bakeout									■	
Delivery of flight hardware										■

Rationale and Results

Ballutes. The scale ballute module, originally proposed for this AME task, evolved into one smaller ballute module box and two small passive sample trays, as shown in figure 33, based on the need for more flexibility in the payload layout. Ball Aerospace provided strips of seven different ballute materials, listed in table 2, that have been accordion folded into the trays to allow investigation of blocking and cold welding effects. The ballute materials will be flown on the underside of the MISSE–6B baseplate.

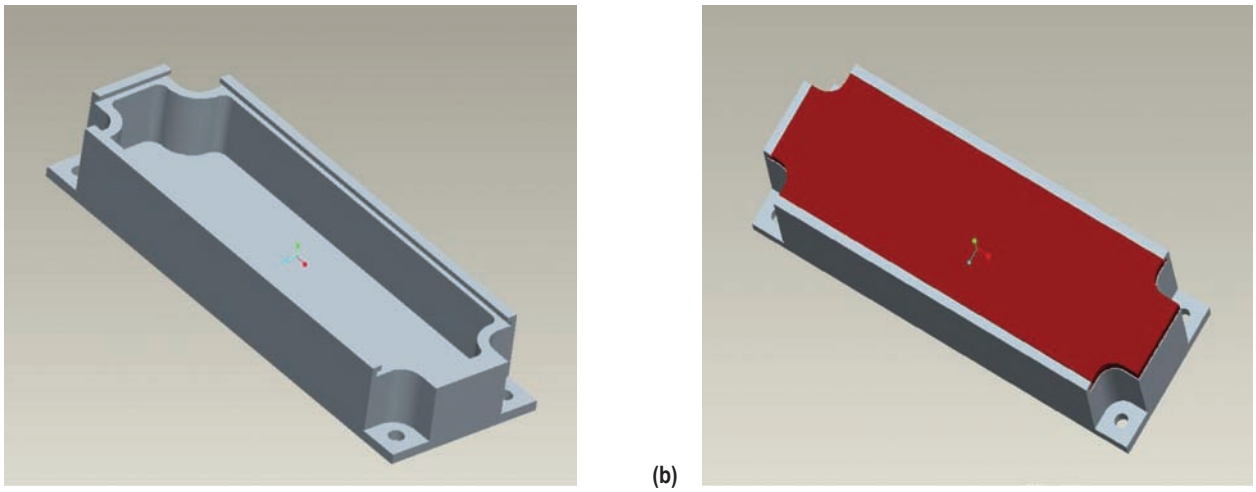

Figure 33. Empty modular box (a) will be packed with ballute material (b).

Table 2. Ballute materials selected for MISSE–6.

Material	Thickness (μ)	Material	Thickness (μ)
Seamed Upilex S	12.5, 25	Seamed PBO	7.5
Upilex S	7.5, 12.5, 25	PBO	7.5

Aluminum-Lithium Alloys. Al-Li alloy 2195 is currently used on the Shuttle ET because of its strength and weight savings over other Al alloys. The crew launch vehicle (CLV), cargo launch vehicle (CaLV), and CEV plans call for using Al-Li 2195 to save weight. While a large amount of data is available on the mechanical properties of Al-Li, very little is known about its durability in the space environment. Al-Li 2090 and Weldalite Al-Li were flown on the third evaluation of oxygen interaction with materials (EOIM–3) Shuttle flight experiment in 1992. These samples lost mass because of interaction with AO in low-Earth orbit (LEO), though it should be noted that these samples were untreated. A conversion coating may provide adequate protection from the space environment. MSFC will provide Al-Li 2195 frames, wide enough to allow optical property measurements, that will be used to hold down thin polymeric film samples. These frames preflight weight has been determined so any losses in mass can be measured when the samples are returned.

Thermal Protection Materials. One of the traditional goals of the MISSE program has been to under-stand the interactions among the various space environment factors and their combined effects on materials and to use this flight data to anchor ground testing. The LNTPMTP tested a variety of CMCs, ablator materials, and tile materials in a simulated LEO environment with the thermal protection materials having the most promising results selected for flight on MISSE–6, (table 3). Material sample ground-based testing included space radiation exposure equivalent to 30-days duration Earth-Moon mission profile. Other samples were tested in the MSFC Hypervelocity Impact Test Facility to simulate meteoroid/space debris impact. A third set of samples, consisting of all CMCs, were exposed to 2×10^{20} atoms/cm^2 of 5-eV AO. Silicon carbide-silicon carbide (SiC-SiC) and hafnium carbide (HfC) coated carbon-silicon carbide (C-SiC) appeared to have good durability in the simulated AO environment, as shown in figure 34, so these were selected to fly on MISSE–6. In addition to pristine test materials, one set of samples was damaged and then repaired using techniques refined during Return to Flight (RTF) investigations. ARC also provided 12 samples of proprietary thermal protection materials in support of aerocapture technology.

Table 3. LNTPMTP materials selected for MISSE–6.

Manufacturer	Material	Type
C–CAT	SiC-coated ACC–6	CMC
C–CAT	SiC-coated ACC–6	CMC damaged and repaired
PSI	SiC-coated C–C	CMC
Materials and Electrochemical Research Corporation	SiC/HfC-coated C–C	
General Electric	SiC/HfC-coated C-SiC	CMC
NASA ARC/Boeing	Boeing rigid insulation-20 (BRI–20)/high-efficiency tantalum-based ceramic (HETC)/RCG	Tile
Raytheon	Hotblox® ceramic	Ablator
Raytheon	Hotblox Lite ceramic	Ablator
ATK Thiokol COI Ceramics	SiC-SiC	CMC

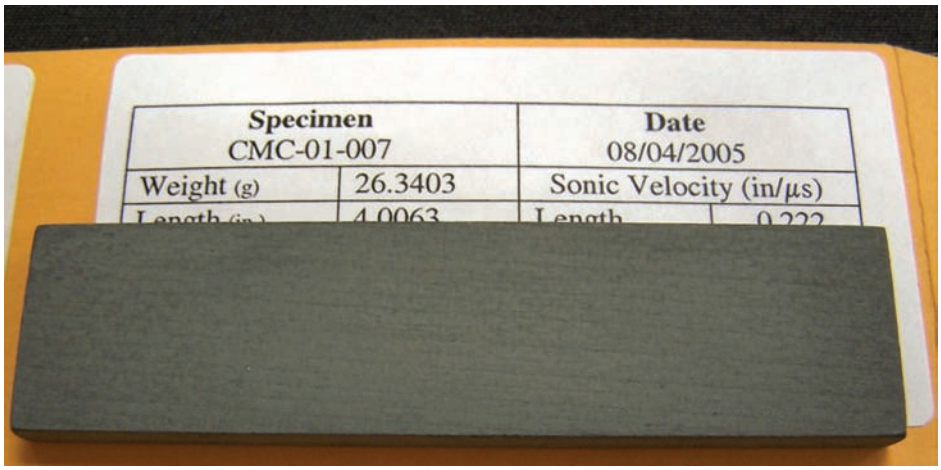

Figure 34. SiC-coated ACC–6, thermal protection material, performed well after ground-based testing exposed it to AO. A similar sample was selected for flight on MISSE–6.

Beta cloth is a woven glass-fiber mat impregnated with Teflon® and used primarily as an outer cover for MLI blankets. The U.S. Environmental Protection Agency (EPA) has called for perfluorooctanoic acid (PFOA) elimination in Teflon manufacture. As of early 2006, Saint-Gobain (formerly Chemfab), the manufacturer of beta cloth for ISS insulation blankets, complied with the EPA and is using Teflon manufactured without PFOA in their beta cloth. It is not known at this time if PFOA elimination will affect the durability of beta cloth in the space environment, therefore, ground testing with AO and UV is planned. For comparison, samples of the PFOA-free version and the old version of beta cloth will be flown on MISSE–6. Beta cloth with grounding thread was also selected for flight on MISSE–6.

AZ Technology has provided a number of electrically conductive thermal control coatings for MISSE–6 in both white and flat black. Electrically conductive coatings will be a vital part of lunar dust mitigation. Through the ISS office, AZ Technology has also provided samples of AZ93, AZ93 with protective Teflon coating, and electroless nickel (Ni). These materials will be compared to samples from the same batch to be tested in simulated solar environment at MSFC.

Crack Repair Materials. An on-orbit repair system material that was selected for MISSE–6 is the non-oxide adhesive experimental (NOAX) polymer sealant that is impregnated with C-SiC powder. NOAX was tested as a crack repair material for reinforced carbon-carbon (RCC), as used on Space Shuttle leading edges during EVAs on STS–114 in July 2005 and on STS–121 in July 2006. Samples of NOAX have been provided for MISSE–6 to determine long-term durability in the space environment.

Radiation Shielding Materials. Radiation shielding is needed to protect humans during long-duration space missions. Two different sets of materials will address this concern on MISSE–6. Radiation Shield Technologies' Demron™ fabric is a lead-free cloth that advertises protection from ionizing radiation and x-rays, and it may be useful in a space suit or an MLI blanket. Three different versions of Demron, provided by the manufacturer, were selected for MISSE–6.

Materials supplied by Plasma Processes, Inc., are addressing the need for spacecraft structural materials that can provide radiation shielding. The company provided multilayer samples with low-Z (low atomic number) composition, which is optimum for shielding against galactic cosmic rays and solar proton events.

Another way to address radiation shielding on the Moon and Mars is by in situ resource utilization. MSFC has been developing several methods for processing regolith to form ceramic compounds. Samples of both lunar simulant and martian simulant processed into shielding materials will be flown on the wake face of MISSE–6.

Thin Films. Table 4 lists the thin-film samples selected for MISSE–6 from SRS Technologies. The solar sail films will be flown with magnesium fluoride windows to protect them from AO. The windows will transmit 90 percent of the UV light to the samples and also act as contamination witness samples.

Table 4. Thin-film samples selected for MISSE–6.

Material
EP2550
Conductive white EP2550
Conductive white clear polyimide 1 (CP1)
IR transparent black CP1
Conductive black CP1
AO-resistant CP1
Zero CTE film
CP1 retains from GRC's Plum Brook Station solar sail

Other Samples. In addition to these materials samples, certain common materials will be flown to determine AO fluence.

Implication for AME Goals. This AME flight experiment will increase the CRL of all the tested materials to CRL 7 and give NASA the opportunity to flight-test materials needed for the CLV, the CEV, the CaLV, the Lunar Precursor and Robotic Program (formerly the Robotic Lunar Exploration Program), and the James Webb Space Telescope. Since the samples were tested in ground-based facilities for flight qualification, NASA acquired valuable ground-based testing data to help downselect optimum materials for Exploration spacecraft. By playing an active role in the MISSE experiments and cooperating with other NASA Centers and industry, MSFC engineers and scientists will expose materials to the combined effects of the space environment and gather information that will enhance the design, durability, and safety of future spacecraft.

Potential Future Research

Next Steps. Postflight activities will focus on analyzing the MISSE–6 samples and comparing data from space exposed samples to data from samples tested in space environment ground simulators. Data on materials performance will be placed in the Materials and Processes technical information system (MAPTIS) databases, which are accessible to spacecraft designers. The MISSE program will

continue with MISSE–7. Results from prior MISSE experiments can be used to downselect materials for future MISSE experiments. MSFC should continue to play a role in MISSE so the Center can obtain space exposure data on materials used for future space hardware.

Value of Next Steps. What is learned through postflight analyses of candidate materials will be relevant to the selection and continuing characterization of structural, thermal, and radiation protection materials required for future human space exploration programs and for solar sail, tether, and ballute technologies. Understanding the effect of the space environment on CMCs and ablatives that may be used in heat shields and on the multipurpose materials that also may provide shielding from harmful radiation is especially vital to the successful development of CEV and the safety of its occupants.

Usefulness of Future Research. The anticipated result of this effort is concrete evidence as to whether certain spacecraft materials will be able to withstand the damaging effects of space for a reasonable amount of time. The results of materials tests on MISSE–6 and other MISSE flights will directly benefit designers as they select materials for new exploration hardware and other space flight hardware, providing them with the only in situ environmental data on some of these materials. These data are crucial in determining which materials are best suited for longer duration missions in the unforgiving space environment.

Additional Information

A NASA Technical Paper will be published by the PI detailing the materials selected for flight on MISSE–6, reasons for the selection, and test data gathered during preflight evaluation.

Acknowledgements

The author gratefully acknowledges the following people for providing samples for MISSE–6: Pete Valentine and Andrew Hodge (MSFC), Michael Gubert (Jacobs Sverdrup), Jim Masciarelli (Ball Aerospace), Garrett Poe and Mark Johnson (SRS Technologies), Mairead Stackpoole (ELORET/ARC), Johnny Fu (ARC), Sajjad Reza (Lockheed Martin), Jim Zwiener (AZ Technology), Tex Clark (Radiation Shield Technologies), Elizabeth Schofield (Plasma Processes, Inc.), Subhayu Sen (BAE Systems), Clare Sokup (Sheldahl), and Rajib Dasgupta (JSC). The author also acknowledges the assistance of Alex Rawleigh, Lisa Roth, Larry Foreman, Paul Johnson, and Bennie Brantley in the hardware development and Ed Watts, Don Burch, and David Wilkie in sample preparation. Many thanks to Beth Cook (MSFC AME Project Lead) and Twila Schneider (Integrated Concepts and Research Corporation) for their support.

The success of the MISSE experiments would not have been possible without the significant contributions of Michael Stropki (AFRL), Robert Walters (Naval Research Laboratory), William Kinard (LaRC), and Gary Pippin (Boeing Phantom Works).

3.3 Measurement of High-Temperature Creep Resistance via Electrostatic Levitation

PIs—Jan Rogers, NASA MSFC; Robert W. Hyers, University of Massachusetts (UMass), Amherst; and Peter Liaw, University of Tennessee (UT), Knoxville.

Co-Is—Jonghyun Lee, UMass and James J. Wall, UT, Knoxville.

Objective

The overall objective of this research was to develop, validate, and utilize an electrostatic levitation (ESL) method for the measurement of creep in materials at high temperature. ESL provided a means to suspend, rotate, and heat a 2-mm diameter spherical specimen, free from contact with any container or test equipment. The project was a collaborative effort involving research teams from MSFC, UMass, and UT. The objectives for each team were as follows:

- MSFC.
  - Design, develop, integrate, and operate sample rotation and analysis systems.
  - Perform ESL-based creep studies.
- UMass.
  - Develop software for rotation rate analysis and online optical strain measurements.
  - Perform finite element modeling of stress and strain distributions in spheres and spheroids due to centrifugal acceleration, including different constitutive relations for creep.
- UT.
  - Make or obtain samples suitable for ESL and conventional creep tests.
  - Perform conventional creep tests for comparison with and the validation of ESL measurements.
  - Perform scanning electron microscopy (SEM), transmission electron microscopy (TEM), and neutron diffraction studies and analyses.

Description of Research

Method. Continuing pressures for higher performance and efficiency in propulsion are driving ever more demanding needs for high-temperature materials. The combination of high stresses and high temperatures may result in creep-induced system failure. The characterization of creep properties is very important where long service life at high temperatures and high stress is anticipated, such as in turbomachinery. Some additional applications of interest to NASA include combustion chambers for advanced chemical rockets, turbomachinery for jet engines, and power conversion in nuclear electric/nuclear thermal propulsion. Some very high-temperature materials are being developed including platinum group metals, carbides, borides, nitrides, and silicides. However, the measurement of creep properties at very high temperatures is, by nature, problematic. Emerging materials with useful high-temperature properties often outperform structural tooling in creep apparatus at the desired testing temperatures. Further-

more, at sufficiently high temperatures, diffusive flow between the specimen and fixture tooling occurs, changing the composition of both. High-temperature physical property data are essential for materials selection and engineering design for refractory applications. Desired temperatures for measurements to support some NASA propulsion and high-temperature applications can exceed the standard operating temperature for most conventional test apparatus which are contained in a furnace (≈1,700 °C). During ESL, electrodes suspend the sample, free from all physical contact during characterization studies.[1] Figure 35 shows images taken during a heating cycle of a sample during ESL. This technique can be used to process a wide variety of materials including metals, alloys, ceramics, glasses, and semiconductors. Additional information about the MSFC ESL facility can be found at:[2] http://esl.msfc.nasa.gov/.

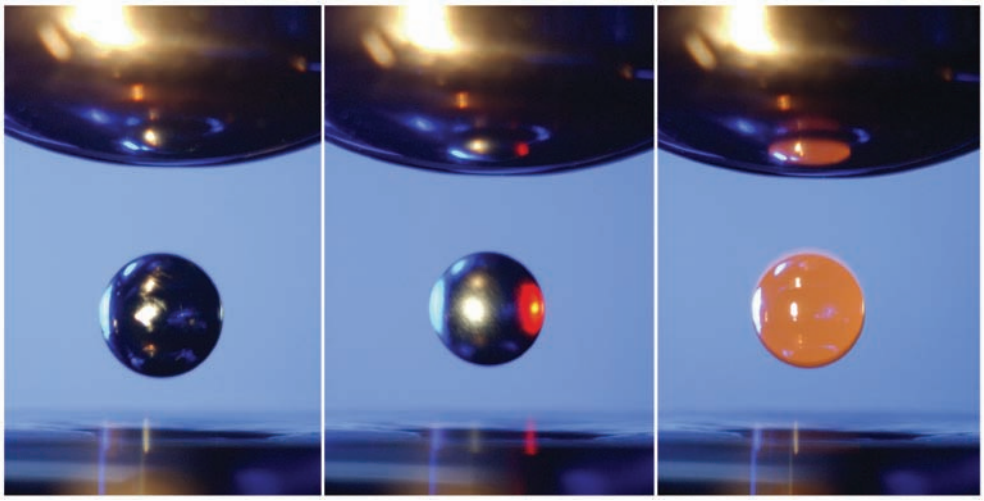

Figure 35. 2–3 mm diameter sample levitated between electrodes and heated by laser.

For these high-temperature creep studies the sample is deformed by centripetal acceleration from rapid rotation. The deformed shapes are analyzed to determine the strain. The rotation was instigated by photon pressure exerted by an incident laser directed off center from the sample in the horizontal plane. Time-resolved deformation behavior of the samples was obtained by high-resolution digital photography. The edges of the sample at different stages of deformation were detected from the images using the *Machine Vision* software developed in the previous work.[3]

Niobium (Nb), a widely used refractory metal and the basis for a number of refractory alloys, was selected for the experiments to develop and validate the ESL creep testing method. Note that the melting point of Nb is 2,468 °C.[4] The ESL studies utilized Nb spheres of 2-mm diameter. Samples were machined into spheres from ESPI Metals, Inc. 99.9-percent purity Nb rod stock. Spheres were made to a tolerance specification of American Bearing Manufacturers Association Grade 200 by Industrial Tectonics Inc. A fiduciary mark scribed on each specimen with a diamond saw facilitated the measurement of the sample rotation rate. The maximum temperature attainable by conventional creep tests for an effective comparison was determined to be 1,985 °C. Note that this was achievable only in a specialized setup at laboratories that specialize in high-temperature testing. Typical creep measurement apparatus are limited to ≈1,700 °C. Application of the heating laser to the sample initiated angular acceleration about

the vertical sample axis at a rate of ≈780 rps/hr. The final angular velocity was measured as 4,878 rps. Deformation of the sample was observed after 300 min and the experiment was continued until the sample dropped due to instability (up to 420 min). Sixth-order Legendre polynomials, equation (1), were fitted through the points on the images corresponding to the sample edges to define the time evolution of deformation (assuming axisymmetry) as follows:

$$r(\theta) = \sum_{i=0}^{6} b_i P_i(cos\,\theta) \ , \tag{1}$$

where a_i are constants, θ is the latitude, and $r(\theta)$ is the radius at a specific latitude. For convenience in implementing a numerical approach for analysis, the Legendre polynomials were rewritten as,

$$r(\theta) = a_0 + a_1 \cos\theta + a_2 \cos^2\theta + \ldots + a_6 \cos^6\theta \ . \tag{2}$$

Video clips, with a frame rate of 10 Hz, of each deforming sample were captured at 30-min intervals before deformation was observed, and every 10-min thereafter. Each video clip contained 100 images of the deforming sample. Each image was analyzed to determine the strain. The average and standard deviation of the deformation at each time are presented for one measurement in figure 36. Solid circles and triangles represent polar and equatorial radii, respectively, and the vertical bars show one standard deviation of the corresponding measurements (in one video clip). Note that the equatorial radius decreases in the beginning, due to surface evaporation of the sample in high vacuum, and subsequently increases as the sample creeps. The increase in the standard deviation of the equatorial radius was caused by slight nonaxisymmetrical deformation on the equatorial plane. Example images of a deforming sample are shown in figure 37.

A set of conventional creep tests were performed on high-purity Nb samples to offer a direct comparison to the ESL creep test. Button-head tensile specimens, with a gauge diameter of 4.55 mm and a gauge length of 25.4 mm, were machined from a 99.9-percent purity Nb rod stock by ESPI in Ashland, OR. The conventional creep tests were performed at Pittsburgh Materials Technology, Inc. (PMTI) using a testing apparatus equipped with an ultrahigh-temperature furnace. The apparatus and samples were adherent to American Society for Testing and Materials (ASTM) Standard E–139. A series of isothermal creep tests were performed to determine the stress exponent, which was subsequently compared to the values obtained using the ESL method. The applied stresses of 1 MPa, 1.5 MPa, and 2 MPa were chosen to allow direct experimental comparison with the ESL creep test. Three creep tests were performed at each of the three load levels. Note that the initial creep test was performed at 2,000 °C, with an applied stress of 2 MPa. Due to an observed interfacial instability between the sample and grips at this temperature, all subsequent tests were performed at 1,985 °C.

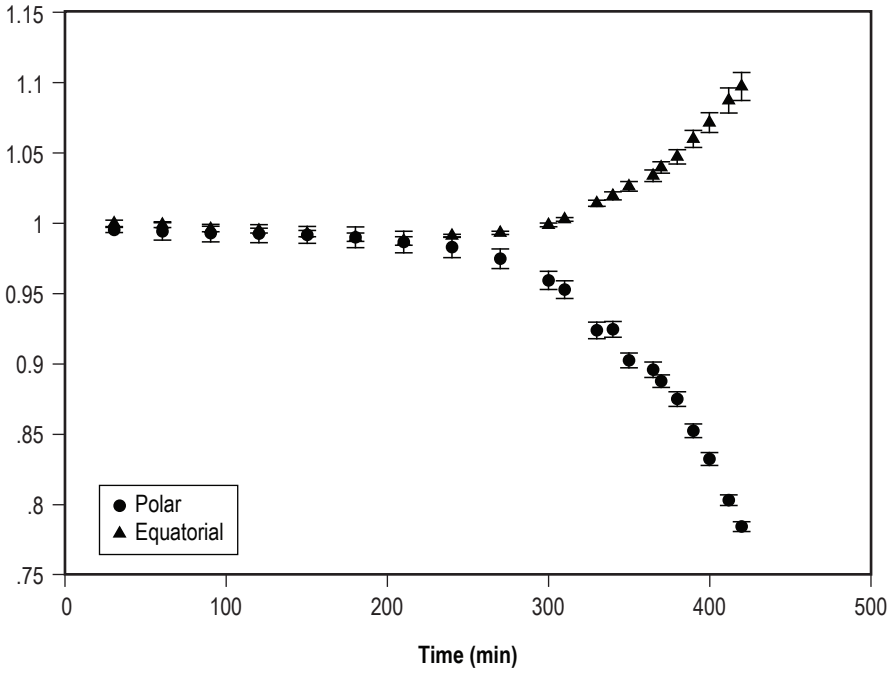

Figure 36. Plot of the change in both the polar and equatorial radii of the sample.

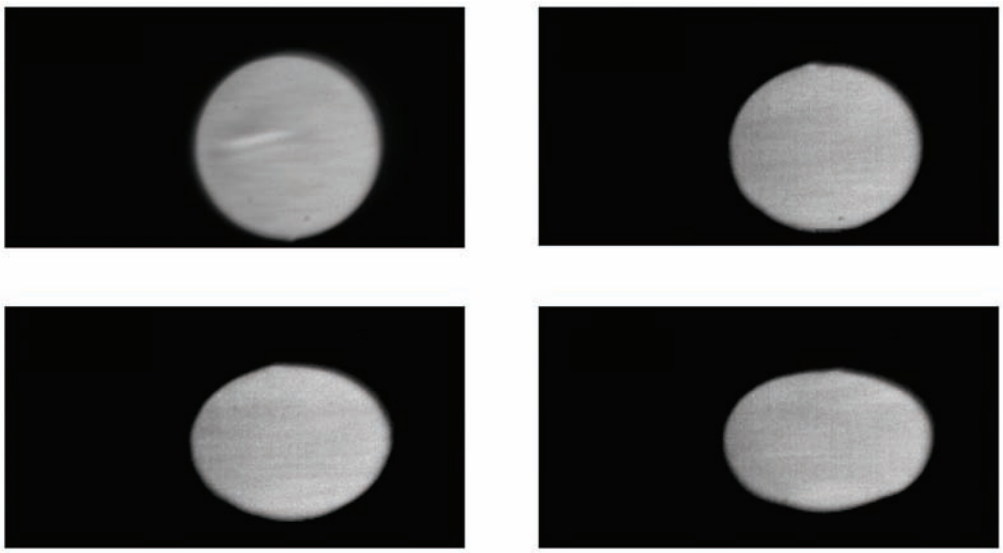

Figure 37. Captured images of a deformed Nb sample. The equatorial radius increases and the polar radius decreases as the deformation proceeds.

Each specimen was loaded into a mounting fixture and placed into a cylindrical furnace. A vacuum was then pumped down to $<2\times10^{-7}$ torr over 24–48 hr. The specimen was then heated to the target temperature over ≈1 hr under zero load. A subsequent hold period of 10 min under a zero load was used for the thermal homogenization. After this period, the preset load was applied and the sample elongation

was recorded at regular intervals. Elongation was measured visually by a technician, using a Gaertner scope, as no extensometer was available that could operate at the test temperature.

Rationale. Results from Keissig and Essmann, demonstrated that creep properties may be determined in electromagnetic levitation tests of rotating spherical samples.[5] Levitated spheres of test material heated to the measurement temperature were rotated at a sufficient rate that centrifugal acceleration caused significant plastic deformation in the sample. This project sought to utilize and validate application of the containerless method of creep measurements using an ESL research platform. ESL provides several advantages over other levitation methods for studies of creep deformation. The optical viewing path is not obscured by coils needed in electromagnetic systems. In addition, ESL studies can be performed on a wider range of samples, including electrically nonconductive materials. The containerless ESL technique provided the acquisition of high-temperature data without interference from a crucible. Prior work demonstrated the feasibility of inducing sample rotation during ESL via photon pressure and using an electromagnetic motor.[6–8] Replicating the results of Nb required a rotation rate of approximately 4,000 Hz in ESL.[1] This rotation rate could be attained using photon pressure from the 200-W YAG laser available at MSFC. As such, the addition of an electromagnetic motor to the MSFC ESL facility was critical to the success of this project.

Schedule

The project duration was approximately 2.25 yr.

Year 1. Development and integration of laser steering apparatus and optical systems. Sample fabrication and test method development. Development of analysis software, and initiation of finite element modeling efforts. Validation studies at Japan Ultrahigh Temperature Materials Laboratory (JUTEM) using ASTM Standard E–389: Standard Test Methods for Conducting Creep, Creep Rupture, and Stress Rupture Tests of Metallic Materials. JUTEM efforts were not successful in providing high-temperature data and were discontinued.

Year 2. The second year activities included development and implementation of the electromagnetic motor to permit independent control of the sample rotation and heating (discontinued because the apparatus overheated at high-rotation rates), development and use of final creep protocols, anneal methods, and performance of ESL studies for comparison with final validation studies. Software development and finite element modeling completed. Sample fabrication and validation studies at PMTI. Additionally, SEM and neutron diffraction on the creep-deformed specimens (ESL and conventional) were performed to compare texture formation in the specimens during creep testing using the two methods. TEM studies are planned under the no-cost extension of this work by UT.

Results

ESL Creep Testing. Creep deformation of approximately 20 samples was measured in ESL at temperatures of 1,950–2,300 °C. These tests demonstrated the capability of the ESL method to determine the stress exponent in a single test on high-precision samples that deform axisymmetrically. Validation testing performed at 2,000 °C showed excellent agreement with conventional testing at 1,985 °C (table 5).

Table 5. Stress exponent estimated from the ESL creep test compared to the existing data.

Stress Exponent	
ESL test, UMass, 2006	2.517
Conventional test, UT, 2006	2.4
Kiessig and Essmann, 1985	2.476
Frost and Ashby, 1982	4.4

Validation With Conventional Creep Testing. The elongation, time, and temperature (constant) data were used for analyses of the conventional creep tests. The creep rate curves, $\delta\varepsilon/\delta t$, were defined by fitting the experimental strain versus time data points in the stage 1–3 transition region with a third-order polynomial and taking the time derivative. The steady state creep rate was then defined as the inflection point on each creep curve ($\delta^2\varepsilon/\delta t^2=0$).

To evaluate the stress exponent of creep in Nb at 1,985 °C, the steady state creep rate from each test, as determined from the experimental data previously described and shown in figure 38, were plotted against time on a log-log plot as shown in figure 39. The data points were fit with a linear function. The stress exponent (slope of the fitted line) was determined to be 2.4.

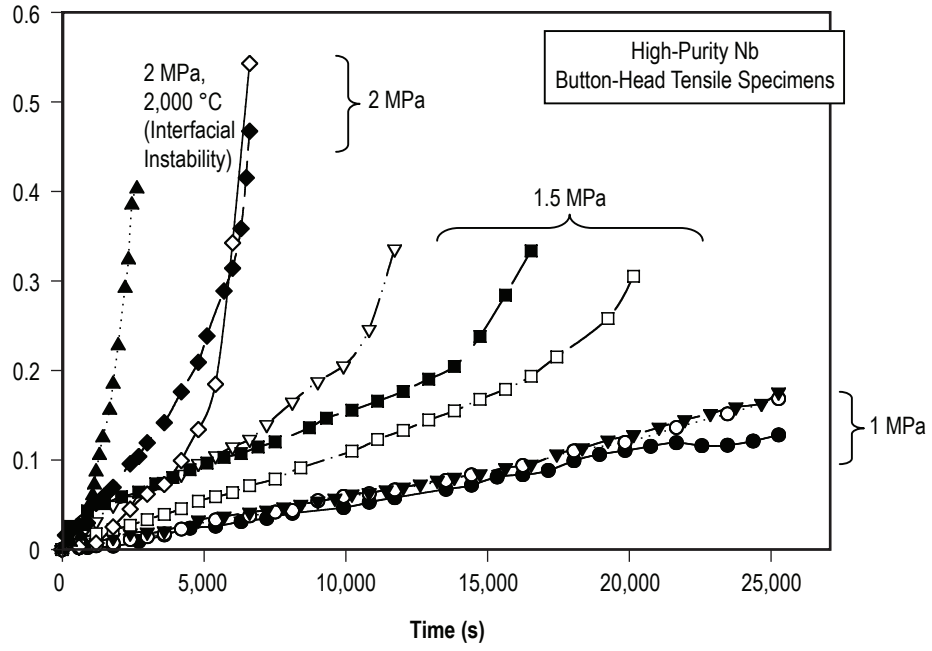

Figure 38. Strain versus time for conventional creep measurements, Nb at 1,985 °C under 1, 1.5, and 2 MPa.

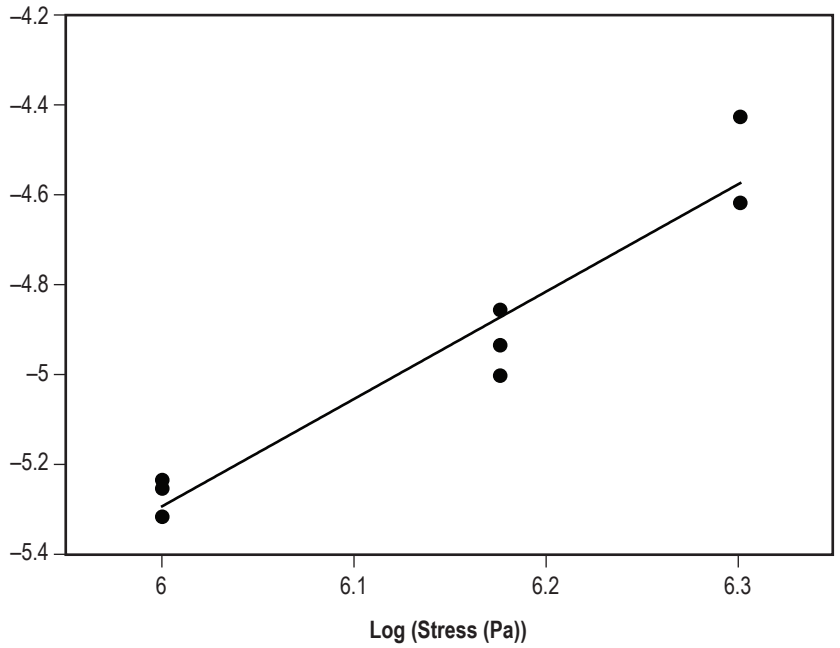

Figure 39. Log-log plot of the steady-state creep rate versus applied stress of Nb at 1,985 °C. The line was fitted with the R^2 value of 0.929.

Modeling. Finite element analyses were used to ascertain the relationship between the deformations observed using the ESL technique and the stress exponent.[9] A sensitivity analysis developed from this finite element model, table 6, shows that the method can very precisely determine the stress exponent in high-precision spheres. These calculations justify the use of very high-precision spheres in future experiments.

Table 6. Range of errors in the stress exponent due to measurement error.

Measurement Accuracy (PPM)	Error Range	Stress Exponent				
		1	2	3	4	5
900	From To	–0.18 0.2	–0.99 0.98	–0.89 0.9	–0.81 0.81	–0.75 0.75
700	From To	–0.14 0.15	–0.76 0.77	–0.7 0.7	–0.63 0.63	–0.58 0.59
500	From To	–0.1 0.11	–0.54 0.55	–0.5 0.5	–0.45 0.45	–0.42 0.42
300	From To	–0.06 0.06	–0.33 0.33	–0.3 0.3	–0.27 0.27	–0.25 0.25
100	From To	–0.02 0.02	–0.11 0.11	–0.1 0.1	–0.09 0.09	–0.08 0.08

Microscopy and Neutron Diffraction. Figure 40 shows SEM images of microstructure in the ESL-deformed samples. The samples showed shear steps that are indicative of the deformation that occured during creep. Figure 41 shows the microstructure of the as-received material. Neutron diffraction measurements were performed at the Los Alamos Neutron Science Center (LANSCE) on the high-pressure preferred orientation (HIPPO) diffractometer to measure texture/orientation in the as-received Nb rods, annealed spheres, and ESL crept samples. The as-received rods showed BCC fiber texture due to the manufacturing process. It was found that the annealing step in the ESL prior to rotation caused massive structural coarsening in the samples, resulting in the formation of single crystals. The ESL crept samples showed streaking of Laue reflection spots, indicative of plastic deformation. In some cases, the ESL deformed samples showed a degree of polygonization of the single crystals, due to high-temperature deformation.

Laue diffraction patterns are formed by a ring of ionization tubes (neutron detectors) surrounding the sample and coaxial with the incident neutron beam. The radiation diffracts to spots in the case of single crystals, and rings in the case of polycrystalline samples. The Laue diffraction patterns show that the annealing step coarsened the spherical sample into a randomly oriented single crystal (possibly a bicrystal), as shown in figure 42. The streaked Laue spots, shown in figure 43, are the result of crystal lattices bending due to a dislocation structure that developed during creep deformation. Note that the weak streaks are diffraction rings from the polycrystalline Al sample holder. TEM analysis is planned at UT to provide additional insight into the dislocation structure of the deformed samples.

AME/In-Space Propulsion Technology Applications. The high-temperature materials which will be advanced by this study represent materials needed for propulsion technologies required to take instruments to new vantage points in-space. Pressures for higher performance and efficiency in propulsion are driving ever more demanding needs for high-temperature materials and characterization data. For example, nuclear thermal propulsions systems operate at ultrahigh temperatures and require components which can tolerate these temperatures. To design components, characterization data including creep resistance, density, and coefficient of thermal expansion (CTE) are needed for emerging refractory materials. As a consequence of this project, equipment upgrades have facilitated access to additional physical property data, previously difficult to impossible to measure. For instance, improvements in the optical systems developed for the high-temperature creep studies have enabled the MSFC ESL facility to provide important thermophysical properties such as density and CTE data at high temperatures.

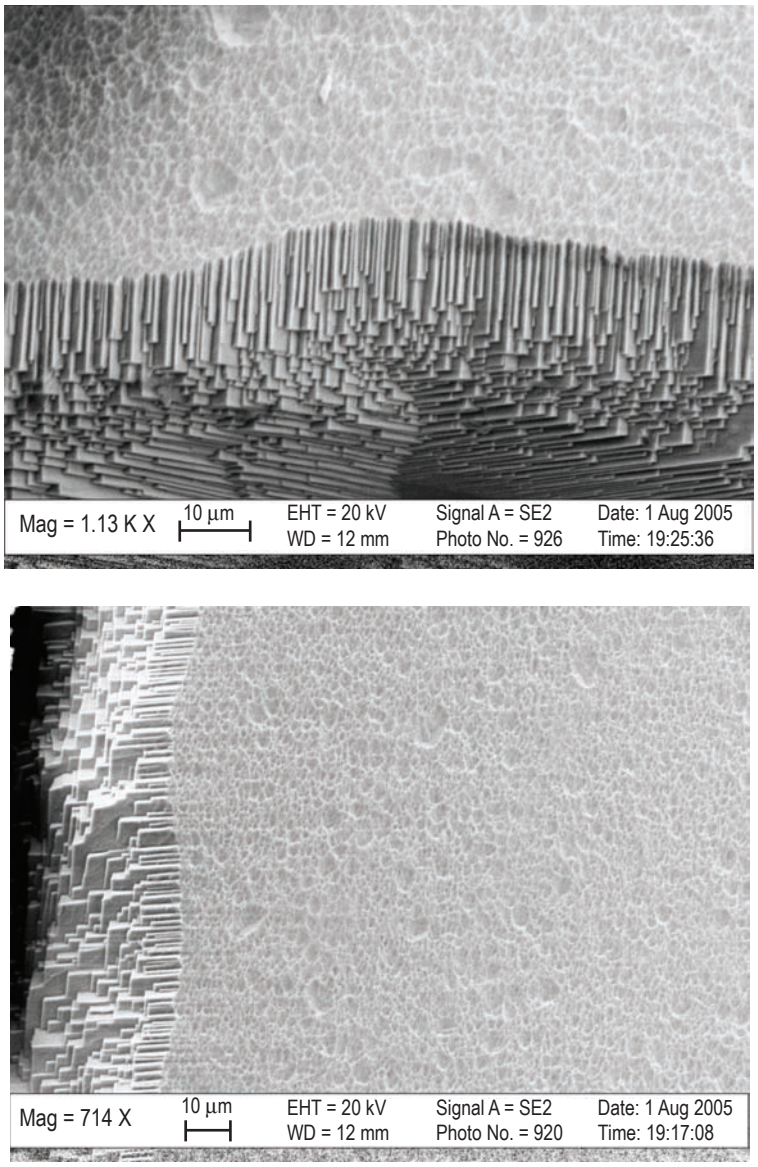

Figure 40. ESL deformed sample etched and viewed in SEM. Preferential etching shows slip steps and monocrystalline structure. Steps are likely (110) planes. Upper shows transition region at bottom pole of the sample. As axis is traversed, shear stress changes direction (i.e. slip begins occurring normal prior to plane).

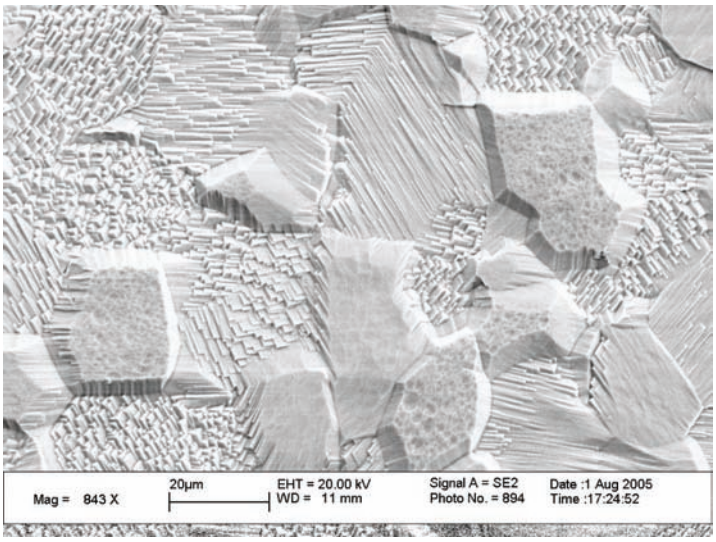

Figure 41. Etched microstructure of as-received Nb.

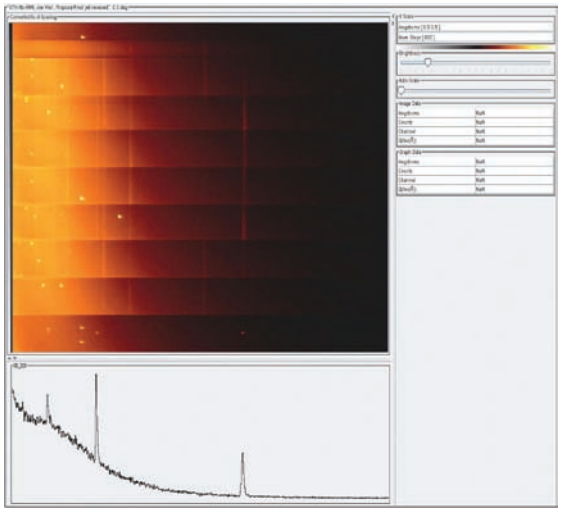

Figure 42. Laue spots. Sample annealed in ESL.

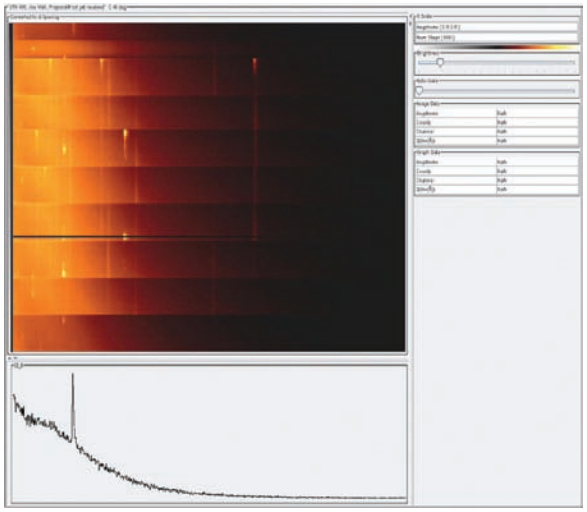

Figure 43. Laue spots. UTK –038. Detector is at 2 theta = 90°.

Possible Future Research

The application of this new technique to materials of interest to NASA and the aerospace community is the next step for this technology. A proposal entitled "Partnership for Advancing High-Temperature Materials" was submitted in response to the 2006 NASA Innovative Partnership Program (IPP) call for proposals. ATK, the GE Global Research Center, and the Naval Surface Warfare Center (NSWC) have expressed interest in this work and are the external partners for this proposal. Collectively, they have offered $254k of in-kind support for joint efforts to characterize materials they are developing. The

MSFC ESL facility can provide creep and other physical property measurements for materials being developed by the external partners for propulsion and high-temperature applications. Ultrahigh temperature ceramics from the NSWC and ATK (melting temperatures >3,000 °C) are candidate materials for TPS applications—in particular for those with high-heat loads. TPSs represent a critical technology for aerocapture. Missions involving aerocapture, aerobraking, and aeroentry require advanced heat shields/TPSs. These materials are also candidates for advanced nozzle concepts and rocket component applications. Refractory alloys and high-temperature superalloys proposed for the IPP study could find applications in a variety of spacecraft and propulsion systems. The proposed effort would advance the knowledge base and TRL for high-temperature materials which could support numerous NASA applications including in-space propulsion, structures, and thermal protection.

Conclusions

- Creep deformation of Nb at 1,985 °C was measured using both an ELS method and a conventional testing method.

- The stress exponent from the ESL and the conventional creep tests were 2.517 and 2.4, respectively, and showed a good agreement with data from the literature; furthermore, the stress exponent may be determined precisely from a single test in ESL versus many tests using conventional methods.

- The ESL method provides a unique capability for measuring creep at temperatures >2,000 °C, as is required for numerous advanced aerospace applications.

Acknowledgments

This research was sponsored in part by NASA under grants NNM04AA78G, NNM04AA19A, and the AME Program. ESL experimental results were made possible through the dedicated efforts of the MSFC ESL operations team—Trudy Allen, Glenn Fountain and Tom Rathz.

References

1. Rulison, A.J.; Watkins, J.L.; and Zambrano, B.: *Review of Scientific Instruments*, Vol. 68, No. 7, pp. 2856–2863, 1997.

2. Lee, J.; Bradshaw, R.C.; Rogers, J.R.; et al.: *Material Science and Engineering* A In Press, 2006.

3. Bradshaw, R.C.; Schmidt, D.P.; Rogers, J.R.; et al.: *Review of Scientific Instruments*, Vol. 76, 2005.

4. Frost, H.J.; and Ashby, M.F.: *Deformation-Mechanism Maps*: *The Plasticity and Creep of Metals and Ceramics*, Pergamon Press Inc., New York, NY, 1982.

5. Kiessig, H.; and Essmann, U.: *Scripta Metall. Mater.*, Vol. 19, No. 8, pp. 989–992, 1982.

6. Hyers, R.W.; Johnson, W.L.; Savage, L.; and Rogers, J.R.: *12th Experimental Methods for Microgravity Materials Science Symposium*, TMS, 2000 (CDROM).

7. Rhim, W.K.; and Paradis, P.F.: *Rev. Sci. Instrum.*, Vol. 70, No. 12, pp. 4652-4655, 1999.

8. Rhim, W.K.; and Ishikawa, T.: *Rev. Sci. Instrum.*, Vol. 72, No. 9, pp. 3572–3575, 2001.

9. Lee, J.; Hyers, R.W.; Rogers, J.R.; et al.: *Acta Mat.*, Submitted 2006.

3.4 High-Temperature Emissivity Measurement System

PIs—Todd Schneider; Jan Rogers; and Jason Vaughn, NASA MSFC.
David Crandall and Don Wilkes, AZ Technology, Inc.

Background and Objective

A common feature of all systems that must operate in the space environment is the fact that all heating and cooling processes are ultimately accomplished through radiative heat transfer. Every surface of a spacecraft, whether it is a small communications satellite or a large manned platform, such as the ISS, is designed to radiate energy so that the spacecraft systems stay within their operational temperature range. A key physical property of materials that governs how efficiently a material will radiate its thermal energy is known as emissivity.

In the case of a spacecraft material that is being illuminated by the sun, the emissivity of the material will determine how much of the sun's energy is radiated into space. The emissivity will therefore affect the ultimate equilibrium temperate of the material. Unfortunately, the value of emissivity is dependent on temperature and the surface condition of the material. Therefore, to accurately design or configure a material for use in space, one must measure the emissivity of the actual material over its intended operational temperature range.

The high-temperature emissivity measurement system (HiTEMS) has been created to provide this critical thermal performance data. HiTEMS represents an important new capability that will provide emissivity information for a wide range of materials and over a large temperature range. Emissivity information from HiTEMS promises to provide spacecraft designers with precise information about the thermal performance of materials. By providing this specific information, design engineers will no longer have to make worst case assumptions about the thermal performance of materials, and will therefore be able to significantly reduce design margins. The reduction in design margins means possible savings in system mass, radiator area, or even material cost.

The HiTEMS system is presently in the construction phase. The key technology items have been purchased and assembly is due to begin in October, 2006. HiTEMS is scheduled for completion in December 2006. Upon completion of the hardware systems, several calibration tests are planned to confirm functionality. At that time HiTEMS will be available to conduct tests for NASA teams, universities, and private corporations.

Project Description

Understanding the thermal performance of materials is critical to the creation of any system. In the case of a spacecraft component, which must radiate its thermal energy, there is no more important parameter than the emissivity. Emissivity is a measure of a material's radiating efficiency. An emissivity of 1 implies that the material is 100-percent efficient at radiating energy. An emissivity of 0.2 implies that the material radiates only 20 percent of that which it is capable of radiating.[1]

The importance of emissivity can be further understood by referencing the equation that governs the power radiated by an object. This equation is known as Stefan's Law,

$$P = e\sigma A\left(T^4 - T_c^4\right) \ . \tag{3}$$

where P is power, e is emissivity, σ is the Stefan-Boltzmann constant, A is the surface area, T is the object temperature, and T_c is the cooler background temperature.

Given that the value of emissivity can range from 0 to 1, it is clear that the actual value of emissivity chosen can radically change the thermal design of an object or system. Unfortunately, emissivity is itself dependent on the temperature of the object, as well as the surface finish of the object as table 7 clearly shows.

Table 7. Range of Al emissivity values based on temperature and surface finish obtained from the table of emissivity values located on the Omega Corp. Web page: http://www.omega.com/literature/transactions/volume1/emissivitya.html.

Material	Temperature °F (°C)	Emissivity
Aluminum		
Unoxidized	77 (25)	.02
Unoxidized	212 (100)	.03
Unoxidized	932 (500)	.06
Oxidized	390 (199)	.11
Oxidized	1,110 (599)	.19
Oxidized at 599 °C (1,110 °F)	390 (199)	.11
Oxidized at 599 °C (1,110 °F)	1,110 (599)	.19
Heavily oxidized	200 (93)	.2
Heavily oxidized	940 (504)	.31
Highly polished	212 (100)	.09
Roughly polished	212 (100)	.18
Commercial sheet	212 (100)	.09
Highly polished plate	440 (227)	.04
Highly polished plate	1,070 (577)	.06
Bright rolled plate	338 (170)	.04
Bright rolled plate	932 (500)	.05
Alloy A3003, oxidized	600 (316)	.4
Alloy A3003, oxidized	900 (482)	.4
Alloy 1100–0	200–800 (93–427)	.05
Alloy 24ST	75 (24)	.09
Alloy 24ST, polished	75 (24)	.09
Alloy 75ST	75 (24)	.11
Alloy 75ST, polished	75 (24)	.08

Given the importance of emissivity on the thermal performance of a material, as well as the complicated dependence on temperature and surface finish, the HiTEMS project was initiated to make precise measurements of emissivity over the temperature range of interest for a given material.

HiTEMS is designed to measure emissivity over a wide temperature range, 27–2,700 °C (300–3,000 K). In addition, it is also designed to accommodate a large set of materials including metals, alloys, composites, processed surfaces, and painted or coated surfaces.

To cover this wide temperature and material type range, the HiTEMS capability was divided into two separate laboratory systems. Each system utilizes a high-vacuum chamber, covers a specific temperature range, and incorporates a unique sample holder.

The EM50 system provides emissivity over the temperature range of 27–1,300 °C (300–1,600 K). This system is designed to accommodate disc type samples that are approximately 1-in (2.5 cm) diameter. The samples can range in thickness from 1/32 in (0.08 cm) to 1 in (2.5 cm). The samples are heated through direct contact with a stainless steel heater block incorporated into the sample holder.

The ESL system is designed to measure emissivity over the temperature range 1,200–2,700 °C (1,500–3,000 K). The ability to heat the sample to such extreme temperatures is a result of the fact that the samples are levitated in an electric field and therefore are not in contact with a sample holder. This system provides crucible-free sample heating. A laser system provides the heat that raises the sample temperature. All samples used in the ESL must be spherical in shape and can range in diameter from 0.08–0.1 in (2–3 mm). Although the sample size is limited, a wide range of materials, including painted surfaces, can be accommodated.

Each system within the HiTEMS capability utilizes SOA optical detection systems to make emissivity measurements. The basis of the detection system is an FTIR spectrometer. The use of an FTIR spectrometer provides emissivity information over a wide wavelength spectrum. The FTIR spectrometers are combined with a proprietary optics design provided by the project industry partner AZ Technology, Inc.

Two techniques are employed to produce emissivity values over the entire HiTEMS temperature range—direct emission and reflectance. In the higher temperature ranges the samples generate sufficient IR emission to distinguish them from any background signals. However, in the case where the sample is near room temperature (RT), a reflectance technique is used. The reflectance technique utilizes a light source that illuminates the sample and the light reflected from the sample is measured. This technique provides a means of distinguishing the sample thermal information from the large background of components that are at a temperature close to the sample temperature.

One more subtle difference between the two test systems is that each system produces a particular value of emissivity that is dependent on the sample geometry. The specific difference between the two systems is that the planar geometry of the sample in the EM50 system yields total normal emissivity, while the spherical sample geometry in the ESL system provides total hemispherical emissivity. The primary difference between these values has to do with the particular application of the thermal design. Total normal emissivity is typically used for the case where one object is radiating with respect to another object, for example two components inside a rocket assembly. On the other hand, total hemispherical emissivity, is applied to the case where an object would be radiating to a much larger background, such as deep space. In practice, the two values are typically within a few percent of each other and the distinction can be ignored. However, this information is provided to the customer to ensure proper application of the data in the case where high-precision calculations are required.

Project Schedule

HiTEMS is a complex project involving two laboratory systems, custom optical devices, multiple investigators, and an important industry partner. Given the complexity of the project, it was decided to divide the effort into a design phase and a construction phase.

The phase-1 design effort started in June 2005 with a conceptual design review and ran through April 2006 with a final design review, presented by AZ. During the phase-1 effort several important milestones were reached as follows:

- Contracted with industry partner AZ Technology, Inc.
- Specified and purchased FTIR spectrometers and black body sources.
- Developed EM50 sample holder/heater.
- Created optical system designs custom to each test system.

Phase 2 of the HiTEMS project was initiated in May 2006 and is scheduled for completion in December 2006. This phase of the project is dedicated to construction and testing. Important accomplishments include the following:

- Bench-top testing of measurement techniques.
- Long-lead custom optics components ordered.
- Completion of fabrication drawings.
- Development of control system software.

Assembly of the ESL optics systems will begin in October 2006. The EM50 system will be assembled next with an estimated completion in November. Both systems will then enter an activation and checkout phase that should produce the first data sets in late December 2006.

Results

The HiTEMS project is still in the construction phase, however progress has been made on the development of the two test chambers required for the project, as seen in figures 44 and 45.

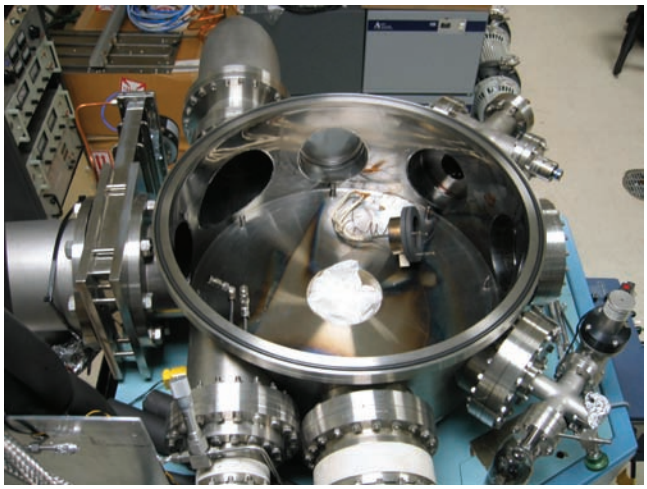

Figure 44. EM50 vacuum chamber.

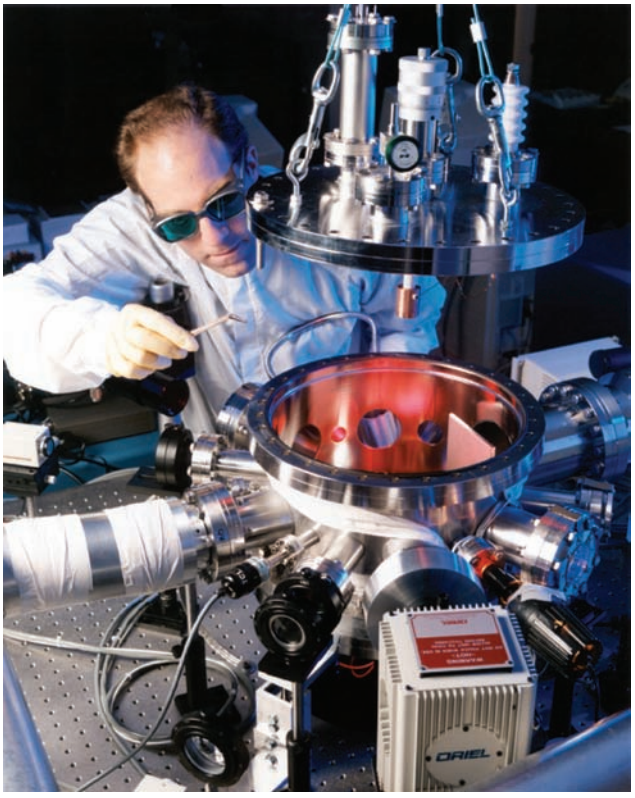

Figure 45. ESL vacuum chamber.

Final fabrication drawings have been completed by AZ. Figures 46 and 47 show the primary components utilized in each system and their precise placement.

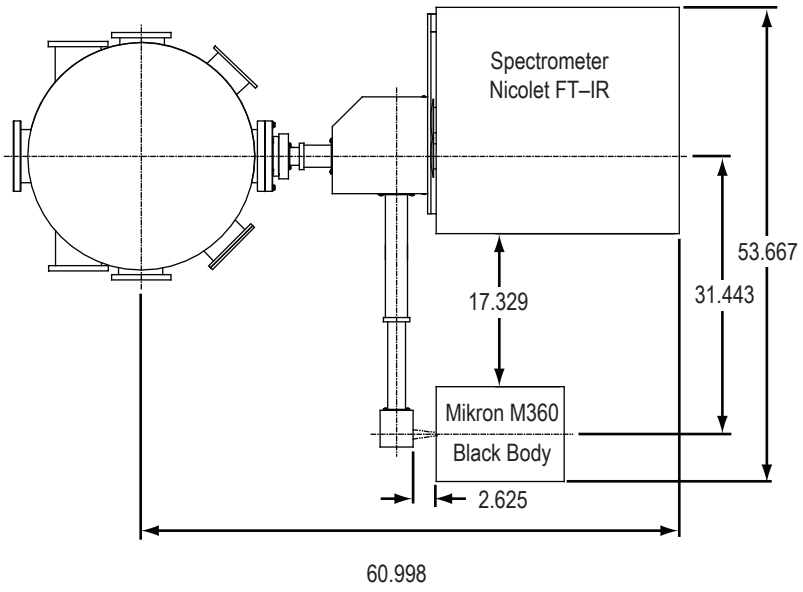

Figure 46. EM50 system layout.

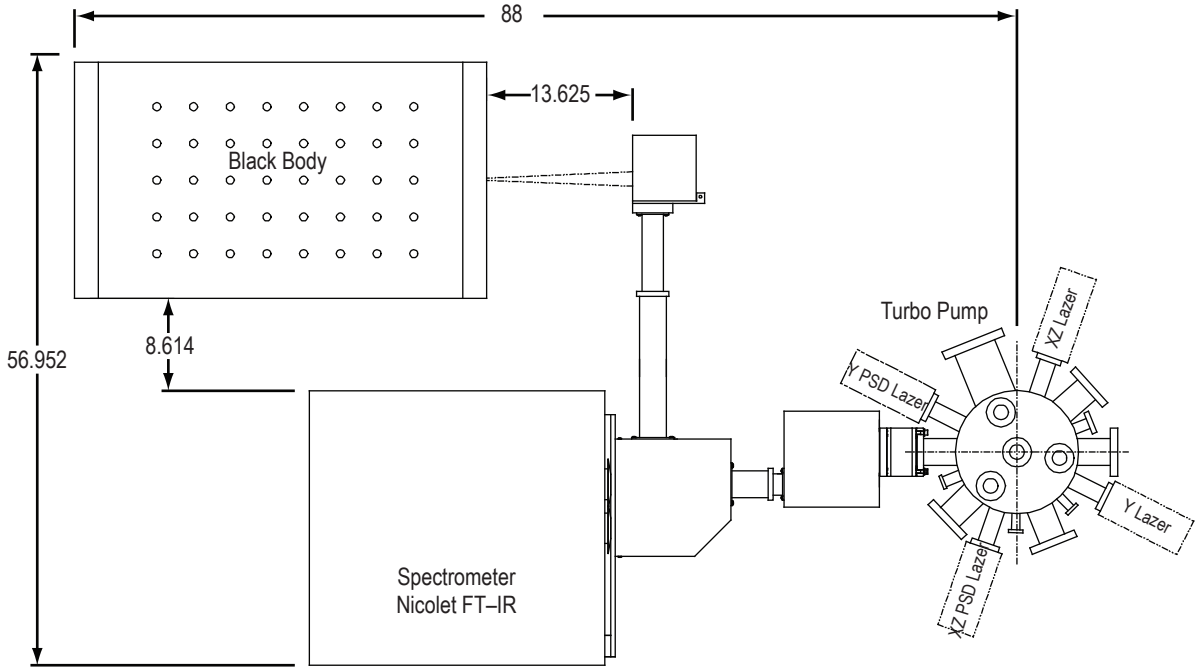

Figure 47. ESL system layout.

Beyond the development of the hardware, shown in figures 44–47, component-level tests have been conducted by AZ. Each FTIR spectrometer has been thoroughly tested over its respective wavelength range. Two important fabrication problems were discovered during this testing and brought to

the attention of the manufacturer, who immediately corrected the problems. With fully functional FTIRs in-hand, AZ conducted tests to establish baseline sampling and over-sampling rates. They also created a LabVIEW software interface which will step the user through the measurement process and display and record the data from the FTIR spectrometer.

Finally, AZ added an important feature to the HiTEMS capability—a custom optical temperature measurement. The original project designs called for separate sample temperature measurements to be made by the user and entered into the software control system. However, now there will be redundant sample temperature measurements. AZ has developed a temperature measurement based on data that was being acquired for the emissivity determination. So, the results from the AZ method of sample temperature measurement will be compared to independent optical pyrometer measurements to ensure that an accurate sample temperature is reported.

HiTEMS and Advanced Materials for Exploration

The production of emissivity data over the operating temperature range of a material will have a direct impact on spacecraft, rovers, radioisotope thermal generators, chemical propulsion, and habitat systems that are all part of NASA's exploration road map. Every space system operating in a vacuum environment requires emissivity information as part of the thermal system design. HiTEMS promises to deliver that information with added precision and over a temperature range that has not been previously available.

Most spacecraft rely on a radiator system to reject heat that is developed by on-board electrical systems. In the past, the radiator has been designed using a worst case value for emissivity. Now, the design margin on the radiator can be significantly improved by using HiTEMS data that is produced using actual flight materials measured at their operating temperature.

HiTEMS was also built to impact the creation of new materials and new material processes. The next generation of new materials will require the measurement of thermal property data for that material. As emissivity changes depend on the material and the surface finish, HiTEMS will provide designers with needed information on these new materials. The same is also true for new coatings that can be applied to existing materials. New coatings that promise to reduce system mass will be important for future spacecraft, but it is unlikely that existing emissivity data can be applied. Therefore, HiTEMS will fill in the data gap and possibly accelerate the use the new coatings.

The challenges of space exploration are great and more often than not materials are needed that must perform at extreme temperatures and under high stress. The key to ensuring that the materials chosen for these difficult applications will perform properly is having accurate material property measurements. HiTEMS was created to produce emissivity data specific to the material and surface finish being considered and under extreme temperature conditions.

The Future of HiTEMS

In the near term, the focus of work on HiTEMS will be getting it completely operational and to verify it is functioning properly. Once the hardware is in place and activated, a series of cross-calibration

tests will be undertaken. The two systems that make up the HiTEMS capability have an overlap in their temperature ranges. So, a material will be chosen that will be tested in both systems at 1,500 K. The emissivity number obtained from both systems will be compared to ensure good agreement. In addition, a sample will be measured in HiTEMS and then placed in a separate test system that employs the ASTM standard for emissivity measurement. Those two measurements will be compared and the results used to validate the HiTEMS technique.

Once the HiTEMS system is declared operational, it can immediately be used in the design and construction of the CEV, lunar rovers, lunar power systems, and satellite systems. Each system can realize significant savings by reducing design margins as a result of obtaining emissivity information that is specific to a given application. The possibility of using new materials or coatings can be considered as the long-needed emissivity data for those materials or coatings can now be supplied.

Although HiTEMS was created to contribute to NASA's AME Program, it has applicability to many different areas outside of NASA. Companies that utilize material vacuum processing could improve their processes by utilizing emissivity data generated by HiTEMS. In the case of metal forming and casting companies, there is a clear need for specific emissivity information at the process temperature. These companies typically utilize pyrometers for making temperature measurements. Each of the pyrometers requires the emissivity of the sample to be entered into the device before it produces a temperature. This has led to large temperatures errors as the emissivity can only be guessed. HiTEMS promises to provide precise emissivity information over a wide range of temperatures to improve the production of metal casting and forming companies. Similarly, coating companies and even semiconductor processing companies could improve the thermal performance of many of their systems by utilizing HiTEMS.

Acknowledgments

HiTEMS was fully supported by the AME Program. Special thanks to Beth Cook for her vision and generous support. Thanks also to Twila Schneider for her assistance as AME Project Coordinator. Thanks also to Tom Rathz, Trudy Allen, Glenn Fountain, and David Wilkie for their contributions to the design and construction of HiTEMS.

References

1. OptoTherm, Inc. Web page with emissivity description: http://www.optotherm.com/emiss-table.htm

3.5 Phase Contrast X-Ray Imaging for Supporting Space Exploration

PI—Dr. Zhengwei Hu, NASA MSFC VP01/BAE Systems.

Objectives

Developing advanced materials for specific applications requires adequate nondestructive evaluation techniques for quality inspection and control. This is particularly true for developing light-weight high-performance structures that are used under extreme conditions for space missions, such as insulating foam and leading-edge materials etc. Shuttle foam, a low-density cellular composite, is structurally used for thermal protection of the external fuel tank during Shuttle launch. Critical foam debris generation, which led to the loss of the Columbia and its seven-member crew in 2003, highlighted the great need to better control foam quality. However, low density, weakly absorbing Shuttle foam has posed a great challenge to the nondestructive evaluation tools currently used. Motivated by solving this problem and filling a gap in space exploration, the PI first conducted feasibility test experiments on foams by exploiting the use of x-ray coherence for phase imaging (instead of absorption-based imaging) by access to the advanced photon source (APS). The experiments turned out to be very promising. With funding support from AME, the work has then focused on the following objectives:

- Develop and test phase contrast two- and three-dimensional imaging capability for supporting the quality inspection techniques of Shuttle foams for future exploration vehicles.
- Nondestructively evaluate the variations of defects with different depths varying from outer layers to inner layers of foam insulation.
- Extend to other advanced materials for evaluating the suitability of the imaging technique for broad applications.
- Develop loading capability for in situ imaging observations.

Both in-house development and tests and synchrotron x-ray imaging experiments were carried out successfully with hard work and coordinated efforts. The PI was successful in competing for synchrotron beamtime through peer-reviewed processes. Detailed information on the intrinsic Shuttle foam quality revealed nondestructively has provided valuable information for foam quality control and failure analysis. Numerous reports on the findings of the Shuttle's foam defects and behavior were provided to MSFC's Engineering Directorate and the AME office to support NASA's mission. The work has also made an impact outside the NASA community through presenting invited talk presentations, etc. The findings have shown the great need to better control foam quality by advancing foam technology. This research effort has opened up new opportunities to solve some challenging issues in space exploration.

Description of Research

Methods. Shuttle foam insulation BX–250, a polyurethane foam applied on domes, ramps, and areas where foam is applied by hand, was primarily used for this study. While emphasis was placed on Shuttle foam, other materials including carbonized foam and composites of polyethylene-epoxy

and carbon-carbon (C–C) were used in experiments to assess the broad applicability of phase contrast x-ray imaging for nondestructive characterization. Phase contrast imaging approaches and loading methods were developed and employed to nondestructively evaluate the foam's defects and behavior. For each tomographic three-dimensional image, about 800 projection images were taken over a 180° angular range. Images were recorded using a high-resolution charge coupled device (CCD) camera. Beamtime for synchrotron experiments were obtained through effective scientific merit-based national competitions.

Rationale Behind Research Method. Absorption-based x-ray radiography and computed tomography (CT) are widely used for NDE. They work well in metallic or heavy-element systems, detecting defects such as cracks and/or differentiating heavy-element areas from light-element regions in terms of the different degree of intensity attenuation of the transmitted beam along the beam path. The mechanism of image formation of theses traditional imaging methods is solely absorption based, they are not effective in mapping the structure and/or defects inside low density or weakly absorbing materials such as Shuttle foam because the absorption contrast is too low to be visible on images. This difficulty remains a bottleneck for developing reliable and durable lightweight materials and/or structures for space exploration. The PI proposed to use phase contrast imaging for circumventing the difficulty— which has turned out to be effective and significant. Adding the phase information of x-rays into image formation significantly enhances image contrast and hence image sensitivity. This offers new opportunities for quality inspection and control of materials and/or materials processing for supporting space exploration.

Schedule

The project schedule tasks, shown in table 8, included material selection and sample preparation, experimental method and analytical capability development, competing for and scheduling beamtime, designing and conducting experiments, data analysis, report writing, etc.

Table 8. Project schedule.

7/20/2004–1/31/2005	Experimental and analytical capability development, demonstration of the feasibility of phase contrast imaging of Shuttle foam, and report delivery.
2/1/2005–9/30/2005	Experimental methods development, study of defects at foam's boundaries and of the effectiveness of phase imaging to other materials, and report delivery.
10/1/2005–4/30/2006	Study foam's characteristics at the innermost foam regions (the interface between the foam and substrate), combined in situ loading and imaging method development, and report delivery.

Results

This work demonstrated the great potential of phase contrast x-ray imaging to nondestructively characterize advanced lightweight materials and/or structures and provides reliable, detailed information critical to quality control that was previously impossible. Combined in situ loading and imaging visualization methods have been developed that offer a powerful way to better understand how foam behaves under conditions—greatly benefitting foam processing and development.

Phase contrast tomographic observations have revealed a great variation and high anisotropy in foam structure in terms of cell size, shape, and wall and strut thickness. Roughly speaking, the largest and smallest principal dimensions of the regular cells of foam layers are, on average, ≈0.22 mm in the foam-rise direction and ≈0.14 mm in one of the other directions normal to the foam-rise direction, respectively. Foam layers are separated by complicated zig-zag knit lines or boundaries that are characterized by highly irregular cells whose wall thickness is several times that of the regular cells in the layers, as shown in figure 48. Such a marked difference between the layers and boundaries may have significant consequences to the foam's properties and behavior, in particular to how foam responds to loading, an important question related to Shuttle foam shedding that doomed Columbia in February 2003 and has grounded further Shuttle flights since the launch of Discovery on July 26, 2005 due to its recurrence. While voids, which are one of the major foam defects, exist throughout foam regions and vary considerably in size, they tend to form more readily along the boundaries and the interface between the foam and the Al substrate, as illustrated in figures 48 and 49, with an average size of ≈1 mm in the foam rise direction and ≈0.5 mm in the other two directions.

Pressure tests show that the foam's strength vary considerably from one region to another as a result of variations of foam's quality and density. To fully understand the mechanisms by which foam failure occurs under conditions, systematic in situ experimental work needs to be carried out. For this, an in situ loading method has been developed and tested. Preliminary results are encouraging. Not only do they further confirm that structural details revealed in phase contrast images indeed are the real structure and defects present inside the foam, but also shed light upon the role of defects played in foam failure. An example is given in figure 50, showing that cracking took place at a knit line that occurred due to the exerted pressure. Further work would provide deeper insight into foam failure and impact foaming technology advancement.

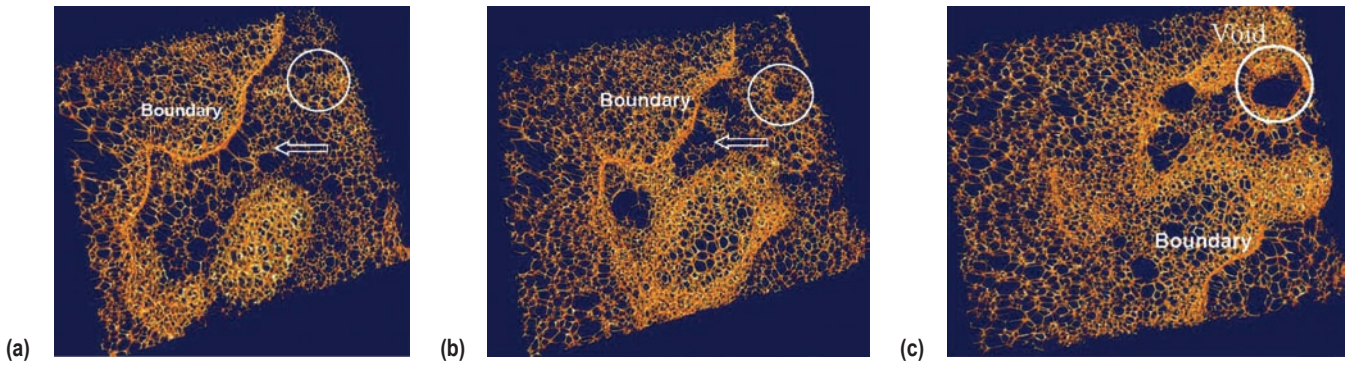

Figure 48. Phase contrast three-dimensional images showing a zig-zag boundary and defects inside the foam; (a), (b), and (c) correspond to internal foam regions at different depths. The marked void has a dimension of more than 1.5 mm along the foam-rise direction.

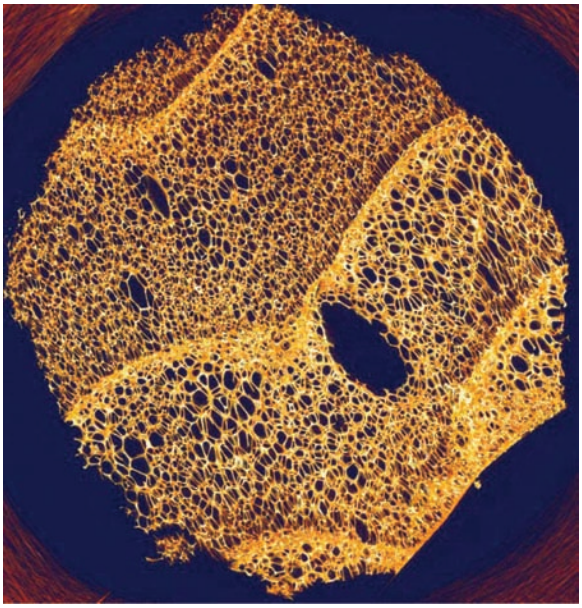

Figure 49. Phase contrast tomographic image showing intact foam structure and defects inside a foam insulation region at and near the interface between the foam and the Al substrate.

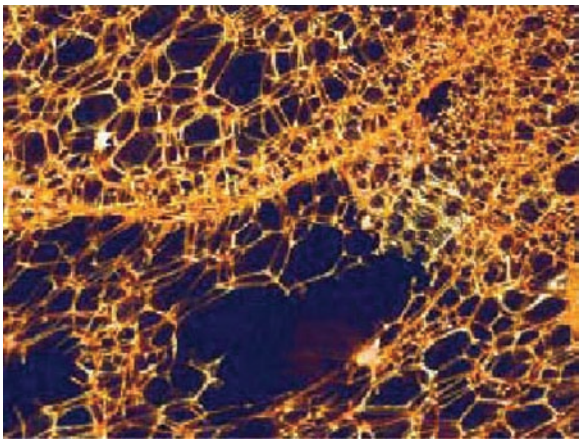

Figure 50. Phase contrast three-dimensional image revealing internal foam cracking and/or spalling along a knit line induced by pressure loading.

To assess the broad applicability of the new imaging technique, sets of lightweight composite that, like the Shuttle foam, are difficult to characterize, have been experimentally inspected with phase contrast imaging. Figure 51 (a)-(c) show images of intact pore structures inside a carbonized foam sample. The nonuniformity of the pore structure within the sample is nondestructively revealed in great

detail. Note that the structural nonuniformity has significant effects on the physical properties of interest. The results indicate that the difficulty of obtaining structure uniformity and integrity may remain a bottleneck in developing highly reliable advanced materials with controlled properties and performance. With improved imaging sensitivity, polyethylene fibers in the matrix of epoxy (fig. 52) and RCC microcracks (fig. 53) are clearly visualized in a nondestructive manner.

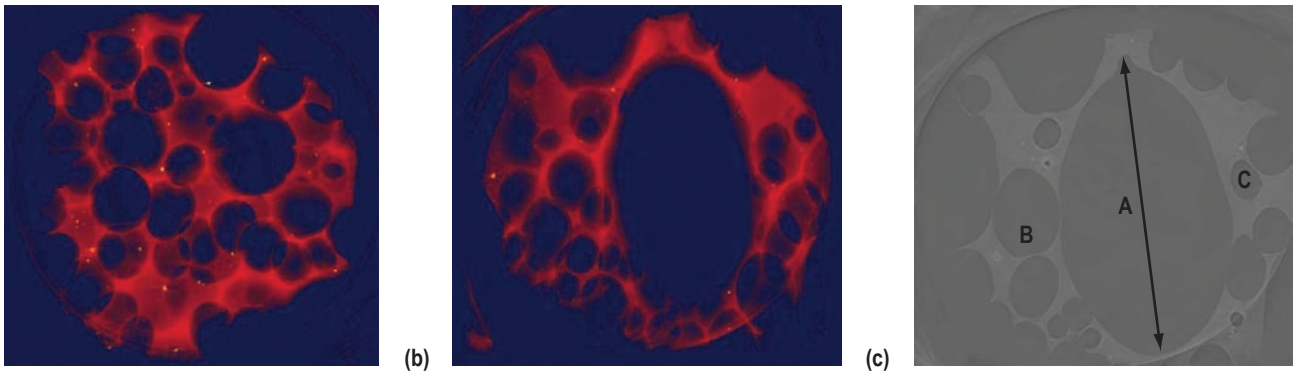

Figure 51. Phase contrast tomographic images showing internal pore structure of a carbonized foam. Three-dimensional images (a) and (b) correspond to internal regions at different depths and (c) is a tomographic slice. Pore size (a) 4.5 mm, (b) 1.4 mm, and (c) 0.6 mm.

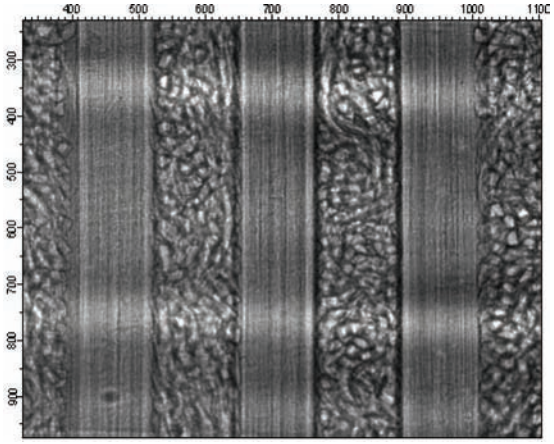

Figure 52. X-ray image showing internal polyethylene fiber structure of a radiation shielding composite sample.

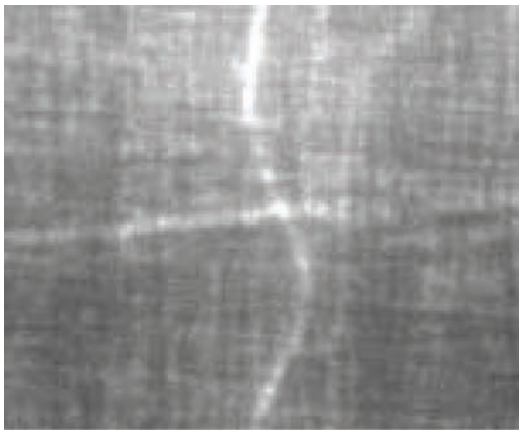

Figure 53. X-ray image showing internal fiber structure and microcracks of an RCC sample.

How the Work Helps AME. The work has shown that the new phase contrast x-ray imaging technique has the great potential to become a new powerful tool for quality inspection and control of advanced materials and/or materials processing. The obtained results have demonstrated the applicability of phase

contrast imaging to a range of materials that are important to space exploration. Furthermore, the unprecedented details on the Shuttle foam's cellular structure, defects, and failure under loading have provided reliable information on the foam's quality and the way foam fails under loading, which has been invaluable to improving the quality of the Shuttle foam insulation. The work represents a unique contribution of cutting-edge science to NASA's effort to understand and solve important Shuttle foam problems. The impact of this work made within and outside the NASA community has benefitted AME considerably and MSFC as a whole.

Future Research and Importance

Compared with other methods, phase contrast x-ray imaging is noninvasive and extremely sensitive to density variations and/or defects. The findings also raise questions concerning the quality of structurally complicated foam insulation. Since thermal protection is an indispensable and vital part of the Space Shuttle and future space launch vehicles, it is essential to carry out systematic experiments and tests on foams prepared under different processing conditions to understand what they really are and how they behave differently under loading. Such insight into the foam's quality and response to loading would help advance foam technology to deliver foam insulation with better performance.

Given that no standard x-ray imaging tool is currently available enabling low-density material structures to be noninvasively visualized with sufficient sensitivity and resolution, it would be important to advance new x-ray imaging techniques to fill the gap. This effort could considerably benefit NASA's mission, leading to a new NDE or quality inspection tool for in-house use and ultimately for in-flight applications.

Acknowledgments

The author would like to thank J. Walker, M. Suits, R. Kaul, F. De Carlo, B. Lai, D. Keane, B. Tiemen, P. Fernandez, C. Roehrig, R. Richmond, and P. Peters for their help, support, encouragement, collaboration, and discussions. Thanks go to the AME, SD–46, and the Engineering Directorate for their support. The research was funded by the AME and supported by the Biotechnology Science Program and the In Situ Fabrication and Repair Program. Use of the APS was supported by the DOE, Office of Science, under W–31–09–Eng–38.

4. PROPULSION MATERIALS

4.1 Thrust Chamber Liners

PIs—Richard (Dick) Holmes and Sandra (Sandy) Elam, NASA MSFC.

Objective

Advanced materials research for thrust chamber assemblies will enable engines to perform at higher temperatures with improved operating margins. These advancements can be applied to nuclear propulsion, as well as the engines being considered for the CLV. Some engine operating conditions are severe enough to erode thrust chamber throat sections, such as the Space Shuttle main engine (SSME) shown in figure 54, but new material systems produced with the vacuum plasma spray (VPS) process have demonstrated the ability to reduce or eliminate such erosion. Using VPS to form the thrust chamber liner with an FGM has produced a highly effective and durable protective layer on the hot wall of the liner. A small thrust chamber liner was successfully fabricated and has survived 220 hot-fire tests with no erosion and no degradation to the hot-wall protection. Current efforts are addressing the fabrication issues associated with scaling up the process to make larger thrust chamber liners for specific engine systems. The small demonstration liner was successfully fabricated using a mild steel mandrel, but attempts to make larger units were unsuccessful due to larger stresses from the differences in CTE between the liner and mandrel materials. An alternate mandrel design with stainless steel, approximating the CTE of the copper alloy combustion liner, is being investigated to eliminate these CTE concerns for larger liners.

Description of Research

Description of Research Method. For this AME task, investigators are designing and building a 40-k lbf (40,000 lb. thrust) thrust chamber liner using an alternate mandrel design as the next step to building a full-size model. Tasks included the following:

- Demonstrating processes and new mandrel design with large diameter pipe sections.
- Designing and machining a mandrel made of stainless steel coated with a thin iron layer to create a CTE compatible with that of the liner material.
- Using the new mandrel and VPS, shown in figure 55, to manufacture a thrust chamber liner made of GRCop-84 and an FGM formed protective layer of NiCrAlY, shown in figure 56.
- Joining the liner with an existing thrust chamber support jacket and manifolds to form a completed assembly for hot-fire testing.
- Conducting hydrostatic proof tests at NASA MSFC, Huntsville, AL.
- Characterizing materials properties of VPS formed materials.

Figure 54. Rocket engines, such as the SSME shown here during the STS–110 launch, must operate in harsh environments with high temperatures, high pressures, and reactive propellants. Advances in materials and processes used to produce engine components will improve future engine designs.

Figure 55. To make a thrust chamber liner with VPS, materials are deposited on a mandrel to form a near-net shaped part. This process is being developed to provide durable, robust, high-temperature protective coatings for propulsion engine components.

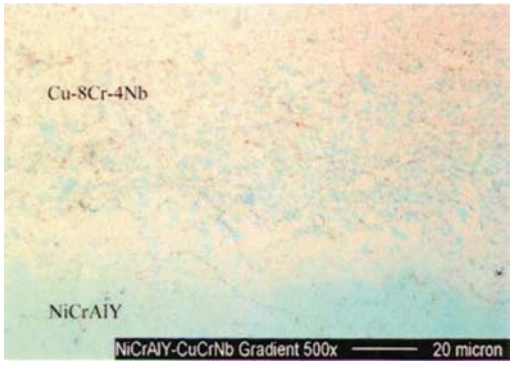

Figure 56. FGM formed with VPS.

Rationale Behind Research Method. VPS was chosen for the following properties:

- No distinct bond joint between materials.
- Material systems tailored for specific designs.
- Durable thermal protection.
- Gradient absorbs differences in CTE

Schedule. This 3-yr effort was initiated in FY 2004 and will conclude with a completed 40-k lbf thrust chamber assembly in FY 2006. No follow-on efforts have been funded at this time.

Results

Figure 57 shows some of the hardware results of this project. Previous work demonstrated pristine condition after 220 hot-firing tests for an FGM copper alloy liner, VPS formed on a mild steel mandrel. Scale up of the VPS/FGM process to SSME size, produced stress cracking because of CTE mismatching between the mild steel mandrel and GRCop-84 liner. VPS forming using 12-in diameter stainless steel (SS) pipe sections showed that matching CTE of the mandrel with that of the GRCop-84 eliminated cracks. A SS mandrel with a VPS coating of mild steel was developed and tested for matching CTE. The mild steel coating, which could be removed by mild acid etching, was added to allow the SS mandrel removal. After the FGM NiCrAlY/GRCop-84 liner was VPS sprayed, heat treated and the SS mandrel removed, cooling channels were machined. The VPS/FGM liner was machined, with cooling channels cut for calorimeter testing. Utilization of the VPS/FGM 40-k lbf. combustion chamber liner as a calorimeter will provide hot-fire testing at no cost to the project, as the calorimeter will be used to collect thermal data for other scheduled programs.

Figure 57. Hardware produced using VPS.

Based on extensive testing on subscale component hardware, liners fabricated with VPS and the FGM of NiCrAlY/GRCop-84 can be extremely durable. They can also be capable of withstanding higher operating temperatures and oxygen-rich environments without any apparent degradation. Therefore, such liners can expand the operating margins of specific combustion chambers. While traditional liners formed from NARloy-Z often require routine polishing to remove surface roughness, the subscale unit with the VPS liner developed no surface roughening. Accordingly, routine maintenance efforts for engine hardware could be significantly reduced. Table 9 compares the results of this project with the current liners on the SSME.

Table 9. Subscale cycle test comparison. VPS was used to form an FGM 5-k lbf thrust chamber liner that has shown no wear after 220 hot-fire tests, and performed outstandingly compared to previous testing on a NARloy-Z liner, currently used in the SSME main combustion chamber (MCC).

Vacuum Plasma Spray FGM GRCop-84 Liner	NARloy-Z Liner (Current SSME Liner)
2006 technology evaluation	1976 SSME qualification testing
220 cycles (1,100 s)	118 cycles (353 s)
Maximum temperature = 1,250 °F (950 K)	Maximum Temperature = 1,100 ºF (866 K)
No hot-wall cracks or surface roughening initiated; no liner degradation	Cycles <30, hot-wall cracks and surface roughening initiated
Cycles ≈55, heat-load decreased 30%, less coolant required	Cycles ≈70, heat-load increased; surface polishing required

Material Properties

In previous work, tensile and physical property samples were tested to further characterize the VPS material and compare it to NARloy-Z. Two different powder mesh sizes, –270 and –325, were evaluated with the GRCop-84 samples. To aid in future thermal analyses, samples of VPS NiCrAlY were fabricated and tested. Data were collected for thermal conductivity, ultimate tensile strength (UTS), and 0.2 percent yield strength (YS), low-cycle fatigue (LCF). Figures 58 and 59 plot the strength results. Material samples were heat treated at temperatures above 1,700 °F and aged to simulate a specific braze cycle. Consistent with previous samples, both the ultimate and yield strength of GRCop-84 (either mesh size) were significantly higher than NARloy-Z over the entire temperature range. Figure 60 shows that VPS GRCop-84 at the higher temperature of 650 °C (1,200 °F) is far superior in LCF than NARloy-Z at 538 °C (1,000 °F).

During the first year, 12-in diameter SS pipe sections were used to test the process and demonstrated that matching the CTE of the mandrel with that of the copper alloy eliminated stress so that no cracks were experienced during manufacturing. The second year, the 40-k mandrel and liner were manufactured by Plasma Process, Inc. (PPI), a Huntsville, AL company that shares U.S. Patent 6,314,720 with NASA for VPS processing to form FGMs. In the third year of the project, MSFC investigators are working with PPI to complete the thrust chamber liner assembly, as shown in figure 61.

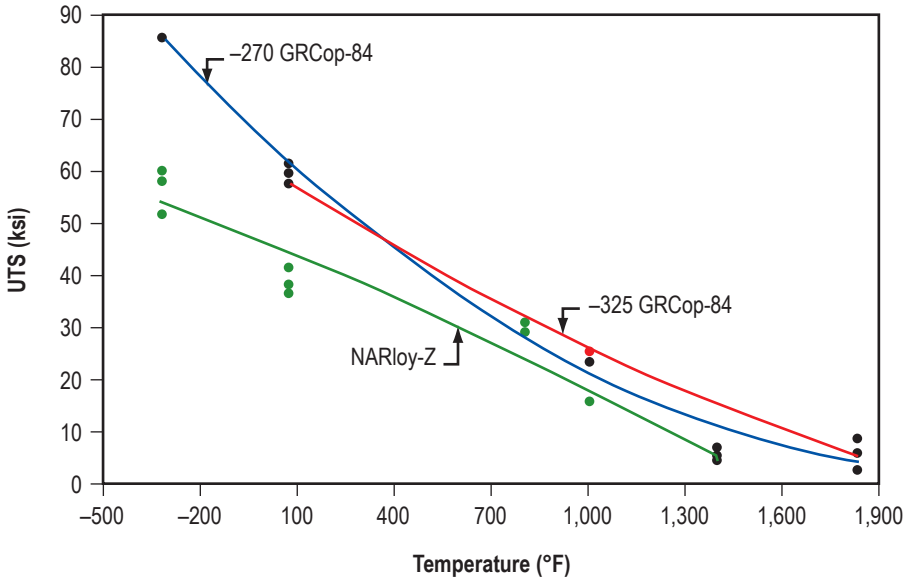

Figure 58. UTS versus temperature for VPS GRCop-84 and NARloy-Z.

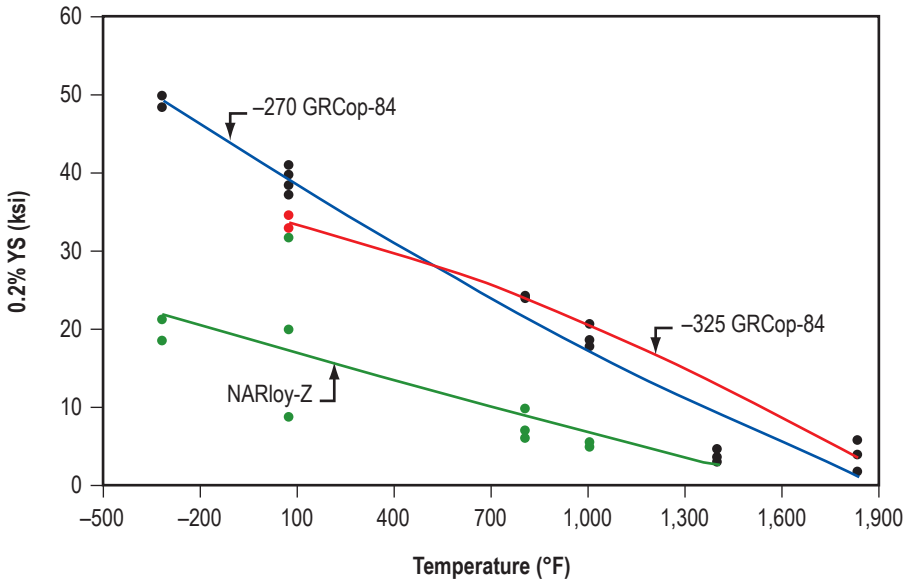

Figure 59. YS versus temperature for VPS GRCop-84 and NARloy-Z.

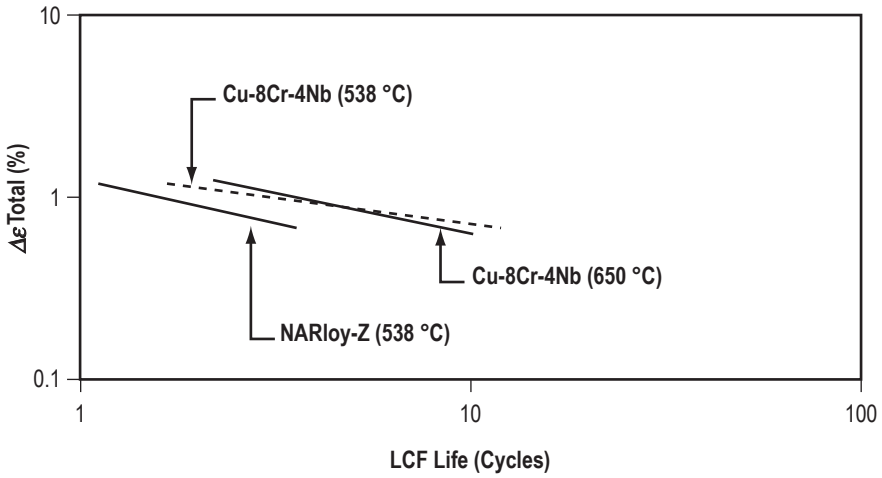

Figure 60. LCF comparison of VPS GRCop-84 to NARloy-Z.

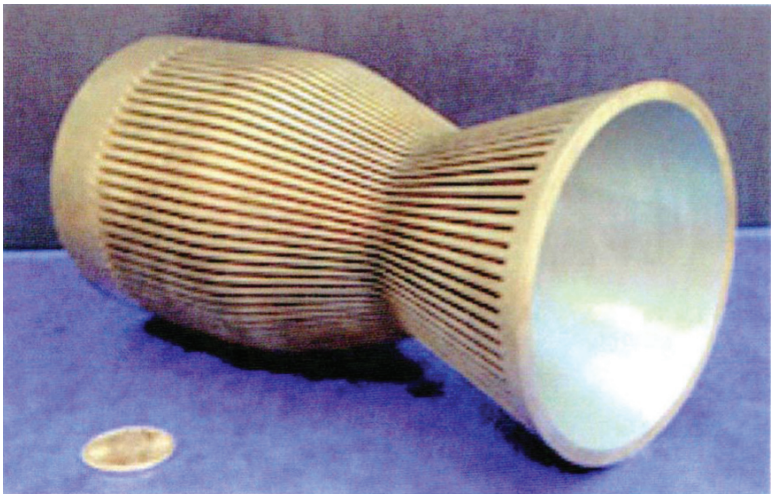

Figure 61. 5-k lbf thrust chamber hardware. A subscale 5-k lbf thrust chamber liner was successfully fabricated with VPS using GRCop-84 and a protective FGM layer of NiCrAlY on the hot wall.

Hot-fire testing on a small 5-k lbf thrust chamber liner, shown in figure 62, provided a CRL 5 for the technology at this time. Successful fabrication of the 40-k lbf thrust chamber liner will further increase the CRL. Additional testing in a simulated environment with a full-size thrust chamber assembly would elevate the CRL to 7. Elevation of this materials technology will create robust, long-life hardware for safe space exploration.

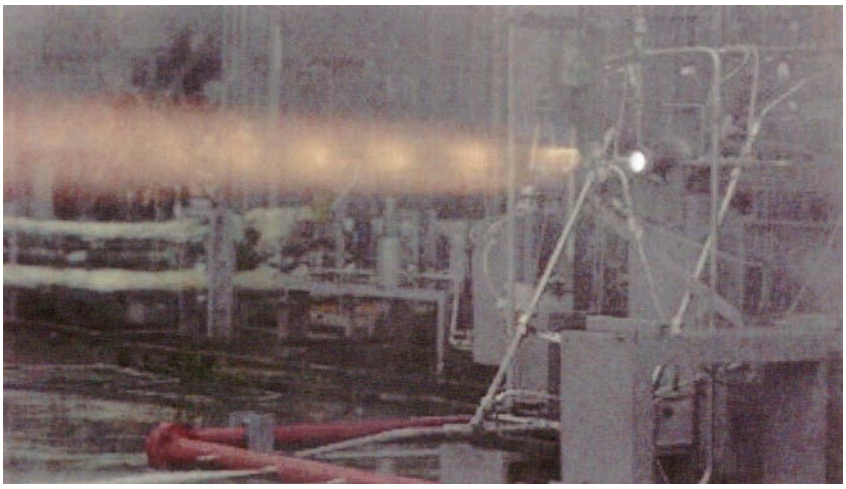

Figure 62. Hot-fire testing at MSFC. MSFC has the facilities to conduct hot-fire testing of thrust chamber assemblies and experts who can characterize materials properties. This is a hot-fire test on the 5-k lbf thrust chamber liner.

Possible Future Research

The next step is to manufacture and test full-size thrust chambers with FGM liners in simulated environments and evaluate and characterize the materials systems for design and life prediction. The new liner can be scaled up and tested on a full-size engine system and results can be compared to traditional materials.

Efforts for the thrust chamber liner were focused on a NiCrAlY protective layer that endured temperatures up to 2,600 °F (1,700 K). Higher temperature capability will be possible by adding Zr (ZrO_2) to the FGM. Zr coatings are expected to handle temperatures up to 4,000 °F (2,478 K), which may be attractive for nuclear propulsion applications.

From 1984–1986 durable protective thermal barrier coatings were developed in the MSFC VPS Laboratory for the SSME high-pressure fuel turbopump (HPFTP) turbine blades. Existing coatings were cracking and spalling off requiring excessive engine maintenance. Oxides were attributed to weak bonding, which was minimized by a vacuum plasma process of spraying the coatings on in a vacuum chamber that had been evacuated and backfilled with a partial pressure of argon to prevent oxidation. The VPS coated turbine blades were considered to be qualified for space flight by satisfactorily passing 25 hot-firing tests cycling between 1,700 °F oxihydrogen combustion and quenching with liquid hydrogen at –423 °F. Turbine blades VPS coated with an NiCrAlY alloy showed no spalling or wear after 40 hot-firing cycles while baseline turbine blades spalled in less than five cycles.

VPS composite cartridges were successfully from developed from 1992–1996 in Marshall's VPS Laboratory and Microgravity Research for space furnaces, combining high-CTE metals with low CTE and brittle ceramics. This was necessary because scientists wanted to grow semiconductor gallium

arsenide crystals, that eat through most metals at high temperatures, in space furnaces at 1,260 °C. A protective ceramic coating was needed on the inside of an Nb alloy cartridge for protection in the event the quartz ampoule containing the gallium arsenide ruptured. A functional gradient coating technique was developed in which the ceramic coating was first VPS sprayed on a revolving mandrel, followed by transitioning from a 100-percent ceramic coating to a 100-percent Nb alloy with no bondline between them. The mandrel was subsequently removed leaving a metallic cartridge with a protective FGM ceramic coating on the inside, while any differences in CTE between the two materials minimized by the transitional FGM.

Blanching, caused by the oxidation reduction action of continuous multiple explosions in the combustion chamber of liquid rocket engines, had long been recognized as the main cause of rocket engine failure. Many efforts had been made to apply protective coatings on the inside hot wall of the combustion chamber; however, every coating had always blistered off immediately on hot-fire testing. All these coatings had bondlines with the combustion liner and it was reasoned that a functional gradient coating tied into the liner with no bondline should offer a very tenacious bonding under extreme conditions. Also, the VPS process offered the only known means of performing this task. In 1997, funding was obtained from Marshall's Center Director's Discretionary Fund (CDDF) to combine the three existing technologies and build a robust, low-cost liquid rocket engine combustion chamber suitable for advanced propulsion systems. Cu-8Cr-4Nb alloy, developed at NASA GRC was used because of its excellent high-temperature strength, creep resistance, and LCF behavior combined with exceptional thermal stability. Researchers had demonstrated that powder metallurgy (P/M) Cu-8Cr-4Nb exhibited better mechanical properties at 650 °C (1,200 °F) than NARloy-Z did at 538 °C (1,000 °F). More recently, Cu-8Cr-4Nb has been given the trade name of GRCop-84.

A thermal model showed that NiCrAlY, applied as a 0.0035-in thick functional gradient coating to the hot wall of the proposed combustion chamber, would lower the operating temperature of the liner 20 percent, from 1,000 °F to 800 °F, for longer life. At the same time, the NiCrAlY coating would operate at a temperature of 1,700 °F, which was the same temperature the coating operated when VPS coated on the HPFTP turbine blades. The NiCrAlY coating not only served as a protective coating against oxidation/blanching, but also as a thermal barrier coating in lowering the operating temperature of the Cu-8Cr-4Nb liner. CDDF funding of $80k was used to VPS/FGM form a Cu-8Cr-4Nb/NiCrAlY liner to fit an existing spool piece. The assembly was successfully hot-fire tested and was the first time a liquid rocket engine (thruster) combustion chamber had been hot-fire tested without the protective coating blistering off. This project was completed in FY 1998. The CDDF project was combined with funding from task NRA8–21 to build and initiate hot-fire testing on the 5k-lbf VPS/FGM thrust chamber in FY 1999–FY 2001. Additional funding was obtained from the X–33 Program to supplement NRA8–21 work, continue to hot-fire test the 5k-lbf thruster, and build X–33 sized and other high-thrust-level liners. When the hot-fire testing reached 108 cycles in FY 2002, work began on building an SSME-sized combustion liner with Space Launch Initiative (SLI) and Advanced Space Transportation Program (ASTP) funding. When stress cracking was discovered in the VPS-formed SSME combustion liner due to the CTE mismatching problem, FY 2004 AME funding was provided to conduct the 12-in diameter SS pipe studies that confirmed matching the CTE of the mandrel to that of the CRCop-84 liner eliminated cracking. Then additional funding was provided by AME in FY 2006 to build mandrels and VPS/FGM 40k-lbf liners for hot-fire testing as a calorimeter at no cost to the project.

Subsequent scale up of the VPS/FGM process will produce robust, long life, high performance, and dependable liquid rocket engines needed for travel to Mars with safe return. The VPS/FGM process also promises to provide engines capable of containing the extreme temperature conditions of thermonuclear propulsion. Most recently the VPS/FGM process has been expanded to provide durable, high-temperature protective coatings for injector faceplates. These faceplates, shown in figure 63, were successfully hot-fire tested and demonstrated similar performance to that of the thrust chamber liner with no erosion and no degradation to the protective layers applied with VPS. This process might also be used to apply maximum bond strength coatings to a variety of space vehicle surfaces, such as leading edges and turbine blades.

Figure 63. Injector fabrication—Four coating options applied to injector designs.

Bibliography

1. Elam, S.; Effinger, M.R.; Holmes, R.; et al.: "Lightweight Chambers for Thrust Cell Applications," *36th AIAA/ASME/SAE/ASEE Joint Propulsion Conference and Exhibit*, Huntsville, AL, July 17–19, 2000.

2. Elam, S.; Holmes, R.; McKechnie, T.; et al.: "VPS GRCop-84 Chamber Liner Development Efforts," *52nd JANNAF Propulsion Meeting/1st Liquid Propulsion Subcommittee Meeting*, Las Vegas, NV, May 10–13, 2004.

3. Elam, S.; Lee, J.; Holmes, R.; et al.: "Lightweight Chambers for Thrust Assemblies," *52nd International Astronautics Conference*, IAF–01–S.3.05, Toulouse, France, October 1–5, 2001.

4. Hickman, R.; McKechnie, T.; and Holmes, R.: "Material Properties of Vacuum Plasma Sprayed Cu-8Cr-4Nb for Liquid Rocket Engines," 37th AIAA/ASME/SAE/ASEE/Joint Propulsion Conference, Salt Lake City, Utah, July 8–11, 2001.

5. Hickman, R.; McKechnie, T.; Holmes, R.; and Elam, S.: "Material Properties of Net Shape, Vacuum Plasma Sprayed GRCop-84," *40th AIAA/ASME/SAE/ASEE Joint Propulsion Conference*, AIAA 2003–4612, Huntsville, AL, July 2003.

6. Holmes, R.R.; and McKechnie, T.N.: "Vacuum Application of Thermal Barrier Plasma Coatings," 1988 Conference on Advanced Earth-To-Orbit Propulsion, NASA/University of Alabama in Huntsville, May 10–12, 1988.

7. Holmes, R.R.; and McKechnie, T.N.: "Vacuum Plasma Spray Coating," *Advisory Group for Aerospace Research and Development Conference Proceedings*, No. 449, Application of Advanced Material for Turbomachinery and Rocket Propulsion, NATO, 1989.

8. Holmes, R.R.; and McKechnie, T.N.: "Plasma Spray in the Space Program: Evolution From Thermal Barrier Coatings to Structures and Back," Thermal Barrier Coatings for Aerospace Applications, Toronto, Canada, October 22–23, 1992.

9. Holmes, R.; Burns, D.; and McKechnie, T.: "Vacuum Plasma Spray Forming NARloy-Z And Inconel 718 Components for Liquid Rocket Engines," *Third National Thermal Spray Conference*, edited by T. F. Bernecki, ASM International, Long Beach, CA, pp. 363–368, 1990.

10. Holmes, R.R.; Zimmerman, F.R.; Krotz, P.D.; et al.: "Thermal Spray of Refractory Metal Powders for High-Temperature Furnace Applications," *TMS Annual Conference*, Denver, CO, February 1993.

11. Holmes, R.; Zimmerman, F.; McKechnie, T.; and Krotz, P.: "Enhanced Near Net Shape Ceramic Refractory Composite High-Temperature Cartridges by VPS Metallurgical Alloying Technique," *14th International Thermal Spray Conference*, Kobe, Japan, May 22–25, 1995.

12. Holmes, R.R.; Ellis, D.; McKechnie, T.; and Hickman, R.: "Microstructure and Mechanical Properties of Vacuum Plasma Sprayed Cu-8Cr-4Nb," *10th JPL/MSFC/AIAA Advanced Propulsion Research Workshop*, Huntsville, AL, April 5–9, 1999.

13. Holmes, R.R.; Ellis, D.; and McKechnie, T.: "Robust Low-Cost Aerospike/RLV Combustion Chamber by Advanced Vacuum Plasma Process," *36th Space Conference*, Cape Canaveral, FL, April 27–30, 1999.

14. Holmes, R.; Elam, S.; McKechnie, T.; et al.: "Robust, Low-Cost Liquid Rocket Combustion Chamber by Advanced Vacuum Plasma Process," *Annual TMS Meeting*, New Orleans, LA, February 10–16, 2001.

15. Holmes, R.; Elam, S.; McKechnie, T.; et al.: "Robust Low-Cost Liquid Rocket Combustion Chamber by Advanced Vacuum Plasma Process," *39th Space Congress*, Cocoa Beach, FL, April 29–May 2, 2002.

16. Krotz, P.; Liaw, Y.; Holmes, R.; et al.: "Enhanced Near Net-Shape Ceramic Refractory Composite High-Temperature Cartridge by VPS Metallurgical Alloying Techniques," *Eighth National Thermal*

Spray Conference, edited by C.C. Berndt and S. Sampath, ASM International, Houston, Texas, pp. 729–733, September 1995.

17. McKechnie, T.; Krotz, P.; Liaw, Y.; et al.: "VPS Forming of Refractory Metals and Ceramics for Space Furnace Containment Cartridges," *Fifth National Thermal Spray Conference*, edited by C. Berndt and T. Bernicki, ASM International, Anaheim, CA, pp. 297–301, June 1993.

18. McKechnie, T.; Krotz, P.; Liaw, Y.; et al.: "Near Net Shape Forming of Ceramic Refractory Composite High-Temperature Cartridges by VPS," *Seventh National Thermal Spray Conference*, edited by C. Berndt and S. Sampath, ASM International, Boston, MA, pp. 457–463, June, 1994.

19. O'Dell, J.S.; McKechnie, T.N.; and Holmes, R.R.: "Development of Near-Net Shape Refractory Metal Components Utilizing Vacuum Plasma Spray," *Tungsten Refractory Metals and Alloys 4*, Metal Powder Industries Foundation, Princeton, NJ, pp. 159–169, 1998.

4.2 Electrically Heated Module for Hot-Hydrogen Materials Development

PIs—Ron Litchford, NASA MSFC/ER32 and John Foote, NASA MSFC/ER32 (Jacobs).

Co-PIs—Narayanan Ramachandran, BAE Systems and Samim Anghaie, INSPPI, University of Florida.

Objective

Hydrogen rocket performance is fundamentally constrained by material thermal limits and corrosive reactions at high-operating temperatures. Consequently, advanced hydrogen-resistant materials and associated testing capabilities are needed to expand the accessible temperature range to as high as 3,000 K. Promising contemporary approaches for realizing additional extensions in operating temperature include utilization of modern coating techniques and advanced high-temperature materials such as bi-/tri-carbides of the uranium (U)-Zr-X type, carbon nitrides of U and Zr, and ceramic metallics (CERMETs) based on a tungsten (W) matrix. Recently, NASA MSFC began making investments to advance and establish processing and fabrication techniques for these types of materials, but proper characterization also requires the establishment of testing capabilities for exposing representative samples to severely corrosive hot-hydrogen environments.

To date, hot-hydrogen materials characterization at MSFC has followed a two-prong strategy. The first prong is based on development of a materials specimen test fixture attachment for an existing 1–MW multigas arc heater facility, as illustrated in figure 64. This effort was sponsored as an MSFC Focus Area IR&D Project 05–80 and recently culminated in the establishment of an operational test capability. The second prong is based on design and fabrication of an RF heated fuel element simulator, under the sponsorship of the Nuclear Systems Project Office, and is expected to attain operational status in 2007. These two apparatus are independently configured to satisfy separate test objectives and therefore serve nonconflicting, complimentary functions.

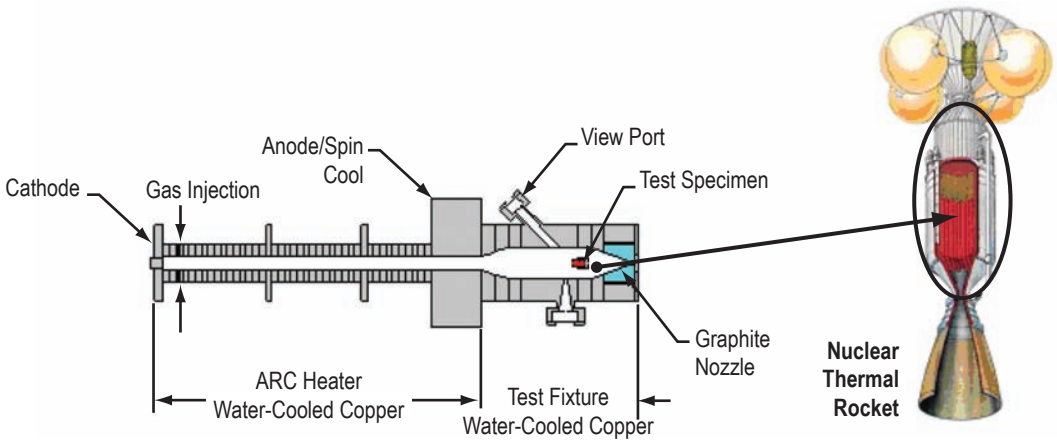

Figure 64. Arc heater facility for passive exposure of hot-hydrogen materials.

The technical objective of this project was to enhance the capability of the arc heated hydrogen material specimen tester through incorporation of an electrically powered resistive heater module for testing and characterizing hydrogen-resistant material specimens to a maximum surface temperature of 3,000 K. The module heater element would accept a short length, standardized tubular material specimen and was designed for direct attachment to existing hyperthermal environment simulator hardware. In this system, hydrogen gas is preheated in a 1-MW arc heater and forced to flow through the central passage of the tubular specimen, where additional heat can be electrically generated and transferred to the backside of the specimen. Such an arrangement allows for precise tuning of hydrogen gas temperature at the module entrance and precise electrical power deposition in the specimen, allowing for exact duplication of thermal hydraulic conditions at any specified location in a high-performance solid-core nuclear thermal rocket reactor. This would be a powerful and unique capability without contemporary comparison, and would enable low cost, rapid turnaround testing of advanced high-temperature nuclear fuels in a nonirradiated environment. It would also permit direct experimental access to hydrogen corrosion phenomena at extreme temperature under flowing conditions with unprecedented real-time diagnostic access.

Technical Approach

Our technical approach for the project followed a well-defined sequence of tasks. First, baseline environment/specimen requirements and specifications were set and a conceptual design was developed that accounted for mechanical/flow path interfaces, water coolant interfaces, electrical power supply/components/connections, heater element configuration, and diagnostics. The outcome of that activity was a basic configuration layout that guided follow-on mechanical design activities and comprehensive thermal fluid simulations with conjugate heat transfer. Performance characteristics for the system were confirmed through simulations, and the mechanical design satisfied thermal and stress analyses constraints for ensured safe operation. Finally, design drawings were developed and specifications were set for special test equipment and components. Potential vendors for these procurements were identified and preliminary cost estimates were developed for a follow-on acquisition and fabrication phase.

The major design requirements were as follows:

- Recreate thermal hydraulic environment traceable to nuclear thermal rocket (NTR) solid-core reactor.
- Maximize utilization of existing passively heated test fixture.
- Hydrogen flow rates of 7–10 g/s.
- 35-atm maximum chamber pressure.
- Sustained high-temperature operation.
  - 3,500 K maximum hydrogen temperature.
  - 3,000 K maximum specimen temperature.
  - Resistive heater element temperature >3,000 K.
  - Resistive heating power to enable $T_{specimen} > T_{hydrogen}$.

• Optical access for direct pyrometer measurement of specimen temperature.

The layout of the baseline arc heated hot-hydrogen test apparatus is shown in figure 65. Note that the rod-shaped material specimen is held in the hydrogen flow with a W spider and that heating of the specimen occurs entirely through the transfer of heat from the gas to the sample. More representative simulation of the nuclear fuel environment requires that heat somehow be deposited into the material specimen so it becomes hotter than the gas and the direction of heat transfer is reversed. The proposed electrically heated module would replace the rod-shaped specimen with a through-flow tubular configuration surrounded by a resistive heater element.

The baseline test fixture hardware had previously been designed and fabricated as part of MSFC Focus Area IR&D Project 05–80 and served as the departure point for our design. This hardware, shown in figure 66, includes access for optical-based diagnostic measurements and incorporates a refractory metal heat shield with backside Zr felt insulation to ensure thermal integrity. It was deemed prudent at the outset to retain these features in the new electrically heated specimen module design.

The resistive heating module is required to be geometrically compatible with the baseline test fixture hardware and must feature proper stability in the flowing hydrogen environment under the entire range of operating pressure and temperature. Rod, tube, bar, plate, or circular shapes could be used to construct the resistive heater element, but a coil-shaped configuration was considered superior since it would be compatible with the test fixture geometry and provide more uniform heating.

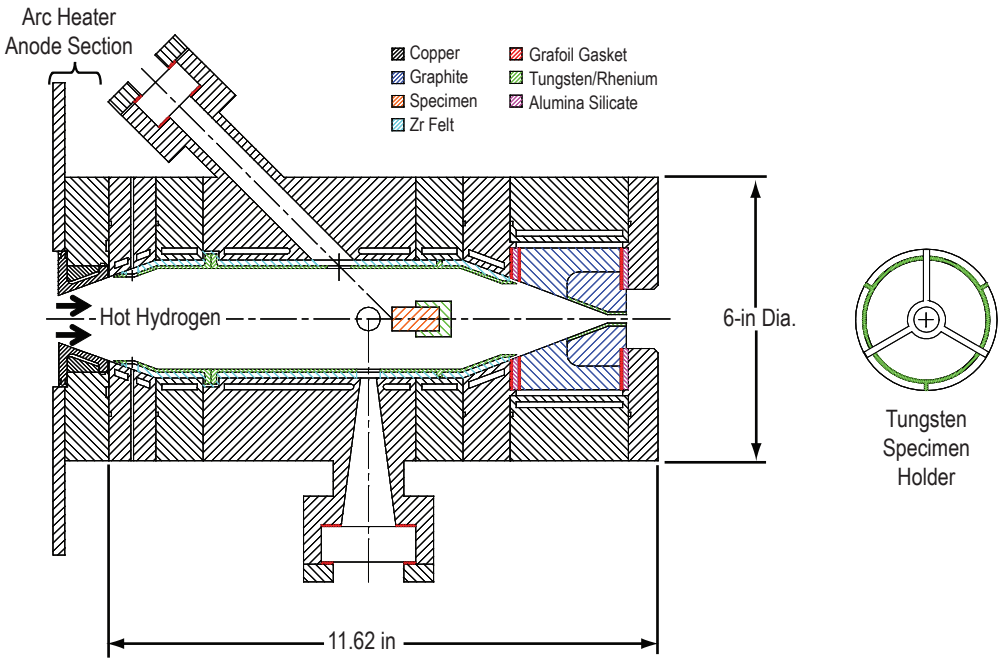

Figure 65. Test fixture layout for passive exposure of hot-hydrogen materials.

Figure 66. Test fixture hardware for passive hot-hydrogen materials exposure.

At the outset of the project, a variety of materials were to be considered for construction of the resistive heater element. The alternatives included coated high-density graphite or glossy carbon material and refractory metals. In a vacuum environment, it is not possible to operate a resistive heating element at temperatures above 2,000 K due to excessive sublimation of graphite. On the other hand, in high-pressure hydrogen (100–500 psi), high-density graphite heating elements could be operated at temperatures up to 2,300 K without significant loss of carbon and hydrocarbon formation. Glossy carbon features lower corrosion and evaporation rates and could be operated at temperatures up to 2,500 K. For operation at temperatures above 2,500 K, however, it would be necessary to cost the graphite heating element using transition metal refractory carbides such as tantalum or hfCs. Thus, the design phase of the project included detailed material and chemical compatibility analysis for coated graphite materials.

A total of 9 mo was allotted for completion of the project. This accelerated project schedule limited the scope to a design study only and no detailed tests were planned. However, some exploratory testing was undertaken to assess the degree of chemical compatibility of glossy carbon and coated graphite with hot hydrogen to a maximum temperature of 3,200 K.

Research and Development Results

Using the predefined requirements and specifications as a guide, we first arrived at the conceptual design illustrated in figure 67. The general idea was to direct the hot hydrogen from the area heater to a constant arc test section in which tubular or solid cylindrical specimens, up to 8-cm diameter, would be surrounded and heated by a curved slat resistive heating element. An alumina/Zr insulator shield would be located between the heater element and the water-cooled copper walls of the test section. A thin sheath of W alloy (W-Ni-Cu) would be placed between the heating element and the insulating material to partially reflect radiative heat back toward the material test specimen.

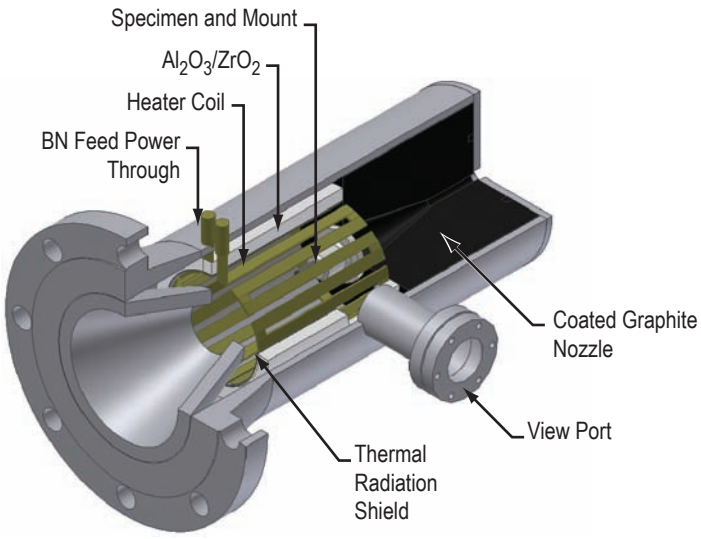

Figure 67. Conceptual design of electrically heated hot-hydrogen materials compatibility test fixture.

Further refinement of the design concept was achieved by imposing geometrical constraints associated with the preexisting test fixture hardware. The objective was to modify the design as a means of maximizing use of existing hardware and minimizing new hardware fabrication requirements. This effort resulted in a convergence of the design with notable simplifications. In particular, the refined design would only require the construction of a single new test section module that would contain the heater element. Other retrofits included a new specimen mount and a new W/Re alloy shield/funnel section, as shown in the final design layout in figure 68. Standard size pieces and fittings were used to keep the number of custom components to a minimum. The key advantage of this approach was the fact that only a single stack of the passive heating test fixture hardware needed to be replaced, yielding system simplicity and cost containment without sacrificing testing capability. Moreover, the original optical access segment could be retained to provide line-of-site pyrometer measurement of specimen surface temperature.

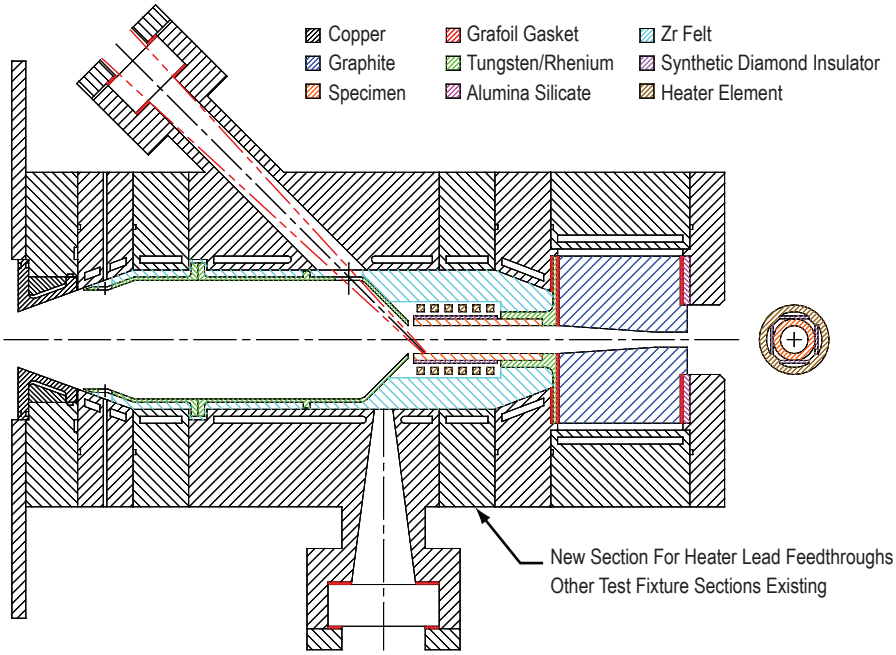

Figure 68. Final design layout of electrically heated hot-hydrogen materials compatibility test fixture.

Critical innovative design features were mainly associated with the resistive heater element itself. The major technical issues of concern included materials selection for the heater element and its structural support, electrical power feed-through/connections, and heater performance characteristics. Careful examination of the design problem resulted in two possible material alternatives for the curved slat heater element material. The alternatives being either coated graphite or W/Re alloy construction. As currently envisioned, the heater element would be supported by the tubular specimen using four synthetic diamond wafers, as illustrated in the layout of figure 68. Since diamond exhibits excellent TC characteristics while acting as a near perfect electrical insulator it was believed to be the prime candidate structural support material. How well synthetic diamond can endure the corrosive hot-hydrogen environment was a major unknown, however. To address some of these material compatibility issues during the early stages of the design, some basic hot-hydrogen exposure tests were developed.

A variety of high-density graphite materials and glossy carbon were considered for the design of the resistive heating element module. Since continuous operation at temperatures above 2,300 K was required, it was decided to examine the viability of graphite coated with transition metal carbides such as Nb, Ta, or HfCs. During the early stages of the project, and in conjunction with another ongoing research project, several coating trials were performed on three different types of graphite material to down select the type of graphite that could be used for the curved slat heater. Generic graphite, JP1060, and isographite were explored as possible substrate candidates for subsequent deposition by direct and reactive electron beam physical vapor deposition (EB–PVD). Preliminary trials were conducted with TaC deposited by reactive ion beam assisted (RIBA) deposition since it has the greatest potential for producing single-phase TaC through control of carbon deposited on the substrate. Following these early trials, the down selection to NbC was made due to the large number of TaC samples that contained other phases including Ta_2C. Coating trials were then carried out with NbC on half-cylinder 3.5-in long

samples using both direct and reaction EB–PVD. The samples were then hot hydrogen tested in a furnace. The results were mixed with regards to the type of graphite and which method of NbC deposition performed the best due to the geometry of the substrate material. Since the substrates were longer than the hot zone for the initial hot-hydrogen testing, increased thermal shock led to premature spallation of the samples. Due to time limitations on this project, it was decided not to pursue the coated graphite option and the focus was shifted to the design of a W-based curved slat heating element. Tungsten and its alloys are fully compatible with hydrogen at temperatures up to 3,500 K. The main constraint with the W heating element is the fabrication of a single-piece heating element with proper dimensions and power leads.

A detailed thermal and mechanical analysis was performed to generate design specifications and performance characteristics of the W-based resistive heating element module. The electrical resistivity of chemical vapor deposition (CVD) W in the operational temperature range of the hot-hydrogen test facility is within 5–10 $\mu\Omega$–cm. With the geometrical dimensions of the test section as a constraint, the thickness of the curved slat heating element was adjusted to provide sufficient heating to maintain the test specimen at maximum temperature of 3,500 K. The power requirements for the heating module was determined using detailed CFD and conjugate heat transfer analyses of the entire test section that included typical test specimens and hot-hydrogen flow, as well as thermal losses to the boundary. The resulting design of the tungsten curved slat resistive heating element is shown in figure 69.

A modified version of FLUENT was combined with a conjugate heat transfer model for thermal fluid simulation and analysis of the electrically heated test fixture layout, shown in figure 68. This simulation assumes axial symmetry and accounts for compressible dissociating turbulent hydrogen flow with radiative heat transport. The computational domain for the simulations is provided in figure 70. In this particular case, 10 g/s of hot-hydrogen flow is heated to 2,500 K in the arc heater and enters the test fixture at 35 atm in a uniformly mixed state.

Results from the simulation with a heater temperature set to 3,500 K are summarized in figure 71, which shows the stream function and temperature distributions in the test fixture. A clean flow structure and good temperature distribution was obtained at the entrance to the tubular specimen. Note that the tubular sample is approximately twice the length of the heater in this particular case. The simulation also shows that the heater element performs well and is effective in transferring heat to the backside of the material sample so the temperature gradient is directed inward through the tube to the hydrogen gas. It was found that the specimen temperature could be readily raised and stabilized using the heater element power as a control parameter. The temperature distribution in the specimen and the internal surface temperature along the tube are shown more clearly in figure 72.

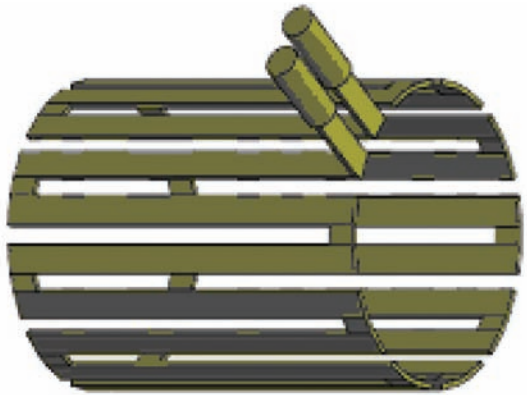

Figure 69. Design of W-curved slat heating element.

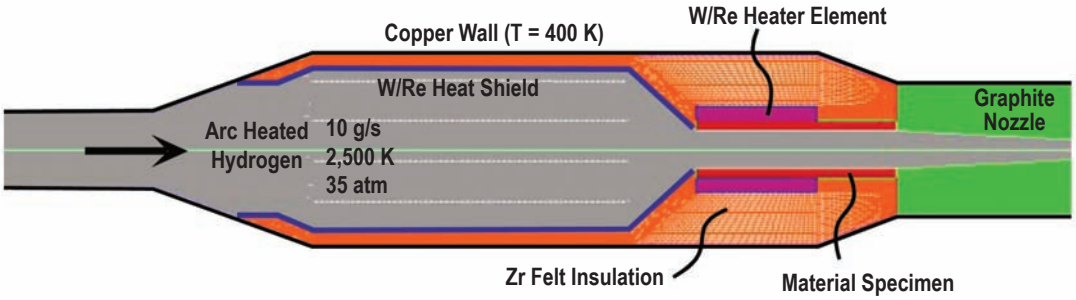

Figure 70. Computational domain for thermal fluid simulations.

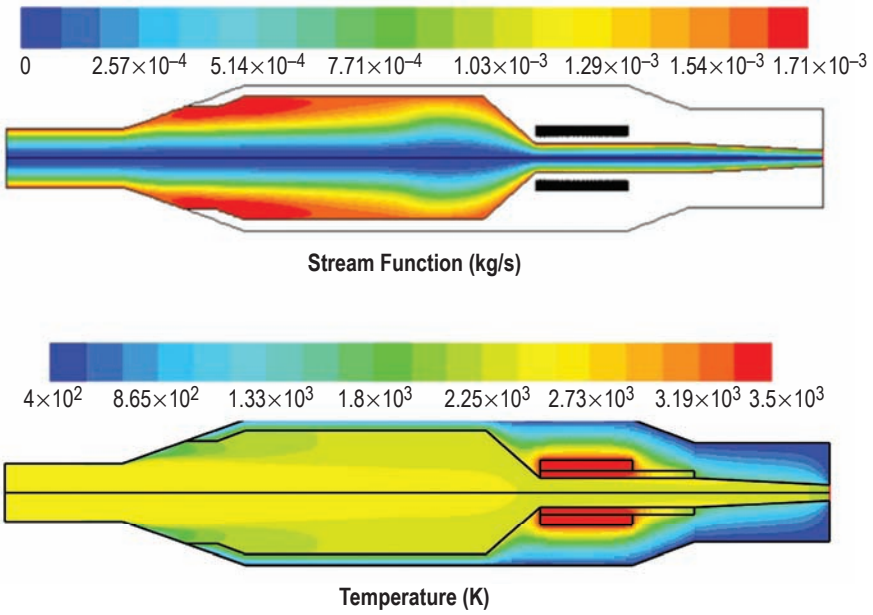

Figure 71. Calculated stream function and temperature distributions in test fixture.

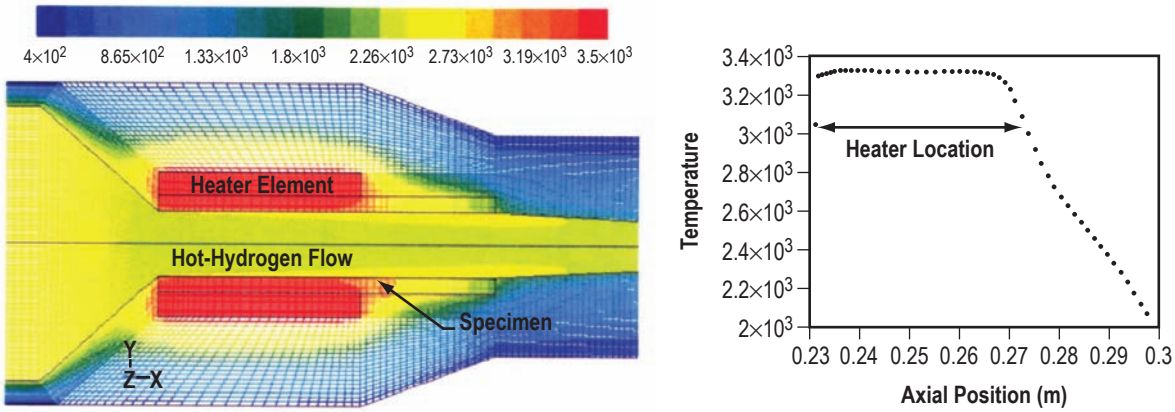

Figure 72. Internal and inner surface specimen temperature distributions.

Project closeout plans include test and evaluation of design components and materials. Using the passively heated test fixture hardware, hot isostatic pressing (HIP) processed CERMET specimens will undergo long-duration exposure to flowing hot hydrogen as a screening evaluation for potential NTR utilization. These specimens have been fabricated, as shown in figure 73, and are immediately available for installation and testing purposes. If this is successful, we also plan to demonstrate fabrication of a tubular HIP CERMET specimen sized to fit the proposed electrically heated test module. Concurrent with these long-duration tests series, we will also expose some synthetic diamond wafers that will be inserted edgewise into the graphite nozzle assembly. The sample wafers have already been procured and inserted into the nozzle in preparation for the test series.

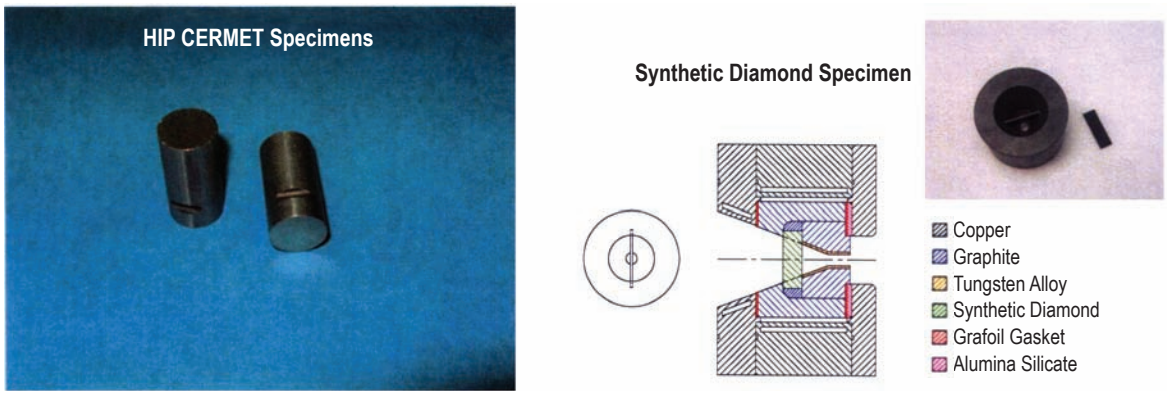

Figure 73. HIP CERMET specimens and synthetic diamond wafer specimens.

Further closeout plans include continued refinement of the thermal fluid simulations and completion of the test fixture design drawings with detailed cost analysis. The current rough estimate for the cost of the electrically heated specimen module is approximately $100k. Most of this cost is associated with the fabrication of the W/Re heater element and the new heat shield insert.

Follow-On Research and Development

The arc heater facility for hot-hydrogen exposure of nuclear thermal propulsion materials is fully operational and performance mapping activities have been completed. The passively heated test fixture hardware has been fabricated and delivered, with installation in progress as of this writing. Baseline testing and capability demonstrations are scheduled for fall 2006. Supporting materials compatibility testing on corrosion-resistant CERMET specimens and synthetic diamond wafers will be undertaken as part of the planned test series. Nuclear Research Council (NRC) licensing activities for the use of depleted uranium (DU) in this facility are in progress and expected to be completed in FY 2007.

Recommendations for follow-on R & D include fabrication and/or procurement of the resistively heated specimen module components and performance/capability demonstration testing. Ideally, the system would be used for exposure of DU containing tubular fuel specimens, with HIP processed CERMETs as a high-priority candidate. Development of the resistively heated module would also enable evaluation of advanced hydrogen-resistant coatings under realistic thermal hydraulic conditions. Because the backside heating configuration can generate an inverted temperature gradient within the specimen, it should also be possible to simulate and investigate the mysterious midband corrosion phenomena previously encountered during the ROVER/NERVA nuclear testing programs.

Solar Electric Propulsion

During FY 2006, funds were provided to the NASA MSFC In-Space Propulsion Technology Office to support two material research tasks in the area of solar electric propulsion (SEP). Electric thrusters use electrical energy to ionize and accelerate a gas propellant to much higher exhaust velocities than can be achieved by chemical engines. Operating at high exhaust velocities in space allows a significant reduction in the amount of propellant required by the spacecraft, which in turn reduces the amount of mass that needs to be launched into orbit for a given mission. However, the thrust generated by electric propulsion is significantly lower than that of chemical rockets, hence electric propulsion systems must operate for significantly longer periods of time to provide a given change in spacecraft velocity. Unlike chemical engines, which may provide high thrust for several minutes followed by long coasting periods, electric thrusters typically operate for hundreds to thousands of hours over the life of a mission. While solar-powered electric propulsion is not suitable for time constrained piloted missions, electric thrusters are routinely used for satellite orbit station keeping. In addition, they have been proposed as economical cargo delivery systems for the Moon and Mars, and are ideal for the high-impulse robotic science missions of interest to NASA.

The common goal of the two FY 2006 SEP material research tasks is to improve the life of Hall-effect thrusters, a type of electric thruster in which ionized plasma is electrostatically accelerated by magnetically trapped electrons circulating about the exit plane of an annular ceramic chamber, as shown in figure 74. Electrons emitted by an external cathode are drawn to a positively charged anode within the chamber, and are trapped into spiral orbits along magnetic field lines created by embedded magnets within the chamber. Some electrons escape to the anode, ionizing a xenon gas propellant along the way. The positively charged xenon ions are accelerated out of the thruster by the negative charge of the magnetically trapped electrons, and the beam is subsequently neutralized by additional electrons from the external cathode. During operation, collisions between high-energy xenon ions and the ceramic channel causes the ceramic material to erode, as shown in figure 75, eventually exposing the embedded magnets and leading to the end of useful thruster life.

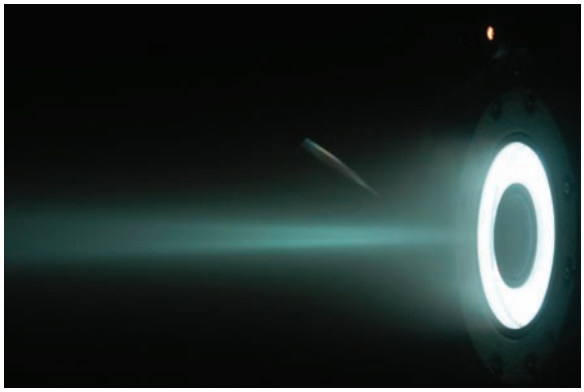

Figure 74. Hall-effect thruster in operation (courtesy NASA GRC).

Figure 75. Characteristic erosion of Hall-effect thruster (NASA GRC).

The first funded task continues the development of an advanced numerical simulation of xenon plasma and material surface interactions that ultimately determine the lifetime of Hall thrusters. With funds provided by the In-Space Propulsion Technology Office, the University of Michigan (UM) received a grant from NASA GRC to develop numerical simulations that can more accurately predict Hall thruster erosion rates as a function of thruster operating condition, magnetic field configuration, and ceramic channel geometry. Over the past year, UM initiated work on a model to predict material erosion on the inner and outer channel walls of a hall thruster. Comparisons of code predictions with experimental erosion data obtained from the NASA–77M Hall thruster operating at 500 V, measured over three 100-hr increments, have shown good agreement as demonstrated in figure 76. In a continuation of this work, the materials research funds are being used to extend the numerical analysis and apply the more sophisticated code to the high-voltage Hall accelerator (HIVHAC) currently being developed at NASA GRC. Specific tasks undertaken during this effort include the following:

- Modeling the plasma as a steady two-dimensional flow.
- Modeling plasma potential and ion and neutral number densities along the channel using a UM two-dimensional hydrodynamic Hall thruster code.
- Modeling the xenon ion-atom scattering processes based on calculated ion and neutral density profiles.
- Incorporating geometric effects associated with changes in the ceramic channel dimensions as a result of material erosion.
- Validation of code results against existing experimental Hall thruster data.

The second SEP materials research task is designed to analyze and test the strength and fracture resistance of the advanced state-of-the-art (ASOA) HIVHAC boron nitride (BN) ceramic channel relative to anticipated launch environments. The ASOA HIVHAC thruster is a unique Hall thruster design that utilizes in situ replacement of the BN ceramic channel during operation to improve Hall thruster life. The objective is to verify the structural integrity of the BN Hall thruster discharge channel mounted in the HIVHAC development thruster configuration, shown in figure 77. Specific tasks include the following:

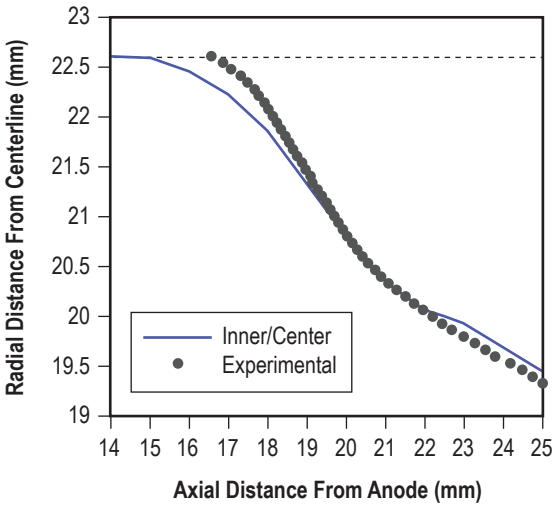

Figure 76. Comparison of numerically predicted and experimentally measured inner channel erosion of the NASA–77M Hall thruster after 200 hr of operation.

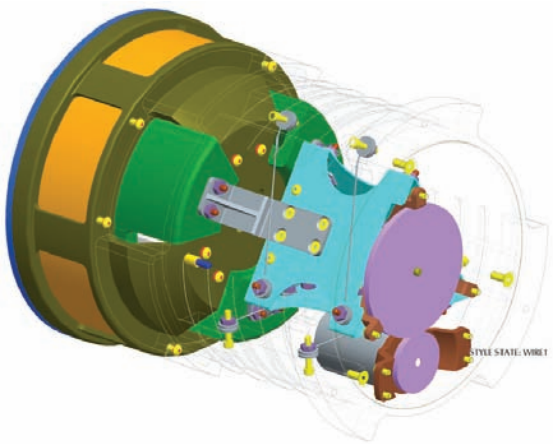

Figure 77. Schematic of the GRC NASA–103M ASOA HIVHAC developmental Hall thruster.

- Modal and displacement analysis of the existing HIVHAC prototype thruster.
- Fabrication of two BN ceramic discharge chambers (test article plus a spare) to refurbish the existing HIVHAC thruster to a beginning-of-life configuration.
- Performing structural characterization tests, to qualification levels, of the BN discharge channel mounted within the HIVHAC prototype Hall thruster.

Planned tests include resonant frequency and modal surveys through sinusoidal excitation, as well as random vibration and classical shock testing. This task will substantially reduce the risks associated with ASOA thruster in situ channel replacement, potentially leading to significantly improved Hall thruster lifetimes.

5. VEHICLE HEALTH

5.1 High-Temperature and Radiation-Resistant Electronic Devices for Exploration Missions

PI—Ching-Hua Su, NASA MSFC

Co-PIs—Sandor Lehoczky, NASA MSFC and Witold Palosz, BAE

Introduction

Presently, electronics that operate and control functional systems on board space vehicles must be protected from hostile conditions because the available silicon (Si)-based technology will not meet the requirements for many applications operating in hostile environments. Electronic and optical devices capable of operating at higher temperatures are needed for long-duration exploration mission because—

- In present control systems, all electronics are centralized in a protected area that is cooled to provide an ambient environment. Advanced high-temperature electronic and optical devices

  – Reduce the weight and power requirements of wire harnesses and cooling systems.
  – Enhance reliability.

- High-temperature embedded electronic sensors are needed to monitor the condition and effectiveness of the heat shielding materials, such as those used in aerocapture applications, as well as to optimize the material thicknesses required and eliminate unnecessary weight.

- For an orbiting nuclear power reactor, the size of the radiator for the cold end of a heat engine (i.e., the reactor) decreases very rapidly as the cold-end temperature is increased. Raising this temperature will allow a much more compact design but will require control electronics operating at higher temperature than possible with Si-based electronics.

More radiation-resistant electronic devices are highly desirable because—

- During long-duration deep space exploration the galactic radiation, especially high-energy solar flares and the coronal mass ejection (CME), can damage the currently used Si-based electronic components. Excess damage can degrade, or even terminate, the performance of various mission-critical components. In the absence of shielding provided by the Earth's magnetic field even more extensive shielding will be required during long-duration deep space missions. Because extensive shielding of sensitive electronics against radiation results in significant wasted payload weight, more radiation resistant electronics devices that require less shielding are highly desirable.

- An efficient operation of nuclear reactors requires monitoring and control of the power distribution generated in the reactor core. At present, a three-dimensional map of the core is developed from an array of thermocouples and neutron flux detectors that must be replaced every 3 yr. With integrated drive electronics and multiplexing and more radiation damage resistant detector materials, the replacement time could be at least doubled.

In the past few years, a class of new materials has emerged with superior properties that are much more suitable than Si for use as high temperature and radiation-resistant electronic devices. In general, these materials share the following intrinsic properties: Wide electronic bandgap, high-TC, high-breakdown electrical field, high-current density, high-thermal stability, and chemical inertness. These general properties lend themselves to exploitation in nearly any electronic device with special applications in high-power electronics, high-frequency applications, and electronic or optical sensors to be used in hostile environments. It has also been reported that materials and devices useful for high-temperature operations tend to be more resistant to radiation damage. The potential high temperature and radiation resistant materials include SiC, $Si_{1-x}Ge_xC$, ZnO, GaN, AlN, $Ga_{1-x}AlxN$, and BN. Although there are numerous reports on the preparation and characterization of these materials, the technology of making devices out of the materials is at its infant stage with a TRL of 2–3. Up to now, there was only one high-temperature demonstration that involved an SiC junction field effect transistor that demonstrated the operation of digital logic gates at 600 °C, as compared to the maximum operating temperature of 200 °C for Si-based technology.

Objectives. The objectives of the proposed project are to perform tests of optoelectronic devices under elevated temperatures and high-energy radiation and develop technology for the production of high-temperature and radiation-resistant electronic devices.

Accomplishments

The technical accomplishments during this project include the following:

Selection and Procurement of Diodes. Selection of diodes for testing was based on the survey of companies listed in the Thomas Register of American Manufacturers (www.thomasnet.com). Of 212 companies found to offer light emitting diodes (LEDs), two manufacturers were found to offer diodes rated for operation at up to 100–150 °C (only III–V, no SiC or nitrides). Representative diodes selected and procured for testing are listed in table 10. It was found that diodes OD–470L, –520L, and –620L have acrylic elements and get destroyed at about 150 °C, thus further testing has not been done. Instead, a noncommercial, developmental blue diode from TopGaN, Ltd. has been acquired for testing. Due to limited availability, not all types of diodes could be tested under all conditions, and diode JANTX1N–6610 was not available at all.

Table 10. Diodes selected to be tested.

Diode	Color	Structure	Manufacturer
JANTX1N–6493	Red	GaAsP/GaP	1
JANTX1N–6494	Yellow	GaAsP/GaP	1
JANTX1N–6495	Green	GaP/GaP	1
JANTX1N–5765	Red	GaAsP/GaAs	1
JANTX1N–6092	Red	GaAsP/GaP	1
JANTX1N–6093	Yellow	GaAsP/GaP	1
JANTX1N–6094	Green	GaP/GaP	1
JANTX1N–6609	Red	GaAsP/GaP	1
JANTX1N–6611	Green	GaP/GaP	1
OD880–FHT	IR	GaAlAs	2
OD880–LHT	IR	GaAlAs	2
OD880–WHT	IR	GaAlAs	2
OD880–6FS	IR	GaAlAs	2
T1472a	Blue	InGaN	3

1—M Universal Semiconductors, Inc.
2—Opto Diode Corp.
3—TopGaN, Inc.

Procurement and setup of annealing furnace and the facility for the measurements of emitting spectrum and intensity. Several tubular resistance-heating furnaces as well as temperature controllers were procured and installed. The facility for the measurements of emission intensity and spectrum of diodes consists of the following:

- SD2000 spectrometer from Ocean Optics Inc. (OOI).
- Fiber optic integrating sphere for emission measurements from OOI.
- Adjustable current LED power supply from OOI.
- OOIIrrad-C software for irradiance measurement from OOI.

The facility was installed as shown schematically in figure 78. The elements of the system integrating sphere, power supply, spectrometer, and software were acquired from OOI. The diode was plugged into the power supply, which is placed on top of the integrating sphere with the diode at the mouth of the sphere. The signal from the spectrometer was processed by the computer. For the measurements, the diodes were powered with 20-mA current.

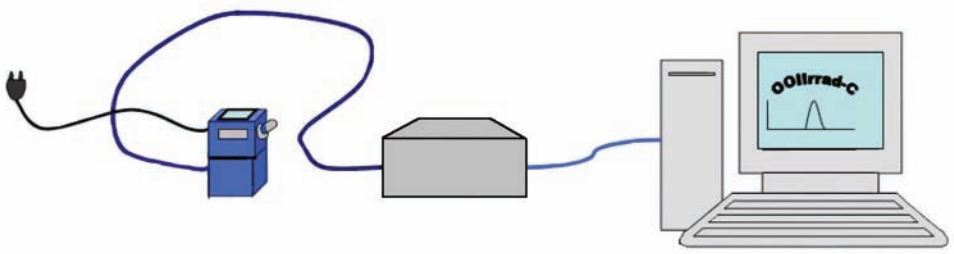

Figure 78. Setup for measurements of emitting spectrum and intensity of LEDs.

Light Emitting Diode Annealing. The immediate effect of temperature on diode performance is due to a change of the physical properties of the system (carrier mobility and concentration, width of the band gap) with temperature and is reversible. Long-term temperature effects are due to structural changes in the diode, primarily through diffusion of dopants. In the first series of our measurements, the diodes were being annealed at selected temperatures and from time to time their integral intensity was measured at RT. In the second series of experiments, the measurements were made in situ when the diode was at different preselected temperatures. For the first series of annealing, the diodes were placed in furnaces at a selected temperature. After a predetermined time they were cooled down, their light intensity and wavelength were measured, and then the annealing at that temperature was continued. The main annealing temperatures were 200, 250, 300, 325, 350, 375, 400, 450, and 500 °C. The total annealing time was up to a few thousand hr and a total of more than 2,500 tests have been performed. A complete failure of the diodes occurred by mechanical failure (disintegration of the housing or detachment of the pin), an apparent electrical short, or electrical disconnect. A typical annealing result is plotted in figure 79 where the integral intensity of two JANTX1N–6609 (red) and –6611 (green) LEDs were measured as a function of annealing time up to 6,800 hr (283 days) for an anneal at 300 °C. The measured intensity decreases as a function of annealing time as expected and the data on two LEDs of the same type are consistent. The following is a summary of the high-temperature annealing tests results:

- At lower temperatures, i.e., below 350 °C, most of the diodes still maintained over 50 percent of their RT intensity after annealing for more than 1 wk.

- For annealing temperatures above 400 °C, most of the diodes had their intensity reduced by more than 50 percent of the original values within 1 day.

- The heterostructured diodes seem to withstand annealing better than the amphoterically doped LEDs (presumably due to difference in the interdiffusion process).

- The worst endurance for temperature annealing was observed with the blue diodes.

- A high rate of deterioration and failure was also observed for some IR diode types.

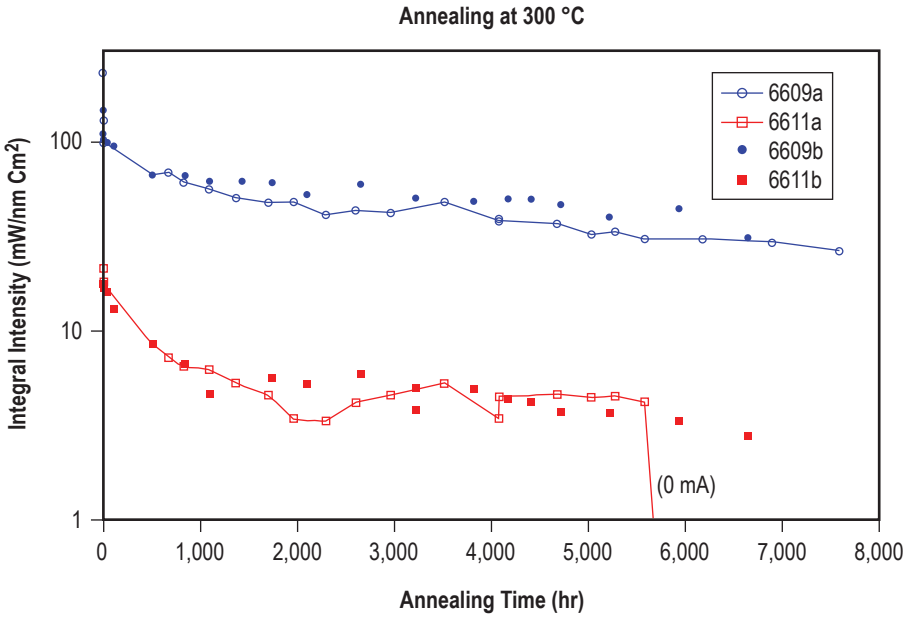

Figure 79. The measured integral intensity of two JANTX1N–6609 (red) and –6611 (green) LEDs as a function of annealing time for an anneal at 300 °C.

For the second series of measurements, i.e., the in situ integral intensity measurements at high temperatures, a small furnace was placed on top of the integrating sphere and the diode was placed in the furnace. The measurements were made at temperatures up to 350 °C (250 °C for the blue emitting diode) and more than 800 tests have been performed. In general, the light intensity decreases with an increase in temperature and the rate of decrease depends primarily on the diode type. The amphoterically doped LEDs (IR range) lost half of their starting intensity already at 60–80 °C, and lost over 90 percent of their intensity at about 200 °C as shown in figure 80(a). In heterostructured diodes, the intensity drop is slower, e.g., 50 percent of RT intensity is still present at temperatures of 120–140 °C for red diodes, and 260–270 °C for green ones. Similar results were found for brand new and long-term annealed LEDs. An increase in temperature increases the wavelength of the peak at a rate between 0.06 nm/°C for the GaN diode and 0.25 nm/°C for some IR LEDs (figure 80(b)). While the change in peak wavelength with temperature is approximately linear for heterostructure diodes, it decreases at higher temperatures for IR LEDs. In conclusion,

- The commercially available In-Ga-Al-As-P type of electronic devices deteriorates after a short time (less than 1 day) annealing at temperatures above 400 °C.

- The heterostructured diodes, such as GaAsP/GaP, can endure annealing better than the amphoterically doped LEDs, such as GaAlAs.

- The functionality of LEDs deteriorates very fast as the operating temperature increases, e.g., the integral intensity dropped to below 10 percent at temperatures above 150 °C.

- It is recommended to explore the potential wide-bandgap semiconductors, such as SiC, ZnO, GaN, AlN, BN, diamond, etc. as material candidates for use in high-temperature environments.

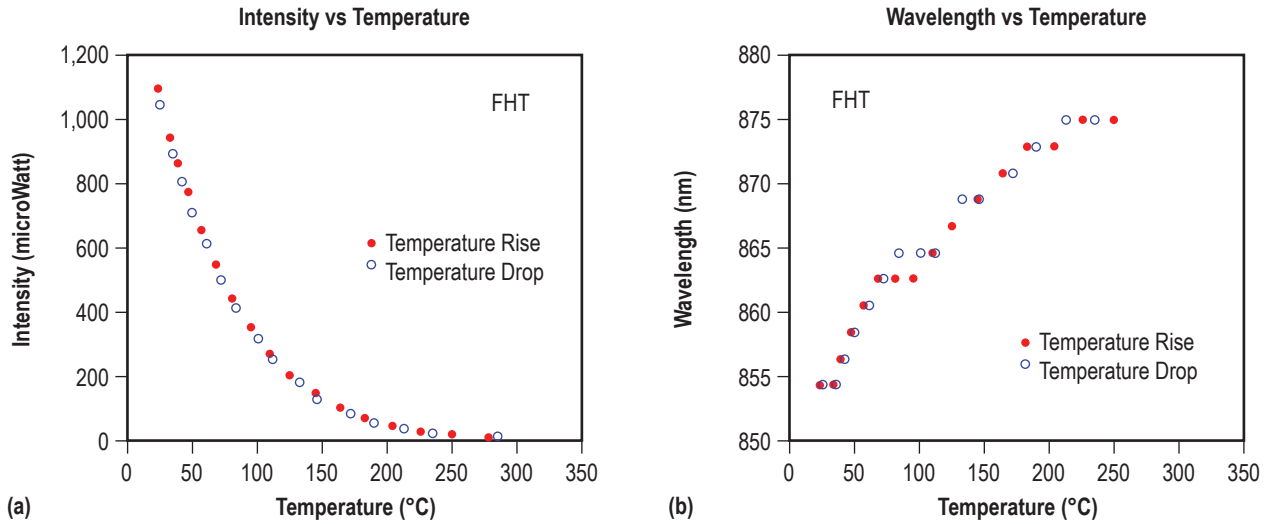

Figure 80. The in situ measured intensity (a) and wavelength peak (b) as a function of temperature for the IR diode OD880–FHT.

Tests of electronic devices under high-energy radiation were not conducted because of the termination of the Radiation Shielding Materials Program and the Deep-Space Test Bed Facility. The galactic radiation mainly consists of high-energy protons (10–200 MeV and higher) whereas the photon source at the Space Environmental Effects Program Office is in the 0.7–2.5 MeV range.

The high-temperature crystal growth and materials processing facility has been assembled and installed for the project, as shown in figure 81. The facility consists of the following:

- High-frequency generator and load coils for induction heating.
- Vacuum chamber and thermal insulation assembly for high-temperature heating applications.
- Vacuum pump system to allow chamber evacuation.
- Pyrometer instrumentation for temperature measurement.
- Water-cooling and power distribution networks.

Because of budgetary constraints, the old Lepel 15kW, 264 kHz RF generator was repaired and used. Several new 3 1/4-in diameter, two- or four-turn load coils were formed from 0.25-in diameter soft copper tubing. The cocil configurations were elevated for optimum power transfer into the sample chamber by adjustments to the generator internal turning coils and various grid and plate current values. The four-turn version of the coils was chosen for the final heating configuration.

Figure 81. High-temperature crystal growth and materials processing facility.

The cylindrical double-walled vacuum chamber, seen in figures 82(a) and (b), enclosing the thermal insulation and the sample chamber was fabricated from fused silica. The inner tube diameter is ≈2 in and the outside tube diameter is ≈3 in. The ½-in gap between the cylinders facilitates the cooling of the inner cylinder (vacuum enclosure) by circulation of water in the passageway between the cylinders. The thermal insulation around the enclosed growth chamber was fabricated from low-TC carbon composite rigid boards manufactured by Carbon Composite, Inc. All of the components within the load coil, including the cooling water, were found to be nearly transparent to the 264-KHz RF radiation, except for the sample chamber.

The multipurpose vacuum pump system includes a fore pump, a turbo pump, and related control electronics and vacuum gauges. It has an attached residual gas analyzer (infriction, transpector 2). The pumps provide vacuum levels in the chamber of about 1.0×10^{-5} torr following several hours of outgassing at subsequently increasing temperatures up to 1,700 °C. The main residual gas component was found to be air (O_2 and N_2) and a much lesser amount of CO_2. The Mikron IR MI–GA 140 pyrometer was positioned to provide a direct site of the top enclosure of the cylindrical graphite growth chamber through a 3/8-in hole in the insulation and a transparent window at the top of the chamber. The growth chamber, shown in figure 83(a), was fabricated from solid 1-in diameter graphite rods and had an inside diameter of 0.7 in. Besides providing confinement for the SiC powder source material and the vapor, it also served as the heating element and its cap served as the substrate.

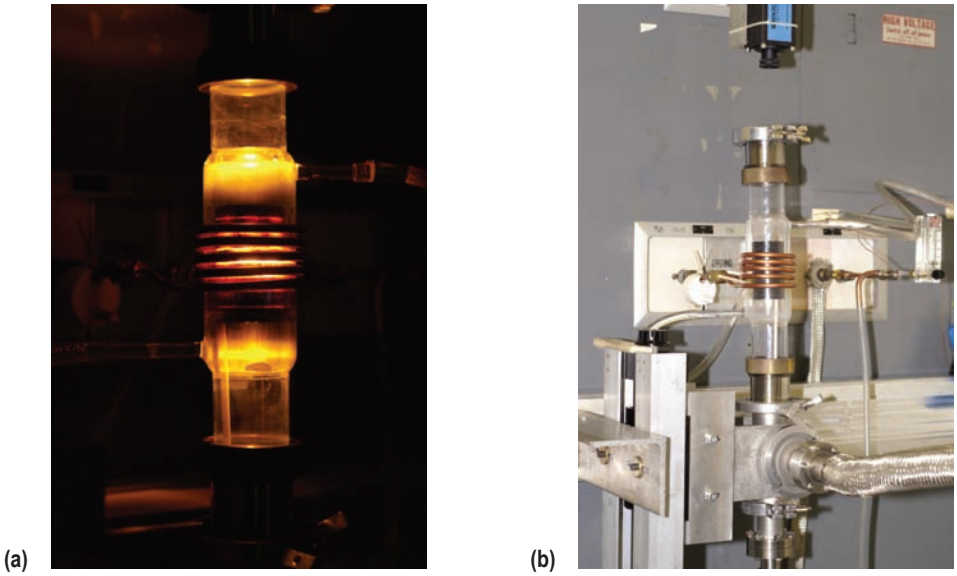

Figure 82. (a) Vacuum chamber and insulation assembly and (b) assembly during high-temperature operation.

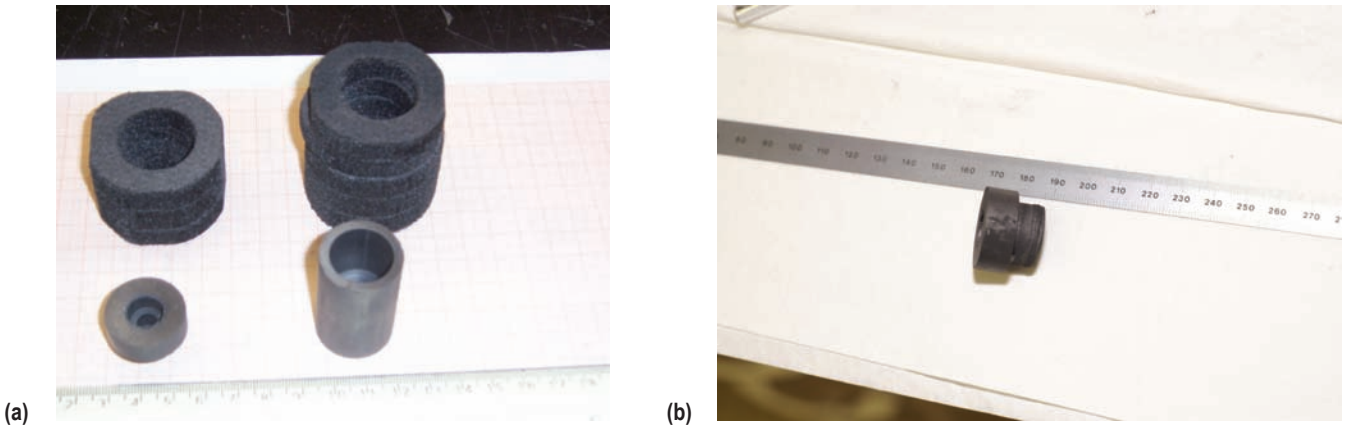

Figure 83. (a) Graphite sample crucible and the closure cap that also served as the substrate and (b) substrate (closure cap) and deposited crystalline SiC.

Several heating experiments were performed to determine the optimum generator parameters, and tuning coil, and load coil configurations to obtain the desired approximately 2,300 °C growth temperatures. For a given experiment, 1.55-g SiC powder was placed at the bottom of the growth chamber. The separation between the powder and the substrate (bottom of the cap) was 1 cm. The temperature was slowly (over several hr) raised to 2,315 °C to allow extensive outgassing of the various components in the vacuum enclosure. About 20 percent or 3 KW of the available power was needed to maintain the temperature. The average residual gas pressure at this temperature was about 2×10^{-5} torr. Following temperature equilibration at 1,315 °C, about 30 min, the vacuum chamber and thus the sample chamber was raised in relation to the load coil to cause lowering of the substrate temperature relative to

the source temperature, and thus initiate crystal growth. For the first experiment the initial substrate temperature was 2,170 °C, providing an approximately 145 °C/cm temperature gradient over the 1-cm gap. During the next 1 hr and 30 min the substrate temperature dropped to 2,160 °C, the following hr to 2,150 °C, then the next 45 min to 2,145 °C. The experiment was terminated after approximately 3 hr 42 min. During this time all of the SiC had evaporated and was successfully deposited onto a 2-mm thick layer on the 1.8-cm diameter substrate (figure 82(b)). A microscopic examination of the deposited crystalline layer showed a highly regular cellular structure. Such structure is usually an indication of growth interface breakdown caused by too rapid growth. For the next experiments, the substrate temperature was increased from 2,170 °C to 2,270 °C to reduce the temperature gradient by a factor of 3.2 and to reduce the growth rate. This experiment was terminated after approximately 30 min of growth time, because of a malfunction in the cooling system. Nevertheless, a substantial layer of SiC was deposited on the substrate during the 30 min. A microscopic investigation of the layer showed, in contrast to the previously observed cellular structure, a greatly improved, more uniform surface morphology. The results clearly demonstrate the importance of vapor transport rate, and perhaps substrate temperature, on surface morphology and crystal defect formation. Between these and an additional SiC growth experiment, the facility was made available to successfully melt and cast several metallic alloy samples at approximately 1,700 °C in support of another unrelated IR&D project. During the long time period spent on high-temperature development testing and the various experiments, the thermal insulation had somewhat degraded and is currently undergoing refurbishment. In summary, a versatile RF heating facility for heating and processing various materials at temperatures up to 2,315 °C, or probably significantly higher, in vacuum has been constructed. It was then successfully used to evaporate SiC and deposit the vapor on lower temperature substrates to facilitate crystal growth. The experiments suggest a definite correlation between the temperatures used and surface morphology development.

Possible Future Research

Develop technology by producing the heterostructured optoelectronic devices made from the candidate wide-bandgap semiconductors such as SiC, ZnO, GaN, AlN, BN, diamond, etc., for applications in high-temperature environments as follows:

- Continue research on the crystal growth of SiC and other high-temperature materials by vapor transport in our RF heating facility.

- Construct a CVD facility to grow heterostructured optoelectronic devices on top of the grown crystals.

- Perform annealing tests on these devices.

6. STRUCTURAL MATERIALS

6.1 A Developmental Program in Macroscopic Tether Materials

PI—David Beale, Auburn University.

Objective

Realization of electrodynamic (ED) tethers, momentum exchange tethers, cables, and stringers for exploration and orbital considerations are hindered by material concerns. The objective is to expedite the advancement of existing material technologies and investigate new material technologies. Existing technologies that were advanced include the following:

- Coating technologies needed for AO/UV protection of high-strength synthetic fibers, like ZYLON®. Task 1 evaluated, compared, and characterized existing and SOA coating technologies, such as those that have been advanced by previous NASA NRA contractors.

- Braid construction of various combinations of high-strength synthetic fibers and/or Al wire and/or fiber optic. Task 2 goals were improved tether properties and capabilities such as survivability in AO, UV, and micrometeoroid environments; tensile strength; and conductivity. Task 3 included an investigation into electrical shunting in a Hoytether configuration.

New material technologies were advanced in task 6 as follows:

- New coatings based on electroless or electrodeposition in a multistep process, producing an outer layer of Au or Al on a high-strength synthetic fiber.

- New pigments to similarly coat tether fibers, where TiO_2 is transferred by dipping in an amorphous colloidal suspension.

Installing and enhancing the capabilities of the new NASA braider in the MSFC PRL (task 2a) advanced future macroscopic material capabilities.

Description of Research/Results/Possible Future Work by Task

The project was divided into six tasks.

Task 1—Investigation Into Existing Coating Technologies. Reports from contractors were evaluated by a panel of faculty (two from polymer and fiber engineering, two from chemistry, and one from mechanical engineering). Certain contractors (Lockheed-Martin, Tethers Unlimited, and J.W. Lee) readily shared information/reports; however, Triton Systems may have wanted to protect their technology

and provided no details. All companies were continuing to develop their coating technologies at the time of the panel evaluation in April 2006. The most significant conclusion was that an objective comparison of coating technologies is all but impossible. Contractors used different denier high-strength fiber substrates, different processing methods (e.g. fiber coating versus braid coating), and different test methods and exposures to simulate response to AO and UV.

The inability to compare different coating technologies led to the panel recommendation to proceed with a benchmark testing program. Contractors would be given ZYLON (HM–278 dtex) prepared and/or braided. Contractors agreed to coat the ZYLON with their best coating for a 1-wk exposure (1 E21 atoms/cm^2 of AO) in the AO/VUV chamber at MSFC, shown in figure 84. Each exposure will contain eight samples fixtured, as shown in figure 84, and this will be followed by SEM analysis, tensile testing, and reporting results. Testing and evaluation is to be completed late fall 2006.

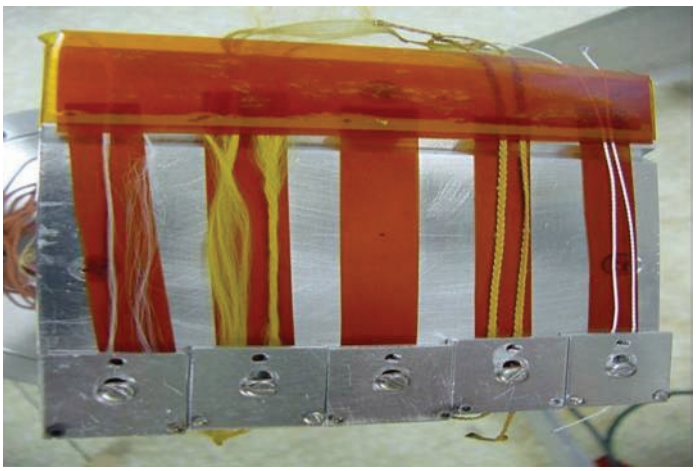

Figure 84. Proposed layout of coated samples in the AO/VUV chamber.

Results. To be included later in addendum.

Possible Future Research. To be included in addendum.

Task 2a—Investigation of Coatings Technologies: Composite and Tether/Cable/Stay Braiding, Machine Installation, and Updating. The braiding machine in figure 85 has been moved and set up at the MSFC PRL where it soon will be online and running. The machine is really two horizontal braiders with 144 packages per braider. The machine was originally located at Redstone Arsenal where it was principally used for braiding composite preform carbon fiber rocket casings over a mandrel. Our early work included arranging/coordinating braider transfer, positioning braider in the assigned space, braider assembly with NASA personnel, initial bolting down of braider, electrical check for grounding and machine improvements, and braiding machine initial testing. The braider on the right in figure 84 will still be capable of creating composites, as it had before at the Army, as it has an overhead gantry system to hold and translate a mandrel for braiding of the composite preform. For the braider on the left to act as a tether or cable braider, it was necessary to provide a method to spool long lengths of cable under

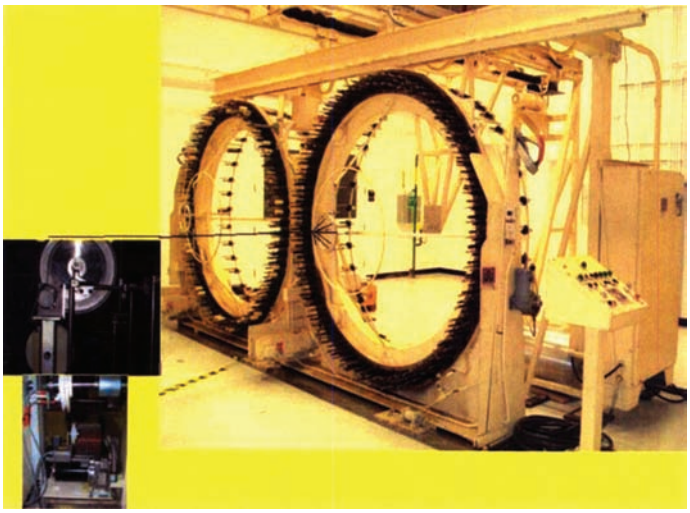

Figure 85. Composite and tether braiding machine installed at MSFC PRL.

tension. To do this, Steeger-USA was subcontracted to provide a take-up system for the left braider. After delivery and installation of the take-up system in fall 2006, a standard operating procedure will be developed, along with a simplified computer control hardware system that is supplemental to control from the console.

Results. To be included later in an addendum.

Possible Future Research

Many different designs of composite tubes, cables, stays, ropes, and tethers can be prototyped on this machine. Future work could include the following:

- Modification of the machine for creation of Hoytethers for tethers and also for long-truss preforms.
- Prototyping of interlacing designs that incorporate high-strength synthetic yarns, metal wires, and/or optical fiber sensors.
- Improvement of the package tensioning system for better quality structures.
- Design and construction of new machinery, specifically for specialized interlacing applications as dictated by the application.

More future work will be included later in an addendum.

Task 2b—Creation of an Embedded Aluminum Wire Into a Single-Strand Braid. ZYLON is a synthetic fiber developed by Toyobo Company Ltd., Osaka, Japan. ZYLON is the strongest manmade fiber in the world—stronger than steel and twice as strong as Kevlar— has very high thermal stability—decomposes in excess of 1,470 °F—and flame resistant (needs at least 68-percent O) as compared to organic fibers.

The objective was to manufacture prototypes of ZYLON and ZYLON/Al wire combination braids for electrodynamic reboost applications. One significant requirement that was achieved in the ZYLON with Al wire constructions, shown in figures 86–90, is the fact that the Al wire did not break before the ZYLON in a tensile test. Strength and conductivity data were gathered and recorded to develop empirical relationships that can be applied in the future for designs with specific requirements. Novel braided structures comprise all metal braids, ZYLON and Al wire braids, braids inside a braid, pseudocore braid, Hoytether braid, and cables in a braid. Novel braided structures were manufactured with available braiding machinery that is generally used for braiding fibrous materials. All metal braids included 8- and 16-Al wire braids.

Figure 86. Sixteen carrier Wardwell braider used for 16 package configurations.

Figure 87. Thirty-two carrier braider used for combining fiber optic with ZYLON and Al.

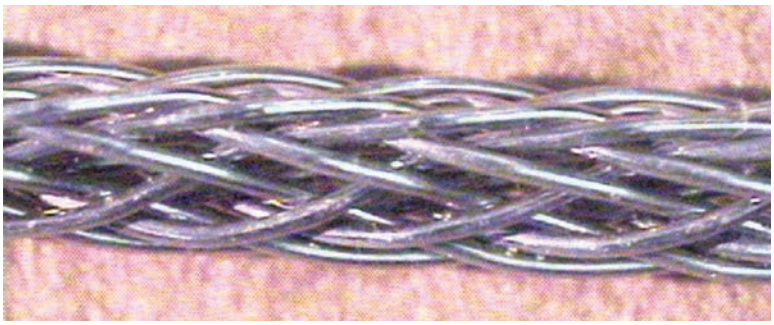

Figure 88. Sixteen Al wires braided together (0.695 g/ft).

Figure 89. Fourteen 278 decitex ZYLON yarns and two Al wires braided together.

Figure 90. Eight 278 decitex ZYLON yarns, six 3270 decitex ZYLON yarns, and two Al wire braids braided together (1.4871 g/ft) creating the pseudocore braid.

Results

Figures 86–90 show the results and they are further summarized in addendum.

Future Research

Utilize the ZYLON with Al construction to a space application with design specifications. Optimize the design of the ZYLON/Al/fiber optic construction to minimize weight for the desired strength and conductivity.

Odd number spools rotate clockwise and even number counter-clockwise, as shown in figures 91–95 and tables 11 and 12.

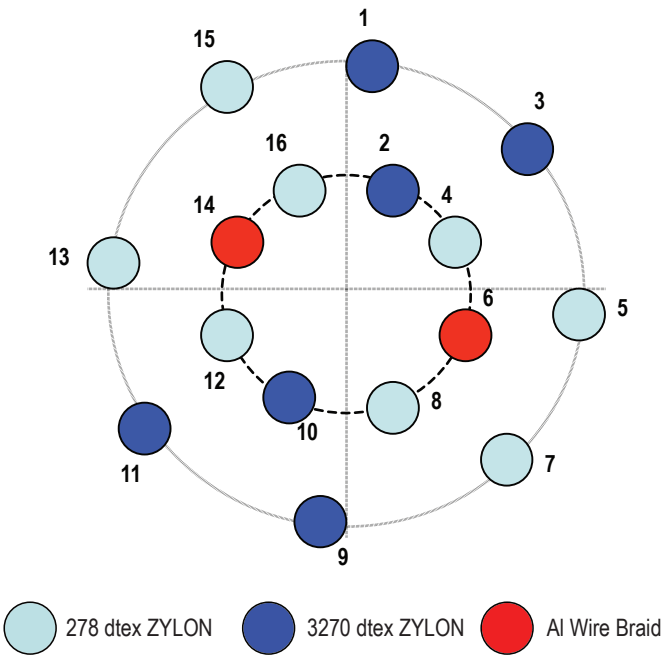

Figure 91. Layout of different carriers for pseudocore braid manufacturing.

Figure 92. Sixteen 278 decitex ZYLON yarns in a braid with four 3270 decitex ZYLON yarns and two 16-AWG wires as axials.

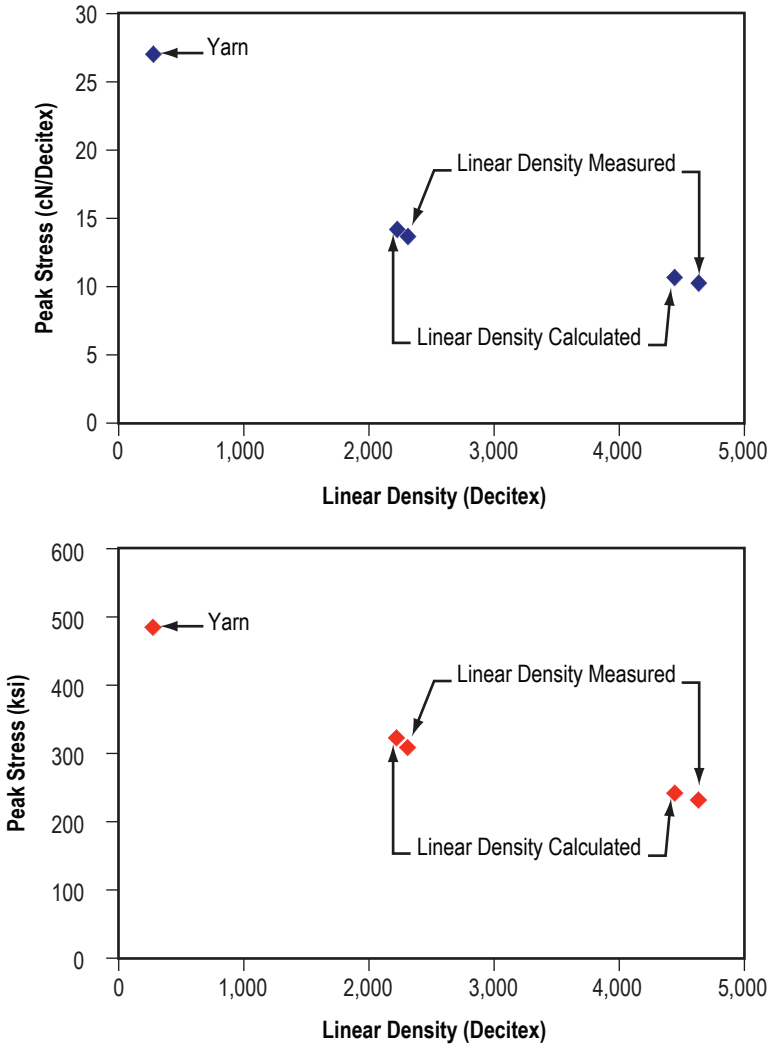

Figure 93. Effect of braiding on ZYLON tensile failure stress.

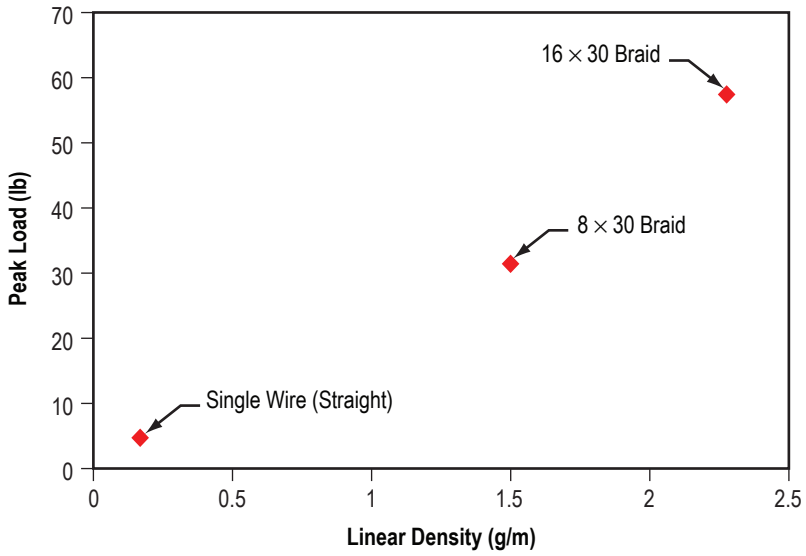

Figure 94. Effect of braiding on peak load of Al wire (30 AWG).

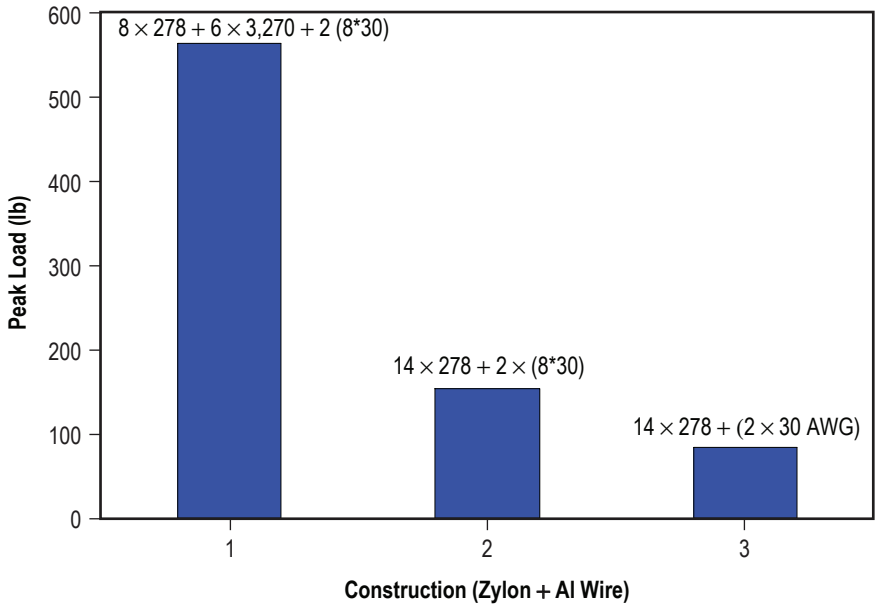

Figure 95. Strength comparison of ZYLON and Al (30 AWG) combination braids.

Table 11. Effect of braiding on tensile strength of bare Al wire.

Description	Construction	Linear Density (g/m)	Peak Load (lb)	
Single wire	30 AWG	0.17	4.78	Calculated
Braid	8×30	1.5	31.57	Measured
Braid	16×30	2.28	57.52	Measured

Table 12. Strength comparison of ZYLON and Al (30 AWG) combination braids.

ZYLON Content (No./dtex)	Al Braid Construction	Linear Density (g/m)	Peak Load (lb)
8/278 + 6/3270	2/8×30	4.88	563.62
14/278	2/8×30	2.7	152.58
14/278	2–30 AWG	0.8	84.24

Task 3—Effectiveness of Electrical Shunting. The goal here is a high-strength Hoytether with electrical shunting at junctions, as shown in figure 96. The rationale behind this work is to combine conductive high-strength strands and an electrically cross-linked Hoytether construction, which is needed where micrometeoroid impact is probable. Hoytether constructions are being investigated and developed in fall 2006 through a subcontract with Tethers Unlimited Inc. Results and future research will be summarized in addendums.

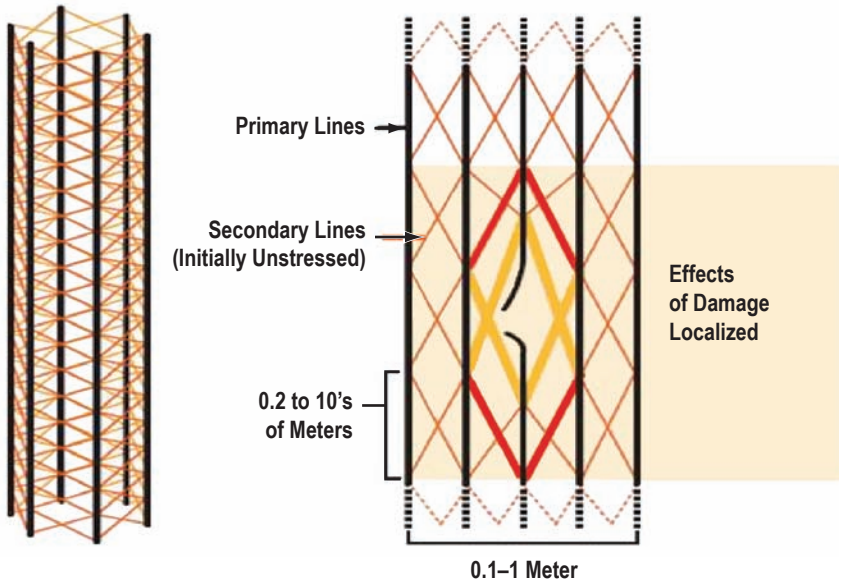

Figure 96. Hoytether configuration.

Task 4—Creation of an All Metal Tether

Task 5—Investigation Into New Tether Materials. This task was reduced and redefined by Joe Bonometti of MSFC, given the substantial investigation performed by Lockheed Martin in a previous NRA. M5, a new high-strength synthetic fiber, not yet commercially available, was investigated for availability. Contact by Kirk Sorensen of MSFC with DuPont, makers of M5, led to negotiations toward a nondisclosure agreement. To date, DuPont has not responded to our invitation for mechanical testing, braiding, coating, and AO/VUV chamber testing. In addition, at least one researcher will be contacted to determine availability of carbon nanotube-based fibers or yarns for AO/UV chamber testing. Results and future research will be included in addendums.

Task 6—Investigation Into Coating/Pigment Technology—Preparation of Surface Coated/Metallized Kevlar and ZYLON Fibers. Lightweight, high-strength tethers, possibly with electrically conductive elements, have been proposed for linking satellites, allowing information exchange, and in-space propulsion. The aim of this research is to develop thin metallic or ceramic coating materials for high-performance fibers, in the form of tethers, that will protect them from degradation in harsh environments (AO and VUV) such as the conditions in LEO. Some of our approaches are expected to allow electrical conductivity.

We chose to use Kevlar and ZYLON yarns as high-performance substrates based on their tensile strength/weight ratios and their commercial availability. It was necessary to apply conductive protective coatings, due to their inherent insulating properties and chemical susceptibility to UV radiation, AO, and solar particle degradation, to achieve these goals. To this end, we have deposited adherent thin layers of Ni, Au, Al, and amorphous TiO_2 onto these fibers for testing in harsh environments. Coating these materials must result in interior and exterior crack-free coverage of the yarns.

Description of Research

We chose to coat polyparaphenylene terephthalamide (Kevlar) and polybenzobisoxazole (ZYLON) based on their strength-to-weight ratios and their surface chemical functionalities. These polymers form strong bonds with Lewis acidic metals making adherent metal-based films realistic goals. Kevlar 49 was obtained from DuPont. ZYLON (273 dtex HM) was obtained from Toyobo of Japan. The fibers were cleaned by sonication in methanol, hexane, and chloroform for 3–4 min each. We chose protective coatings based on four different compatible materials.

Electroless Deposition of Nickel. This solution technique creates adherent conductive Ni coatings on nonconductive substrates using SnCl2 in an adherent monolayer to form, which in the presence of Pd(II) forms a Pd(0) catalyst at the polymer surface at all points where the solution contacts the fibers. The catalyzed fiber surfaces are immersed into an electroless Ni-plating bath based on hypophosphite. The resulting Ni islands grow into thin adherent Ni films.

Deposition of Gold. The second coating technology, shown in figure 97, derives from electroless and electrolytic Au coatings based on Au sulfite and Au cyanide baths, respectively. Clean fibers were treated with Ni coatings as previously described. Gold ions were then reduced from aqueous sulfite solutions onto the Ni metal, generating Au deposits that grow along the fiber surface. An important

observation is that formation of Au layers is not possible in the absence of the Ni deposits since Ni catalyzes the oxidation of sulfite. Since the Ni coated fibers were very conductive, we also used Au electroplating to form bright Au surfaces onto the fibers. We used a commercial Au plating bath diluted by a 10:1 ratio to best plate the fibers.

Deposition of Amorphous Titanium Dioxide. The fourth type of coating, shown in figure 98, is based on the deposition of TiO_2. The surface of the polymeric materials was first activated by immersion of the fibers in a strongly basic organic solution for a few seconds, then soaked in an aqueous solution of Ti(IV) ions. The fibers were then dried at ≈80 °C overnight to produce an amorphous TiO_2 coating. Other fiber samples were treated with the aqueous Ti(IV) solution without the base pretreatment. This process has been repeated to build up successive layers of TiO_2, and will subsequently be used as a binder for particles to act on UV screens.

Deposition of Al/Al_2O_3. The third coating class, shown in figure 99, is based on Al/Al_2O_3 deposition technology using both electroless and electrolytic baths to form smooth hard coatings on the outside of polymer fibers. Electroless Al plating was accomplished from solutions of $LiAlH_4$ and $AlCl_3$ in tetrahydrofuran at RT. The surface of the Ni-coated fibers were activated with $TiCl_4$ in ether, and then immersed into the electroless Al bath for 15 min. Another method for forming Al on Ni, is electroplating the Al from a RT ionic liquid bath composed of trimethylphenyl ammonium chloride and $AlCl_3$. While these baths are ionically conductive, the viscosity is high, which hinders the rate of Al deposition.

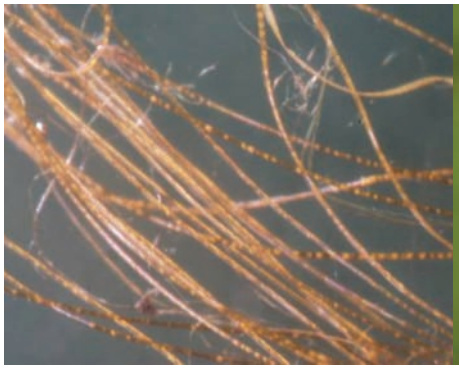

Figure 97. Electroless Au coating on ZYLON with a somewhat uniform appearance.

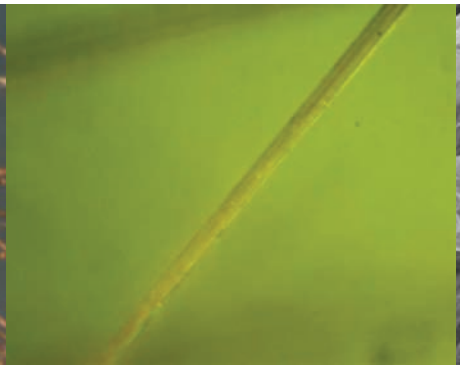

Figure 98. ZYLON fiber coated with TiO_2 glue, note the uniform coating.

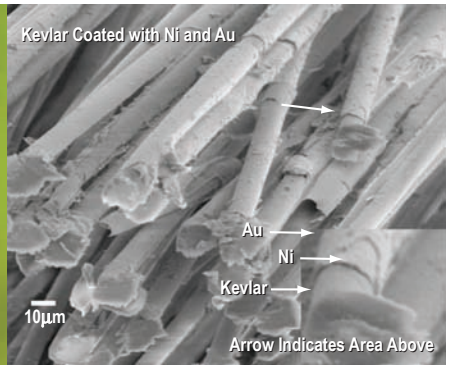

Figure 99. Kevlar coated with Ni and Au, note the two layers.

Characterization of Coatings. After deposition, the fibers were characterized by a variety of methods. The yarns were weighed before and after coating to determine the total mass of coating on the surface. We used a two-point resistance measurement over multiple distances along the yarns to evaluate the electrical conductivity of the fibers. This provided a full-scale characterization for macroscopic cracks in the coatings.

Visible microscopy was performed using either an Olympus BH2 polarizing microscope or an Olympus SZX12 binocular scope. Photographs were taken with a 1-megapixel digital camera that allowed easy visibility of significant lengths of fiber, and revealed larger cracks and places where the coating might have flaked off of the yarn.

SEM measurements were made using a Zeiss DSM 940 for determinations on intact and sectioned fibers coated with Ni and Au, as well as with Ni and Al. This allowed microscale characterization to supplement the large scale. Semiquantitative energy dispersive x-ray (EDX) analyses were performed using a JEOL 7000F field emission SEM. Parallel elemental analysis employing EDX spectroscopy confirmed the presence of Ni, Al, and Au on the fibers.

Tensile strength testing was done on an Instron universal tester using both twisted and untwisted coated yarns. Abrasion testing was done on a Zweigle abrasion tester using a sandpaper abrading surface.

Table 13 shows the schedule. Results and future research will be included in addendums.

Table 13. Schedule.

January–March 2006:	Literature work, ordering, and material acquisition.
February:	Develop cleaning procedures for fibers and perform cleanliness evaluation.
March–June:	Evaluate electroless Ni-plating baths and the as-coated fibers.
June–September:	Develop Au electroless plating and Al electroless and electrolytic plating. Achieve a method for efficient fiber coating with amorphous TiO_2, and characterize coated fibers.
October–December:	AO and UV exposure with conductivity and tensile strength testing.

6.2 Fabrication and Evaluation of Titanium- and Zirconium-Based Wires for Use During Extended Deep-Space Missions: Final Report

PI—Dr. Richard N. Grugel, NASA MSFC.

Objective

Novel materials and designs are necessary for transport vessels and propulsion systems to fulfill NASA's vision of easier access to space and the expansion of human exploration beyond LEO. Spacecraft components must be lighter and stronger than their predecessors and will likely be required to serve new purposes. Furthermore, they must be resilient to the thermal, vacuum, and radiation environments of space for extended periods of time and eventually may need to perform in the near proximity of a nuclear fuel source. The objective of the proposed research is to produce a novel composite wire with improved material properties for use during extended deep-space missions. In terms of value, such wire will contribute to the efficiency and reliability of future spacecraft. The work proposed here will draw upon the tremendous scientific and technical base that has been generated by a common metal product—wire. This knowledge will be applied to a novel series of alloys based on Ti and Zr with the intent of developing composite wires for space applications. It is expected that the fabricated wire will well endure in the space environment with application as tethers, sail components, fasteners, and a myriad of other (including Earth-based) uses. To the best of our knowledge such wire compositions have never been investigated.

Description of Research

Introduction and Background Information. Next generation spacecraft may well employ sails, could rotate about each other via an umbilical tether, and might consist of an array of connected parts. While these vehicles may serve different purposes, a common thread (so to speak) is that wire will likely constitute an essential mainstay to their success. Historically, wire has been used in robes and ornaments dating back several thousand years BC, it comprised the chain mail of knights, and in its barbed variety helped tame the wild west. Wire became known as the steel product of 150,000 uses.[1] It is classified in terms of composition, size, shape, treatment, and application. Drawing metal through a die is the process most often used to make wire. This technique ensures a uniform product and can greatly increase mechanical strength. The proposed work intends to fabricate composite wires based on the eutectoid reaction observed in metal alloy systems; the ASM handbook lists 134 binary systems that have at least one.[2] An eutectoid transformation can be simply expressed as an isothermal reaction in which a solid of one composition (SI) transforms at a lower temperature into two solids of different compositions ($S_{II} + S_{III}$). Consider the well-known plain carbon steel austenite eutectoid transformation (designated as γ-Fe and composed of Fe $\approx$0.8wt%C). When the austenite temperature drops below 727 °C, it transforms to pearlite which is composed of two alternating lamellar phases (αFe+Fe_3C), shown in figure 100.[3] Pearlite has been studied extensively, and has proven applications as a high-strength wire, e.g., tire cords.[3,4–13]

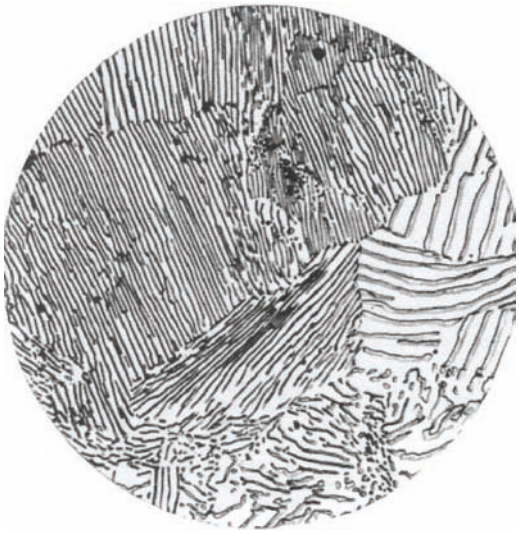

Figure 100. Pearlite X1000 microstructure.

It is well established that the spacing (λ) between the two phases (SII and SIII) decreases as the transformation rate (V), or cooling rate, increases. As the spacing decreases, the mechanical properties improve—particularly the tensile strength. Figure 101 clearly demonstrates how the wire's strength increases by drawing (mechanically working).[4] It is beyond the scope of this proposal to fully elucidate the mechanical properties of pearlitic steels.

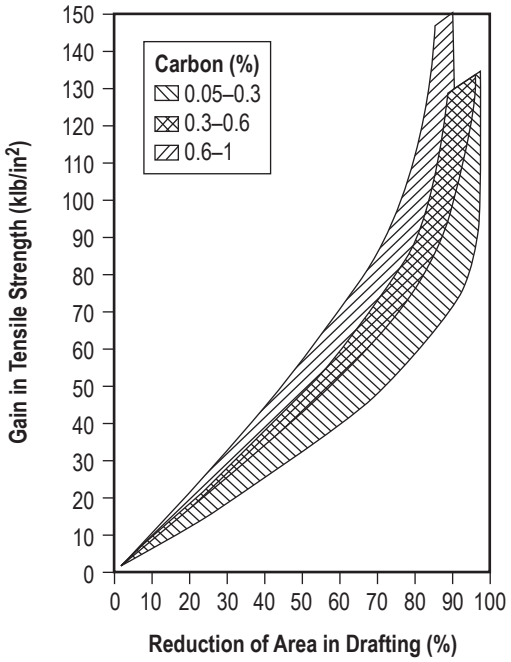

Figure 101. Increase in tensile strength as a function of reduction in wire area by drawing.

Ti and Zr serve as the basis for many well-established aerospace engineering alloys. Eutectoid-type reactions are frequently seen in Ti and Zr systems, but to the best of the proposer's knowledge no attempt has been made to develop and evaluate such alloys. The proposed work intends to apply the tremendous scientific and technical base of the common steel wire to Ti and Zr alloys, with the intent of developing composite materials in support of NASA Exploration interests.

Objectives and Specific Goals

Section 3.3 of the AME Call for Proposals begins "Lightweight, high-strength materials… are always needed for the space vehicle applications." Successful completion of the proposed work will add corrosion resistant, radiation tolerant (space and nuclear), vacuum durable, and low-temperature strength to that sentence of desirable properties. Development and application of the proposed work will contribute to AME objectives by increasing safety, reliability, and affordability over extended duration missions. These materials may well help enable novel space flight capabilities.

Approach and Methodology

The research rational will build upon our knowledge of Fe-based pearlite, a material that has exceptional strength—strength that further increases as a consequence of mechanical processing, such as drawing. Consequently, pearlitic wire could be envisioned as a strong candidate for spacecraft application. Pearlite, however, is a general term applied to any microstructure, generally eutectoid, with a spacing fine enough to break up light to the sheen characteristic of mother-of-pearl. In this regard there are potentially better materials than the steel-based alloys, which are prone to corrosion and low-temperature failures. Here we consider pearlitic microstructures based on Ti and Zr alloys. Ti essentially has the strength of steel, good corrosion properties, and is less dense (4.31 gcm^{-3} versus $\approx$7.8 gcm^{-3}). Sponge Zr has similar tensile strength to Ti, is somewhat less dense (6.49 gcm^{-3}) than Fe, and is widely used in nuclear energy applications due to its low absorption cross-section. In terms of space applications high strength, low weight, and reliability in harsh as well as nuclear (both power and galactic cosmic ray) environments are very desirable characteristics. As mentioned earlier, eutectoid-type reactions occur in many metallic systems, including Ti and Zr, as demonstrated in figures 102 and 103, where a Ti-Ni alloy was cast, heat-treated, and slowly cooled through the appropriate eutectoid reaction.

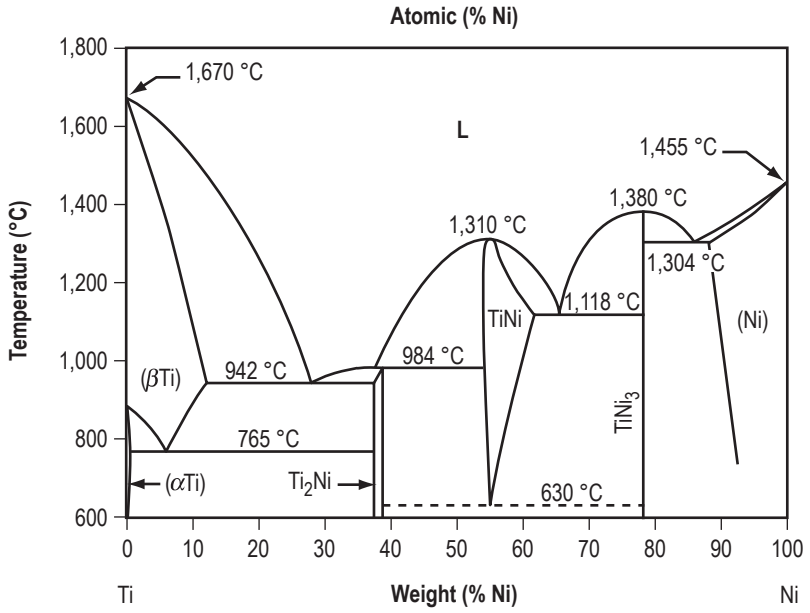

Figure 102. Ti-Ni phase diagram showing a eutectoid reaction at ≈6wt%Ni.

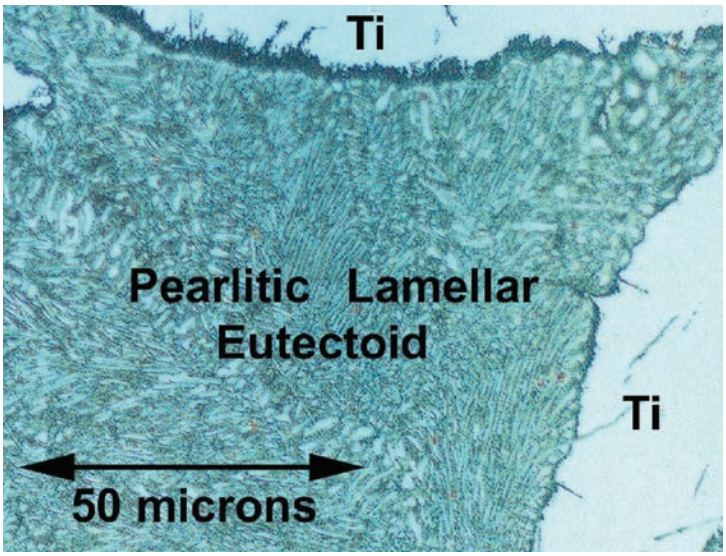

Figure 103. Microstructure after holding at ≈1,000 °C for ≈9 hr and then cooling at 0.3 K/s. A lamellar eutectoid structure is seen between the primary Ti phases.

Schedule

The schedule and the work conducted is well-represented in table 14.

Table 14. Ti- and Zr-based wire fabrication and evaluation task schedule.

Action	Months 1–4	Months 5–7	Months 8–10
Procurement of supplies/equipment	▲	▲	
Sample melting, alloying, heat treatment			
Wire fabrication			
Wire testing and evaluation			
Reports, presentations, papers	▲	▲	▲
Evaluate results for continued funding			▲

The work has investigated a number of alloys as later described. Appropriate compositions were cast into samples, heat-treated, and cooled to form pearlitic microstructures. Microscopic examination was investigated as a function of the cooling rate prior to heat treatment and also after heat treatment. Mechanical testing of the samples was then initiated. A presentation entitled "Fabrication and Evaluation of Ti- and Zr-Based Wires for Use During Extended Deep-Space Missions" was presented June 26–30 at the 2006 National Space and Missile Materials Symposium in Orlando, FL and August 24 at the 2006 MSFC Research and Technology Expo in Huntsville, AL. Unfortunately, progress was significantly curtailed as the laboratory facilities were essentially shut down pending a move.

Results

A recent report pointed out the SOA for high-tensile strength steel cord and wide usage was predicted—more than a million tons yearly. The need to reduce the automobile's weight was also recognized, and a means to do this was to increase wire strength. Steel compositions have increased from hypo (0.7 °C) to hypereutectoid (0.9 °C) to increase strengthening mechanisms, which developed improved deformation processing procedures. Ti- and Zr-based wires can be implemented and evaluated with the potential of improved properties. This TM concentrates on six candidates for pearlitic wire formation, although a number of alloys were investigated. The candidate alloys are Ti-15wt%Ag, Ti-12wt%Pt, Ti-19wt%Pd, Zr-4.6wt%Ag, Zr-8.5wt%Pt, and Zr-4wt%Pd. The respective phase diagrams giving the eutectoid composition and temperature are shown in figures 104–109.

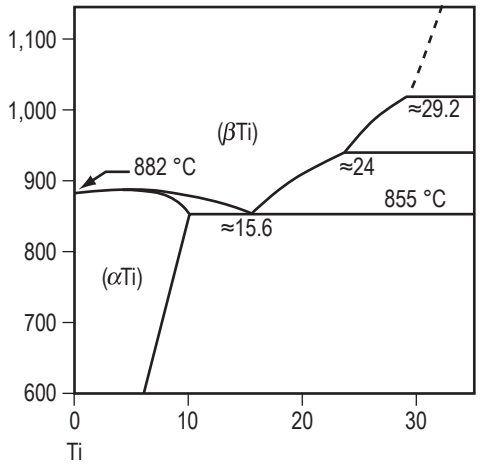

Figure 104. Partial Ti-silver phase diagram.

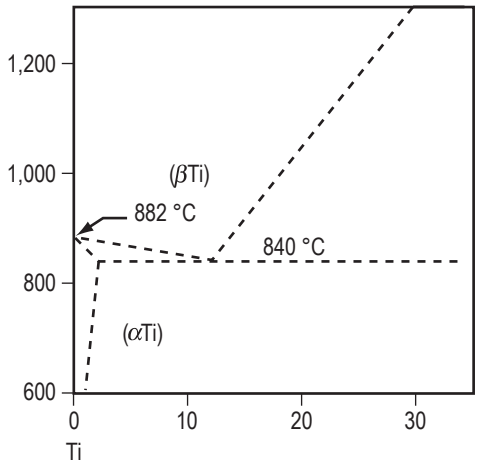

Figure 105. Partial Ti-Pt phase diagram.

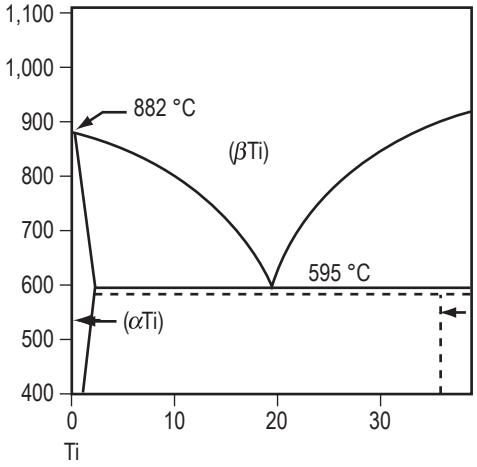

Figure 106. Partial Ti-Pd phase diagram.

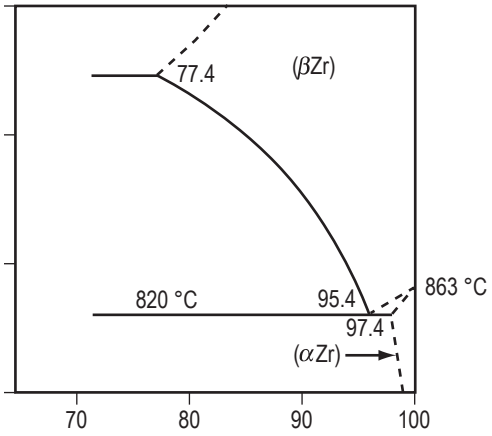

Figure 107. Partial Zr-silver phase diagram.

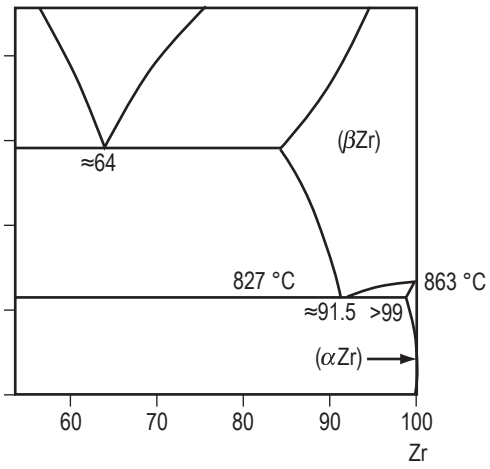

Figure 108. Partial Zr-Pt phase diagram.

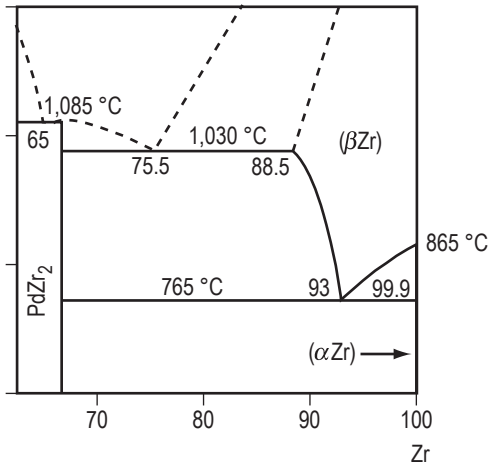

Figure 109. Partial Zr-Pd phase diagram.

Experimentally, alloys of the designated composition were fabricated from pure materials and placed in a graphite crucible approximately 2-in tall with an inside diameter of about 1 in. The crucibles were capped and put on a stand within a quartz tube centered in the coil of an induction furnace. Power was applied to the coil and the rising temperature was monitored by an optical pyrometer. When the measured temperature was approximately 200 °C above the melting temperature of Ti (or Zr), the system power was cut and the crucible was allowed to cool. The alloy was then removed from the crucible and a section was cut out with a diamond saw for metallographic examination. The microstructures of the as-cast samples referenced to the phase diagrams are seen in figures 110–115. The rapid solid-to-liquid transformation precluded formation of the equilibrium pearlitic microstructure and shows a primary array composed of either Ti or Zr dendrites.

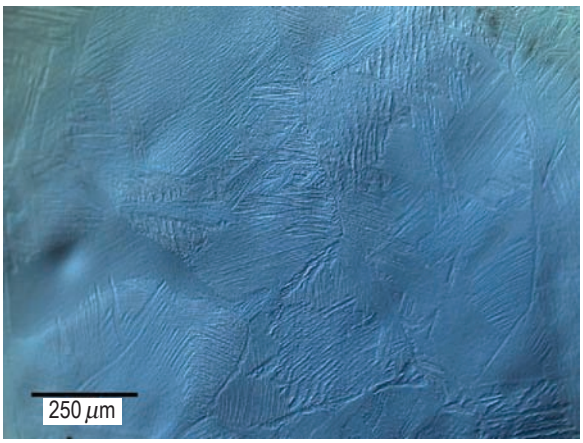

Figure 110. As-cast microstructure of a Ti-15wt%Ag alloy.

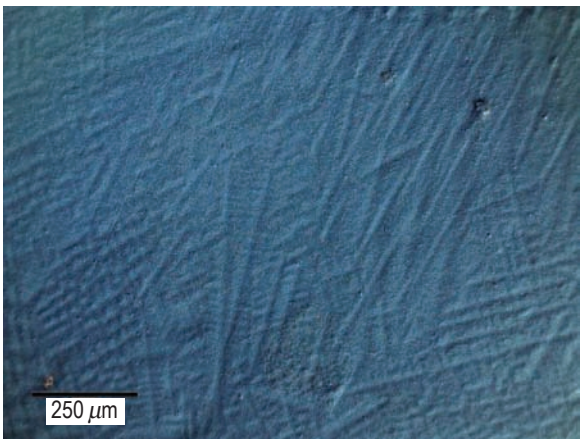

Figure 111. As-cast microstructure of a Ti-12wt%Pt alloy.

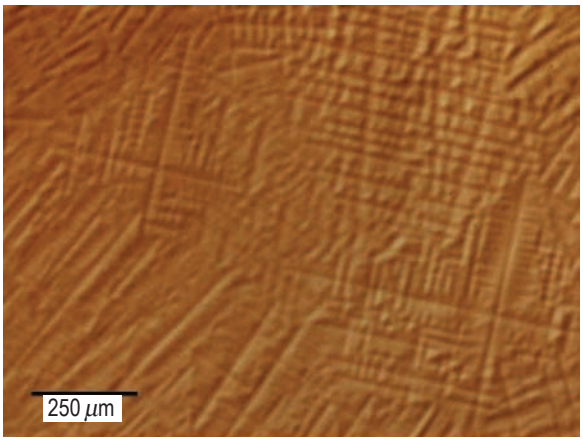

Figure 112. As-cast microstructure of a Ti-15wt%Pd alloy.

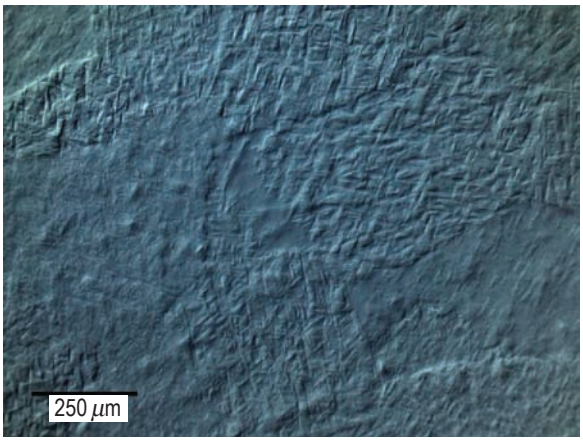

Figure 113. As-cast microstructure of a Zr-4.6wt%Ag alloy.

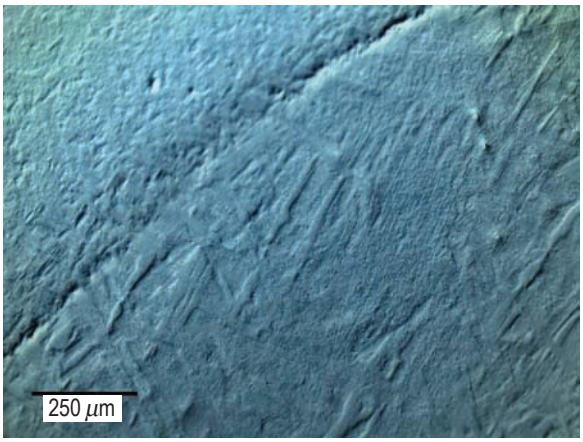

Figure 114. As-cast microstructure of a Zr-8.5wt%Pt alloy.

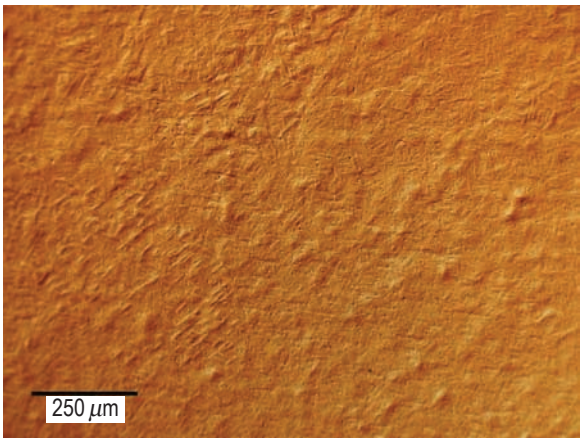

Figure 115. As-cast microstructure of a Zr-4wt%Pd alloy.

The alloys were heat-treated to achieve the desired pearlitic microstructure. They were placed in an alumina tube capable of achieving a vacuum level on the order of 10^{-6} torr. The alumina tube was put in a furnace and the temperature was raised to ≈1,000 °C, a condition necessary to move the alloy into the single-phase region and allow homogenization. After ≈23 hr at ≈1,000 °C, the furnace was programmed to cool at 0.1 °C/min which allowed further homogenization. When the eutectoid temperature was reached the solid state diffusion controlled transformation occurred. Results from the heat treatment are seen in figures 115–120. The eutectoid-type microstructure is clearly seen in figures 116–121, though not always for the entire sample, which is likely a consequence of the phase diagram not being exactly known.

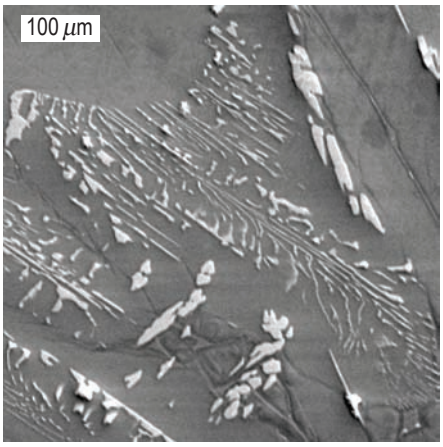

Figure 116. Heat-treated microstructure of a Ti-15wt%Ag alloy.

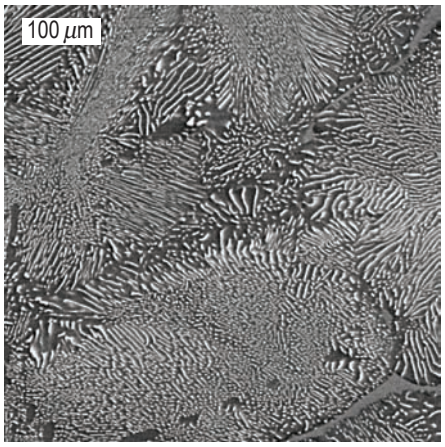

Figure 117. Heat-treated microstructure of a Ti-12wt%Pt alloy.

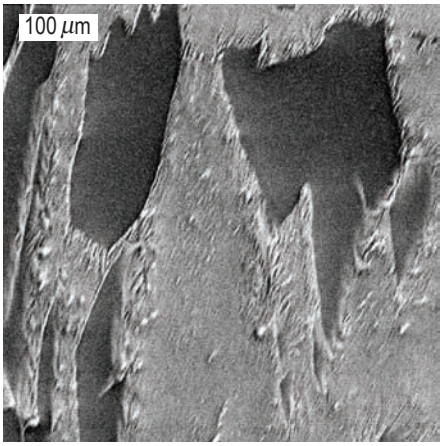

Figure 118. Heat-treated microstructure of a Ti-15wt%Pd alloy.

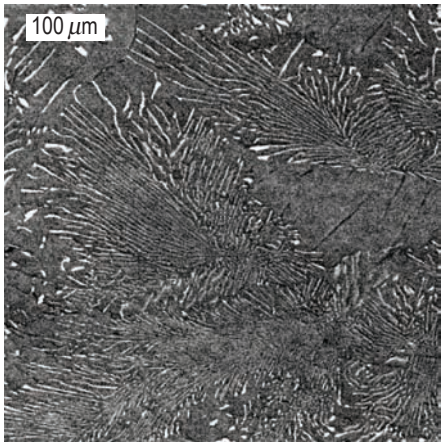

Figure 119. Heat-treated microstructure of a Zr-4.6wt%Ag alloy.

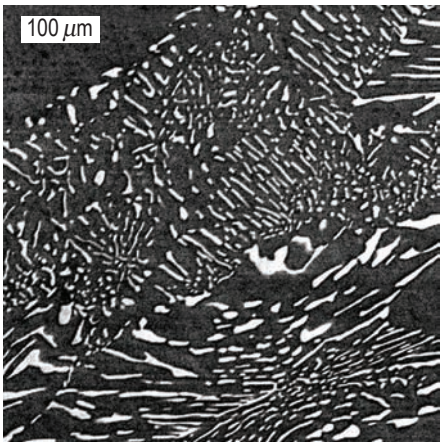

Figure 120. Heat-treated microstructure of a Zr-8.5wt%Pt alloy.

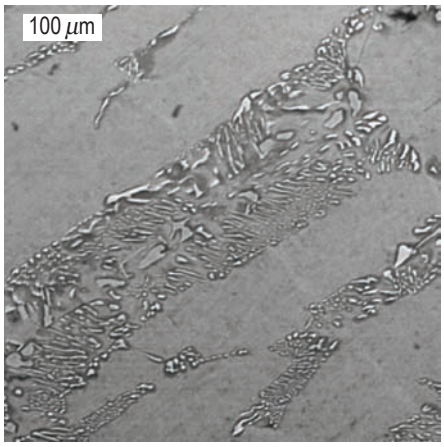

Figure 121. Heat-treated microstructure of a Zr-4wt%Pd alloy.

Preliminary mechanical testing of two alloys—Ti-19wt%Pd and Zr-8wt%Pd—was initiated prior to closing the laboratory. Sections approximately 1 mm × 1 mm × 25 mm were cut from the cast and heat-treated samples. The microstructure of the as-cast Ti alloy, seen in figure 122, had a tensile strength of ≈62,000 psi; the heat-treated sample, figure 123, had a tensile strength of ≈81,000 psi. Similarly the as-cast Zr alloy, figure 124, had a tensile strength of ≈68,000 psi while the heat-treated sample, figure 125, had ≈83,000 psi to failure. These trends between as-cast and heat treated samples were expected, although considerably less than anticipated; this is not unexpected for the first attempts. Finally it is noted that the samples were tested without being subjected to any mechanical deformation.

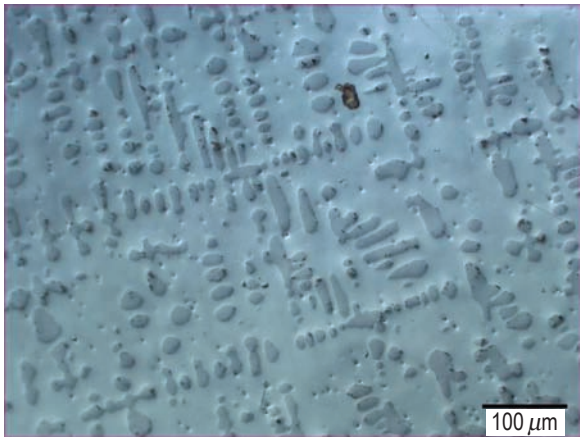

Figure 122. As-cast microstructure of a Ti-19wt%Pd alloy, UTS ≈62,000 psi.

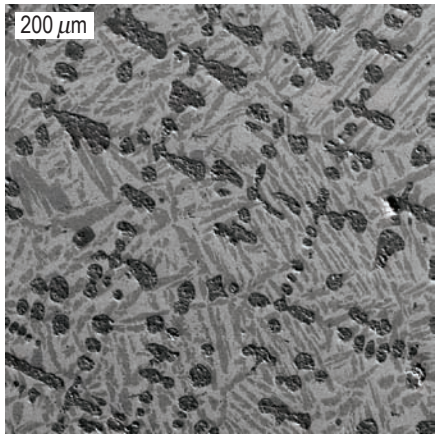

Figure 123. Heat-treated microstructure of a Ti-19wt%Pd alloy, UTS ≈81,000 psi.

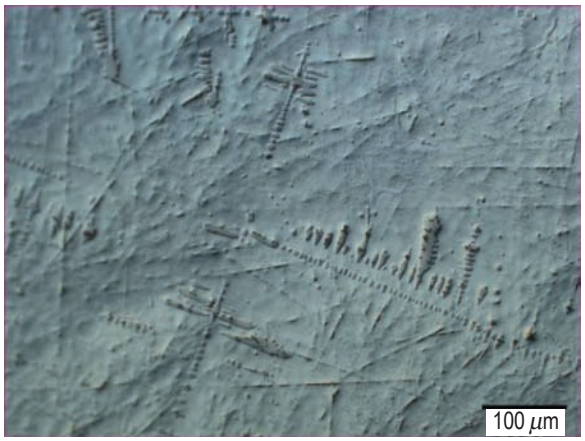

Figure 124. As-cast microstructure of a Zr-8wt%Pd alloy, UTS ≈68,000 psi.

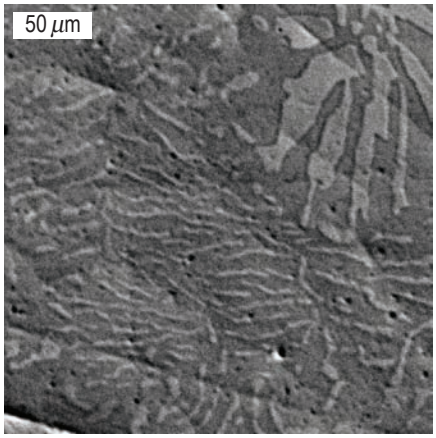

Figure 125. Heat-treated microstructure of a Zr-8wt%Pd alloy, UTS ≈83,000 psi.

Possible Future Work

Future work will center around the following three themes:

– Continued alloy refinement and development—From this work it appears that the published compositions may not be accurate. A fully or slightly hypereutectoid composition is desired, and it seems reasonable that a ternary alloy (for example Ti-V-X) could be developed that would have extra strength due to solid solution hardening.

– Mechanical testing on a preliminary basis needs to be refined and followed up by some initial testing of deformed samples.

– Package the results and contact wire manufacturing representatives to evaluate the feasibility of fabricating a commercial product.

Acknowledgments

The author is grateful to MSFC and the AME initiative for their support of this work. Appreciation is expressed to Curtis Bahr and Martin Volz for their expertise in facilitating this work.

References

1. *The Making, Shaping, and Treating of Steel*, Ninth Edition, United States Steel Corporation, Herbick and Held, Pittsburgh, PA, p 819, 1971.

2. *Binary Alloy Phase Diagrams*, Second Edition, ASM, 1996.

3. *The Making, Shaping, and Treating of Steel*, Ninth Edition, p. 1079, 1998.

4. Zener, C.: *Trans. AIME*, Vol. 167, pp. 550–595, 1946.

5. Sundquist, B.E.: *Acta Met.*, Vol. 16, pp. 1413–1427, 1968.

6. Bolling, G.F.; and Richman, R.H.: *Metall. Trans.*, Vol. 1, pp. 2095–2104, 1970.

7. Puls, M.P.; and Kirkaldy, J.S.: *Metall. Trans.*, Vol. 3, pp. 2777–2796, 1972.

8. F.M.A. Carpay: *Metall. Trans.*, Vol. 5, pp. 2614–2615, 1974.

9. M. Hillert: *Scripta Metall.*, Vol. 11, pp. 311–314, 1977.

10. N. Ridley: *Metall. Trans.* A, Vol. 15A, pp. 1019–1036, 1984.

11. Pearson, D.D.; and Verhoeven, J.D.: *Metall. Trans.* A, Vol. 15A, pp. 1047–1054, 1984.

12. Caballero, F.G.; Capdevila, C.; and de Andres, G.: *Scripta, Mat.*, Vol. 42, p. 537, 2000.

13. Taleff, E.M.; Lewandowski, J.J.; and Pourladian, B.: *Journal of Metals*, p. 25, July 2002.

14. *The Making, Shaping, and Treating of Steel*, Ninth Edition, p. 846, 1998.

15. Nippon Steel Technical Report, No. 88, July 2003.

16. *Binary Alloy Phase Diagrams*, Second Edition, ASM, 1996.

6.3 Low-Temperature Curing Ionic Liquid Resins for Aerocapture

PI—Rhonda Libb.

Objective

This work was undertaken with the goal of developing polyimide and bis(maleimide) resins based on ionic liquids (ILs) to improve the properties of conventional materials for aerocapture and aerobraking applications to attain higher service temperatures, lower cure temperatures, etc. Lightweight high-strength adhesives, bonding agents, and structural materials are needed to support NASA's space exploration initiatives. ILs and their polymers are a novel class of green low-melting organic salts that have very low vapor pressures, and hence low flammability, but large liquidus ranges with thermal stabilities demonstrated to exceed 400 °C. Polyimides and bis(maleimides) are well known high temperature, high-strength polymers that are of interest for numerous commercial applications and as materials for spacecraft. Of particular interest for NASA's AME element is high-temperature polymeric resins and composites for space vehicles. As stated in the 2006 AME flyer "Spacecraft that rely on aerocapture or aerobraking techniques to enter and travel through planetary atmospheres require TPSs that can withstand the extremely high temperatures experienced during these stages of their missions. In addition, these TPSs must be lightweight to reduce payload lifting requirements and must adhere strongly to the aeroshell during atmospheric entry. At the 2004 AME Advanced Space Propulsion Materials Workshop: Aerocapture, the maximum temperature and duration challenges for such adhesives during planetary entry were determined to be 500 °C (932 °F) for a 30-min duration. Current TPS bonding systems have service temperatures between 250–300 °C (482–572 °F), requiring that the outer TPS be thick enough so that this range is not exceeded. Increasing adhesive service temperatures to at least 500 °C (932 °F) would significantly reduce the thickness and mass required for the outer TPS for future exploration spacecraft, particularly those designed to return samples to Earth."

Research Description

The specific objectives for this project were as follows:

- Synthesize and characterize IL-based polyimides and bis(maleimides), then compare the adhesive and mechanical properties to those of conventional materials.

- Prepare carbon composites using IL-based resins and determine their physical and mechanical properties.

Synthesis of Materials. The synthetic methodology employed was to design and synthesize monomers that are based on the chemical structures of conventional materials, using chemical systems that are known to form ILs as templates. 1,3-dialkylimidazolium salts were chosen for this work because they are relatively easy to synthesize, and the aromatic ring present in their chemical structure tends to impart good thermal stability.

Polyimides are typically formed by the condensation polymerization reaction between a diamine and a tetracarboxylic anhydride or acid. The reaction occurs in two steps: 1) Formation of

a polyamide-acid (usually in solution), removal of the solvent, followed by high temperature (250–300 °C) curing to form the polyimide. Water is off-gassed as a by-product of the curing process. Two immediate advantages occur right away from using ILs over conventional materials: (1) No solvent is needed, thus eliminating volatile organic compoundss (VOCs) since either the diamine or the tetracarboxylic anhydride (or both) are liquid and (2) lower curing temperatures (150–200 °C) can be used because the kinetics of the condensation reaction are faster in IL media (according to published literature reports).

LaRC researchers developed a conventional polyimide for space exploration applications known as colorless polyimide 2 (CP2®), shown in figure 126.

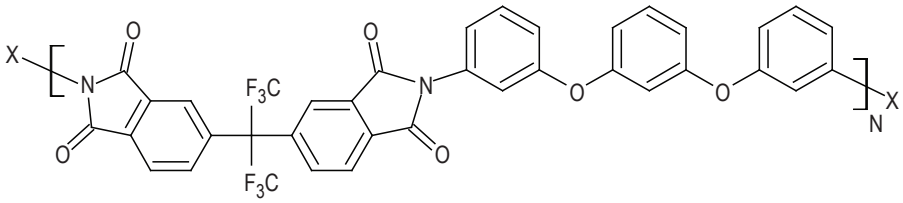

Figure 126. CP2.

Based on this work, an IL CP2 variant, shown in figure 127, was made by replacing diamine used for CP2 with the imidazolium-based IL diamine 2APIBu.

This compound was synthesized in our laboratory from commercially available starting materials. The anion TFSI was chosen because it is known to have high-thermal stability. The reagents are mixed in a 1:1 molar ratio, without solvent, to form a paste. When heated to 150–200 °C for 2–3 hr, the paste cures and forms a clear amber polyimide, shown in figure 128, referred to as ionic liquid polyimide-1 (ILPI–1).

Six other IL polyimides have been prepared in a similar fashion, by keeping the IL diamine constant and varying the tetracarboxylic anhydride.

To obtain materials with high *Tg*, an imidazolium-based IL triamine was synthesized and used to prepare a cross-linked IL polyimide (fig. 129).

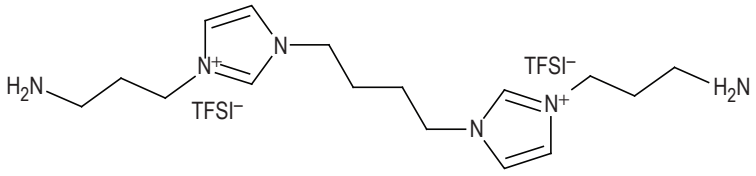

Figure 127. 2APIBu.

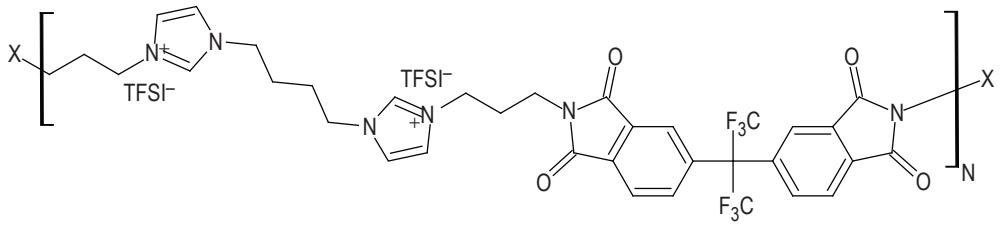

Figure 128. ILPI–1.

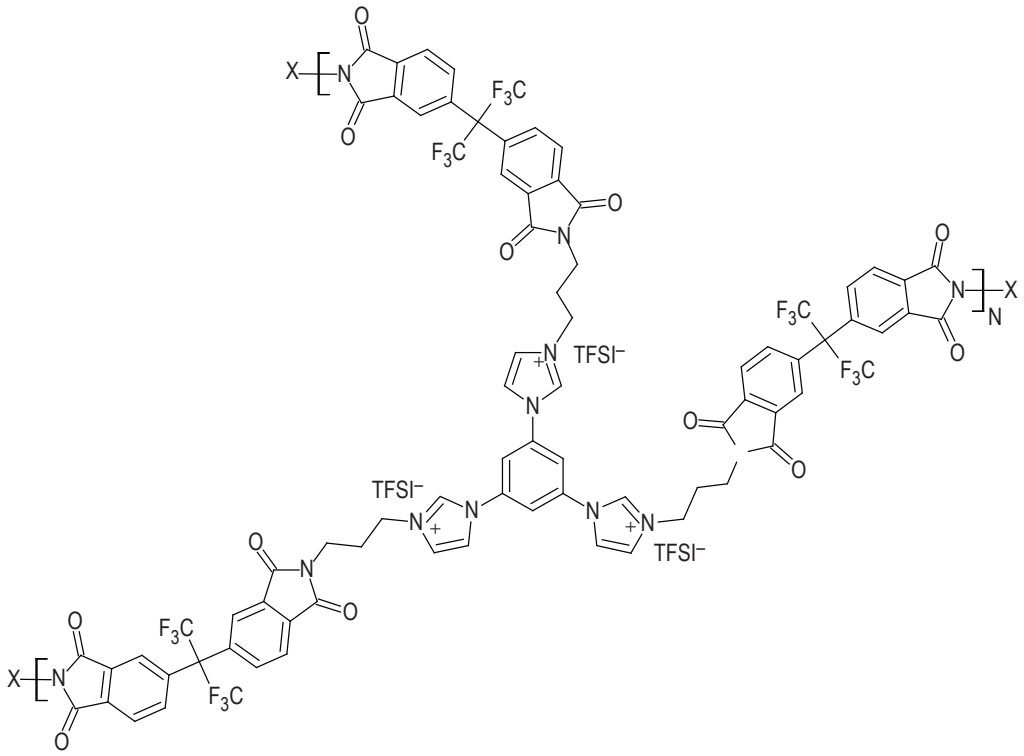

Figure 129. ILPI–5.

Lastly, to achieve materials that can be cured at low-temperature (below 100 °C), bis(maleimides) offer an alternative to polyimides. They possess similar chemical structures, but unlike polyimides, bis(maleimides) contain preformed imide linkages and polymerize via free radical addition mechanisms. In addition to lower curing temperatures, they also produce no water or other volatile by-products upon curing. In conjunction with researchers at the University of Southern Mississippi (USM), an IL bis(maleimide), ILBMI–1, has been synthesized and sent to MSFC for testing (fig. 130).

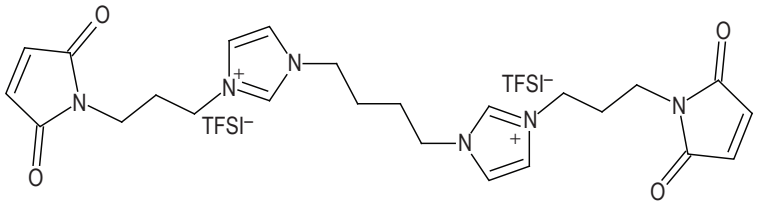

Figure 130. ILBMI–1 monomer resin.

This material can be cured thermally using standard thermal initiators, or cured photochemically using standard UV photo initiators. Additional polymerization occurs at the C–C double bonds located on the maleimide groups at each end of the molecule.,

Sample Preparation and Testing

Initially, it was practical to select a testing method to synthesize only small, limited quantities (5–10 g batches) of the IL polyimide and bis(maleimide) resins. Hence, Al button samples were prepared and adhesive tensile testing was conducted using an Instron machine, as shown in figure 131.

Figure 131. Preparation of Al button samples and adhesive tensile testing using an Instron machine.

Schedule

The task was proposed as a 10-mo effort, as shown in table 15.

Table 15. Task schedule.

Task	FY 2006							
	1		2		3		4	
Design, synthesis, and polymerization of IL monomers		■	■	■				
Preparation of samples and mechanical testing		■	■	■	■			
Perform *Tg* and 500 °C/vacuum tests				■	■	■	■	
Evaluation and final reporting of project					■	■	■	■

Hurricane Katrina and the ending of the BAE Systems RAES contract delayed funding to USM and led to negotiations with TBE via the SDOS contract to cover both this MCP and the IRAD for BAE. Further schedule delays occurred during synthesis due to unexpected purification difficulties. Therefore, the RT curable IL's have not yet been tested. The first batch of material has been received and the button tensile testing can be completed under IRAD as the samples are batch tested for efficiency.

Results

Preparation and Curing of Monomer Resins. Overall, both the IL diamine (2APIBu) and the IL triamine (3APIB) synthesis proceeded smoothly and the products were obtained in reasonable yields. The time required to carry out the synthesis was longer than originally anticipated, primarily because of some difficulties in the purification of intermediates, which have since been overcome. Methods have been developed for producing good quality IL amines that are viscous, odorless liquids at RT.

IL polyimides were prepared using combinations of 2APIBu or 3APIB with various tetracarboxylic anhydrides. Thick paste formed when these materials are mixed in 1:1 molar ratios at RT. Upon curing, the pastes become a clear amber color due to reaction of the tetracarboxylic anhydride with the amine. As the temperature is increased beyond 200 °C, the IL polyimides become quite dark; this is most likely caused by the decomposition of small amounts of residual impurities from the synthesis of the IL amines. Also, the linear polyimides, prepared from 2APIBu, at temperatures above 200 °C were generally soft even fluid; whereas the cross-linked polyimides, prepared from 3APIB, remained solid. Hence, if high T_g, high-service temperature materials are desired, the use of cross-linked IL polyimides is necessary.

CP2 samples were prepared for the purpose of comparing IL polyimides with a conventional polyimide, samples of CP2 were also prepared using published literature methods. Small amounts of both CP2 and ILPI–1 were prepared in small Al pans and heated to 300 °C, as shown in figure 132. As previously stated, water is off-gassed as a by-product of the curing reaction; in conventional polyimides this can create bubbles/voids that reduce mechanical strength. However, with ILPI–1 (as well as other IL polyimides) it was observed that films possessing better quality were obtained.

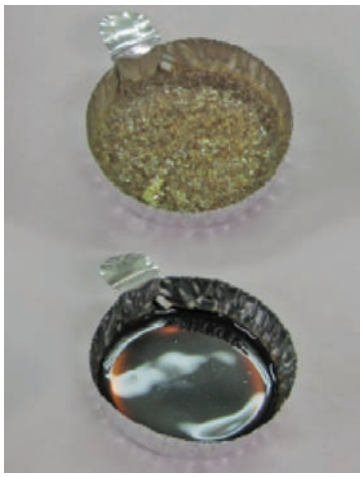

Figure 132. Two polyimide films: (1) CP2, a conventional material (top) developed at LaRC and (2) ILPI–1, an IL-based material (bottom) developed at MSFC. Note that the IL polyimide contains fewer bubbles/voids that can reduce mechanical strength. This probably occurs because the IL polyimides are more mobile at high temperatures, thus the water vapor is able to escape much easier.

Adhesive Testing. Initial results from RT adhesive tensile testing of Al button samples for selected IL polyimides and CP2 are shown in table 16.

Table 16. Results from RT adhesive tensile tests.

Sample No.	Material	Diamine/ IL Cation	Tetra Carboxylic Anhydride	Anion	Curing Conditions (min/°C)	Load at Max Stress (psi)	Surface Coverage (%)	Failure Mode (% Cohesive)
1	CP2	APB	6FDA	–	60/300	1,278	35	100
2	ILPI–1	2APIBu	6FDA	TFSI	60/300	1,632	95	100
5	CP2	APB	6FDA	–	60/300	1,257	90	100
6	ILPI–1	2APIBu	6FDA	TFSI	60/300	722	50	100
7	CP2	APB	6FDA	–	60/300	732	90	100
8	ILPI–2	2APIBu	6FDA	Br	60/300 30/400	812	100	100
9	ILPI–1	2APIBu	6FDA	TFSI	60/300	1,468	95	100

The scatter shown in the results occurs primarily because of variations in the curing conditions and surface coverage. Note that ILPI–1 shows tensile strength comparable to or even slightly greater than CP2. Numerous other polyimide button samples were tested (over 45 total) in addition to those listed in table 15; however, surface coverages were often low and varied considerably from sample to sample due to material leakage before curing was complete, giving unsatisfactory results. This issue can probably be overcome by adjusting the curing time so the material polymerizes sufficiently at a lower temperature and at a higher temperature the viscosity will be high enough that it will not flow and leak out.

Benefit to Advanced Materials for Exploration Technology Goals

The results of this work so far, while preliminary, demonstrate the potential of IL-based polyimides in meeting NASA's space exploration goals. Additional testing is needed before definitive conclusions can be reached; however, initial results indicate that ILPI–1 has adhesive strength at least as good as CP2. Also, the higher thermal stability that is possible with IL-based materials should allow higher service temperatures for aeroshell TPS systems. In addition, we have observed that fewer bubbles/voids, that can reduce mechanical strength, are produced with IL polyimide films. The preparation of composites using these materials will be much easier because the monomer resins can be handled as pastes before curing, which is not possible with conventional polyimides and bis(maleimides). Furthermore, the inherently low-vapor pressure and ability to process IL polyimides and bis(maleimides) without VOCs offer the possibility of both on-board processing inside spacecraft, as well as in-space processing, where conventional VOC materials would be difficult or impossible to handle in hard vacuum.

Future Work

All of the proposed work on this project has not yet been completed and there is much that remains to be done. Because of the present challenges in preparing good quality button samples, the next step will be to prepare dog-bone specimens and perform tensile testing to determine the inherent properties of the neat IL polyimide and bis(maleimide) resins. This can be done with either thin film or thin-sheet samples, depending on the amount of material available. Also, characterization of the physical and thermal properties of the resins, both during and after curing, will be carried out. The two methods that will be employed include: (1) Differential scanning calorimetry (DSC), which gives curing exotherms (T_g) and (2) decomposition temperatures and viscometry, which gives the viscosity as a function of temperature. This information will be used to optimize curing conditions so adhesive samples can be prepared with good surface coverage and reproducibility, as well as to help determine what service conditions the IL polyimides and bis(maleimides) can withstand. Once the properties of the neat materials have been determined, the focus of the work will move to composites, specifically carbon composites.

From a chemistry standpoint, the next step will be to continue to improve and optimize the synthetic procedures for making the polyimides and bis(maleimides) to obtain materials with the highest purity. It is known that certain impurities (e.g., halide ions) can degrade the chemical and thermal stability of ILs; hence one goal is to find ways to minimize or eliminate the use of reagents that produce these impurities. Advances in IL research are occurring at a rapid pace and this growing knowledge base will be used to refine and improve the design and synthesis of new materials.

6.4 Development of a Novel Ni/Al_2O_3 Nanolaminate for Propulsion Applications

PI—Martin Volz, NASA MSFC.

Co-PIs—Raj Kaul, NASA MSFC and Consty Mazuruk, University of Alabama in Huntsville.

Objective

The objective of this project was to develop novel Ni/Al_2O_3 nanolaminate structures. Nanostructured layers of alternating materials represent a new class of materials that can exhibit novel properties far different than the bulk properties of the contributing materials. A nanolaminate is a composite of alternating layers of different materials where the characteristic layer thickness is on the order of nanometers. While the behavior of composite materials is usually governed by the rule of mixtures, where their properties are an average of those of the contributing materials, the properties of nanolaminates are determined by the layer thicknesses and detailed structures of the interfaces between layers. The layer thickness and interface structure can be tailored to optimize material properties such as strength, oxidation resistance, and hydrogen embrittlement. The performance of liquid rocket engines is limited by the material properties of their component parts. Recent development efforts using Ni-based metal-matrix composites (MMCs) have shown promise in applications where strength, oxidation resistance, and hydrogen embrittlement at elevated temperatures are major concerns. An Ni/Al_2O_3 nanolaminate is expected to improve even upon the Ni MMC material properties. Nanolaminates can also be made with novel thermal properties. For example, ultralow TC can be obtained because the high-interface density reduces phonon coupling between dissimilar materials. Such nanolaminates can be used as protective coatings on launch vehicle surfaces exposed to high temperatures or on ballute structures for aerocapture.

Description of Research

Introduction. Tremendous advances in material properties have been achieved through nanoscale engineering. One common method is to disperse nanometer-sized particulates inside a host matrix. This can change some of the basic physical properties such as hardness, thermal expansion coefficient, oxidation behavior, chemical reactivity, optical and electrical properties, etc. Another more recent technique for nanoscale engineering is the development of nanolaminates, a technique that is receiving increasing interest because of the potential impact it could have in aerospace and other industries.

Laminates are essentially composites consisting of alternating layers of different materials. The laminate can be constructed from alternating layers of metals (Ti and Al), alternating layers of ceramic oxides, or even polymers. It is also possible to construct laminates by mixing layers of different kinds of materials, such as metals and nitrides. The key feature of laminates is that when the layer thickness is reduced to nanometer scale, the material can acquire novel properties, far different than the bulk properties of the contributing material. In contrast, bulk composites follow the rule of mixtures, whereby the properties of the composite are essentially an average of the properties of the contributing material. For nanolaminates, the layer thickness and detailed structure of the interface between the layers become the controlling parameters, allowing consideration of new ways to tailor laminate composites to control strength, fracture, and multifunctionality.

An example of a property that nanolaminates can affect is that of hardness. Hardness is increased when the layer thickness is less than the dislocation length for the slip plane motion that characterizes the response of the material to stress. A multilayer consisting of two soft metals, such as Cu-Al, can have strength on the level of GPa when the bilayer period is reduced to a few nanometers.[1] For comparison, the bulk strength of the constituent metals is only in the range of a few tens of MPa. Another property that can change significantly on layer thickness is the TC. This can occur when the layer thickness becomes less than the mean free path of the phonon that transfers the heat. In addition to increased strength and lower TC, nanolaminates have displayed unexpectedly high thermal and mechanical stability and increased wear resistance.

This project has focused on the development of a new nanolaminate, Ni/Al_2O_3. An Ni/Al_2O_3 MMC is one of the best advanced propulsion materials and has been a focus of the aerospace industry for several decades.[2,3] Rocket engine turbine components require high strength, creep and fatigue resistance at temperature, oxygen compatibility, and corrosion resistance. Ni-based alloys and Ni-based MMC's are the materials of choice for these components currently under development.[2] A nano-layered structure made from Ni/Al_2O_3 should enhance these properties significantly further. In addition, hydrogen embrittlement of metal alloys can be reduced by protective alumina coatings that are a natural barrier for H_2.[4,5] A laminate structure can consist of thousands of alumina layers. Such a material is expected to possess a significant resistance against hydrogen.

Another potential application of Ni/Al_2O_3 nanolaminates is ballute structures for aerocapture. The polyimide thin films currently used for ballute structures development could be modified by the deposition of a few micrometers of nanolaminate. Significant strength enhancement and operation at higher temperatures (above 500 °C) is expected. The nanolaminate may possess desirable anisotropy in its thermal properties.[6] Heat flow across the layers would be reduced while heat flow along the layers will be relatively unchanged. The fabrication of a coated polyimide foil with nanolaminate in the roll form is feasible.

Research Methods

The thin films and nanolaminates manufactured in this project were made using the CVD process. Two different CVD systems were employed. A vertical reactor system used a vertical sealed quartz tube and allowed for relatively large samples up to approximately 6-in length. A second system, shown in figure 133, utilized a horizontal reactor. The substrate was placed on a heater inside of a quartz tube. A vacuum pump was used to evacuate the chamber and a pressure of 3–5 mbars was maintained during operation. The precursors for alumina and Ni are located in two temperature controlled vessels. A photograph of the horizontal system is shown in figure 134. Mass flow controllers were used to adjust the flow rate of gases into the growth chamber. Heater controllers were used to control the temperature of the substrate and the exhaust gas furnace. The temperature and resulting pressures of the precursor sources could be controlled with the recirculating chiller.

Considerable effort was expended in determining the optimal processing conditions, including the appropriate pressures, temperatures, and precursor selection. To successfully manufacture the nanolaminate, the deposition temperature for the two different layers has to be the same, otherwise, the temperature has to be adjusted before the other layer is deposited. Temperature switching, however, is

prohibitively long. The deposition temperature level is critical. A lower temperature is more desirable, so nanolayers can be fabricated on polymer substrates. From the practical point of view, the growth rate of the nanolayers has to be fast, so tens of micrometer thick nanolaminates could be deposited within a few hours. Finally, the precursors have to be chemically compatible, that is, they should not interfere with each other during the deposition process.

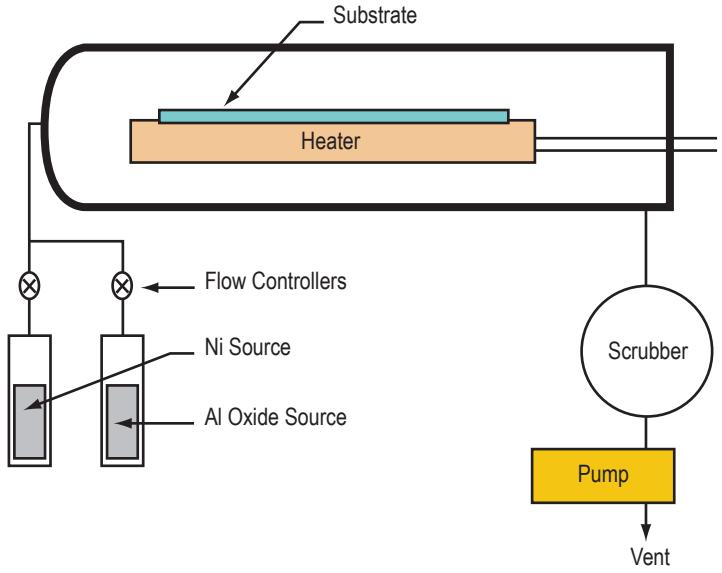

Figure 133. Schematic diagram showing the essential components of the CVD system.

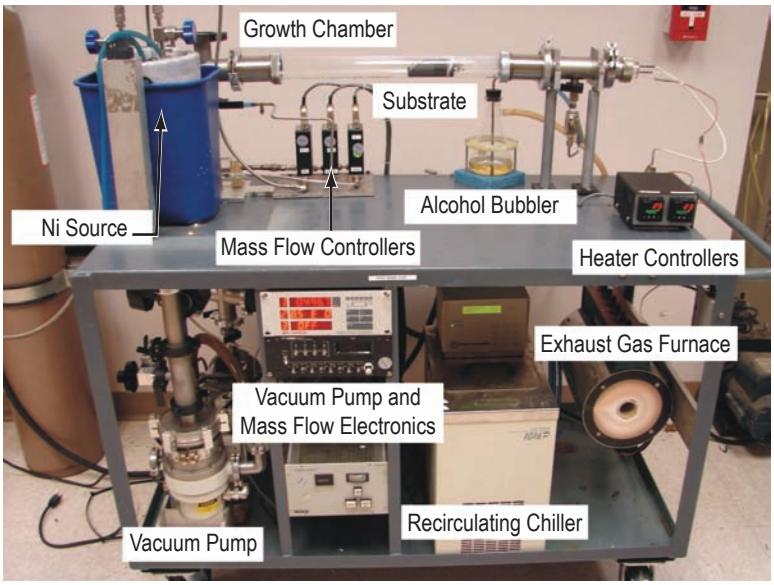

Figure 134. Photograph of the CVD system.

Ni carbonyl (b.p. 43 °C) was selected as the Ni precursor. It is often used in the deposition of pure Ni. It can be deposited in the temperature range of 40–400 °C and results in a deposit with very low carbon, typically with a maximum of 0.02 percent. A series of layers of pure Ni were deposited using the pulsing method. The precursor was maintained at a constant temperature of 10 °C, resulting in a vapor pressure of 340 mbar. The amount of vapor injected could be varied by adjusting the volume between the two valves comprising the Ni precursor feeding line. When this volume was too big, the Ni deposition rate could be as high as 200 nm per cycle. A significant decomposition in the gas phase was then observed, generating a cloud of Ni nanoparticles. This unwanted condition also depends on the size of the reactor. For a horizontal system to deposit 10 nm of Ni, the volume of Ni precursor vapor is estimated to be 0.5 cm^3. Under this condition some nanopowder formation is observed only behind the susceptor. For thicker Ni layers, a few consecutive injections of the precursor were employed. An alumina precursor was found that was compatible with the Ni carbonyl and could be successfully deposited at the same temperature as the Ni source.

Schedule

The original proposed project schedule is shown in table 17. Each of the proposed tasks was undertaken during the timeframe anticipated.

Table 17. Project schedule.

FY 2006 Tasks	D	J	F	M	A	M	J	J	A	S
Modify CVD apparatus	■	■								
Manufacture thin films		■	■	■	■	■	■	■		
Characterize Ni and Al_2O_3 layers			■	■	■	■	■	■	■	■
Manufacture free-standing nanolaminate						■	■	■	■	■
Mechanical testing							■	■	■	■
Final report										■

Results

The initial task of the project was to modify an existing CVD apparatus to enable the reproducible deposition of alternating layers of thin Ni and alumina films. A computer program was written that controlled the precursor input valves and the exhaust gas valve. Initial testing was done using solely the Ni source. The deposition rate was determined by measuring the film thickness and dividing by the deposition time. Film thickness could be measured in a couple of different ways. One way was to carefully weigh the substrates before and after deposition and then calculate the thickness. Another was to measure the thickness directly with a profilometer. After the optimal processing conditions were determined for the individual Ni and alumina layers, nanolaminate deposition was begun. Nanolaminate deposition employed the following timing sequence:

- Inject the Ni precursor.

- Wait for 10 s to evacuate the vapor.

- Inject the alumina precursor.
- Wait 10 sec for evacuation of gas products.
- Repeat the sequence.

Quartz plates, silicon wafers, stainless steel foil, and Al foil were the substrates used. Thick alumina films (≈10 μm) usually peeled off from the glass, presumably due to a significant difference in the thermal expansion coefficient between the substrate and the film.

The thin films and nanolaminates were characterized by a number of different methods. Characteristic x-ray diffraction data is shown in figure 135. The Ni layers are multigrained with prominent (111) and (200) orientations. There are no peaks from the Al_2O_3, indicating that the as-deposited Al_2O_3 is amorphous. An SEM image of a Ni/Al_2O_3 nanolaminate deposited on a metal foil substrate is shown in figure 136. The image is of a sample that was made during the early testing phase of the project. The individual layers are quite thick (≈2 μm) and the sample was made to correlate deposition time with direct measurements of the layer thicknesses. Direct measurement of the layers is not possible with SEM when the individual layers are only a few nanometers thick.

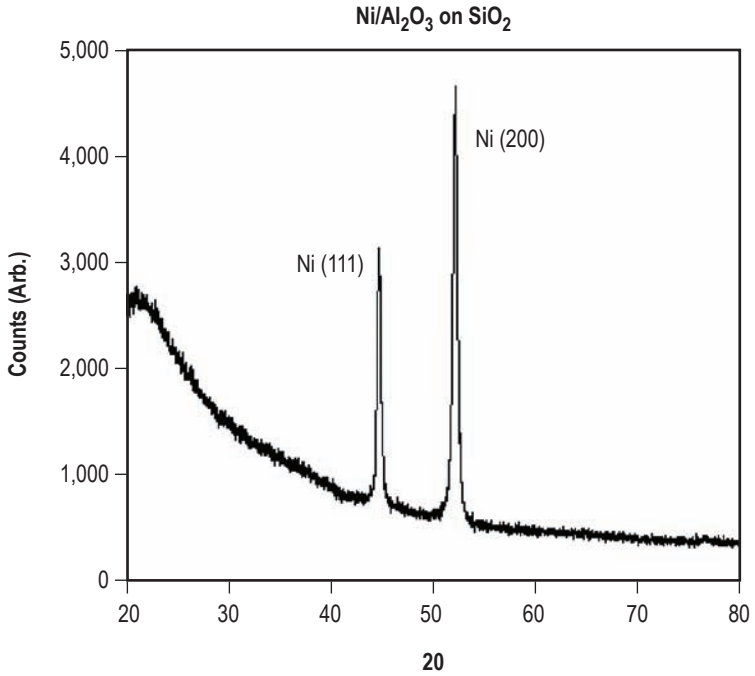

Figure 135. X-ray diffraction data of Ni/Al_2O_3. The Ni grains have both <111> and <200> orientation, and the as-deposited Al_2O_3 is amorphous.

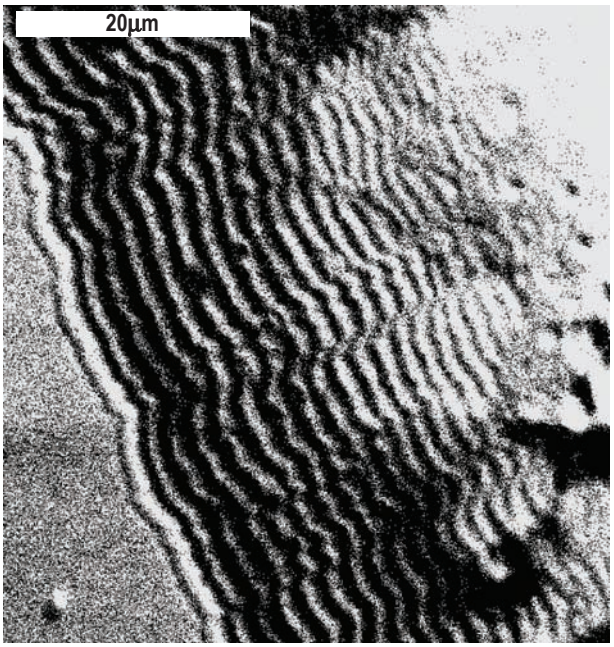

Figure 136. SEM image of an Ni/Al_2O_3 nanolaminate on a metal foil substrate.

Atomic force microscopy (AFM) was also used to characterize the nanolaminates. AFM images of Ni/Al_2O_3 deposited on a metal foil are shown in figure 137. A topographical image is shown on the left and an image obtained from a current sensing technique is shown on the right. In the AFM current-sensing technique, electrical current is passed through the probe tip and into the sample. The brighter areas are Ni, which has a relatively low resistivity. A higher magnification AFM image is shown in figure 138. The thickness of the individual layers in this sample are about 3 nm and can be identified most readily in the top left area of the image. It is difficult to obtain clear images at this level of magnification. The polishing of the samples causes an inevitable amount of smearing at the nanometer scale. Also, the finite size of the AFM's probe tip causes an averaging over an area whose size depends on the quality and size of the probe tip.

Potential Future Research

There are a number of activities that would further the development of Ni/Al_2O_3 nanolaminates. One of these would be annealing studies. For the nanolaminates to be used at elevated temperatures, it is necessary to determine the effect of annealing on the structural integrity and diffusion in the layers. It would be helpful to determine at what temperature excessive diffusion causes the layers to lose their integrity and the nanolaminate to essentially become an alloy. This could perhaps best be determined by doing depth profiling with secondary ion mass spectroscopy (SIMS). Cross-sectional measurements with TEM would also be helpful.

The quality of the nanolaminates may improve with further optimization of the deposition conditions. Specifically, initial mechanical testing found that the nanolaminates were too brittle. This could perhaps be improved by adjusting the Ni/Al_2O_3 thickness ratio. Instead of a 1:1 ratio, the Ni content

could be increased which should improve the ductility of the films. Annealing the films may also cause structural relaxation and improve ductility. Further optimization techniques include the addition of other reactor species. The addition of hydrogen, for example, will help prevent excessive oxidation during the deposition process.

Further tensile pull testing would be useful to determine the strength of the nanolaminates as a function of bilayer thickness. Comparison to other nanolaminate systems, where strength is inversely proportional to the bilayer thickness, is of interest. Such measurements could be done under both ambient conditions and at elevated temperatures.

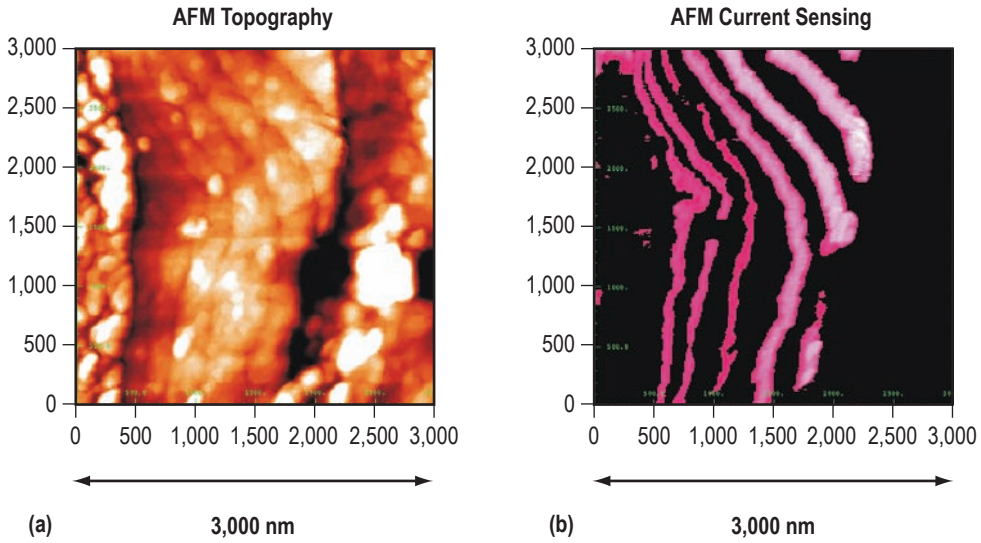

Figure 137. AFM images of Ni/Al_2O_3 deposited on a metal foil. The topographical image is on the left and the image on the right shows gradations in sample resistivity.

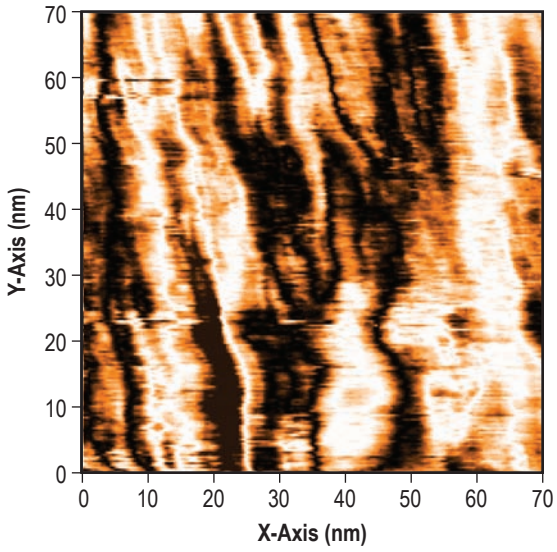

Figure 138. A high-magnification image of Ni/Al_2O_3 deposited on Si. The characteristic thickness of the individual layers is about 3 nm.

Acknowledgements

We are grateful to S. Gorti for the AFM images and for the support by the NASA AME program.

References

1. Misra, H.K.: "Deformation Behavior of Nanostructered Metallic Multilayers," *Advanced Engineering Materials*, Vol. 3, pp. 217–222, 2001.

2. Shelley, J.S.; Leclaire, R.; and Nichols, J.: "Metal-Matrix Composites for Liquid Rocket Engines," *Journal of Metals*, pp. 18-21, April 2001.

3. *Composite Materials*: *Metallic Matrix Composites*, Academic Press, New York, NY, K.G. Kreider ed., 1974.

4. Zielinski, A: "Hydrogen-Assisted Degradation of Some Nonferrous Metals and Alloys", *J. of Mater. Processing Technology*, Vol. 109, pp. 206–214, 2001.

5. Song, R.G.: "Hydrogen Permeation Resistance of Plasma-Sprayed Al_2O_3 and Al_2O_3-TiO_2 Ceramic Coatings on Austenitic Stainless Steel," *Surface and Coatings Technology*, Vol. 168, No. 2, pp. 191–194, 2003.

6. Costescu, R.M.; Cahill, D.G.; Fabreguette, F.H.; Sechrist, Z.A.; and George, S.M.: "UltraLow Thermal Conductivity in W/Al_2O_3 Nanolaminates," *Science*, Vol. 303, pp. 989–990, 2004.

7. THERMAL MANAGEMENT MATERIALS

7.1 Poisoning of Heat Pipes

PI—D. Gillies, NASA MSFC.

Co-PIs—W. Palosz (BAE Systems) and P. Salvail (STS).

Thermal management is critical to exploration efforts. In particular, efficient transfer and control of heat flow is essential when operating energy sources, such as nuclear reactors, to transfer energy to various energy conversion devices and to reject excess thermal energy safely through radiators. Applications in space demand exceptionally long periods of time with equipment accessible for limited maintenance only. Equally critical is the hostile and alien environment that includes high radiation from the reactor and space (galactic) radiation. In-space or lunar applications high vacuum is an issue, while in martian operations the systems will encounter a CO_2 atmosphere. The effect of contact at high temperature with local soil (regolith) in surface operations on the Moon or other terrestrial bodies (Mars, asteroids) must be considered.

Contamination, or poisoning, of the working fluid and variations in residual gas pressure can significantly alter the working fluid evaporation and heat transport rates, as can a change in surface tension properties of the working fluid. Possible sources of such contamination include dissolution of containment and wicking material by the working fluid, diffusion of low-level impurities dissolved in the materials, and diffusion of and reaction with materials such as the regolith minerals from the surrounding environment.

Long-term extensive testing in well-simulated space situations are needed prior to undertaking a final design for heat pipes for missions of several years in duration. In this work the intent is to initiate experiments to evaluate the diffusion of candidate gases through Inconel 625, a high-temperature candidate containment material, and to evaluate reactivity with a lunar regolith stimulant. The composition of Inconel 625 is shown in table 18.

Description of Research

The main thrust of the research have been twofold, first in evaluating and measuring the permeability, solubility and diffusion of gases through Inconel 625. The second series of tests were designed to discern if there is any reaction of Inconel 625 with regolith stimulant materials. Originally, thermosyphons were designed and piece parts manufactured from Inconel 625. The intent of loading them with sodium was delayed by the moving of the sodium loading machine and subsequent start-up problems.

Table 18. Composition range for Inconel 625.

Element	Min	Max
C	–	0.1
Ni	Bal.	Bal.
Cr	20	23
Fe	–	5
Silicon	–	0.5
Manganese	–	0.5
Sulfur	–	0.015
Phosphorus	–	0.015
Molybdenum	8	10
Ti	–	0.4
Cobalt	–	1
Columbium + tantalum	3.15	4.15
Al	–	0.4

Diffusion of Gases Through Inconel 625 Research. Penetration of gases through metals can be a problem over a long time period. The penetration of hydrogen and helium through Inconel 625 samples was examined using a system modified from equipment Originally designed to measure penetration through fused silica for semiconductor crystal growth.[1] Determination of permeability and solubility of hydrogen was done using the system shown in figure 139. A segment of Inconel 625 tube (30-cm length, 16-mm OD, and 260-m wall thickness), sealed at one end, has been connected to a barocel gauge through a valve to a vacuum system. The test tube was enclosed by an external tube connected at one end to hydrogen and Ar tanks (9N purity each), and to a bubbler or vacuum at the other end.

The solubility results obtained from the amount of hydrogen desorbed from the sample are shown in figure 140. For comparison, solubility of hydrogen in Ni is also shown.[2] As shown in figure 139, solubility of hydrogen in Inconel 625 is about an order of magnitude greater than that in pure Ni. The results of our permeability measurements are shown in figure 141. Each experimental point was calculated from an average of several measurements of the rate of pressure increase in the system. The inset shows the raw data that demonstrates the H_2 permeation rate at 0.089 atm is about one order of magnitude lower than that at 1 atm. This suggests at least a partially molecular mechanism of solution of hydrogen in Inconel 625 in our temperature range. Further interpretation of the permeability results, in particular on the effect of H_2 pressure, requires additional studies. Test experiments on helium permeation were also made.

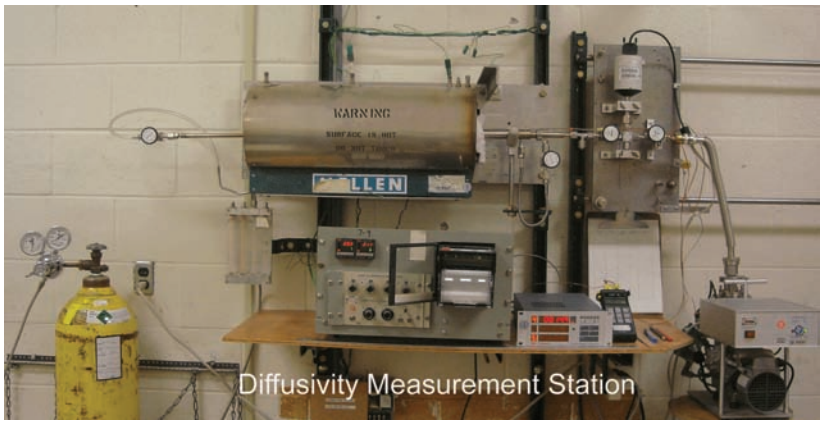

Figure 139. Permeation/solubility measurement system.

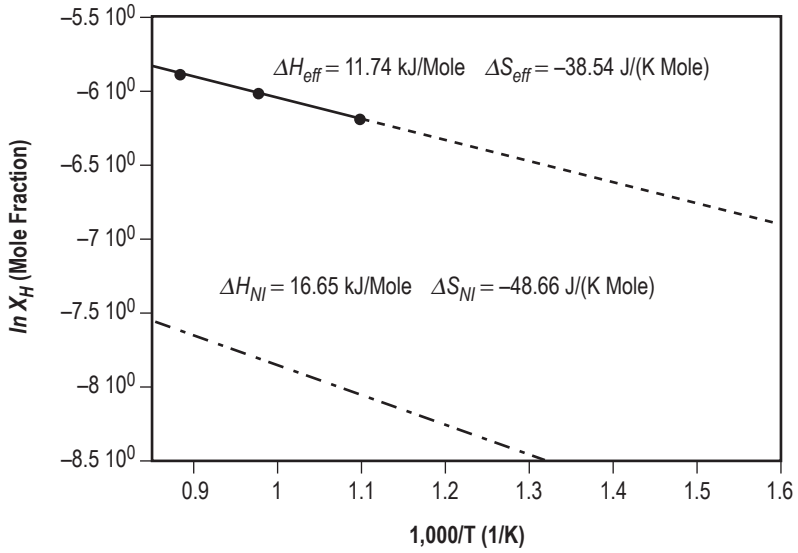

Figure 140. Solubility of hydrogen in Inconel 625 at 1 atm.

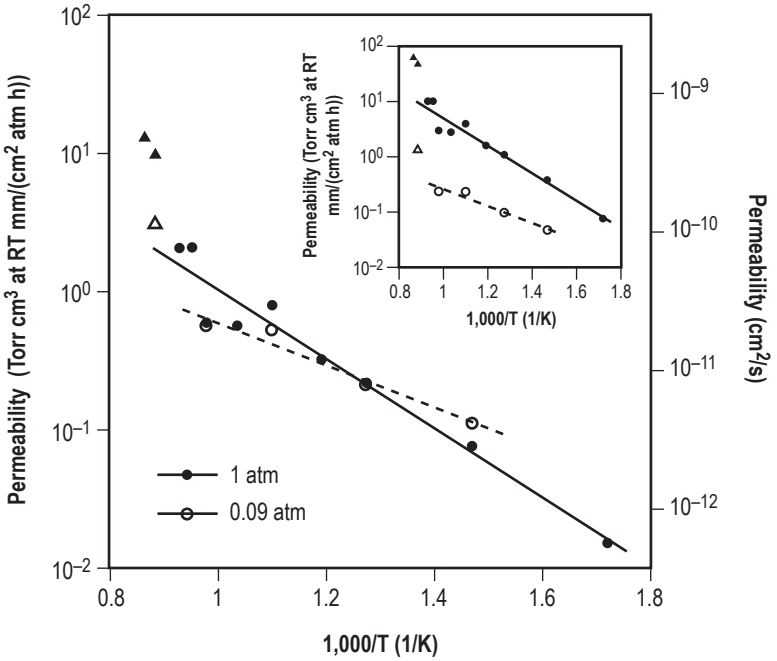

Figure 141. Permeability of hydrogen through Inconel 625.

These experiments have been taking place over 6 mo and are continuing. Based on SIMS analysis of selected samples and numerical simulations of diffusion, the permeability of He in Inconel 625 at 1,040 °C has been estimated to be lower than 10–18 cm^2/s. These results indicate a low rate, and a reasonable assumption is that there would be little or no penetration of sodium through Inconel 625.

Reactivity of JSC–1 Lunar Simulant With Inconel 625 Research Procedure. In the absence of lunar soil, the well characterized JSC–1 simulant material was used in tests to determine if and how it would react with Inconel 625 at elevated temperatures. The composition of JSC–1 is given in table 19 and is compared to a lunar mare soil from Apollo 14. The simulant is prepared by ball milling to 200 mesh, sieving, and then heating in an oven at 150 °C for a week to drive off moisture. Initially, the plan was to place coupons of Inconel 625 in fused silica ampoules with the simulant, evacuate them, and then heat them over periods of time to determine reactivity. However, the simulant devitrified the fused silica at 875 °C and the use of silica as a containment vessel was abandoned. The technique has been modified so that the simulant is loaded directly into 1/4-in diameter Inconel tubes in a glove box. Prior to fabrication, the Inconel stock is cleaned internally and externally to VC standard level per JSC–SN–C–005. The glove box operates with both water vapor and residual oxygen at levels of 1 ppm or lower. The procedure is demonstrated in figures 142 and 143. After loading under approximately 1 atm of Ar, the tube is attached to the vacuum line, shown in figure 143, and the valve opened to pump out the Ar. The samples are then crimped on the inside of the valve, sealed in plastic bags, and then transferred for tungsten inert gas (TIG) welding.

Table 19. Major element compositions for JSC–1.

	JSC–1 (Mean of 3)				Lunar Soil 14163*	
Oxide	Conc.		Std. Dev.		Conc.	
		Weight %		Weight %		Weight %
SiO_2	–	47.71	–	0.1	–	47.3
TiO_2	–	1.59	–	0.01	–	1.6
Al_2O_3	15.02		0.04	–	17.8	
Fe_2O_3	–	3.44	–	0.03	–	–
FeO	–	7.35	–	0.05	–	10.5
MgO	–	9.01	–	0.09	–	9.6
CaO	–	10.42	–	0.03	–	11.4
Na_2O	2.7		0.03	–	0.7	
K_2O	–	0.82	–	0.02	–	0.6
MnO	–	0.18	–	–	–	0.1
Cr_2O_3	–	0.04	–	–	–	0.2
P_2O_5	–	0.66	–	0.01	–	–
LOI	–	0.71	–	0.05	–	–
Total	–	99.65	–	–	–	99.8
LOI = Loss on ignition						

Figure 142. Simulant being loaded in Ar-filled glovebox. Note the box of simulant on the balance pan.

Figure 143. Inconel 625 tube after filling with lunar simulant. The tube is shown attached through a valve to the vacuum line. Arms from the balance are shown on the left.

Thermal treatments consist of heating in a horizontal tube furnace for a period of 1–3 wk at temperatures of 750, 875, 950, and 1,000 °C. As the furnaces are run in air, there is oxidation on the surface of the Inconel tubes. Isothermal furnace liners made from the same alloy have been successfully run in air in our laboratory at temperatures up to 1,100 °C without problems. A posttreatment photograph of the tube, figure 144, shows that oxidation does not affect the integrity of the tube. The TIG welds can be seen. Figure 145 shows a tube after it was opened and the heat-treated simulant was removed. While not obvious in this photograph, there is some "clinkering" of the material. The sintered lumps are presumably formed from liquid phases produced during the heat treatment. As shown in table 18, the simulant contains over 3-percent alkali oxides, which would result in liquid forming at temperatures below 900 °C.

The powder is then examined by x-ray diffraction in a Rigaku D–MAX powder diffractometer using Cu K radiation and Materials Data Incorporated software for data collection and interpretation. As this does not necessarily include the material closest to the inner walls of the Inconel tube, the tube is sectioned down the center to examine particles that could have reacted and/or adhered to the tube walls. The curvature of the tube makes focusing difficult in an optical microscope, so the venerable procedure used to make TEM replicas is used to produce a flatter surface. This involves putting drops of acetone on the inside of the tube and covering with a special plastic that is allowed to partially dissolve in the

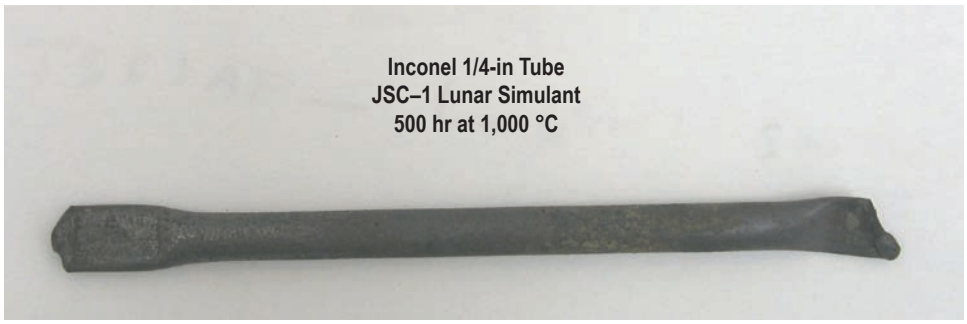

Figure 144. Inconel tube containing lunar simulant JSC–1 after 500 hr at 1,000 °C.

Figure 145. Postheat treatment simulant after opening the Inconel tube.

acetone. An intimate contact with the wall surface is formed, which faithfully replicates it. Following the evaporation of the acetone, the plastic is removed and with it comes particulate matter from the wall surface. Very few particles were obtained, and to examine these in the SEM, the plastic was then dissolved off in acetone, leaving the particles in a filter paper. Double-sided carbon tape was then used to gather the particles from the filter paper and they were then examined in the electron microprobe analyzer (EPMA) using EDS for elemental identification.

Results

X-Ray Diffraction Results. A powder diffraction pattern of JSC–1 is shown in figure 146. The pattern shows a complex series of diffraction lines, as normally found with mixtures of minerals. The glass phase has contributed to the background hump at 25–30° 2θ, and at angles below 10° 2θ (not shown). Comparison of the strongest lines with known databases enables the pattern to be identified as mainly

anorthite ($CaAl_2Si_2O_8$), with some albite ($NaAlSi_3O_8$). This is a typical plagioclase feldspar and confirms EPMA work done at MSFC.[4] Following treatment at 950 °C, the basic pattern remains similar, but there are subtle differences. The post 950 °C treatment sample pattern is shown in figure 147. Of specific interest is the peak at 18.3° 2θ. This corresponds to a major peak in chromite, a spinel containing Fe, Cr, and O, but no silicon. Chromite is a high-symmetry mineral with very few peaks. All others would be masked by the plagioclase pattern. A very small amount of chromite is present in JSC–1, and at 18.3° 2θ the 111 reflection may be present in figure 146. The simulant is believed to contain approximately 98 ppm of Cr. This evidence is not sufficient to confirm that there is chromite, and it was essential that other techniques be used to investigate this possibility further.

Electron Microprobe Analysis Results. The particulate material collected from the inner surface of the Inconel tube is shown in a secondary electron photograph in figure 148. Clearly, there are two major groups of phases present. This particle is one of many that showed a mixture of metal-rich phase (light phase) and mineral phase. Note the crystalline nature of the material and the octahedral shape of some of the particles. Chromite is a spinel, a diamond-face centered material and is known to form octahedra. Figure 149 shows the EDS pattern from the metallic phase. The spectrum shows all the Inconel elements, as shown in table 17, and also includes evidence of silicate minerals (Mg, Al, Si, O). These latter are probably the result of the spread of the EB, due to the rough surface of the sample. In comparison, the particulate material, in figure 150, shows evidence of high amounts of Cr and O in addition to the expected silicates. The Fe content is low, but the high Cr content indicates that the material has locally picked up Cr, presumably from the Inconel, and it adds to the possibility that the diffraction line in the bulk of the powder contains chromite.

Discussion

There is evidence that the simulant has acquired Cr and formed new mineral phases. This can be explained with respect to the vapor pressures of the elements. Figure 151 is one of three charts demonstrating the variation of elemental vapor pressure as a function of temperature. Elements in the Inconel alloy are shown schematically in this chart, and with values in table 20. The data are taken from Bunshah.[5] It can be seen that Cr has the highest vapor pressure of any of the major constituents, and is an order of magnitude higher than Ni, and several times higher than Fe. Thus, under the vacuum conditions of this experiment the evaporation of Cr would be expected to take place. The reaction with the simulant is more of a surprise, and could indicate possible corrosion on the lunar surface as a possibility. Within the heat-pipe interior, there will be high pressure (up to 1 atm in the case of Na) created by the working fluid, and the equilibrium partial pressure of Cr will be much lower. Also of interest is that other possible heat-pipe candidate materials such as SS contain high amounts of Cr and could also be susceptible to this same problem. It should also be noted that the refractory metals have much lower vapor pressures, while the application of a suitable coating might alleviate evaporation problems.

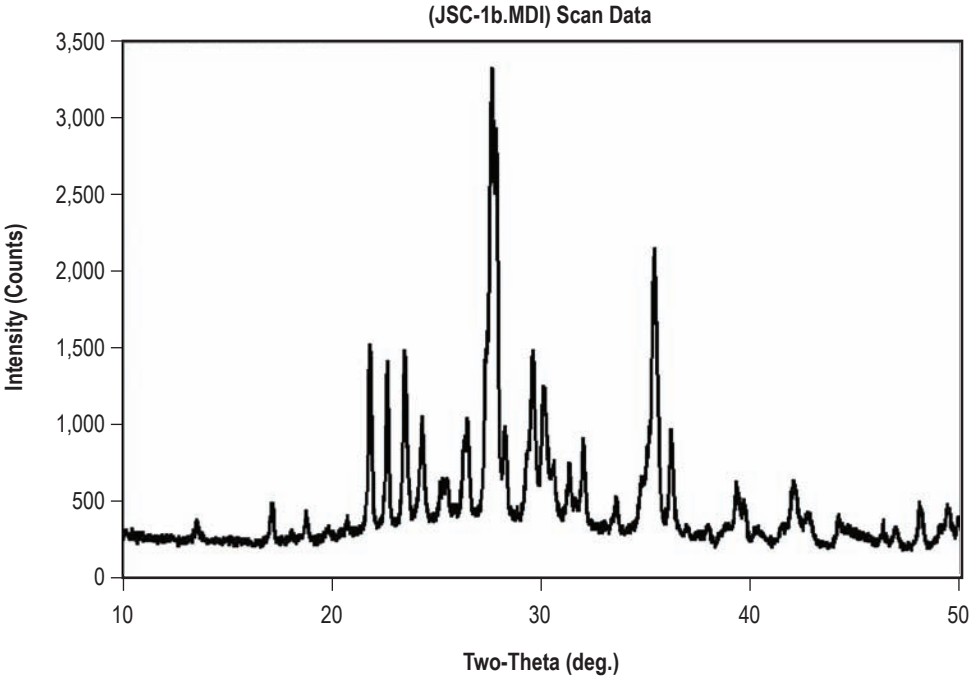

Figure 146. JSC–1 simulant. X-ray powder diffraction pattern taken with Cu K radiation.

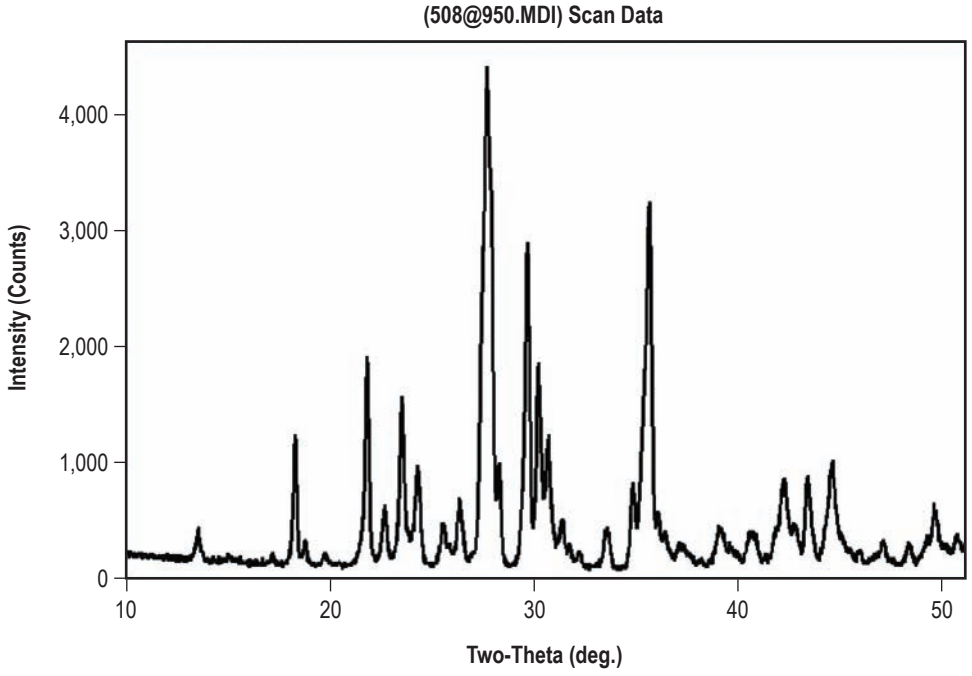

Figure 147. X-ray diffraction pattern from JSC–1 heated for 508 hr under vacuum in Inconel 625.

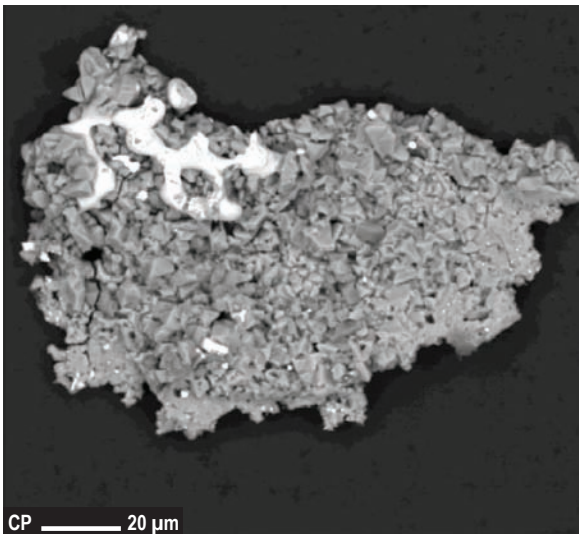

Figure 148. Secondary electron image of particle extracted from Inconel tube.

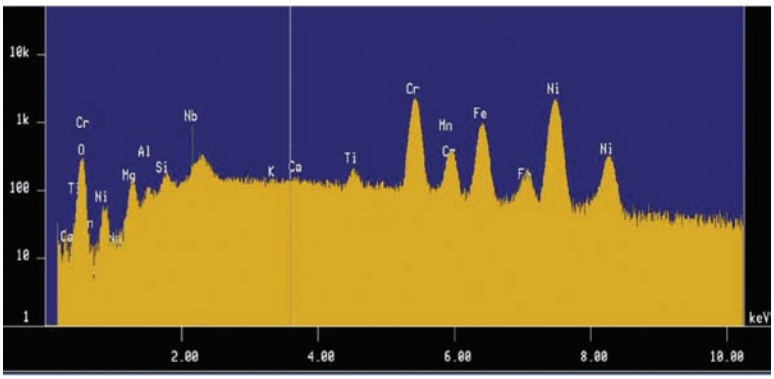

Figure 149. EDS spectrum of metallic (lighter) phase from figure 148.

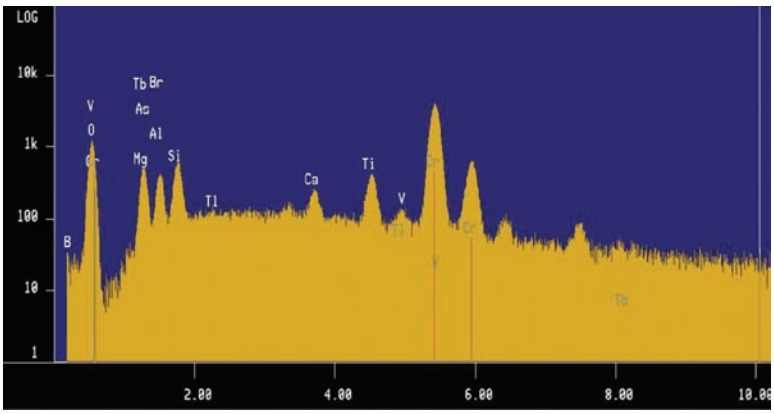

Figure 150. EDS pattern from the particulate matter shown in figure 148.

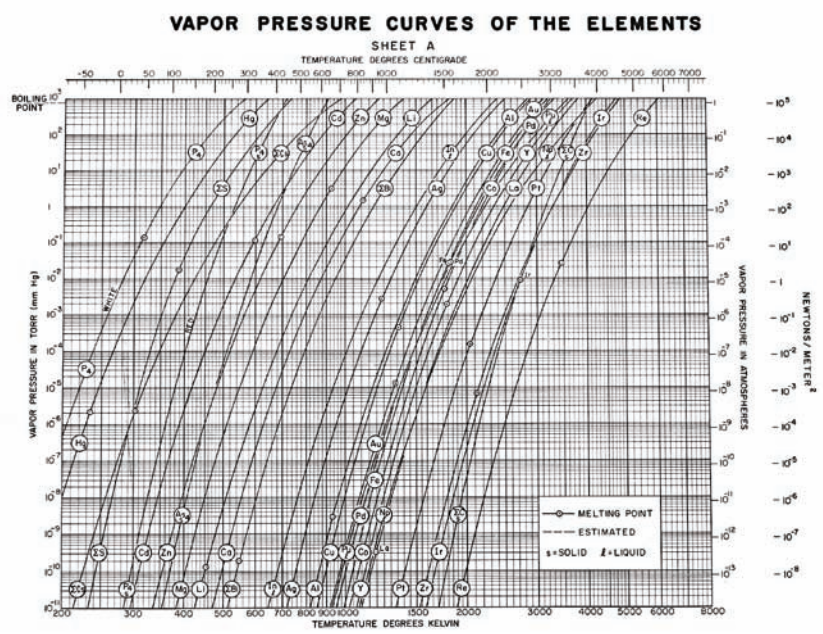

Figure 151. Vapor pressure/temperature curves for elements.

Table 20. Vapor pressures of elements in Inconel 625.

	Ni	Cr	Fe
750 °C	8*10^–11 torr	2*10^–9	1*10^–10
875 °C	1*10^–9	2*10^–8	9*10^–9
950 °C	3*10^–8	6*10^–7	2*10^–7

Possible Future Research

Several important questions remain unanswered. In particular, the possible interaction of Na with the containment metal has not been studied. This can be done by simply loading Na under vacuum into the Inconel and heat treating in the same manner as has been done with the simulant. The Na would then be extracted and analyzed, while the inner surface of the tube would be examined for any reaction. Second, the assembly of thermosyphons should be continued. The piece parts have been fabricated, and only the loading with Na remains to be done. Long-term tests with well-monitored temperatures would show the extent of any poisoning.

Other simple tests would be done, including further x-ray diffraction and EPMA on the treated powders including a mars stimulant that has been heat-treated. Finally, the internal surfaces of the glass tubing from the diffusion experiments would reveal the extent of evaporation of metals from the Inconel.

Acknowledgments

The authors have had stimulating conversations with many persons on this project, especially Bob Reid and Sandor Lehoczky. The EPMA work was done by Paul Carpenter and the design work by Chris Coppens. Finally the support for this work by the AME management team must be recognized.

References

1. Palosz, W.: J. *Crystal Growth*, Vol. 267, pp. 475–483, 2004.

2. Fromm, E.; and Hortz, G.: *Internat. Metals Rev.*, Vol. 25, pp. 269–312, 1980.

3. Mackay, D.S.; Carter, J.S.; Bowles, W.W.; et al.: Engineering, Construction, and Operations in Space IV, American Society of Civil Engineers, pp. 857–866, 1994 or http://ares.jsc.nasa.gov/HumanExplore/Exploration/EXLibrary/DOCS/EIC050.HTML

4. Carpenter, P.: Private Communication.

5. Bunshah, R.F.: *Techniques of Metal Research*, John Wiley, 1968.

7.2 Low-Thermal Conductivity Carbon Fiber

PI—Prof. William Kaukler, Center for Materials Research, UAH.

Introduction

NASA uses low-TC carbon fiber from rayon precursor for rocket nozzles to reduce the erosion rate during burn. Use carbon fiber for hot-structure insulation under TPS (dense C–C shell). carbon insulation required to have matching thermal expansion coefficient to C–C TPS (reduce interfacial stresses at high-thermal gradients).

Some structures employ C–C in contact with carbon insulation fiberform or felt due to the high temperatures. It is not an optimum insulation, but it can withstand the temperatures. When paired with C–C composite TPS shell, other materials like ceramic wools or fibers, may not be compatible unless a buffer interface is added (like an adhesive). There is a need to develop low-TC carbon fiber for insulation purposes when required for compatibility with carbon structures. carbon-fiber reinforcement of composites for TPS should also benefit from reduced TC yet still withstand the highest temperatures.

As for the C–C and carbon-phenolic composites, there may be value in developing lower TC fiber in an effort to reduce recession rates.

Much work is being done to increase carbon-fiber conductivity to make heat sinks and radiators. Nanotubes have been in part developed just for this reason. However, few people are developing low-conductivity fiber. As it is, sources for the rayon-based fiber in this country are going away or gone because of the low demand.

Forms of Carbon Classification

(1.) Fiber from pitch or PAN fiber precursors; high strength, usually high electrical, and TC; variable final properties depending on precursor chemistry and pyrolysis/heat treatment.

(2.) Fiber from rayon, cotton, silk, etc. fiber precursors; generally low TC and lower strength; material of choice for rocket nozzles.

(3.) Fiber formed the vapor phase either CVD or physical vapor deposition (PVD); fluffy fibers of microns in length (but not of the nanotube type) can be made that have low density, high electrical, and TC on individual fibers along their axis but have unknown TC in the random orientated fiber wool aggregate.

(4.) Foam (converted polymer foam or even wood), low density but not so low TC.

(5.) Aerogel, very low density and therefore low TC but low strength and not so heat resistant as other forms of carbon.

(6.) Diamond or diamondlike films, very strong, very hard, very, very high TC; not applicable in any form.

7. Graphite, various forms (foil, crystals, polycrystals), moderate TC, crystal orientation dependent, various densities.

8. Soot; nanoparticles of carbon, generally amorphous, and thus low TC.

9. Amorphous carbon, vapor deposited carbon into dense carbon ware, isotropic conductivities, not as strong as other forms.

10. Buckyballs; C60 type carbon, unknown value of TC.

11. Nanotubes; high TC along tube and high-electrical conductivity or even superconductivity; not useful for large structures due to unavailability.

The TC of carbon fibers varies depending on the heat treatment of the fibers and on the precursor polymer from which they were made. For example, rayon-based fibers have a low TC and that is why it is used in rocket nozzles. Few people in industry are interested in low-TC carbon fiber. However, NASA is keenly interested for such applications. Much work is being done to increase carbon-fiber conductivity to make heat sinks and radiators. However, almost nobody is developing low-conductivity fiber. As it is, sources for the rayon-based fiber in this country are going away or gone because of the low overall demand and insufficient market return just from NASA's purchases.

Rayon-based fibers have a low TC and that is why they are used in rocket nozzles. Indeed, that material is an ablator. There is need to have low-conductivity carbon fiber for both insulating felt and as reinforcement in C–C composites that are ablators for recession control.

After a review of the literature and discussions with experts in the field, the final direction of this project evolved. It was clear that some measure of the TC of carbon-fiber wool at incandescent temperatures was required. The thermal behavior of the fibers at temperatures over 1,000 °C is not known in the public literature. There are reports from tests of various configurations of composites made with carbon fiber and a matrix of carbon, or phenolic, or similar. The concern has been with recession rate of an ablative material or survivability with a C–C composite as a function of fiber arrangement within the matrix. Torch tests that determine weight loss as a function of fiber angle in the weave or impact of additives in the matrix have been made and are somewhat available. Results for carbon-fiber insulation at temperature have not been found.

Measurements of the TC of carbon-fiber wool were undertaken such that the temperatures examined would reach well into the incandescent temperature range where radiative heat transfer can predominate. A radial cylinder geometry was adopted and matched similar methods used at NBS now NIST since the 1960s. The ultimate issue was to determine if the thermal behavior of two markedly different commercial fibers was as significant at incandescent temperatures as it was at RT. If not, then attempts to make low-TC fiber are not worthwhile to pursue. If yes, then we can utilize all the technology already known about making, treating, and coating these fibers to engineer the best insulation for a spacecraft hot structure, or for that matter, to employ in ablators, heat shields, and rocket nozzles.

Objectives

Determine the chemistry of precursor polymers and structures that produce the lowest TC carbon-fiber based on study (cheap) and experiment (expensive).

- Conduct TC testing of existing fibers at incandescent temperatures (not done before).

- Test two fiber types

  – Rayon (≈4 W/mK)
  – PAN precursor (13–350 W/mK).

- Use axial cylinder geometry method developed at NBS.

Description and Rationale

TC data for some carbon fibers, near RT, are available in literature. No TC data are available for carbon fibers of any kind at elevated temperatures, as encountered during atmospheric entry.

High-temperature TC measurements may show that carbon fibers of all types or origins at incandescent temperatures have the same net thermal transport properties—Radiation heat transfer controlled by emissivity, which is mostly material dependent and is the dominant factor; not thermal conduction within fiber. If true, this would direct development toward modifying fiber packing/binding geometry to control optical barriers to heat flow and focus on carbon-fiber surface roughness, which slightly affects emissivity. It may also suggest there would be value to coat fibers to further change emissivity at those temperatures (as yet unknown coating material). It would also remove the need to develop low-TC fibers at fiber structure level.

For TPS work, high-temperature TC of these materials in a vacuum is required. Heat-transfer mechanisms change with temperature and pressure. What has become clearer of late is the need to make measurements of TC at high temperature in a vacuum. To my knowledge, NASA does not have such a facility.

The decision was made to develop an in-house capability to measure the TC of such fibers. The device and method would be developed under this project with testing of commercially available materials undertaken to fill the data void.

Army studies that measured TCs of carbon-phenolic composites for heat shields were undertaken to high temperatures. Rayon and PAN fibers were compared, but the data mostly involved weave charac-teristics and did not look at fiber conductivity specifically.4 Restricting access to such documents is evidence that measurements such as those made in this project may indeed be found within a Government report given the proper clearance.

Paper Study. To the author's knowledge, there is no systematic method to develop low-conductivity carbon fiber. There is so little public interest that it is likely the lowest conductivity fibers have not yet

been made, or if they have they have not been characterized and thus not available. Causes for low-conductivity behavior in carbon fibers are somewhat known. They amount to a generic explanation that the graphite planes in the structure of the carbon fiber itself are poorly aligned and disrupted. This conjecture arises from the desire to make high strength and high-modulus fiber where the best properties were found in the fibers where the coherence and alignment of the graphite planes is maximized. So, the properties that make the fiber low in conductivity are undesirable for most of the carbon-fiber industry. Technology to make high-strength fibers has progressed considerably over the last few decades. There is plenty of literature available on that topic. However, a systematic approach to making low-conductivity fibers has not been taken.

It would be the goal of this project to develop a hypothesis, from available resources, for fabricating low-TC carbon fiber. The performance of the fiber would be optimized for reentry conditions as if it were used for a TPS system. Right now, a distinction of application between insulating felt versus ablative C–C or carbon-phenolic composites cannot be made. This should be determined during the study. Clearly, a practical fiber would have some minimum strength requirement; however one can supposedly alter the fiber structure to the point where the conductivity is very low but at the cost of strength to keep it together. It may well be that rayon precursor fiber is the optimum choice. To a first approximation, the study would look at the fiber precursor choices that, for the most part, determine the inherent conductivity and strength. Review of secondary processes that impact properties will make up the balance of the effort. These include treatments of the precursors before pyrolysis and afterwards that are known to impact strength and conductivity of the stronger types of fiber based on PAN and pitch precursors.

Literature reviews yielded a little insight to making high modulus, therefore high-conductivity fiber. During the stabilization and oxidation stages before pyrolysis, the precursor fibers should be under slight tension to ensure the molecular structures in the fibers will maintain a preferred axial alignment as the fibers shrink, and thereby enhance the packing of the graphite sheets in the final fiber. Better alignment ensures higher strength, higher density, and conductivity of both types. Lower TC likely can be engineered into the fibers by reducing the tension during treatment. Since this practice is independent of the precursor choice, it appears to be one avenue of investigation with any material. Carbon fiber can be made without the tensioning during treatment, but some strength may be desired for hot structure use, if for nothing more than mechanical stability during heatup.

Another aspect of the tensioning requirement may be the straightness of the fibers. Rayon, cotton, and cellulose fibers converted without the tension have a gnarled or irregular configuration. The product tends to look like wool. Testing may be needed to verify that fiber straightness impacts mechanical stability or the more subtle CTE. Otherwise, making random fiber wool with nonstraight fibers may be an approach to reduce the product's TC, while retaining resistance to high temperatures. Some runs of rayon/cellulose/cotton where pyrolysis is taken to a more complete stage than has been done might produce good, stable, heat-resistant fiber.

A low-TC carbon-fiber discussion with E & L consultant Chris Levan on March 3, 2005 follows. Levan retired from BP Amoco after it was bought by Cytec. He worked on the project to make a low-TC PAN fiber substitute for rayon for NASA in the mid-1990s. He affirmed what the author has learned so far, that for low TC one must sacrifice strength and modulus. The precursor molecular structure tends

to align during the pyrolysis and as the carbon-planes form, they become more dense and coherent. The problem is that if disruption of the alignment is taken too far, by improper fiber handling during conversion or by starting with a polymer that has little opportunity for alignment, the fiber will not be strong enough to support itself during processing. This problem is averted by bundling the microscopic fibers into continuous tows of over 1k fibers with typical ranges of 3–12k tows. This way, the fibers are processed efficiently and continuously, rather than in a batch process. The fiber bundles support one another and commercial production is enhanced.

Laboratory Measurements. The apparatus is shown schematically in figure 152 and in the photograph is shown in figure 153. Figure 154 is a schematic of the reusable NBS design that had some desirable features to make it suitable for a wide range of materials. This device has since been decommissioned. A less elaborate configuration was built for use here where components would be replaced after a test. Referring to the figures, we find that an axial wire heater is employed surrounded by the material under test. A metal shell forms the outer cylinder and contains the material under test and makes it conform to a known geometry. Heat generated in the core or filament is radially transferred through the material under test and exits through the shell. B-type thermocouples at the core and the shell show the temperature gradient established and survive the service temperatures encountered. Current and voltage to the heater is measured and yields the power per unit length of the cylinder. This is all operated in a high-vacuum chamber to do the following four things:

(1) Prevent heat transfer by convection of gas within the fiber sample.

(2) Protect the fiber from oxidation loss (burning).

(3) Simulate the vacuum of space this structure would experience.

(4) Reduce heat loss to the apparatus by using the best insulator known to man, vacuum.

The governing equation allows the TC calculation based on heat transferred per unit length of cylinder (q).

$$q = -2\pi r \lambda(T) \frac{dT}{dr} \tag{4}$$

The TC (λ) is a function of temperature. Although not always true, it is likely a linear variation with temperature until the heat transfer mechanisms change balance from fully conductive to fully radiation. Thus, we will find out if it is linear by checking at different temperatures when we assume it is linear between the two temperatures of the test at the time. Thus, we get the average TC for the region a to b along the radius of the cylinder where T_a and T_b are measured. Point a is taken at the location of the thermocouple adjacent to the heating element and b is within the outer shell.

$$\bar{\lambda} = \frac{q\, ln(b/a)}{2\pi(T_a - T_b)} \tag{5}$$

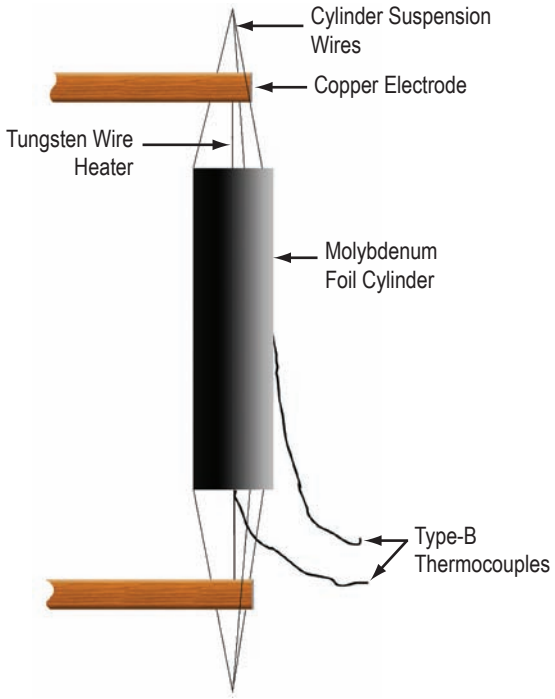

Figure 152. Schematic of the test arrangement for measuring the TC of the fiber.

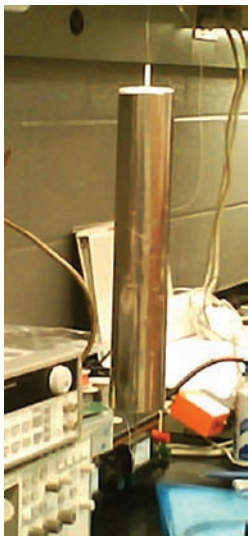

Figure 153. Test cylinder with the heating element running down the center and sheathed with an alumina tube. It was found the alumina tube would melt and destroy the test apparatus.

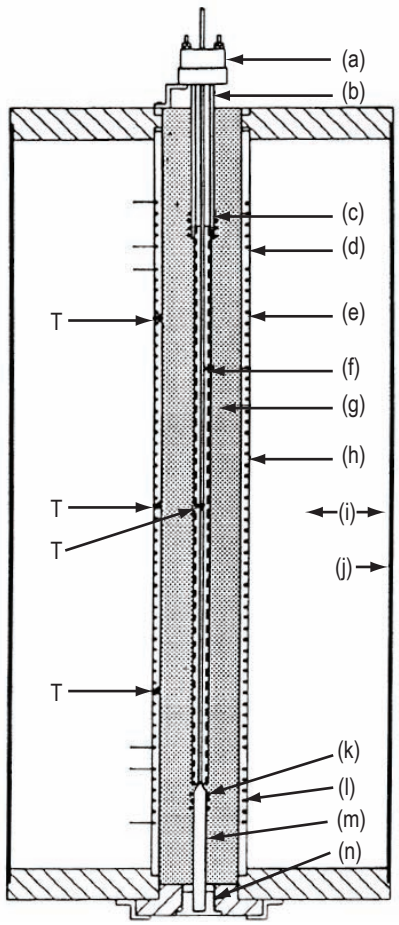

Figure 154. Vertical cross section of the 1963 apparatus:
(a) Terminal head, (b) ceramic support tube,
(c) upper support heater, (d) upper shell heater,
(e) main shell heater, (f) CC, (g) specimen,
(h) ceramic shell, (i) shell insulation, (j) SS case,
(k) lower support heater, (l) lower shell heater,
(m) ceramic support rod, (n) removable plug,
and (o) thermocouple.

Figure 155 shows a chart prepared at NBS (NIST) that was used to identify the method best suited for making TC measurements based on the temperature and conductivity of material. With little thought, one can quickly see that a method for a high-conductivity metal is not suited to the measurement of an insulation or ceramic. From this chart we verify that the ceramic core (CC) approach selected for this project is the most suitable for the material being tested.

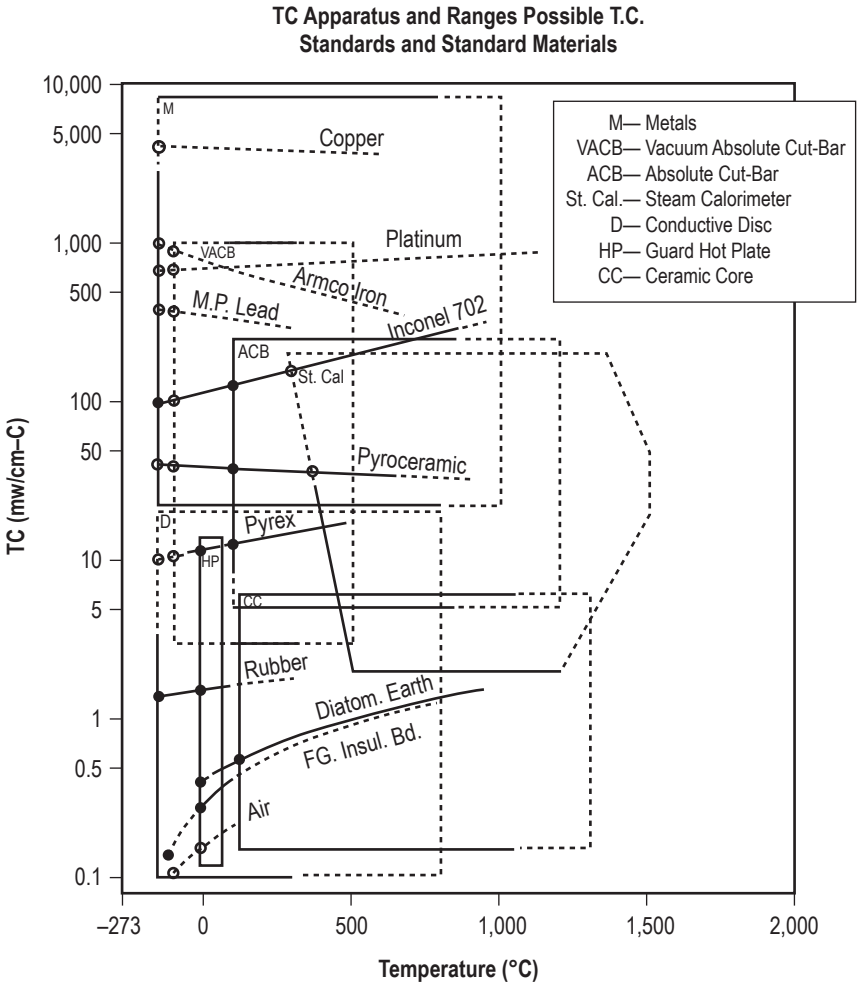

Figure 155. Recommended test regimes to measure TC of materials using various kinds of apparatus. It shows the CC apparatus at NBS (NIST) is best for high-temperature measurement of insulation like this carbon fiber.

Figure 156 shows the heating element designs tested in this project. The final result was a W-26Re wire coated with ceramic cement to keep the carbon fiber from making electrical contact. Careful design of the copper electrodes to feed the element helped keep it straight as it heated up. There were severe expansion problems with the heater until this was resolved.

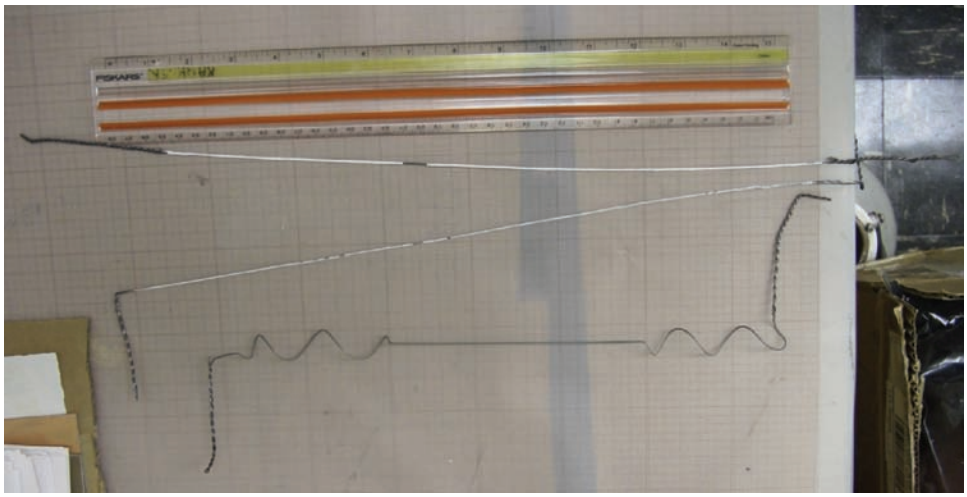

Figure 156. W-26Re alloy heating element prototypes coated with Aremco high-alumina cement for insulation from the carbon fiber. The cement kept the fiber from conducting to the heater. The cement would spall off during the test, but it was held in place by the pressure of the fiber so short circuits did not develop, even when the cement was melted.

Figures 157 and 158 are selected charts from those used to calibrate the apparatus. Here is shown the thermocouple calibration using the freezing point of pure tin (Sn). Without applying correction, we find the readings to be within 2° of the proper value (0.2 percent). Since the temperature difference is desired, such a correction would be dropped in the calculations. The other graph shows the calibration of the measured current to the heater as seen by the data acquisition system. The graph offers a measure of the uncertainty in the measurement. Although the errors are higher near zero current, no measurements of conductivity were performed near this region. Voltage can be measured with high certainty (better than 0.01 percent). Figure 159 shows the interior of the chamber and figure 160 shows the cylinder under test. The purpose was to reach an incandescent temperature on the exterior surface to ensure radiation heat transfer was taking place. This photo shows that. If the cylinder were larger or the maximum heater power lower, this condition could not be met.

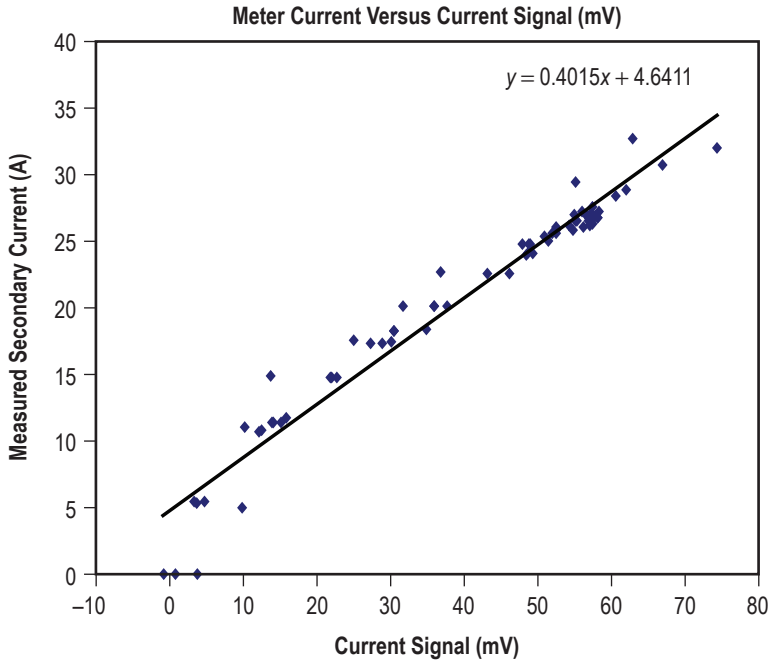

Figure 157. Graph showing calibration of measured current on transformer secondary feeding the heating element and the measured signal to the data acquisition system.

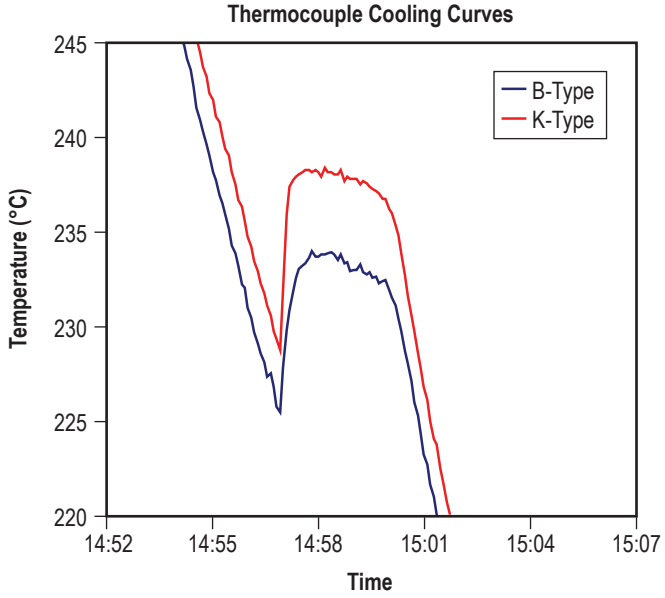

Figure 158. Cooling curve calibration of thermocouples and data acquisition setup. Thermal arrest should be 232 °C, the freezing point of pure Sn. Both readings are good, showing high undercooling as proof the Sn was clean.

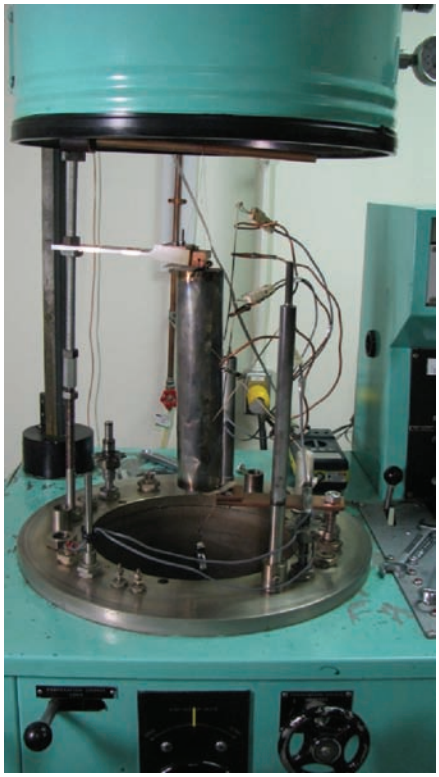

Figure 159. Vacuum chamber interior showing test cylinder heating electrodes and thermocouples.

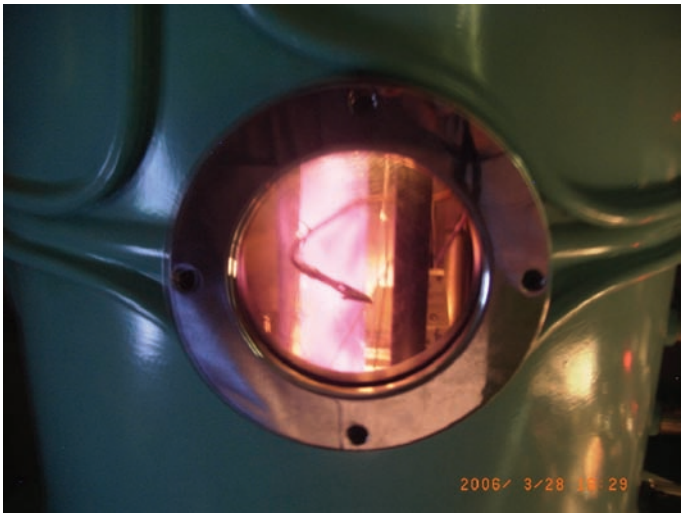

Figure 160. View through test chamber window showing cylinder during incandescent emission on the exterior.

Results With PAN Fiber. Found that the core-to-surface temperature difference scaled linearly with power to the heater. This indicates that the ratio of heat transferred by the two conduction paths through the fiber wool did not likely change as a function of heat. This is further proven when examining the reduced data that is plotted in figure 161. Using the previous equations, the calculations were made and the plot shows the measured TC as a function of average temperature, core-to-surface, for 0.023 g/cm^3 fiber density. This data is from one set of thermocouples and shows the linear dependence on temperature of the TC that was illustrated in the raw data of temperature versus power. This behavior was reproduced with a 30-percent higher fiber packing density in a separate test.

Advancing Exploration With This Technology. Knowing that the TC was not likely dependent on emissivity or surface texture but rather on the structure and composition of the fiber, forces us to focus time and effort on the fiber precursor chemistry and heat treatment. Use of emissivity control coatings, etching, or otherwise modifying the fiber surface texture will not be worthwhile.

Besides a balance of strength, conductivity, and density of the fiber, design of a hot-structure insulator from carbon fiber will benefit from fiber alignment control. Lower conductivity at equivalent density will be achieved by ensuring the fibers are randomly oriented along the heat flow direction.

Structural strength can be maintained by increasing the average fiber alignment normal to the main heat flow direction at the cost of increased density.

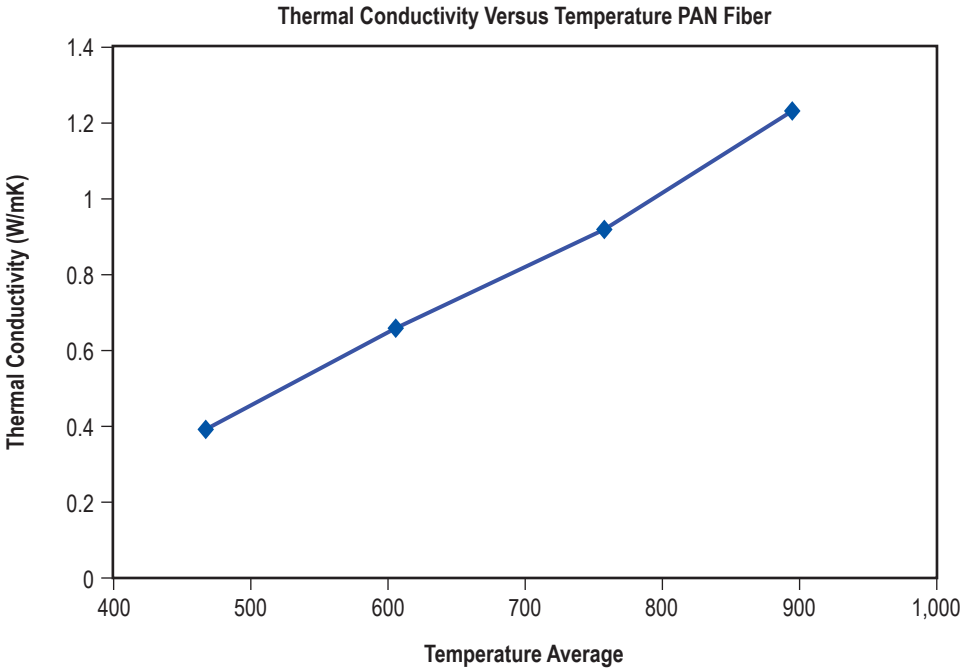

Figure 161. Reduced data from 0.023 g/cc density PAN fiber showing TC versus temperature is a linear function, even through the radiation heat-transfer regime.

Fiber curling would be advantageous to confine conducted heat within the fibers along their fiber axes and reduce the tendency to form aligned fiber clusters.

The stronger, stiffer, more crystalline, and conductive fibers are generally very straight and difficult to curl. Increasing the amounts of imperfections in the fiber structure should help develop more curl in the fibers and make better insulation.

Future

More tests with different sets of parameters should be completed to corroborate the initial findings of these experiments.

To further improve the insulation properties of low-conductivity carbon fibers, heat treatment processes could be applied to the fibers. High-temperature prolonged treatments have been shown to increase TC and strength. However, the literature only reports the results that were positive for improving the properties in these directions.

If heat treatment, other processing factors like porosity and dissolved nitrogen and the orientation of the fiber can be controlled, it may be possible to engineer improved insulation for TPS hot structures. Should be expanded to include other carbon-based materials that might prove valuable for thermal protection.

Addendum

Carbon fibers can be classified into categories on the basis of modulus, strength, and final heat treatment temperature. Based on carbon-fiber properties, carbon fibers can be grouped as follows:

- Ultrahigh modulus (UHM) type (modulus >450 Gpa).
- High modulus (HM) type (modulus between 350–450 Gpa).
- Intermediate modulus (IM) type (modulus between 200–350 Gpa).
- Low modulus and high tensile (HT) type (modulus <100 Gpa, tensile strength >3 Gpa).
- Superhigh tensile (SHT) type (tensile strength >4.5 Gpa).

Based on precursor fiber materials, carbon fibers are classified as follows:

- PAN-based carbon fibers.
- Pitch-based carbon fibers.
- Mesophase pitch-based carbon fibers.
- Isotropic pitch-based carbon fibers.
- Rayon-based carbon fibers.
- Gas-phase grown carbon fibers.

Based on final heat treatment temperature, carbon fibers are classified into the following:

- Type-I, high-heat treatment (HHT) carbon fibers, where final heat treatment temperature should be above 2,000 °C and can be associated with high-modulus type fiber.
- Type-II, intermediate-heat treatment (IHT) carbon fibers, where final heat treatment temperature should be around or above 1,500 °C and can be associated with high-strength type fiber.
- Type-III, low-heat treatment carbon fibers, where final heat treatment temperatures are not greater than 1,000 °C. These are basically low modulus and low-strength materials.

Manufacture

In *Textile Terms and Definitions*, carbon fiber has been described as a fiber containing at least 90-percent carbon obtained by the controlled pyrolysis of appropriate fibers. The term graphite fiber is used to describe fibers that have carbon in excess of 99 percent. A large variety of fibers called precursors

are used to produce carbon fibers of different morphologies and different specific characteristics. The most prevalent precursors are polyacrylonitrile (PAN), cellulosic fibers (viscose rayon, cotton), petroleum or coal tar pitch and certain phenolic fibers. Carbon fibers are manufactured by the controlled pyrolysis of organic precursors in fibrous form. It is basically a heat treatment of the precursor that removes the oxygen, nitrogen and hydrogen to form carbon fibers. It is well established in carbon fiber literature that the mechanical properties of the carbon fibers are improved by increasing the crystallinity and orientation, and by reducing defects in the fiber. The best way to achieve this is to start with a highly oriented precursor and then maintain the initial high orientation during the process of stabilization and carbonization through tension.

Figure 162 shows a schematic drawing of carbon fiber preparation from PAN fibers. The following are the three successive stages in the conversion of PAN precursor into high-performance carbon fibers:

- Oxidative stabilization—The PAN precursor is first stretched and simultaneously oxidized in a temperature range of 200–300 °C. This treatment converts thermoplastic PAN to a nonplastic cyclic or ladder compound.

- Carbonization—After oxidation, the fibers are carbonized at about 1,000 °C without tension in an inert atmosphere (normally nitrogen) for a few hours. During this process the noncarbon elements are removed as volatiles to give carbon fibers with a yield of about 50 percent of the mass of the original PAN.

- Graphitization—Depending on the type of fiber required, the fibers are treated at temperatures between 1,500–3,000 °C which improves the ordering and orientation of the crystallites in the direction of the fiber axis.

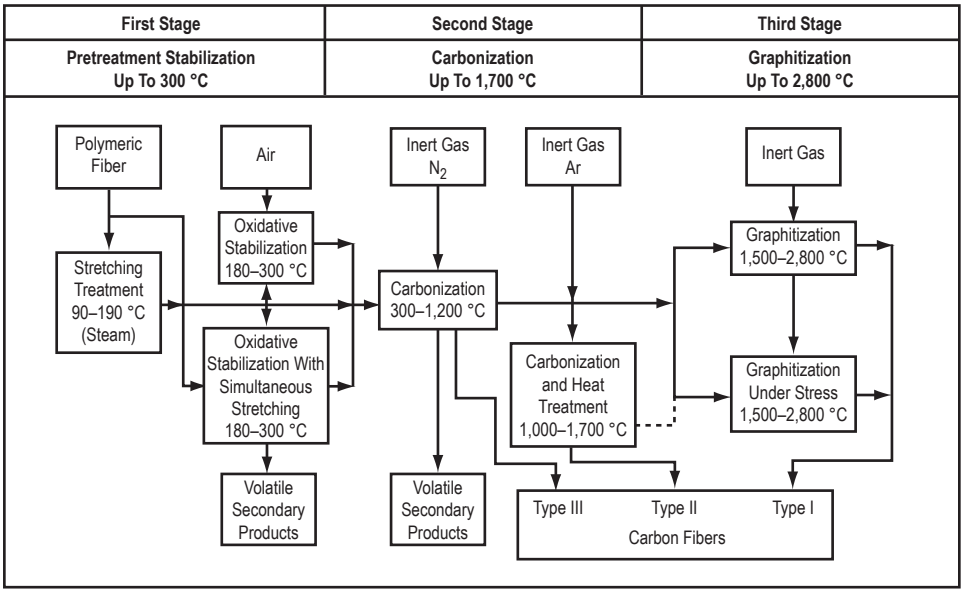

Figure 162. Schematic representation of carbon fiber preparation from PAN fibers.

Figure 163 shows the reactions involved in the conversion of cellulose into carbon fibers. Converting rayon fibers into carbon fibers is a three-stage process as follows:

- Stabilization—An oxidative process that occurs through steps. In the first step, between 25–150 °C, there is physical desorption of water. The next step is a dehydration of the cellulosic unit between 150–240 °C. Finally, thermal cleavage of the cyclosidic linkage and scission of ether bonds and some C–C bonds via free radical reaction (240–400 °C) and, thereafter, aromatization takes place.

- Carbonization—Between 400–700 °C, the carbonaceous residue is converted into graphitelike layers.

- Graphitization—Graphitization is carried out under strain at 700–2,700 °C to obtain high-modulus fiber through longitudinal orientation of the planes.

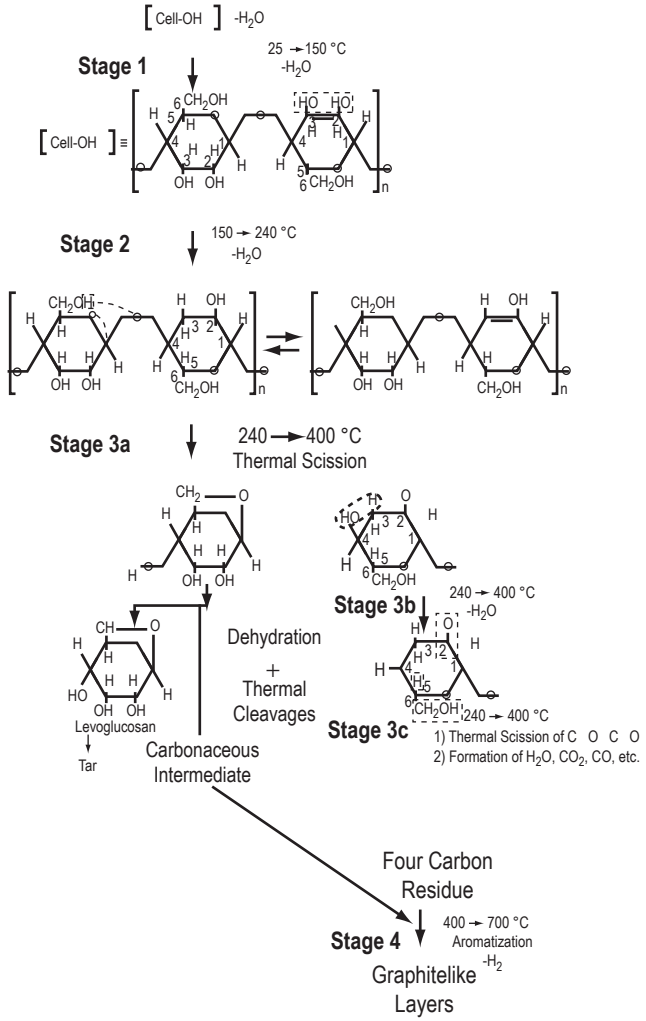

Figure 163. Reactions involved in the conversion of cellulose into carbon fibers.

The carbon-fiber fabrication from pitch (fig. 164) generally consists of the following steps:

- Pitch preparation—An adjustment in the molecular weight, viscosity, and crystal orientation for spinning and further heating.

- Spinning and drawing—Pitch is converted into filaments with some alignment in the crystallites to achieve the directional characteristics.

- Stabilization—Some kind of thermosetting to maintain the filament shape during pyrolysis. The stabilization temperature is between 250–400 °C.

- Carbonization—Temperature is between 1,000–1,500 °C.

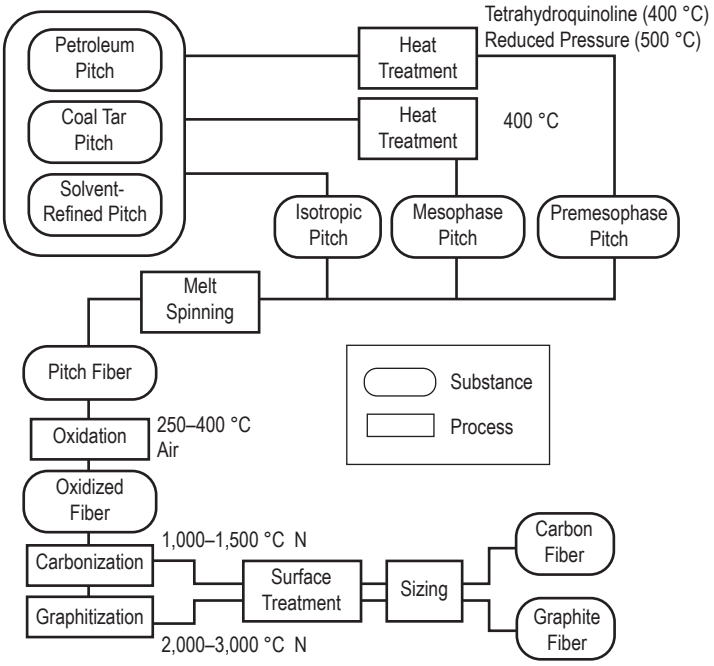

Figure 164. Manufacturing process schematic for pitch-based carbon fibers.

Structure

The characterization of carbon-fiber microstructure has been mainly been performed by x-ray scattering and electron microscopy techniques. In contrast to graphite, the structure of carbon fiber lacks any three-dimensional order. In PAN-based fibers, the linear chain structure is transformed to a planar structure during oxidative stabilization and subsequent carbonization. Basal planes oriented along the fiber axis are formed during the carbonization stage. Wide-angle x-ray data suggests an increase in stack height and orientation of basal planes with an increase in heat treatment temperature. A difference in structure between the sheath and the core was noticed in a fully stabilized fiber. The skin has a high axial preferred orientation and thick crystallite stacking. However, the core shows a lower preferred orientation and a lower crystallite height.

Properties

In general, it is seen that the higher the tensile strength of the precursor the higher the tenacity of the carbon fiber. Tensile strength and modulus are significantly improved by carbonization under strain when moderate stabilization is used. X-ray and electron diffraction studies have shown that in high modulus type fibers, the crystallites are arranged around the longitudinal axis of the fiber with layer planes highly oriented parallel to the axis. On the whole, the strength of a carbon fiber depends on the type of precursor, the processing conditions, heat treatment temperature and the presence of flaws and defects. With PAN-based carbon fibers, the strength increases up to a maximum of 1,300 °C and then gradually decreases. The modulus has been shown to increase with increasing temperature. PAN based fibers typically buckle on compression and form kink bands at the innermost surface of the fiber. However, similar high modulus type pitch-based fibers deform by a shear mechanism with kink bands formed at 45° to the fiber axis carbon fibers are very brittle. The layers in the fibers are formed by strong covalent bonds. The sheetlike aggregations allow easy crack propagation. On bending, the fiber fails at very low strain.

Applications

The two main applications of carbon fibers are 1.) Specialized technology, which includes aerospace and nuclear engineering, and 2.) general engineering and transportation, which includes engineering components such as bearings, gears, cams, fan blades and automobile bodies. Some new applications of carbon fibers have recently been found such as bridge rehabilitation in the building and construction industry; decoration in automotive, marine, and general aviation interiors; general entertainment and musical instruments; and after-market transportation products.[5,6] Conductivity in electronics technology provides additional new applications.[7] Table 21 illustrates some of the characteristics and applications of carbon fibers.[8]

Table 21. Characteristics and applications of carbon fibers.

Characteristics	Applications
Physical strength, specific toughness, lightweight.	Aerospace, road and marine transport, sporting goods.
High-dimensional stability, low CTE, and low abrasion.	Missiles, aircraft brakes, aerospace antenna and support structure, large telescopes, optical benches, waveguides for stable high-frequency (Ghz) precision measurement frames.
Good vibration damping, strength, and toughness.	Audio equipment, loudspeakers for hi-fi equipment, pickup arms, robot arms.
Electrical conductivity.	Automobile hoods, novel tooling, casings and bases for electronic equipments, EMI and RF shielding, brushes.
Biological inertness and x-ray permeability.	Medical applications in prostheses, surgery and x-ray equipment, implants, tendon/ligament repair.
Fatigue resistance, self-lubrication, high damping.	Textile machinery, general engineering.
Chemical inertness, high corrosion resistance.	Chemical industry; nuclear field; valves, seals, and pump components in process plants.
Electromagnetic properties.	Large generator retaining rings, radiological equipment.

The production of highly effective fibrous carbon adsorbents with low diameter, excluding or minimizing external and intradiffusional resistance to mass transfer, and therefore, exhibiting high sorption rates is a challenging task. These carbon adsorbents can be converted into a wide variety of textile forms and nonwoven materials.[9] Cheaper and newer versions of carbon fibers are being produced

Addendum to Low-TC Carbon Fiber Final Report

Introduction

NASA uses low-TC carbon fiber from rayon precursor for rocket nozzles to reduce erosion rate during a burn. Aerospace engineers use carbon fiber for hot-structure insulation under TPS (dense C–C shell) in spacecraft design. Carbon insulation is required to maintain a matching CTE to C–C TPS, to reduce interfacial stresses at high-thermal gradients. Figure 165 shows a C–C TPS shell that has carbon fiber insulation mounted behind it alongside an artist's concept of a spacecraft during reentry.

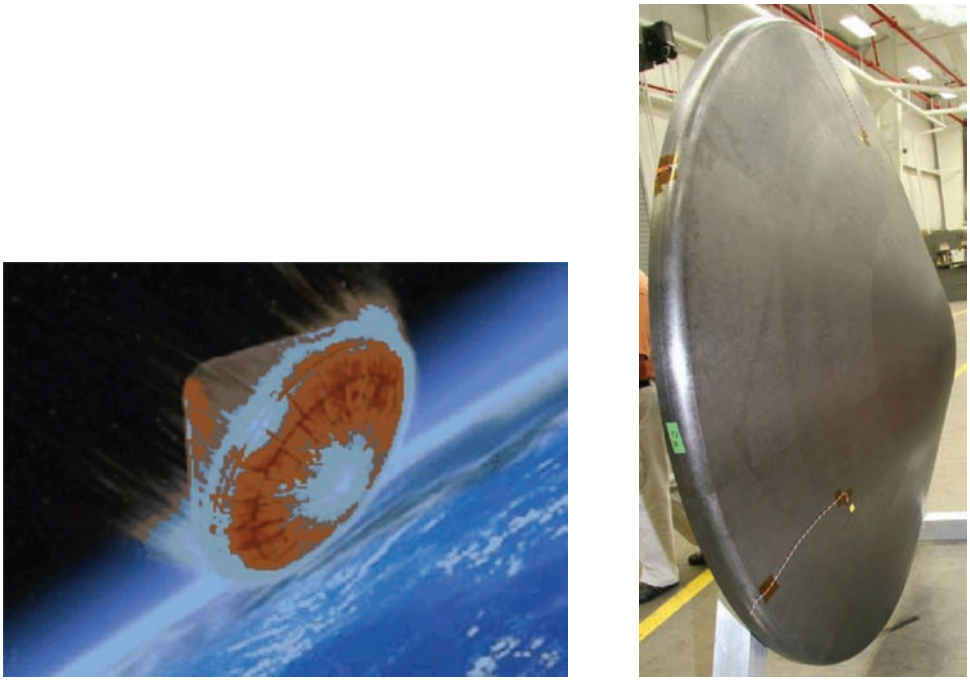

Figure 165. C–C TPS.

Steve Moon at Grey Research provided the C–C shell photographs shown in figures 166 and 167. It is not an optimum insulation but it can withstand the temperatures. When paired with C–C composite TPS shell, other materials like ceramic wools or fibers may not be compatible unless a buffer interface is added (like an adhesive that can fail prematurely due to the inherent weaker materials involved). There is a need to develop low-TC carbon fiber for insulation purposes when required for compatibility with carbon heat-shield structures.

Figure 166. Rear view of the C–C TPS from figure 165.

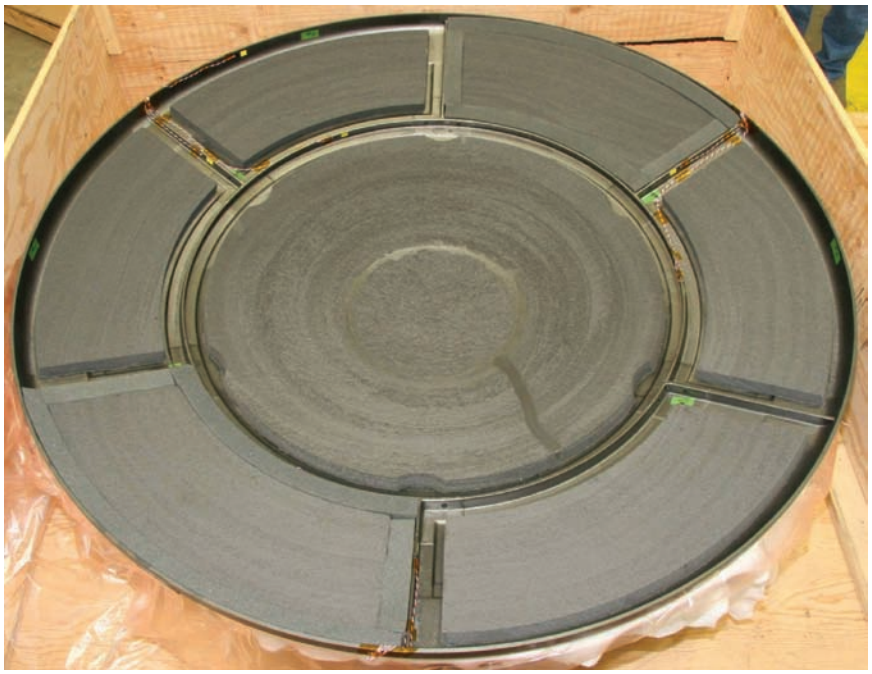

Figure 167. Same view as figure 166, but Calcarb Ltd. carbon fiber insulation is installed.

In addition, for the C–C and carbon-phenolic composites, used as the TPS or heat shield, it is worthwhile to develop lower TC fiber in an effort to reduce recession rates. Engineering such fibers was the original goal of this project but there was no baseline for conductivity properties among the various fiber sources.

Much work is being done to increase carbon fiber conductivity to make heat sinks and radiators. Nanotubes have been in part developed just for this reason. However, few people are developing low-conductivity fiber. As it is, sources for the rayon based fiber in this country gone because of the low demand.

The TC of carbon fibers varies depending on the heat treatment of the fibers and on the precursor polymer from which they were made. For example, rayon-based fibers inherently have a low TC and that is why it is used in rocket nozzles. Few people in industry are interested in low-TC carbon fiber. However, NASA is keenly interested for such applications. Much work is being done to increase carbon fiber conductivity to make heat sinks and radiators.

After review of the literature and discussions with experts in the field, the final direction of this project evolved. It became clear that some measurement of the TC of carbon fiber wool at incandescent (service) temperatures was required. The majority of the time for the project was to make such measurements. However, at the end of the project, new information came to light. The following quote from the final report is no longer true: "The thermal behavior of the fibers at temperatures over 1,000 °C is not known in the public literature. Results for carbon fiber insulation at temperature have not been found." It turns out that Calcarb Limited, a company in Scotland, makes carbon bonded carbon fiber (CBCF) insulation and published TC data (fig. 168) for a vacuum at the same temperatures as this work. Their product is presently being evaluated as a hot-structure insulation for C–C heat shields at MSFC. Note that this product uses rayon-based fiber and is not made in the U.S.

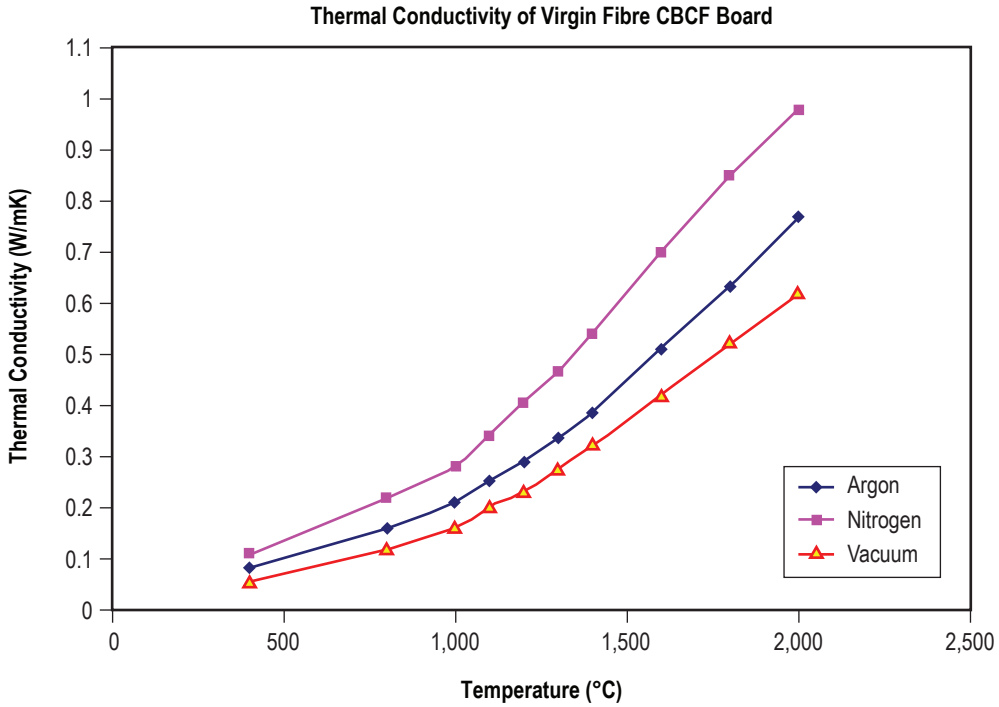

Figure 168. Calcarb Ltd. data for their lowest density product (= lowest conductivity). This material has 0.15 g/cm^3 density, or an order of magnitude higher density than the fiber wool used here.

TC measurements of the carbon fiber wool were undertaken such that the temperatures examined would reach well into the incandescent temperature range, where radiative heat transfer can predominate. Radial cylinder geometry was adopted and matched similar methods used at NBS, now NIST since the 1960s. The ultimate issue was to determine if the thermal behavior of two markedly different commercial fibers was as significant at incandescent temperatures as it was at room temperature. If not, then attempts to make low-TC fiber are not worthwhile to pursue. If yes, then we can throw all the technology already known about making, treating, and coating these fibers into engineering the best insulation for a spacecraft hot structure, or for that matter, to employ in ablators, heat shields, and rocket nozzles.

Objectives

Determine the chemistry of precursor polymers and structures that produce the lowest TC carbon fiber based on study (cheap) and experiment (expensive). As it turned out, rayon fiber precursors are still the winner here. This avenue of research was no longer pursued.

Conduct TC testing of existing commercial fibers at incandescent temperatures. Test two fiber types (1) Rayon (≈4 W/mK) and (2) PAN precursor (13–350 W/mK). TCs are for the fibers at RT and are for comparative purposes. Use the axial cylinder geometry method developed at NBS.

Paper Study

To the author's knowledge, there is no systematic method to develop low-conductivity carbon fiber. There is so little public interest that it is likely the lowest conductivity fibers have not yet been made. Causes for low-conductivity behavior in carbon fibers are somewhat understood. They amount to a generic explanation that the graphite planes in the structure of the carbon fiber itself are poorly aligned and disrupted. This conjecture arises from the desire to make high strength and high-modulus fiber where the best properties were found in the fibers where the coherence and alignment of the graphite planes is maximized. So, the properties that make the fiber low in conductivity are considered undesirable for the fiber market. Technology to make high-strength fibers has progressed considerably over the last few decades. However, a systematic approach to making low-conductivity fibers has not been taken. Knowing why the fibers have lower conductivity does not mean that the technology exists to make the lower conductivity fibers. One can disrupt the structure in the fiber to the point that it has no strength or becomes brittle. Unfortunately, that threshold is not known.

Laboratory Measurements

The apparatus is shown in figure 169 schematically. Details of the apparatus and background for the technique are in the Final Report that preceded this addendum.

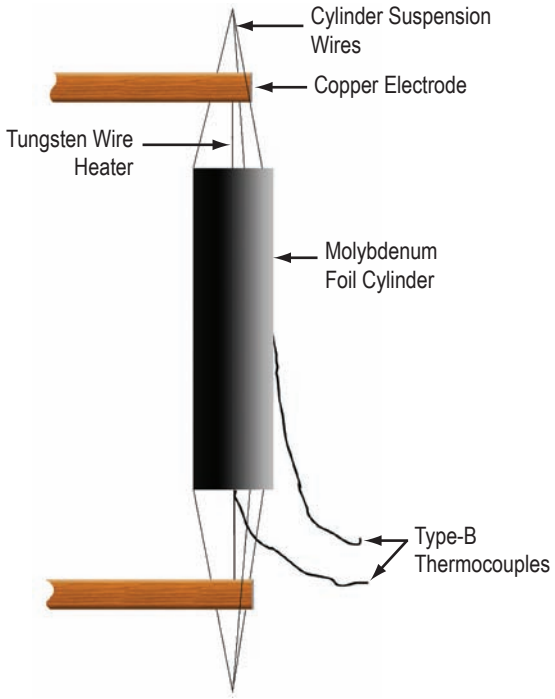

Figure 169. Test arrangement schematic for measuring TC of the fiber.

The following governing equation allows the calculation of the TC based on heat transferred per unit length of cylinder (q):

$$q = -2\pi r \lambda(T)\frac{dT}{dr} \tag{4}$$

The TC (λ) is a function of temperature. Thus, we use the average TC (λ bar) for the region a to b along the radius of the cylinder where T_a and T_b are measured. For this TM, point a is the location of the thermocouple adjacent to the heating element and b is within the outer shell where the metal overlaps and forms a pocket for the thermocouple as,

$$\bar{\lambda} = \frac{q\,ln(b/a)}{2\pi(T_a - T_b)} \tag{5}$$

Results With PAN Fiber—Previously Reported

It was found that the core-to-surface temperature difference scaled linearly with power to the heater. This indicates that the ratio of heat transferred by the two conduction paths through the fiber wool did not likely change as a function of heat. This is further proven when examining the reduced data that is plotted in figure 170. Using the equations shown earlier, the calculations were made and the plot shows the measured TC as a function of average temperature (core to surface) for 0.023-g/cm^3 fiber density. This data is from one set of thermocouples and shows the linear dependence on temperature of the TC that was

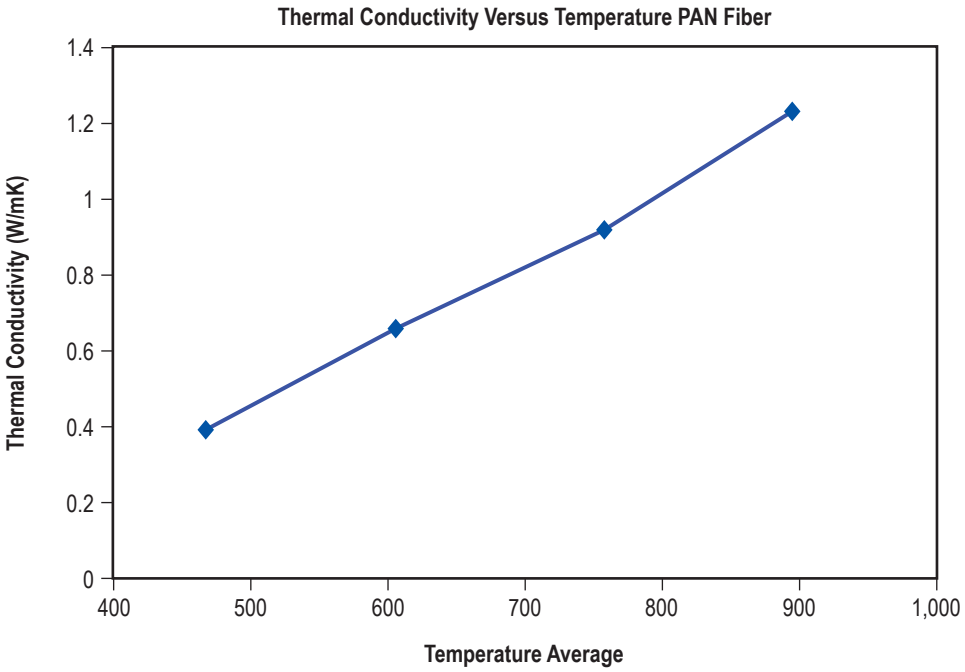

Figure 170. Reduced data from 0.023 g/cc density PAN fiber showing TC versus temperature is a linear function, even through the radiation heat-transfer regime.

illustrated in the raw data of temperature versus power. This behavior was reproduced with a 0.017-g/cm^3 lower fiber packing density in an earlier test. The second test at 0.023 g/cm^3 was designed to be 30-percent density that the first test at 0.017 g/cm^3.

Results With Rayon Fiber—New Reporting of Results

The conductivity data for the rayon precursor fiber were surprisingly different from the PAN results. Due to the low quantity of fiber available, only one density of packing was run (0.018 gm/cc). One caveat is required to interpret the curves shown in figure 171. The upper curve is abnormally high because, as it turns out, the thermocouple on the cylinder wall for that data set was accidentally placed over a region where the fiber packing was less dense inside the cylinder and transported a lot more heat by radiation to that thermocouple. This was verified by observation during the run by noting the distribution of temperature as a variation of the glow emitted from the surface. Although normally the data should be rejected, the run was not repeated and the data does follow the trend from the other set of thermocouples thus raising the confidence that the shape of the curve is valid. This point bears further analysis because this data set shows a slight curvature whereas the PAN fiber showed only a linear trend. This does not raise questions about the data quality because, coincidentally, in time for this analysis, independent measurements of a commercial rayon fiber matte became available that support the interpretation of the rayon data obtained here. Speculation that conductivity was not radiation dependent based on PAN results only are now unjustified. The Calcarb Ltd. data and the recent rayon fiber measurements both show there is an increase to conductivity due to radiation transport at higher temperatures. This can only be explained by the emissivity of the fibers being different (PAN versus rayon).

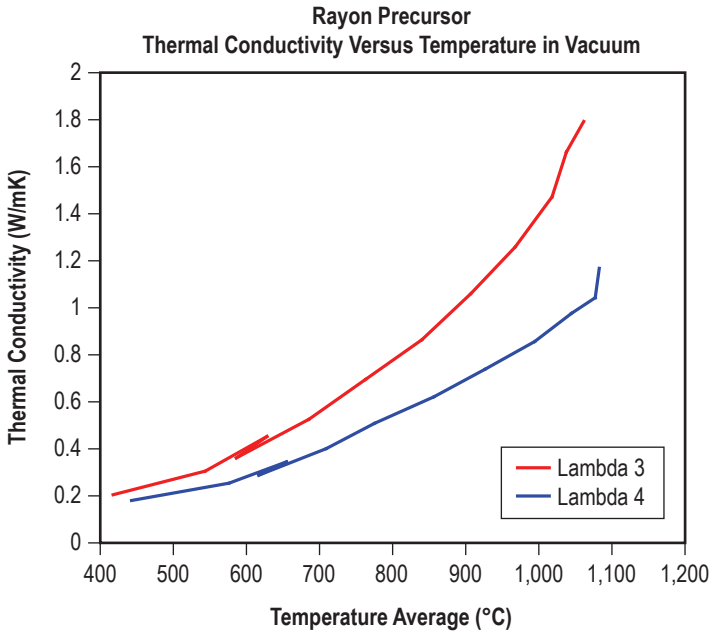

Figure 171. Reduced data from rayon fiber showing TC versus temperature. Unlike the PAN data, there is some upward curvature in the data, although there is no breakpoint or inflection at around 900 °C where radiative heat transfer begins to be significant.

Advancing Exploration With This Technology

Knowing that the TC can be dependent on emissivity forces us to focus time and effort on heat treatment and surface texture or coatings. Use of emissivity control coatings, etching or otherwise modifying the fiber surface texture will be worthwhile when working with the lower conductivity rayon fibers. It could not be worthwhile to modify the slick surfaced PAN fibers if they are used as insulation. These conclusions are the opposite from those made after only PAN fibers were tested. The new recommendations only have meaning if the fiber emissivity plays a role in the conductivity. Proof of this rationale would most quickly be shown by etching or coating the PAN fiber and remeasuring the curve to see if nonlinear behavior develops where the curve climbs upward from a straight line at higher temperatures.

Fiber curling would be advantageous to confine conducted heat within the fibers along their fiber axes and reduce the tendency to form aligned fiber clusters. The stronger, stiffer, more crystalline and conductive fibers are generally very straight and difficult to curl. Increasing the amounts of imperfections in the fiber structure should help develop more curl in the fibers and make better insulation. Increased randomization of the fiber-emitting surface orientation would produce a better insulation, but only when the fiber emissivity plays a role in overall conductivity like the rayon fibers did.

Future

To further improve the insulation properties of low-conductivity carbon fibers, heat treatment processes could be applied to the fibers during processing. High-temperature prolonged treatments have been shown to increase TC and strength. They also can modify the surface texture of the fiber. Generally, increased heat treatment temperatures smooth the fiber surface and thus strengthen it. However, heat treatment in contaminated atmospheres has damaged the surface and roughens it. This certainly would increase emissivity and should impact radiation heat transfer. If heat treatment, other processing factors like porosity and dissolved nitrogen and the orientation of the fiber can be controlled, it will be possible to engineer improved insulation for TPS hot structures. One can expand the effort to include other carbon-based materials that might prove valuable for thermal protection such as the C-phenolic and C–C composites.

This researcher, in collaboration with another at MSFC, is investigating an alternative method to form rayon precursor fiber without using the environmentally dangerous chemical process the EPA essentially outlawed from being used in the U.S. Since this rayon has not yet been made, it is premature to consider that carbon fiber made by this novel process would meet NASA's needs. However, with the research from this project, we have the knowledge to steer the process toward making the lowest TC carbon fiber.

References

1. "SACMA Releases Carbon Fiber Industry Statistics," *Composites News*, No. 1, 1998.

2. "SAMPE Plenary Describes Carbon Fiber Capacity, Trends," *Composites News*, No. 6, 1998.

3. "Carbon Fibers Seen as Having Big Long Term Growth Infrastructure is Next Big Trend Driver," *Advanced Materials & Composites News*, No. 3, 1999.

4. US5536486, Carbon Fibers and Nonwoven Fabrics, 2004.

5. "Rehabilitation Bridges: Carbon Fiber-Reinforced Polymer Shows Promise for Repairing Structures," *Advanced Materials, and Composites News*, No. 2, 1999.

6. "New Company Launches Carbon Fiber Fabrics for Decorative Applications," *Advanced Materials & Composites News*, No. 8, 1998.

7. "Carbon Fibers Electrical Conductivity Found to Offer New Uses," *Composites News*, No. 3, 1998.

8. Donnet, J.B.; Bansal, R.C.: *Carbon Fibers*, publicated by Marcel Dekker Inc., p. 370, 1990.

9. *Composites Edge*, 1992.

10. Valentine, P.G.; Nygen, R.E.; Burns, R.W.; et al.: "High-Heat Flux Testing of CFC Composites for the TPX Physics Experiment," *Seventh International Fusion Reactor Materials Conference*, Obninsk, Russia, September 25–29, 1995.

11. Guthrie, J.D.; Battat, B.; and Severin, B.K.: *AMPTIAC Material EASE*, Vol. 11, AMPTIAC, Rome, NY, 2000.

12. Healy, W.M.; and Flynn, D.R.: "Thermal Modeling of Multiple-Line Heat-Source Guarded Hot-Plate Apparatus," STP 1426, *ASTM International Standards*, Insulation Materials, Testing and Applications, V4, ISBN 0–8031–2898–3, 2002.

13. Farmer, R.W.: "Alternate Heat Shield Concepts for Ballistic and Extended Range Reentry Systems," *Advancements in Heat Shield Technology Symposium*, Bob Jones Auditorium, Redstone Arsenal, AL, September 14–17, 2004.

14. Cytec Engineered Materials: *Cytec Carbon Fibers* http://www.cytec.com/business/engineeredmaterials/CFInternet/cfperformance.shtm

7.3 Electronically Biased Thermal Protection System

PI—Prof. William Kaukler, Center for Materials Research, UAH.

Co-PI—Palmer Peters NASA MSFC Retired.

Objectives

Plan to reduce spacecraft TPS surface temperatures during planetary atmosphere entry (aerocapture) to increase survivability and lower avionics temperatures. Present study tests feasibility that a reduction of temperature is possible by rejecting simulated reentry plasma electrically. Follow-on study would be to justify the electronically biased thermal protection system (EBTPS) as a weight saving measure (given additional weight required to store and deliver power). At the time of this report, we report some success of achieving the proof of concept and show a net cooling by electrically biasing. The limitation of test conditions showed a measurable but small effect. Testing in a vacuum chamber with higher power plasma sources of the proper gas composition is expected to magnify the degree of cooling.

Description and Rationale

In an attempt to lower the peak heating and reduce the magnitude of some of the reentry challenges, we have proposed to modify plasma surface interactions that could occur at that time. The primary mode of accomplishing this is by voltage biasing the TPS surface in an attempt to change composition of the plasma sheath, its flow around the surface, and hopefully the rate of energy transfer between the sheath and the surface. Practical limits of proof of the benefits of the technique are limited to in situ measurement of the TPS backside temperatures as a bias is applied. What many people do not realize is that the high temperatures of reentry are not alone the cause of damage to the spacecraft aeroshield. Torch testing is commonly used to test TPS materials and is no exception here. Besides simulating the temperatures of reentry, the bigger facilities properly simulate the heat load and the gas compositions of reentry. It is in fact the high-heat load that damages the TPS with high-velocity plasma flow (multi-Mach number) and not so much the temperature. Thus, we would like to have had access to one of these torch facilities to test the bias concept. As it turned out, most of the work and time reported here was about duplicating the test conditions without access to a proper torch facility. The generic EBTPS setup is shown in figure 172. Voltages required to accomplish this were not deemed to be very high (tens of volts), but the currents required for high-percentage modifications, could be significant. Other potential problems involve oxidation of the TPS surface that should be an electrical conductor to maintain current flow if constant voltage is applied. Of course alternating fields could produce displacement currents.

A destination with an atmosphere totally different than Earth's can be expected to behave differently. Carbon dioxide, for instance, could ionize differently, producing both oxygen (an oxidizer) and carbon monoxide (a reducing agent). These factors will be examined in more detail after the fundamental mechanisms are better understood and the destination atmospheres more clearly defined. Applications to small patches on damaged leading TPS surfaces may turn out to be of considerable interest also, since it is difficult to produce in situ patches that can survive conditions challenging to even the original hardware.

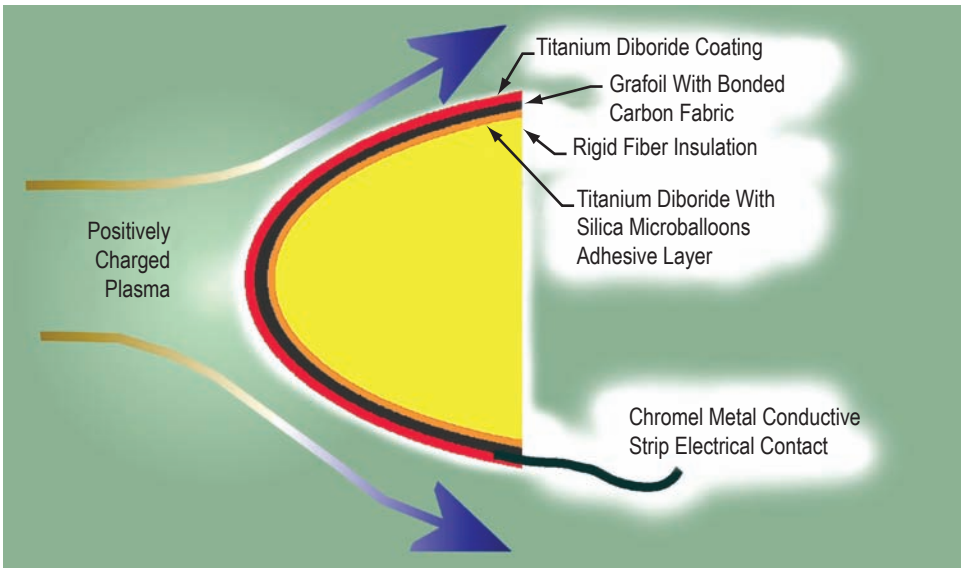

Figure 172. Generic schematic of the EBTPS as a leading-edge structure.

Testing requires simulation of reentry plasma heating of 1,200–1,650 °C. The majority of this effort was creating the test conditions (plasma, targets) and making measurements.

Electronically Biased Thermal Protection System Background

There is anecdotal evidence where studies that involved generation of plasmas by RF fields in the vicinity of hypervelocity aircraft surfaces (model testing) resulted in the lowering of drag. Apparently, the effects are not fully understood and are still under investigation by external groups. However, this anecdotal evidence supports our approach methodology. Progress in this project is hindered by the lack of the appreciable properties data associated with applying the phenomena discussed. Thus more laboratory testing is called for which normally would be underpinned with extensive literature support. From our experience with RF sputtering, we know that electron mobility is much higher than ion mobility and that during half cycles the electrons will be removed at an electrode while ions are scarcely displaced. This leads to a dark space in the vicinity of an ungrounded electrode, rectification, and negative biasing of the surface. This biasing attracts positive ions to the surface and if floating potentials exceed approximately 90 V, measurable sputtering occurs from positive ions, such as argon (i.e. small quantities of surface atoms are physically knocked from the surface, slowly eroding it). Most of Earth's atmosphere is nitrogen and oxygen both of which desire gaining electrons. Losing electrons is oxidation (LEO) and gaining electrons is reduction (GER), thus, oxygen oxidizes materials strongly by taking electrons. A negative bias would thus repel negative ions, pushing the environment away from the biased surface and modifying the ion surface, and probably the neutral particle-surface interactions. How well this lowers drag requires further study. The alternating currents associated with this electron transport and the potentials reached depend upon a number of variables. Applied dc voltages can be used for additional biasing, but any charges building up on an insulating surface, will be like charging a capacitor. We are aware of three refractory ceramics that are electrical conductors that might be employed here: (1) Yttria stabilized Zr, only conducts at elevated temperature with oxygen ions as charge carriers, (2) Ti diboride, exhibits conductivity with electrons as charge carriers with resistivity comparable to Fe, and

(3) boron carbide which is difficult to get and to shape. Ti diboride is the material we will concentrate on first. It is strong, hard, and has moderate density (mp 2,850 °C, density 4.45 g/cc) Unfortunately, based on literature, its continuous use temperature limit is specified as being between 1,000–2,000 °C. Most likely, the lower limit is associated with effects of oxidation, however, our need for a better understanding of how the TiB_2 changes at high temperature prompts us to investigate such changes very sensitively by measuring the electrical resistance of thin films in situ and other properties as a function of time and temperature. B_4C is electrically conductive and is also high-temperature resistant (mp 2,350 °C). It is strong, hard, and has low density as well, sg 2.52. If refractory conductors can be demonstrated to operate at required temperatures (1,500–2,000 °C, considered desirable), then biasing of a dc nature will make sense; otherwise, attention to maintaining a bias by RF or other ac sources will need to be investigated more thoroughly. With this approach, two exposed electrodes would be made at the surface. This limits things somewhat, since only negative biasing seems reasonable at both electrodes associated with the RF source. If both electrodes are placed on the leading surface, however, both of those surfaces will become negatively biased dc-wise, just 180° out of phase for the RF-component, which will be so rapid for the high frequencies used that ion-surface interactions will scarcely notice that component. Even assuming that electrons cannot be conducted (we have several concepts to test for relative biasing) from the leading to trailing surfaces, then appreciable changes in the flow around the structure should occur, as noted in the drag reduction studies on hypervelocity aircraft.

Extending the distance over which aerodynamic braking slows the craft, while dissipating energy in the atmosphere, will reduce the peak heating that is of primary concern. Our contribution will be to investigate the mechanisms involved, including any decreases to heating of the TPS surfaces under bombardment by plasma torches having an appropriate ionized atmosphere, as has been done to simulate effects on surfaces reentering the atmosphere from space. It appears that the maximum heating occurs shortly after impacting the boundary, near 100 Km, where a rapid change in density of Earth's atmosphere occurs. It should be noted that the effects will be subjective.

Plan

Only by testing can the concept be verified. Reentry simulation is best performed by a plasma arc torch such as is most often used by NASA for testing TPS materials. Such torches have selectability and adjustability of the composition of the gasses that impinge on the target surface. Test time on these torches is nearly impossible to obtain due to Return to Flight preparations. A demonstration of whether or not the concept is feasible is in order. To this end, a test rig using a several H–O torches and several home-brew arc plasma sources to reach high temperatures was employed in our lab. Prototype EBTPS's were tested in this crude test fixture. Figure 173 shows one of the first test articles made along the lines of figure 172. This was saved for testing after short-life test targets were used first. Candidate surface materials were carbon, TiB_2, and BC.

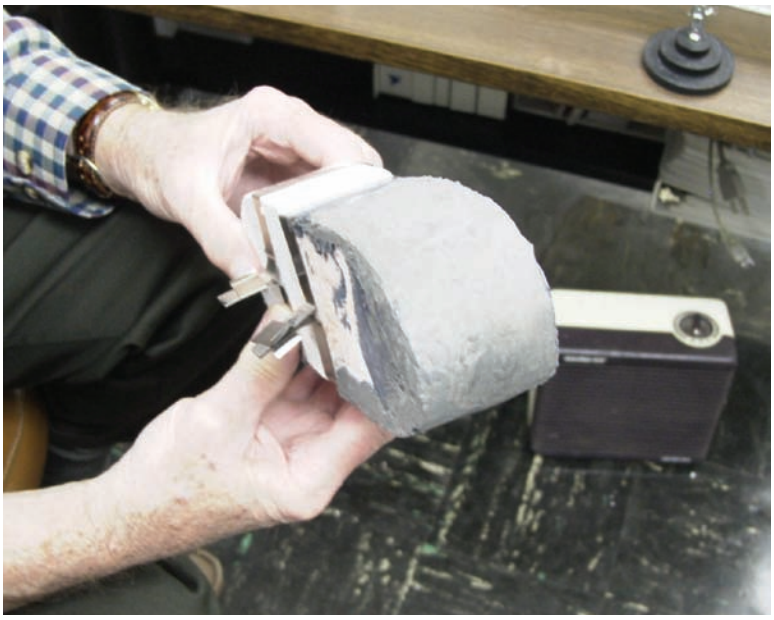

Figure 173. Prototype test article following the structure laid out in figure 172.

Figures 174 and 175 show a couple of the first test articles run under an H–O torch. The H–O torch should produce thermal plasma, as it offers the highest gas torch temperatures possible. During the first tests with the external mixing torch, shown in figures 175–177, an ohm meter showed conductivity of 100,000 ohms during torch operation. This was evidence of plasma formation and allowed us to proceed to the next step. The longevity of the prototype under thermal stress was not a concern at this time. What is paramount is the determination of whether properly applied electrical current to the TPS can reduce the surface temperature such that the TPS life is prolonged. Although a coating of TiB_2 was planned as the protective and conductive TPS outer surface, it was decided to show feasibility using relatively robust carbon in the form of graphite as the model of the TPS. Testing in air at these temperatures causes these graphite targets to burn away, or through, in several minutes, but not before reaching up to 2,000 °C. The test arrangement planned is shown in figures 175–177.

Figure 174. First torch test article of Grafoil (C) shaped over insulating brick. Lifetime of target was very limited and offered no measure of bias effects.

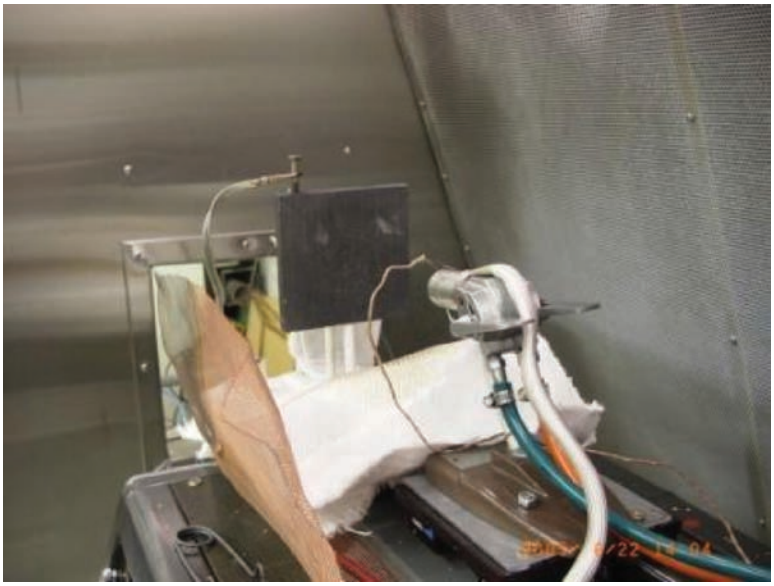

Figure 175. Plate of graphite under test with H–O torch. Longer target life was found, but no measurable bias influence. Likely very low plasma yield.

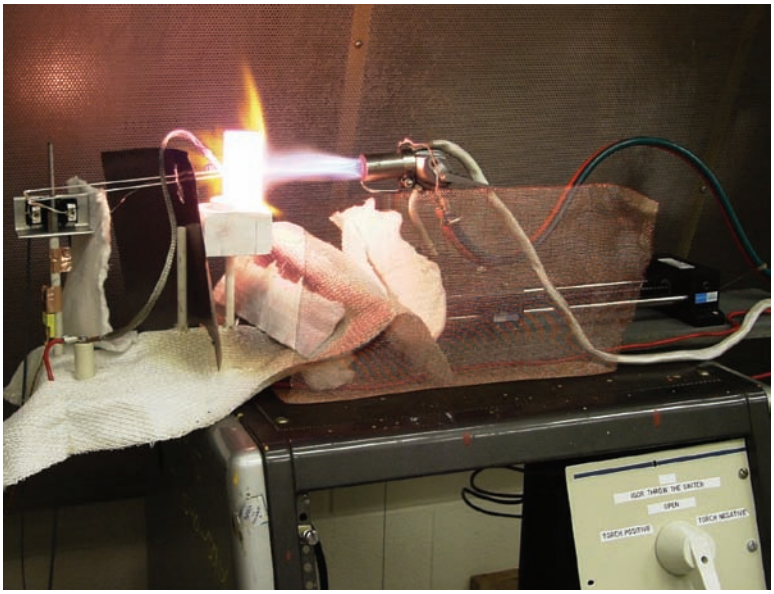

Figure 176. Graphite TPS leading-edge test article under test with H–O torch. No measurable bias influence. Poor plasma yield was the problem.

Figure 177. A close-up view of the test in figure 175 showing thermocouple placement. Two B-type and one K-type thermocouples were used.

The best results of cooling were obtained by using an H–O torch (fig. 178), but different results came about from using a home-built plasma torch using a TIG welding unit. This latter device provided a 4-kW plasma beam that could easily cut through copper and tungsten.

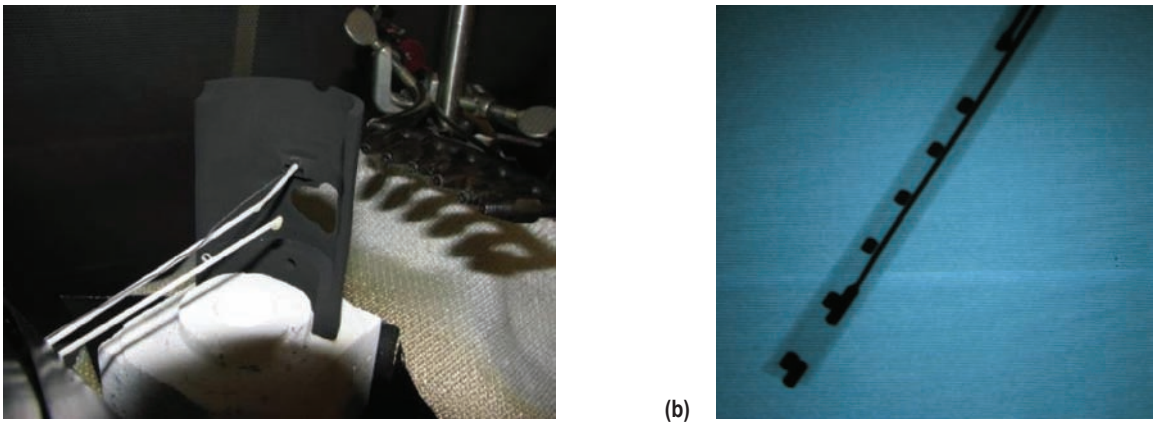

Figure 178. (a) Backside of test article after torch test using multiheaded H–O torch. Alumina sheathed thermocouples were melted (over 2,000 °C) and (b) x-ray radiograph of the B-type thermocouple after this test. The platinum wires inside were melted well back (over an inch) from the tip. This test did produce measurable bias influence with the greater plasma yield.

Results

There were no positive results until sufficient plasma formation could be achieved. Several config-urations of target and H_2/O_2 torches were tried with no measurable effects of protection by the applied bias until a multiheaded internal mixing H–O torch was used and its distance reduced to prevent plasma-ion recombination. Figure 179 shows one plot of the temperatures versus time and the bias voltage over top. No effect of bias can be seen here. Dilution by the surrounding air would be reduced by shortening the distance to the target. The mass of the target was also found to be a limitation since the high-TC graphite would cool the target at the torch impingement point. Smaller and thinner targets were employed to improve heating and increase sensitivity to the measurement. The risk was reduced sensitivity since the active surface area was lower. This would reduce interaction or residence time. Figures 180 and 181 show the final working configuration. These compromises were accounted for and at last the first measurable cooling effect from the applied DC bias was discovered. The small percentage of temperature change was masked by the high temperatures but after the temperature slope with time was calculated, coincidence of the bias voltage and the slopes were found. The cooling effect of 10-V positive bias amounted to ≈5° using the multiheaded torch. What was unexpected and a lesson learned was that the response to bias was not instantaneous, but lagged the bias voltage switch. Instead of a millisecond response, the thermal mass of the target showed a temperature change over a period of seconds (figs. 182–184). While not important for protection, this was important for interpretation of results.

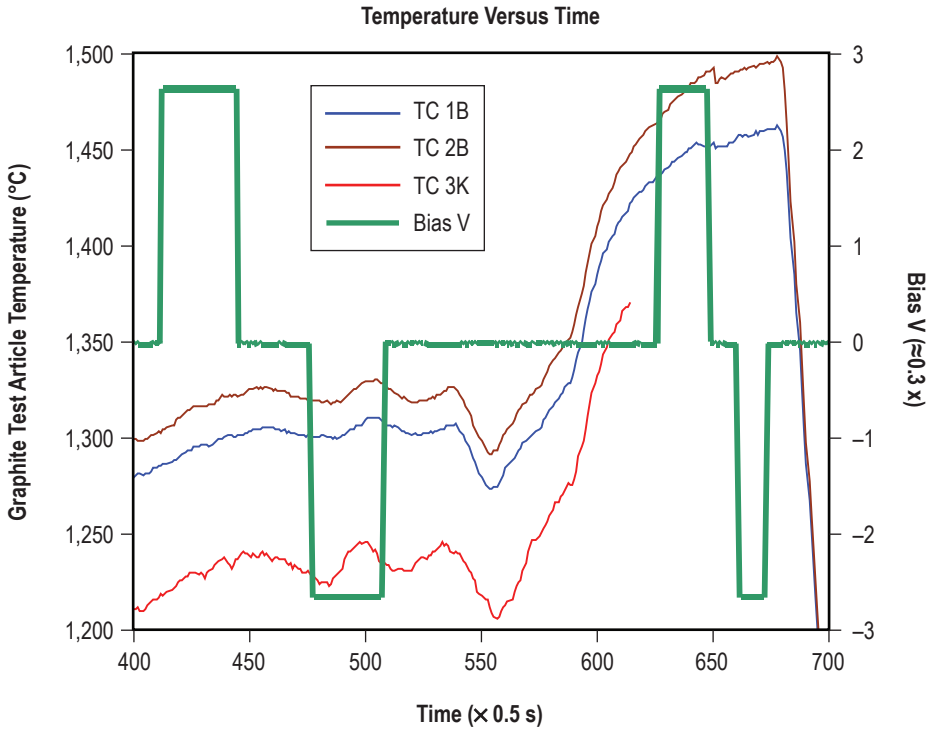

Figure 179. Temperatures obtained during a test run with the external mixing H–O torch. No influence of the bias is seen.

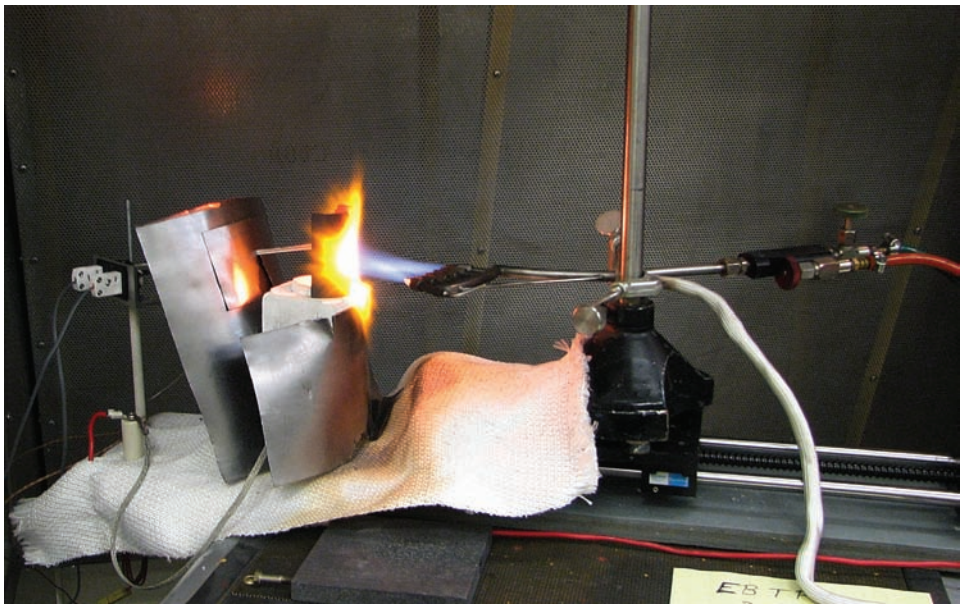

Figure 180. Multiheaded H–O torch and graphite target. This configuration produced positive results with the bias.

Figure 181. A close-up view of the target as it was heated by the torches.

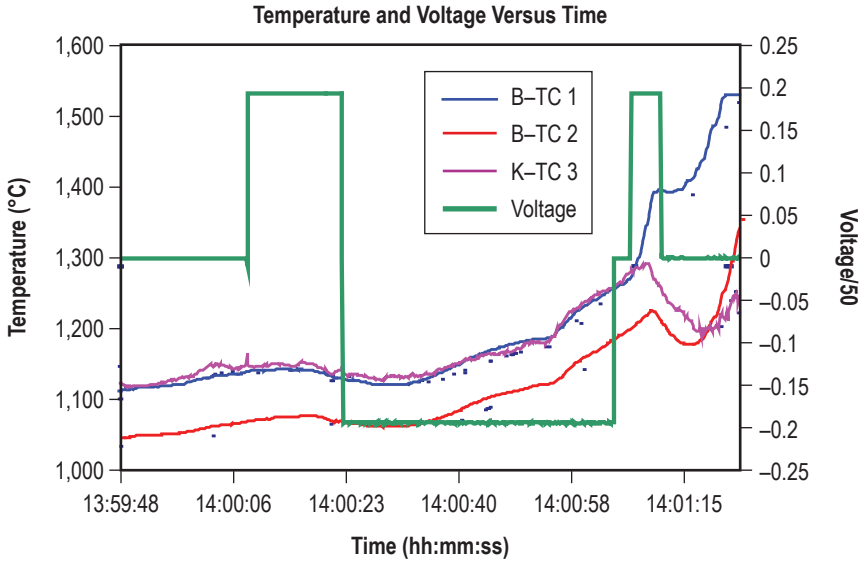

Figure 182. Segment from temperature plot with multiheaded torch showing temperature changes as bias applied.

Figure 183. Segment from derivative of temperatures plot showing transients in temperature as the bias is applied and removed. The magnitude of the derivative decreases over time as the positive bias was applied and increases once the bias was turned off.

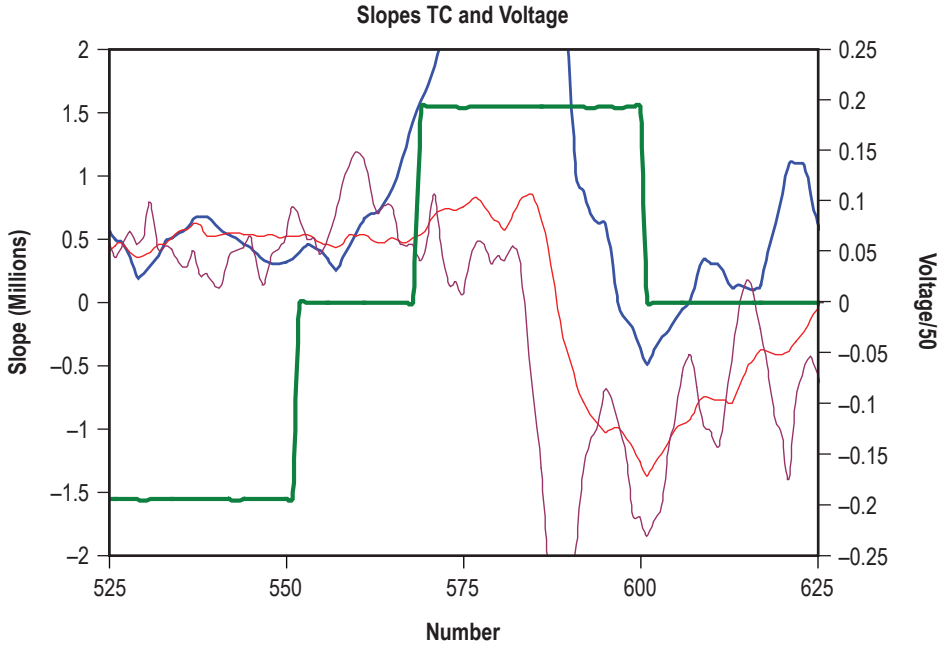

Figure 184. Another segment of the slope plots showing transients as in figure 183.

Figures 185 and 186 show our home-built plasma torch. The plasma gas was argon in this case. This differs from the plasma in the H–O torch which had oxygen ions in it. The target was a graphite rod of either 1/4-in OD or 3/8-in OD. Bias was applied from a car battery and showed impact on the target temperatures. The plasma drove the target to an equilibrium voltage of –9.4 V (no bias). A positive bias gave a significant heating effect. Since the negative bias, which should have shown a cooling effect, was only a few volts more than the equilibrium voltage, it seemed the next tests should include a higher bias voltage to better exceed the natural voltage cause by this torch.

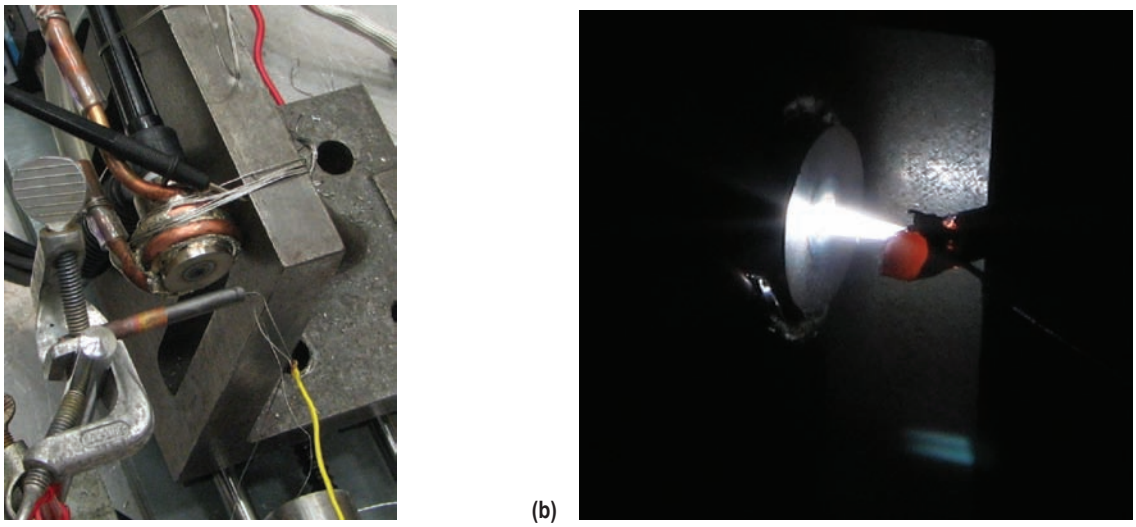

Figure 185. Home-built plasma torch made from TIG welding apparatus (a) shows the torch and the carbon rod target with thermocouples inserted into the end of the rod and (b) shows the torch in action.

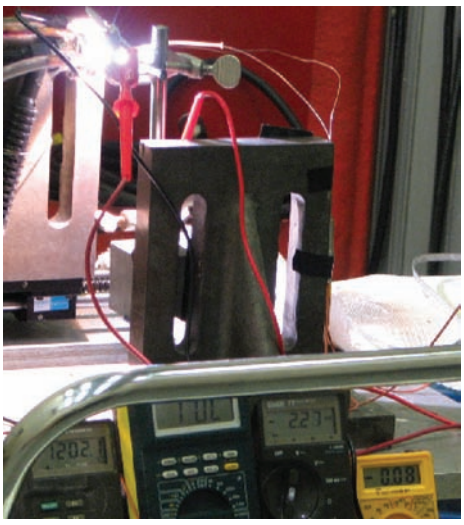

Figure 186. The plasma torch in action and the various meters used to collect the data. Two K-type thermocouples were employed and the bias current and voltage were monitored. The thermocouples only lasted a few runs or less due to the high temperatures and had to be replaced frequently.

Figure 187 shows the temperature plots taken from a video made during the test where the values in a spreadsheet were read off from the meters used to monitor each signal. The data acquisition system employed earlier was not available at the test site where the torch was built. Figure 188 shows the slope or derivative plots of temperature. There are obvious changes in temperature as the bias goes positive and perhaps there is an influence on temperature with the small negative bias. This is further proof that an applied bias influences the TPS temperature and that the working premise is valid.

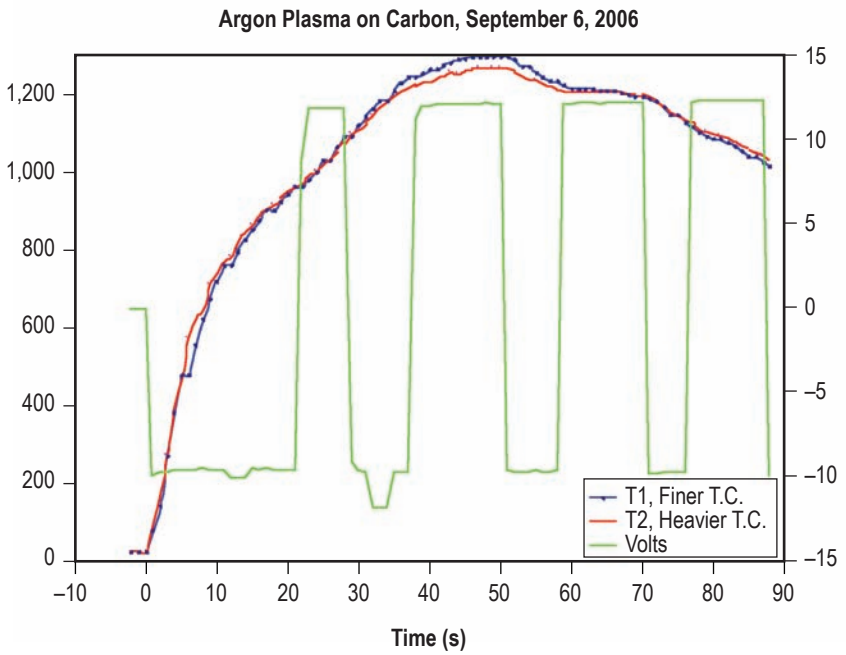

Figure 187. Temperature plots of graphite rod target in the pencil beam of the home-built plasma torch. Some variations of the temperature can be detected as the bias is applied.

Due to time and funds available, a vacuum plasma test chamber could not be developed, therefore the RF bias technique was not attempted.

Helps Advance Exploration. Feasibility of the technology was demonstrated—ramifications: Need to see how different gasses and pressures influence the quality of cooling and tune for other planetary destinations. Need to make comparative tests of protective ability using side-by side tests with and without bias.

DC bias of a few volts did reduce the TPS temperature when exposed to high-temperature plasma that provides longer TPS material life, improved reliability, and potential weight savings of spacecraft.

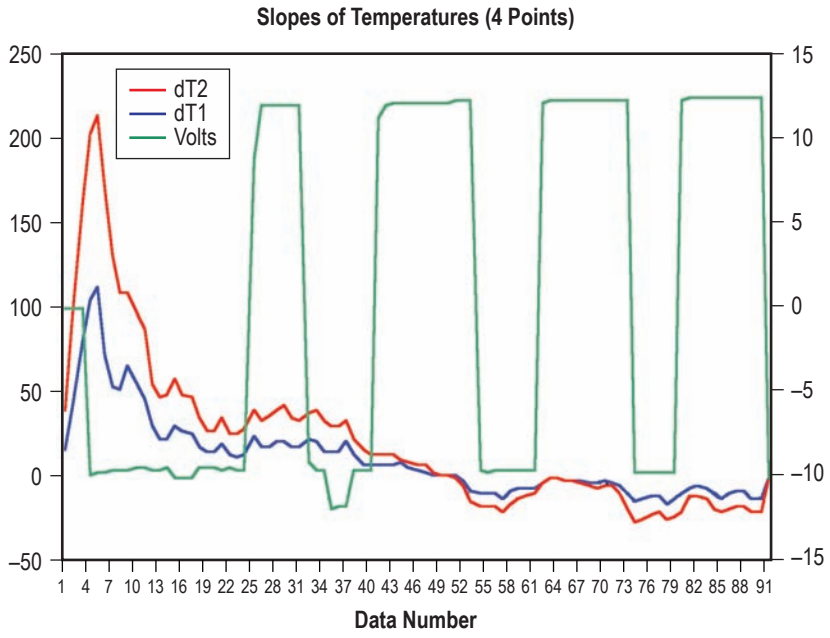

Figure 188. Slopes of temperatures versus time plotted with the bias voltage. There are clearly seen places where the temperature drops and rises (positive slope=temperature rising, negative slope=cooling, lower slope=cooling, higher slope=heating) as the bias was lowered and raised in voltage. The zero bias or equilibrium voltage was –9.7 V due to the plasma impingement.

Future Work and Direction

Testing should be continued in a vacuum plasma chamber capable of better simulating the reentry conditions. More complex testing and development of RF biasing should be initiated. Target construction and power distribution are the challenges here. Testing can only be done in a vacuum chamber.

The amount of protection the biasing offers is still to be learned. Different materials may benefit more and in different ways from the bias, depending on the material being tested and the fidelity of the plasma reentry simulation.

Variable control or modulation of the bias may offer further enhancement of the technique and provide power and weight savings. The addition of novel supporting technologies, like supercapacitors, provides synergistic opportunities to enable the new technology and offer options in spacecraft design as shown in figure 189.

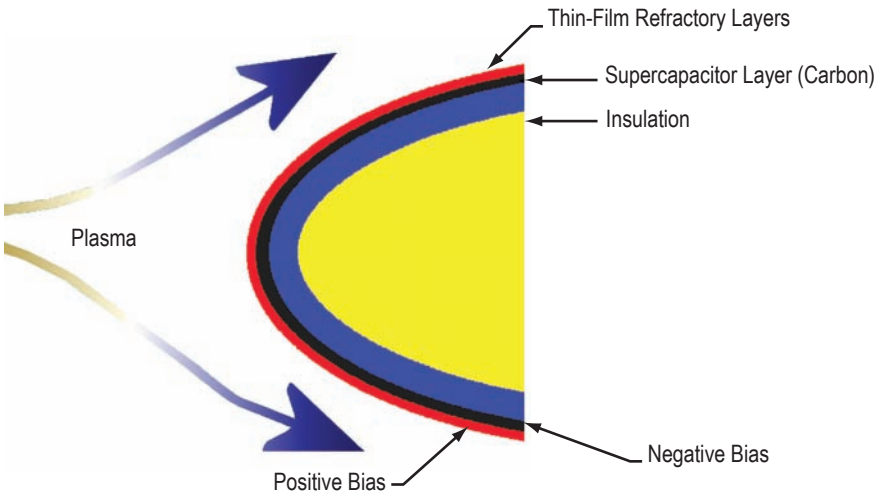

Figure 189. EBTPS concept using supercapacitor structure made from carbon as the liner for the TPS. This offers a means of providing the bias current during reentry whereas the capacitor was slowly charged on the way to the planet using a small power source or solar cells.

Discussion About Particle/Surface Interactions by Palmer Peters. The degradation of spacecraft materials is strongly influenced by particle/surface interactions. Most notable, and now better understood, are the effects of AO on LEO spacecraft. Oxygen atoms, produced by solar UV at such altitudes, represent ≈95 percent of the local environment and, even without adding the high impact orbital speed, will strongly oxidize combustible materials at RT. Ionized components were found to produce negligible effects in LEO studies, compared to neutral oxygen atoms. Ground-based simulations of LEO conditions were found to be very difficult with neutrals, however. To attain thermal velocities equivalent to the orbital velocity requires temperatures exceeding the melting point of any material known, and mechanically imparting such velocities cause failures of any turbine blades or other structures well before reaching such velocities. However, velocities produced by accelerating charged oxygen atoms with electric fields to orbital velocity creates a kinetic energy corresponding to only 5.08 eV, hardly a high-energy particle. Controlling particle direction and neutralizing it before impact represented additional problems, since atom ions repel and fly apart from a beam unless electrons are injected and a neutral plasma is maintained. Neutralization without modifying other characteristics is also not very simple. To some extent, just exposing materials to an oxygen discharge is a good indicator of what to expect, except for effects of ram and wake directions in orbit and the many active species degrading materials in such plasmas, including free radicals from the decomposed materials. Such differences from LEO conditions can give false indications of susceptibility to LEO degradation. While it was noted that biasing had little effect in LEO because of the lack of ions, it is recognized that this is not the case during reentry conditions. During maximum heating, the most stressful period for leading-edge materials, plasma is formed, as evidenced by the loss of signals (LOS) from an inability to transmit through a conducting medium, flashing bright lights, intense reactions, heating, etc. It is recognized that under these conditions there is a potential that 6-V bias of correct polarity could stop the impact of an undesired atom, or 12 V could stop a singly charged molecular ion. Not knowing the exact composition of the reentry plasma presents

similar problems to simulating LEO conditions that ultimately required flight experiments. However, many characteristics of the LEO results were correctly predicted and observed. It is our hypothesis that similar benefits will arise from understanding the characteristics of the charged environment during maximum stress on the leading-edge materials that now must operate with a small safety factor for known materials that are in use. Any temperature reduction of such leading edges is very desirable.

The following are several results that suggest our hypothesis is correct:

- Applying RF bias to models of hypervelocity aircraft in wind tunnel tests had been reported to reduce drag, which was not explained and was even questioned. These results, however, can be explained by the difference in mobility of electrons and ions. The low-mass electrons can be accelerated up to their mean-free-path length in both directions during an RF cycle, while the heavy ions respond very little.

- If not grounded, an electrode will become overpopulated with electrons during the half-cycle driving them to the electrode. Thus, the electrode will become a negatively charged cathode, which attracts positive ions, but repels negatively charged particles, preventing them from hitting the surface. Oxygen and likely nitrogen, both of which have nearly filled valence shells (6 of 8 for oxygen, 5 of 8 for nitrogen) have strong affinities for electrons and attempt to take them from any source, producing oxidation of the source material. The oxygen can thus become negative in the plasma, and depending on available electrons, the nitrogen also. There is evidence of this in argon sputtering films with oxygen dosed in. The Ar ion is positive and bombards the cathode target, sputtering it as a film on a substrate attached to a grounded anode. However, the oxygen bombards the anode, sputtering the film back off of the substrate, indicating the oxygen is in a negative state.

- Using an O–H torch to simulate the high temperature and look for effects of bias gave a very small effect of cooling when positive bias was applied. The low density of ions compared to a plasma discharge, and the slow time constant of the observed effect suggest that a slowly charging capacitance was involved before maximum effect was observed, however, unless hydrogen (+) ions had a higher mobility and reducing effect, it is not clear why more negative O and electrons would not be striking the surface under positive bias, causing heating.

- Pure Ar was also used as part of the study because our plasma torch gouged the targets so rapidly with oxygen present that their destruction, as well as the destruction of our plasma torch parts, limited the time available to do any measurements. The results were opposite of those for the O–H torch, since a 12-V positive applied bias caused an increase in temperature. Ar (+) ions were repelled by the positive target, but oxygen (–) and electrons were attracted. This would seem to increase bombardment and oxidation, and thus heating, as observed again with a time constant of over 10 sec to approach maximum effect, as if some charging of the surface (capacitance) is involved. In addition, an ungrounded target floated to ≈9 V negative when bombarded with the argon plasma source, suggesting that either negative particles predominantly reached the surface, or that secondary yields of positive ions striking the surface exceeded one.

It is apparent that our plasma source needs to be characterized more thoroughly if we are to investigate the kinetics and better understand what is going on. We are at a very early stage of producing appropriate plasma beams, characterizing them, measuring the effects of their surface bombardment with

adjustable biases, and floating. It is too early to make definitive statements concerning what is happening with any certainty.

Estimating the effects during reentry conditions depends strongly on a number of parameters including the reacting species concentrations when the velocity is known (to calculate flux), the fraction that are charged and with which polarity (to study bias effects), the temperatures of the leading surface and the gas or plasma in front of it (for radiation transfer ($\sigma T4$) considerations), the deceleration, and change in altitude rates (for energy change considerations) to name a few. A surprising lack of data seemed to exist representative of a reentering Shuttle for this study and considerable time was expended gleaning information from the Columbia Accident Investigation Board report and other less common technical sources (table 22). Any better data available would be appreciated.

Table 22. Calculations of atmospheric environments.

Below 30,000 ft the atmospheric pressure is supposed to vary as:
D(Y)=exp((–3.211*10^–5)*Y), where Y is altitude in ft.
Above 30,000 ft the atmospheric pressure is supposed to vary as:
D(Y)=1.6114*exp((–4.771*10^–5)*Y), where Y is altitude in ft.
above is based on empirical fit to data given by Lewis H. Abraham in Baumeister and Marks (1967, Chap. 11), as discussed in
William R. Bennett, Jr., Scientific and engineering problem solving with the computer, Prentice-Hall, Inc., Englewood Cliffs, New Jersey (1976).

Y (ft)	Y (km)	EXP	D(Y),fraction. of Sea Level	≈Molecules (cc)	D(Y) (g/cc)	D(Y) (kg/cu m)
0	0	0	1×10	2.460×10^{19}	1.257×10^{-3}	1.257×10
1,000	0.3048	–0.03211	9.684×10^{-1}	2.382×10^{19}	1.217×10^{-3}	1.217×10
2,000	0.6096	–0.06422	9.378×10^{-1}	2.307×10^{19}	1.179×10^{-3}	1.179×10
3,000	0.9144	–0.09633	9.082×10^{-1}	2.234×10^{19}	1.142×10^{-3}	1.142×10
4,000	1.2192	–0.12844	8.795×10^{-1}	2.163×10^{19}	1.105×10^{-3}	1.105×10
5,000	1.524	–0.16055	8.517×10^{-1}	2.095×10^{19}	1.071×10^{-3}	1.071×10
10,000	3.048	–0.3211	7.254×10^{-1}	1.784×10^{19}	9.118×10^{-4}	9.118×10^{-1}
15,000	4.572	–0.48165	6.178×10^{-1}	1.52×10^{19}	7.765×10^{-4}	7.765×10^{-1}
20,000	6.096	–0.6422	5.261×10^{-1}	1.294×10^{19}	6.614×10^{-4}	6.614×10^{-1}
25,000	7.62	–0.80275	4.481×10^{-1}	1.102×10^{19}	5.633×10^{-4}	5.633×10^{-1}
30,000	9.144	–0.9633	3.816×10^{-1}	9.388×10^{18}	4.797×10^{-4}	4.797×10^{-1}
35,000	10.668	–1.66985	3.034×10^{-1}	7.463×10^{18}	3.814×10^{-4}	3.814×10^{-1}
40,000	12.192	–1.9084	2.390×10^{-1}	5.879×10^{18}	3.004×10^{-4}	3.004×10^{-1}
45,000	13.716	–2.14695	1.883×10^{-1}	4.632×10^{18}	2.367×10^{-4}	2.367×10^{-1}
50,000	15.24	–2.3855	1.483×10^{-1}	3.649×10^{18}	1.864×10^{-4}	1.864×10^{-1}
55,000	16.764	–2.62405	1.168×10^{-1}	2.874×10^{18}	1.469×10^{-4}	1.469×10^{-1}
60,000	18.288	–2.8626	9.204×10^{-2}	2.264×10^{18}	1.157×10^{-4}	1.157×10^{-1}
65,000	19.812	–3.10115	7.251×10^{-2}	1.784×10^{18}	9.114×10^{-5}	9.114×10^{-2}
70,000	21.336	–3.3397	5.712×10^{-2}	1.405×10^{18}	7.18×10^{-5}	7.180×10^{-2}
75,000	22.86	–3.57825	4.5×10^{-2}	1.107×10^{18}	5.656×10^{-5}	5.656×10^{-2}
80,000	24.384	–3.8168	3.545×10^{-2}	8.72×10^{17}	4.456×10^{-5}	4.456×10^{-2}

Table 22. Calculations of atmospheric environments (Continued).

Y (ft)	Y (km)	EXP	D(Y),fraction. of Sea Level	≈Molecules (cc)	D(Y) (g/cc)	D(Y) (kg/cu m)
85,000	25.908	–4.05535	2.792×10^{-2}	6.869×10^{17}	3.51×10^{-5}	3.51×10^{-2}
90,000	27.432	–4.2939	2.2×10^{-2}	5.412×10^{17}	2.765×10^{-5}	2.765×10^{-2}
95,000	28.956	–4.53245	1.733×10^{-2}	4.263×10^{17}	2.178×10^{-5}	2.178×10^{-2}
100,000	30.48	–4.771	1.365×10^{-2}	3.358×10^{17}	1.716×10^{-5}	1.716×10^{-2}
110,000	33.528	–5.2481	8.472×10^{-3}	2.084×10^{17}	1.065×10^{-5}	1.065×10^{-2}
120,000	36.576	–5.7252	5.258×10^{-3}	1.293×10^{17}	6.609×10^{-6}	6.609×10^{-3}
130,000	39.624	–6.2023	3.263×10^{-3}	8.026×10^{16}	4.101×10^{-6}	4.101×10^{-3}
140,000	42.672	–6.6794	2.025×10^{-3}	4.981×10^{16}	2.545×10^{-6}	2.545×10^{-3}
150,000	45.72	–7.1565	1.257×10^{-3}	3.091×10^{16}	1.579×10^{-6}	1.579×10^{-3}
160,000	48.768	–7.6336	7.798×10^{-4}	1.918×10^{16}	9.802×10^{-7}	9.802×10^{-4}
170,000	51.816	–8.1107	4.839×10^{-4}	1.19×10^{16}	6.083×10^{-7}	6.083×10^{-4}
180,000	54.864	–8.5878	3.003×10^{-4}	7.388×10^{15}	3.775×10^{-7}	3.775×10^{-4}
190,000	57.912	–9.0649	1.864×10^{-4}	4.585×10^{15}	2.343×10^{-7}	2.343×10^{-4}
200,000	60.96	–9.542	1.157×10^{-4}	2.845×10^{15}	1.454×10^{-7}	1.454×10^{-4}
225,000	68.58	–10.7348	3.509×10^{-5}	8.632×10^{14}	4.411×10^{-8}	4.411×10^{-5}
227,000	69.1896	–10.8302	3.189×10^{-5}	7.846×10^{14}	4.009×10^{-8}	4.009×10^{-5}
230,000	70.104	–10.9733	2.764×10^{-5}	6.8×10^{14}	3.475×10^{-8}	3.475×10^{-5}
240,000	73.152	–11.4504	1.715×10^{-5}	4.22×10^{14}	2.156×10^{-8}	2.156×10^{-5}
250,000	76.2	–11.9275	1.065×10^{-5}	2.619×10^{14}	1.338×10^{-8}	1.338×10^{-5}
260,000	79.248	–12.4046	6.606×10^{-6}	1.625×10^{14}	8.304×10^{-9}	8.304×10^{-6}
270,000	82.296	–12.8817	4.1×10^{-6}	1.009×10^{14}	5.153×10^{-9}	5.153×10^{-6}
280,000	85.344	–13.3588	2.544×10^{-6}	6.259×10^{13}	3.198×10^{-9}	3.198×10^{-6}
290,000	88.392	–13.8359	1.579×10^{-6}	3.884×10^{13}	1.985×10^{-9}	1.985×10^{-6}
300,000	91.44	–14.313	9.798×10^{-7}	2.41×10^{13}	1.232×10^{-9}	1.232×10^{-6}
310,000	94.488	–14.7901	6.081×10^{-7}	1.496×10^{13}	7.643×10^{-10}	7.643×10^{-7}
320,000	97.536	–15.2672	3.773×10^{-7}	9.283×10^{12}	4.743×10^{-10}	4.743×10^{-7}
330,000	100.584	–15.7443	2.342×10^{-7}	5.761×10^{12}	2.944×10^{-10}	2.944×10^{-7}
340,000	103.632	–16.2214	1.453×10^{-7}	3.575×10^{12}	1.827×10^{-10}	1.827×10^{-7}
350,000	106.68	–16.6985	9.019×10^{-8}	2.219×10^{12}	1.134×10^{-10}	1.134×10^{-7}
360,000	109.728	–17.1756	5.597×10^{-8}	1.377×10^{12}	7.035×10^{-11}	7.035×10^{-8}
370,000	112.776	–17.6527	3.473×10^{-8}	8.544×10^{11}	4.366×10^{-11}	4.366×10^{-8}
380,000	115.824	–18.1298	2.155×10^{-8}	5.302×10^{11}	2.709×10^{-11}	2.709×10^{-8}
390,000	118.872	–18.6069	1.338×10^{-8}	3.291×10^{11}	1.681×10^{-11}	1.681×10^{-8}
400,000	121.92	–19.084	8.301×10^{-9}	2.042×10^{11}	1.043×10^{-11}	1.043×10^{-8}

Note: the above calculations give reasonable agreement to 100 km, but above 125 km the composition of the atmosphere begin to change drastically as atomic oxygen starts to increase toward dominance, and solar activity, diurnal, and seasonal effects produce extremes of low and high boundaries for the effects on concentration, density, and pressure. For altitudes above 100 km it is recommended that attention be given to "Aerospace Environment," a chart of properties by Air Force Cambridge Research Laboratories, L.G. Hanscom Field, Bedford, Massachusetts 01730, or other more definitive source for concentrations, pressures, etc.

Addendum to Electronically Biased Thermal Protection System

Abstract

The plan is to reduce spacecraft TPS surface temperatures during planetary atmosphere entry (aerocapture) to increase survivability and lower avionics temperatures. The present study investigates the feasibility that a reduction of TPS temperature is possible by preventing reentry plasma from interacting with the TPS using an applied electric bias. Follow-on study would be to justify EBTPS as a weight-saving measure (given additional weight required to store and deliver power). We report success by achieving the proof-of-concept using different torches to simulate reentry heating. Using a plasma torch fabricated from a welding apparatus, to generate the larger amounts of plasma desired, up to 100 degrees cooling was achieved on carbon TPS material. Testing conditions were never sufficiently faithful to the true environment of reentry. Testing in a vacuum chamber with higher power plasma sources of the proper gas composition will magnify the degree of protective cooling produced by the EBTPS technique.

Description and Rationale

In an attempt to lower the peak heating and reduce the magnitude of some of the reentry challenges, we have proposed to modify plasma surface interactions that could occur at that time. The primary mode of accomplishing this is by voltage biasing the TPS surface in an attempt to change the composition of the plasma sheath, its flow around the surface, and hopefully the rate of energy transfer between the sheath and the surface. Practical limits of proof of the benefits of the technique are limited to in situ measurement of the TPS backside temperatures as a bias is applied. What many people do not realize is that the high temperatures of reentry are not alone the cause of damage to the spacecraft aero shield. Torch testing is commonly used to test TPS materials and is no exception here. Besides simulating the temperatures of reentry, the bigger facilities properly simulate the heat load and the gas compositions of reentry. It is in fact the high-heat load that damages the TPS with high-velocity plasma flow (multi-Mach number) and not so much the temperature. Thus, we would like to have had access to one of these torch facilities to test the bias concept. As it turned out, most of the work and time reported here was about duplicating the test conditions without access to a proper torch facility. The generic EBTPS setup is shown in figure 190. Voltages required to accomplish this did not have to be very high (tens of volts), but the currents required, could be significant. Of course alternating fields could produce displacement currents.

Testing requires simulation of reentry plasma heating over 1,200–1,650 °C. The majority of this effort was creating the test conditions (plasma torch, targets) and making measurements. For this addendum, all additional work reported was from the plasma torch we designed and built ourselves in lieu of having access to a major facility. This offered complete control over the process, but it also somewhat compromised the range of data that could have been collected.

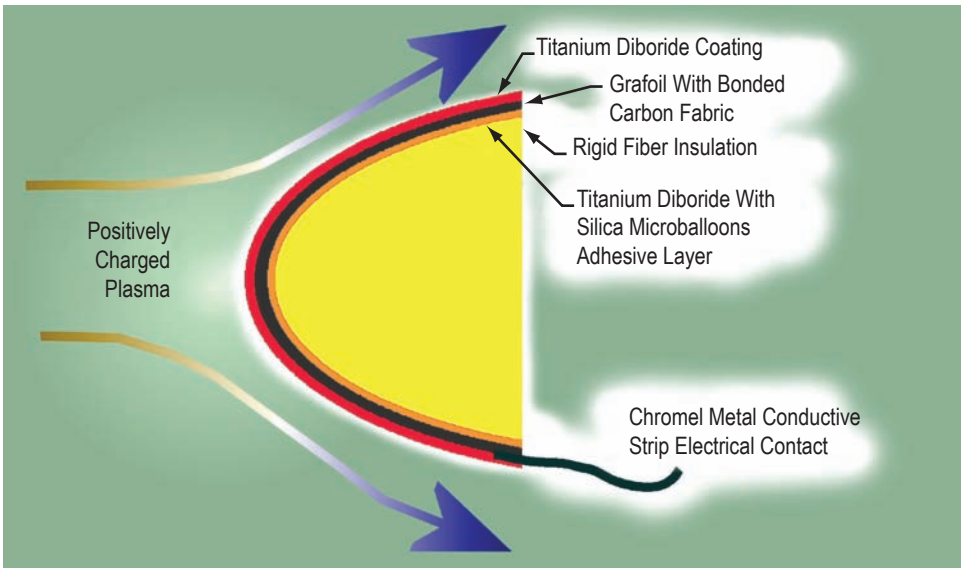

Figure 190. Generic schematic of the EBTPS as a leading-edge structure.

Atmosphere/Spacecraft Interactions and Electronically Biased Thermal Protection System

We are very fortunate that the Earth has its present mass, which is large enough to prevent all but the lightest gas from having any opportunity of escaping into space, yet low enough to have attainable orbital and escape velocities. In the absence of cataclysmic events, it is highly unlikely that much mass escapes from Earth's surface, but if Earth was appreciably more massive, rocket equations show that space travel would be impractical. For Earth's present mass, designing spacecraft to launch into space and reenter safely presents challenges that were only overcome some 50 yr ago. Even for reentry of an orbiting spacecraft, the orbital velocity is sufficiently high to cause severe heating of leading surfaces, and the velocity will be even higher if the spacecraft returns from a distant voyage (approximately the escape velocity without retro firing rockets). Both physical and chemical interactions are dependent upon the atmospheric constituents and the materials of the leading edges of the spacecraft. For Earth, Mars, and other bodies feasible for atmospheric entry and landing, the molecular masses of the atmospheres and velocities of entering spacecraft, relative to the molecules, typically represent too low a kinetic energy per collision to cause direct physical damage to the surface ($1/2\ mv^2$ for a CO_2 molecule impacting a surface with a relative velocity of 7.7 km/s is $\frac{1}{2}*(0.044/6.02\times10^{23})*(7{,}700*7{,}700) = 2.17\times10^{-18}$ joule, or 13.5 eV, while sputtering or knocking atoms off of the surface by impact, even for the highest yield materials begins closer to 40 eV and generally closer to 90 eV). The above calculation is based on a velocity for LEO and molecular carbon dioxide (44 AMU), which is a heavier constituent of the atmosphere. AO, just above the discernible atmosphere boundary, where orbiting is feasible, gives 5 eV for the same calculation using 16 AMU for its mass. Molecules of nitrogen and oxygen and Ar atoms would give proportionally larger masses and kinetic energies, but still less than for carbon dioxide. While such impacts do not physically knock atoms from the surface like billiard balls, the hypervelocity involved corresponds to thermal velocities associated with temperatures of ≈11,000 K per eV, i.e. kT≈eV, where k, Boltzmann's constant is 1.38×10^{-23} joule per K and 1 eV = 1.6×10^{-19} joule. Thus, spacecraft colliding with AO in LEO resembles being impacted by atoms with a peak ram velocity corresponding to a temperature of

≈55,000 K, but with a Maxwell-Boltzmann distribution within the local gas corresponding to ≈600 K to ≈1,800 K, depending on whether solar minimum to solar maximum activity is in effect for heating the neutral portion of the atmosphere (the orbital velocity would be about 8 times the average velocity associated with a 1,000 K atmosphere corresponding to an average solar activity and diurnal effects). The ion and electron densities in the thermosphere are orders of magnitude lower than for the neutrals and represent much lower fluxes to the surface (however, during reentry conditions plasmas are produced). Thus, the impinging atoms have a cigar-shaped distribution, not quite collimated into a beam with divergence somewhat described by radius being ≈1/8 the length, and most of the impacts are not far from normal incidence for surfaces facing the orbital direction.

For typical gas particles striking a stationary surface, the distribution in incidence angles is cosine, because that is how the surface area appears to the incoming particles (normal incidence sees the full area, but atom incidents perpendicular to the normal do not pass through the surface area (cosine 90 is zero and so is the flux)). Such impacts, even for moderate velocities, are assumed to land on the surface, be adsorbed, and come into equilibrium with the temperature of the surface and if desorbed, come off with velocities associated with the surface temperature, with the cosine distribution in the opposite velocity direction. Such particles are fully accommodated by the surface and this allows for appreciable energy transfer if incident kinetic energy and emitted kinetic energies are greatly different (as with the hypervelocity impacts and thermally emitted atoms or molecules discussed here). As velocities become higher, the residence times on the surface during collisions approach the period of lattice vibration, and then become less, resulting in fewer particles being accommodated. In principle, one might envision atoms eventually striking smooth surfaces and specularly reflecting like light rays, with reflected angles equal to incidence angles. For high-energy beam particles, this is somewhat true, except the reflected angles are slightly greater than the incident angles (supraspecular). Understanding such interactions is desirable, especially under free molecule conditions (low density, orbital region), because a specularly reflected particle would correspond to a perfectly elastic collision, exchanging no energy with the surface, but the normal component of momentum would be reversed on collision, creating nearly twice the momentum exchange that would occur for a similar collision where the particle is adsorbed and subsequently comes off the surface at a much lower random thermal velocity with direction described by a cosine. The result for nonaccommodation is that energy is not transferred (no heating), but nearly twice the momentum is transferred (doubles the drag). Because of the difficulties of duplicating orbital conditions for experiments, there are few published results from investigating such kinetics, however, there are indications that at orbital velocities there is not quite full accommodation and imperfect cosine distribution occurs during emission.

How materials selection might influence drag in orbit on a small percentage level is not known. To summarize, at LEO altitudes and circular orbit velocity, a linear velocity times the low density of the atmosphere can approximate initial collisions. Accommodation is believed to be incomplete with perhaps a slight skew toward supraspecular-emitted particles after collisions. Physical sputtering (material removal) is negligible, but oxidation and degradation of combustible surfaces represents a slow, long-term process damaging susceptible surfaces. In principle, an electrical bias of correct polarity and ≈6 V could repel and stop oxygen atom ions from striking leading surfaces, but natural ion densities appear too low to be of consequence. As the spacecraft reenters denser portions of the atmosphere, it passes from conditions that are free molecular, to a highly viscous gas requiring higher-order terms associated with the velocity, especially the velocity squared, in any attempt to model the drag on the

spacecraft, and since the hypervelocity greatly exceeds the speed of sound, a shock front envelops the nose of the orbiter, which normally is inclined close to 30° during reentry. Actual measurements and polynomial fits to the data are options under such conditions (table 23).

Table 23. Actual measurements and polynominal fits to the data based on empirical fit to data given by Lewis H. Abraham in Baumeister and Marks, as discussed in *Scientific and Engineering Problem-Solving With the Computer*, Prentice-Hall, Inc., Englewood Cliffs, NJ, 1976. (1967, Chap 11).

Below 30,000 ft the atmospheric pressure is supposed to vary as:
D(Y)=exp((–3.211*10^–5)*Y), where Y is altitude in ft.
Above 30,000 ft the atmospheric pressure is supposed to vary as:
D(Y)=1.6114*exp((–4.771*10^–5)*Y), where Y is altitude in ft.
above is based on empirical fit to data given by Lewis H. Abraham in Baumeister and Marks (1967, Chap. 11), as discussed in William R. Bennett, Jr., *Scientific and Engineering Problem-Solving With the Computer*, Prentice-Hall, Inc., Englewood Cliffs, NJ, 1976.

Y (ft)	Y (km)	EXP	D(Y), Fraction of Sea Level	≈Molecules (cc)	D(Y) (g/cc)	D(Y) (kg/cu m)
0	0	0	1×10	2.460×10^{19}	1.257×10^{-3}	1.257×10
1,000	0.3048	–0.03211	9.684×10^{-1}	2.382×10^{19}	1.217×10^{-3}	1.217×10
2,000	0.6096	–0.06422	9.378×10^{-1}	2.307×10^{19}	1.179×10^{-3}	1.179×10
3,000	0.9144	–0.09633	9.082×10^{-1}	2.234×10^{19}	1.142×10^{-3}	1.142×10
4,000	1.2192	–0.12844	8.795×10^{-1}	2.163×10^{19}	1.105×10^{-3}	1.105×10
5,000	1.524	–0.16055	8.517×10^{-1}	2.095×10^{19}	1.071×10^{-3}	1.071×10
10,000	3.048	–0.3211	7.254×10^{-1}	1.784×10^{19}	9.118×10^{-4}	9.118×10^{-1}
15,000	4.572	–0.48165	6.178×10^{-1}	1.52×10^{19}	7.765×10^{-4}	7.765×10^{-1}
20,000	6.096	–0.6422	5.261×10^{-1}	1.294×10^{19}	6.614×10^{-4}	6.614×10^{-1}
25,000	7.62	–0.80275	4.481×10^{-1}	1.102×10^{19}	5.633×10^{-4}	5.633×10^{-1}
30,000	9.144	–0.9633	3.816×10^{-1}	9.388×10^{18}	4.797×10^{-4}	4.797×10^{-1}
35,000	10.668	–1.66985	3.034×10^{-1}	7.463×10^{18}	3.814×10^{-4}	3.814×10^{-1}
40,000	12.192	–1.9084	2.390×10^{-1}	5.879×10^{18}	3.004×10^{-4}	3.004×10^{-1}
45,000	13.716	–2.14695	1.883×10^{-1}	4.632×10^{18}	2.367×10^{-4}	2.367×10^{-1}
50,000	15.24	–2.3855	1.483×10^{-1}	3.649×10^{18}	1.864×10^{-4}	1.864×10^{-1}
55,000	16.764	–2.62405	1.168×10^{-1}	2.874×10^{18}	1.469×10^{-4}	1.469×10^{-1}
60,000	18.288	–2.8626	9.204×10^{-2}	2.264×10^{18}	1.157×10^{-4}	1.157×10^{-1}
65,000	19.812	–3.10115	7.251×10^{-2}	1.784×10^{18}	9.114×10^{-5}	9.114×10^{-2}
70,000	21.336	–3.3397	5.712×10^{-2}	1.405×10^{18}	7.18×10^{-5}	7.180×10^{-2}
75,000	22.86	–3.57825	4.5×10^{-2}	1.107×10^{18}	5.656×10^{-5}	5.656×10^{-2}
80,000	24.384	–3.8168	3.545×10^{-2}	8.72×10^{17}	4.456×10^{-5}	4.456×10^{-2}
85,000	25.908	–4.05535	2.792×10^{-2}	6.869×10^{17}	3.51×10^{-5}	3.51×10^{-2}
90,000	27.432	–4.2939	2.2×10^{-2}	5.412×10^{17}	2.765×10^{-5}	2.765×10^{-2}
95,000	28.956	–4.53245	1.733×10^{-2}	4.263×10^{17}	2.178×10^{-5}	2.178×10^{-2}
100,000	30.48	–4.771	1.365×10^{-2}	3.358×10^{17}	1.716×10^{-5}	1.716×10^{-2}
110,000	33.528	–5.2481	8.472×10^{-3}	2.084×10^{17}	1.065×10^{-5}	1.065×10^{-2}
120,000	36.576	–5.7252	5.258×10^{-3}	1.293×10^{17}	6.609×10^{-6}	6.609×10^{-3}
130,000	39.624	–6.2023	3.263×10^{-3}	8.026×10^{16}	4.101×10^{-6}	4.101×10^{-3}

Table 23. Actual measurements and polynominal fits to the data based on empirical fit to data given by Lewis H. Abraham in Baumeister and Marks, as discussed in *Scientific and Engineering Problem-Solving With the Computer*, Prentice-Hall, Inc., Englewood Cliffs, NJ, 1976. (1967, Chap 11) (Continued).

Y (ft)	Y (km)	EXP	D(Y) Fraction of Sea Level	≈Molecules (cc)	D(Y) (g/cc)	D(Y) (kg/cu m)
140,000	42.672	–6.6794	2.025×10^{-3}	4.981×10^{16}	2.545×10^{-6}	2.545×10^{-3}
150,000	45.72	–7.1565	1.257×10^{-3}	3.091×10^{16}	1.579×10^{-6}	1.579×10^{-3}
160,000	48.768	–7.6336	7.798×10^{-4}	1.918×10^{16}	9.802×10^{-7}	9.802×10^{-4}
170,000	51.816	–8.1107	4.839×10^{-4}	1.19×10^{16}	6.083×10^{-7}	6.083×10^{-4}
180,000	54.864	–8.5878	3.003×10^{-4}	7.388×10^{15}	3.775×10^{-7}	3.775×10^{-4}
190,000	57.912	–9.0649	1.864×10^{-4}	4.585×10^{15}	2.343×10^{-7}	2.343×10^{-4}
200,000	60.96	–9.542	1.157×10^{-4}	2.845×10^{15}	1.454×10^{-7}	1.454×10^{-4}
225,000	68.58	–10.7348	3.509×10^{-5}	8.632×10^{14}	4.411×10^{-8}	4.411×10^{-5}
227,000	69.1896	–10.8302	3.189×10^{-5}	7.846×10^{14}	4.009×10^{-8}	4.009×10^{-5}
230,000	70.104	–10.9733	2.764×10^{-5}	6.8×10^{14}	3.475×10^{-8}	3.475×10^{-5}
240,000	73.152	–11.4504	1.715×10^{-5}	4.22×10^{14}	2.156×10^{-8}	2.156×10^{-5}
250,000	76.2	–11.9275	1.065×10^{-5}	2.619×10^{14}	1.338×10^{-8}	1.338×10^{-5}
260,000	79.248	–12.4046	6.606×10^{-6}	1.625×10^{14}	8.304×10^{-9}	8.304×10^{-6}
270,000	82.296	–12.8817	4.1×10^{-6}	1.009×10^{14}	5.153×10^{-9}	5.153×10^{-6}
280,000	85.344	–13.3588	2.544×10^{-6}	6.259×10^{13}	3.198×10^{-9}	3.198×10^{-6}
290,000	88.392	–13.8359	1.579×10^{-6}	3.884×10^{13}	1.985×10^{-9}	1.985×10^{-6}
300,000	91.44	–14.313	9.798×10^{-7}	2.41×10^{13}	1.232×10^{-9}	1.232×10^{-6}
310,000	94.488	–14.7901	6.081×10^{-7}	1.496×10^{13}	7.643×10^{-10}	7.643×10^{-7}
320,000	97.536	–15.2672	3.773×10^{-7}	9.283×10^{12}	4.743×10^{-10}	4.743×10^{-7}
330,000	100.584	–15.7443	2.342×10^{-7}	5.761×10^{12}	2.944×10^{-10}	2.944×10^{-7}
340,000	103.632	–16.2214	1.453×10^{-7}	3.575×10^{12}	1.827×10^{-10}	1.827×10^{-7}
350,000	106.68	–16.6985	9.019×10^{-8}	2.219×10^{12}	1.134×10^{-10}	1.134×10^{-7}
360,000	109.728	–17.1756	5.597×10^{-8}	1.377×10^{12}	7.035×10^{-11}	7.035×10^{-8}
370,000	112.776	–17.6527	3.473×10^{-8}	8.544×10^{11}	4.366×10^{-11}	4.366×10^{-8}
380,000	115.824	–18.1298	2.155×10^{-8}	5.302×10^{11}	2.709×10^{-11}	2.709×10^{-8}
390,000	118.872	–18.6069	1.338×10^{-8}	3.291×10^{11}	1.681×10^{-11}	1.681×10^{-8}
400,000	121.92	–19.084	8.301×10^{-9}	2.042×10^{11}	1.043×10^{-11}	1.043×10^{-8}

Note: the above calculations give reasonable agreement to 100 km, but above 125 km the composition of the atmosphere begin to change drastically as atomic oxygen starts to increase toward dominance, and solar activity, diurnal, and seasonal effects produce extremes of low and high boundaries for the effects on concentration, density, and pressure. For altitudes above 100 km it is recommended that attention be given to "Aerospace Environment," a chart of properties by Air Force Cambridge Research Laboratories, L.G. Hanscom Field, Bedford, Massachusetts 01730, or other more definitive source for concentrations, pressures, etc.

All values should be considered approximations. Above the arbitrary boundary of 400,000 feet (121.92 km) altitude defined as the Entry Interface, EI, the equations become too inaccurate to be acceptable, especially since solar activity, and other effects strongly influence this region, and other approximations are more appropriate.

The heating during entry into the atmosphere occurs after passing the discernible atmosphere boundary, called entry interface (EI), arbitrarily chosen at 400,000 ft or 121,920-m altitude, where the spacecraft speed has not significantly dropped as a result of drag. For orbiter reentries to Earth, gleanings from the Columbia Accident Investigation Board report and data assembled by Joels, et al. have been used here to obtain example conditions.[1,2] The maximum leading-edge temperature reported in the accident investigation was 1,649 °C, developed approximately 651 s after EI, stated as EI+651 s. This is about 100 °C higher than given in Joels' data. We do not know if this was an anomaly associated with the damaged Columbia or not. The maximum Hrate was about 86.72 BTU/ft^{2}s at that time and appears to remain above 80 BTU/ft^{2}s for ≈300 s at the highest heat flux zones of the leading edge in the double-shock region of the span at roughly 50-percent span. The leading-edge temperature remained above 1,500 °C for approximately 300 s also. The drag, relative deceleration, Hrate, and temperature should have been negligible between EI–1,719 s (deorbit burn) and EI+000 s (the EI).

To compare orbital-to-reentry conditions, the previous paragraph can be used to estimate that the drag in circular orbit near 300 km for mean solar and diurnal activity would be of order 10^{-6} torr pressure on leading surfaces and totally negligible on wake surfaces. This corresponds to about 2.8×10^{-6} lb/ft^2 pressure. The ambient pressure at 300 km is an order of magnitude lower, a high vacuum. Here, temperatures have to be regulated by thermal control surfaces, affecting radiation transfer, orientation relative to the sun, and other techniques, to avoid both excess and deficient service temperatures than those desired. According to Joels, et al., the retrofired orbital maneuvering system (OMS) burn for deorbiting occurs for 2–3 min slowing the orbiter to 16,465 mph. According to reference 1 Columbia retrofired for 2 min and 38 s. The next reported speed is 16,432 mph (7.346 km/s) at EI+323, which is consistent. It should be noted that as the altitude drops, the potential energy decrease (weight×altitude change × g) is being converted into other forms of energy, either kinetic energy in the form of increased spacecraft velocity or work done against the atmospheric drag, resulting in higher temperature air and spacecraft surfaces. When a terminal velocity is reached, the latter conversion will be the case. The mass of the reentering orbiter is ≈80,000 kg. Multiplying this by the acceleration of gravity (≈9.5 m/s^2 at 100-km altitude) gives a weight of 760,000 Newtons. Multiplying this by a loss of 9,041-m altitude in 426 s, or 21.223 m/s, gives ≈1.6×107 W of power conversion occurring from potential energy lost. The fact that the orbiter decreases in speed appreciably (from 7,434.8 m/s to 6,290.3 m/s) in the 426 s, instead of increasing, shows the tremendous increase in drag force, the work done through it, and the huge power transferred to heating the atmosphere and the leading surfaces (taking the difference in 1/2mv^2 gives $5.2\times10^{+10}$ joules for the 426 s, or 1.2×10^8 W dissipated by drag on the orbiter). This intense heating begins within min after the EI is reached, as evidenced by the communications blackout that results from the air being ionized starting at ≈50 miles (80.5 km) altitude and continuing for ≈12 min before exit of blackout at ≈34 miles (55 km) altitude, according to Joels, et al.[2] Maximum heating and leading-edge temperatures occur in the middle of this blackout period (≈70 km), where the undisturbed pressure is $\approx4\times10^{-2}$ torr (0.1 lb/ft^2 or psf), the mean free path is ≈1.5 cm, and the ambient temperature is ≈220 K in all directions. These conditions would produce a flux of ≈1,018 molecules/cm^{2}s through any imaginary plane. By comparison, the orbiter rams into this with a velocity still 6,722 m/s, and in 1 s a cm^2 area on the shock front sweeps through a volume that would ordinarily contain ≈7×1,023 molecules, which must be greatly compressed at stagnation (*Qbar* ≈41 psf?), with high shearing between planes within the gas being pushed aside and enormous heating (Hrate ≈9.848×105 W/m2?), as gleaned in table 24 and shown in figure 191. The difference between calculated power dissipated above and the reported Hrate may indicate a majority of the loss in potential and kinetic energies must be going into heating the atmosphere and the remainder, Hrate, into heating the leading surfaces, unless there is confusion in interpreting Hrate.

Table 24. Orbiter reentry conditions based on information from the Columbia Accident Investigation Board report and data assembled by Joels, et al.

Time (s)	Altitude (ft)	Vrel (mph)	H_{rate} btu (sq.ft.s)	Qbar (psf)	L.E. Temp. (°C)	
–1,719	924,014	17,500	0	0	–	–
0	400,000	–	–	–	–	Atmosphere discernible.
270	–	–	–	–	–	2nd recorded excess left wing loading.
323	–	16,432	–	–	–	–
404	243,000	16,164	–	–	–	–
471	–	–	–	–	1,454	–
537	233,426	15,824	83.98	30.88	–	–
557	231,600	15,426	–	–	1,538	–
577	–	–	–	–	–	–
597	229,037	15,470	86.34	–	–	–
613	–	–	–	–	–	Hydraulic sensors in left wing off-scale low.
614	227,400	15,091	–	–	–	Flashes continue.
651	–	≈15063	–	–	1,649	–
657	225,079	15,058	86.72	40.9	–	–
683	223,400	14,621	–	–	–	–
717	221,649	14,600	85.1	45.05	–	–
741	219,000	14,018	–	–	–	–
777	218,783	14,071	–	–	–	–
831	–	–	–	–	1,582	–
851	209,800	13,079	–	–	–	–
897	204,320	12,726	–	–	–	–
906	–	–	–	–	–	Pressure readings lost on both left landing gear tires.
922	200,861	12,385	–	–	–	–
923	200,723	12,371	–		–	Broken communication—last received from crew.
969	–	–	–			Orbiter disintegrating

Although ablative materials that react were used successfully for the Apollo Program heat shields, their large thickness, mass, and single use are undesirable. To protect the leading edges against 1,649 °C temperatures with reusable surfaces requires nonreactive materials with good structural and other compatibility properties, such as matching expansion coefficients with underlying structures. In addition, since the air is heated to very high temperatures and forms plasma, radiation from it to the leading edges is likely greater than vice versa, so emissivity becomes important because power radiated increases as T4, but good emitters are also good absorbers. Mass density of the material is of concern, since excess weight is undesirable. Thermal conductivity is an important consideration, also.

Ceramic materials have desirable nonreactive high-temperature operating characteristics, as shown in Goodfellow catalogs, an example being alumina—melting point (mp) is 2,100 °C and upper continuous use temperature is 1,700 °C.[3] The same properties for hot-pressed silicon carbide are mp 2,650–2,950 °C and upper continuous use temperature 1,500–1,650 °C. This is one reason why it was used for Shuttle orbiter leading-edge coatings. Meeting all required characteristics for the materials limits the number that is suitable. There are still some reservations concerning the characteristics for materials presently developed. Reinforced carbon-carbon (RCC), reported in reference 1, was found to perform surprisingly well under the conditions the components were developed for, as long as its integrity remained intact. A reported area of concern was loss of integrity in the silicon carbide layer that allowed oxidation of underlying structures, and inspection methods were being reevaluated for damage to such

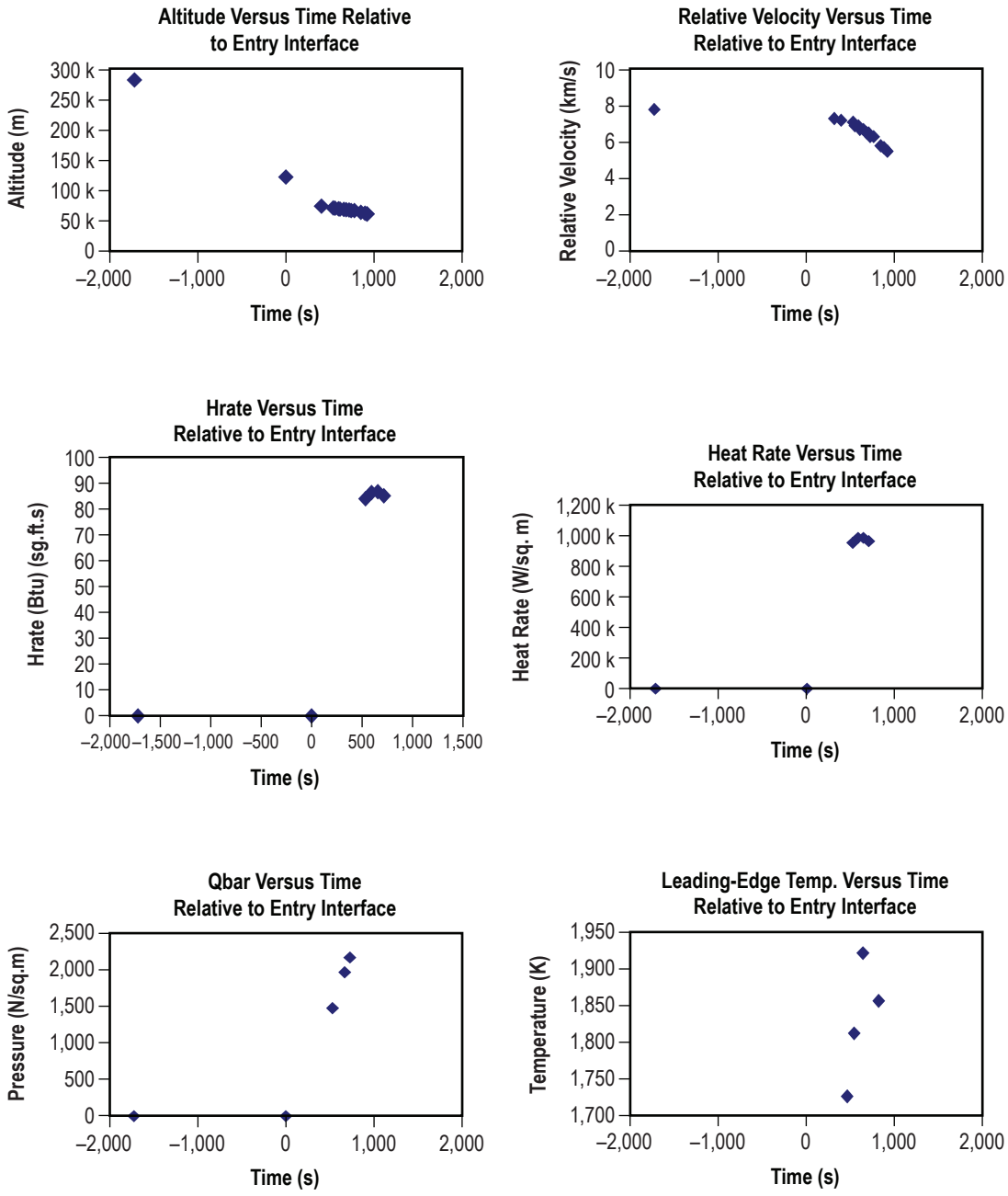

Figure 191. Graphical comparison of the data in table 23.

layers, as well as mechanisms for causing underlying hidden damage. Thus, any ability to reduce the peak temperatures and reduce oxidizers reaching the surfaces during reentry, without introducing other negative effects, is a welcome goal.

Our concept to modify the interaction of the ionized gas with the spacecraft surfaces by appropriate biasing of the surfaces is based on the premise that ions can be repelled, at least over a dark space within the plasma near the surface, modifying their transfer to the surface and around it, with the possibility of

reducing heat transfer, and drag, which could lower the maximum temperatures reached by the surfaces and hopefully the rate of oxidation of any susceptible materials. This could not significantly reduce any oxidation from AO in orbit that might find access through undetected defects, but simpler renewable coatings should prevent those avenues. On the other hand, the most worthwhile application of the bias technique would be probe spacecraft with only one planned atmosphere penetration and landing. It was not possible to create the reentry conditions within the scope of this project, and actual flight experiments would ultimately provide these conditions. However, we have fabricated plasma sources used to impinge argon ions onto carbon surfaces heating them quickly to temperatures on the order of reentry conditions, and even higher, while surrounded by a normal atmosphere. Tests with helium gas for the plasma source were not successful at all as it proved to be too difficult to make it breakdown to plasma with the power supply we had available. Attempts to use directly ionized air instead of argon or helium for the source created such a destructive plasma torch, for our simple design, that it destroyed everything, including itself, even with water-cooled copper and tungsten components, too fast to allow any measurements (where conditions were stable long enough). There were sometimes nonreproducible characteristics between runs, made difficult to evaluate because of the many parameters involved. It is suspected that impurities in the Ar, moisture in the air, etc. may have played a role in such discrepancies.

A negative self-biasing (without applied battery) that was not anticipated was observed. Whether this signifies that reentry conditions already produce desirable fields is not known, but may be worth investigating.

Typical reentry data for a Space Shuttle Orbiter, as reported in the Columbia Accident Investigation Board (CAIB) Report Volume 1, August 2003. Initial orbital altitude was 175 statute miles (281.64 km) and velocity was 17,500 mph (7.82 km/s). Note: ≈95 percent of the atmosphere for this altitude is atomic oxygen (16 AMU). The kinetic energy of a single atom striking the front surface is thus 1/2 mv^2 or 1/2(0.016 kg/6.02×10^{23} atoms)(7,820 m/s^2), which is 8.13×10^{-19} Joule, or divided by 1.6×10^{-19} eV/joule, is 5.08 eV. Thus, a voltage bias of ≈6 V of correct polarity should be able to stop a singly charged oxygen atom from colliding with the surface. The flux to the front surface is ≈density times velocity, or 1×10^{9} atoms/cubic cm times 782,000 cm/s = 7.82×10^{14} atoms/sq cm/s, which would be similar to flux at a static pressure of ≈exp–7 torr, but the ram velocity is over 10× the average thermal velocity at that altitude for average solar activity, so a pressure in excess of exp-6 torr would be needed for similar pressures to the front surface and virtually no pressure to the wake surfaces.

At 8:15:30 am, on the 255th orbit, Commander Husband and Pilot McCool executed a 2-min, 38 s OMS burn at the above altitude, slowing the orbiter down to reenter. When the orbiter reaches 400,000-ft altitude (≈122 km), an arbitrary EI is reached, defined as the point at which the orbiter enters a discernible atmosphere. Columbia reached this point at 8:44:09 am (EI plus 000 seconds, written EI+000) over the Pacific Ocean or 1,719 s from deorbit burn initiation to EI. Relative to EI, times are given as EI plus seconds (earlier would be EI minus seconds, so EI–1,719 is when burn started. For plotting purposes only the seconds will be given along with altitude, Vrel, Hrate, dynamic pressure (*Qbar*), and leading-edge temperature when found.

Plan

Only by testing can the concept be verified. Reentry simulation is best performed by a plasma arc torch such as is often used by NASA for testing TPS materials. Such torches have selectability and adjustability of the composition of the gasses that impinge on the target surface. Test time on these torches is nearly impossible to obtain due to Return to Flight preparations. A demonstration of whether or not the concept is feasible is in order. To this end, a test rig using a several H–O torches and several home-brew arc plasma sources to reach high temperatures was employed in our lab. Prototype EBTPSs were tested in these crude test fixtures. The plasma torch used in the last months of this project is shown in figure 192 and while it is in operation is shown in figure 193. Access to a vacuum chamber to better simulate the rarefied atmosphere of a planet during reentry was not possible for this project.

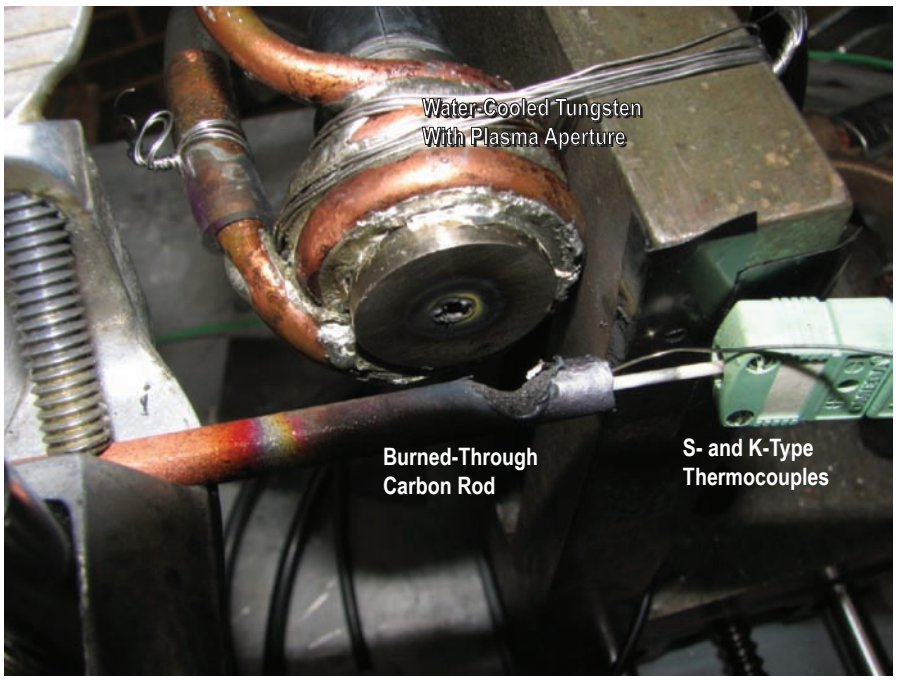

Figure 192. Home-built plasma torch made from TIG welding apparatus. The torch head is the cylinder of tungsten with the hole and the copper coil and the carbon rod target with thermocouples (one S-type and one K-type) inserted into the right end of the rod. This picture was taken after the run was completed and shows the dramatic wear of the carbon rod after a minute of operation.

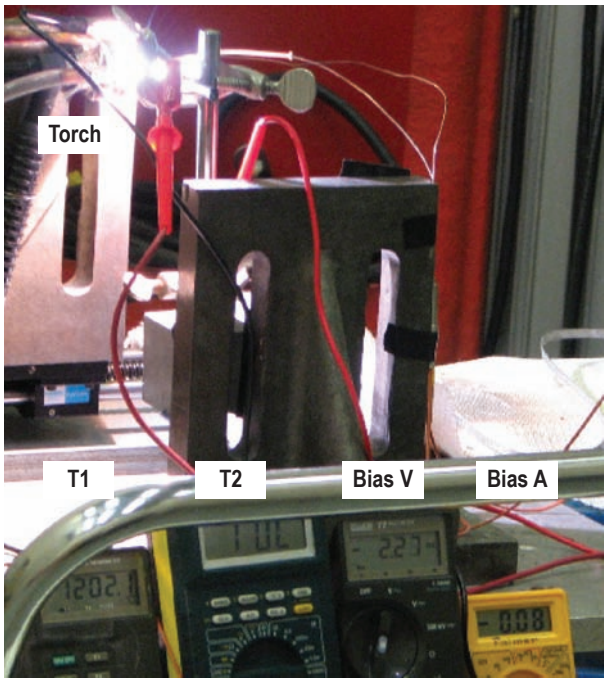

Figure 193. The plasma torch in action and the various meters used to collect the data. Two K-type thermocouples are shown and the bias current and voltage were monitored. The thermocouples had to be replaced frequently.

Results

This addendum to the final report will summarize the testing results accomplished since the final report was submitted. Short duration, 1–2 min experiments using dense carbon rods as targets were devised to determine if bias cooling could be improved. Compared to the HO torch, significant plasma heating was produced by the torch built for these tests. However, all experiments were performed in air and thus were subject to the dilution of the plasma with air and the oxidation of the carbon target that consumed it sufficiently it had to be replaced for each run. Most test parameters depended on the apparatus itself. Bias voltage, bias polarity, plasma-gas composition, target-to-torch distance, and target diameter were among the significant variables examined. Although tests with He gas were made, with poor results, all results shown here were with ionized Ar gas (plasma).

At all times that plasma was directed to the target, a voltage between the target and ground was detected, whether biased or not. A significant current was measured between the target and the bias source when plasma was applied that effectively completed an electrical circuit. This current varied with the bias polarity. It should be noted that the ammeter properly registers the polarity and magnitude of the current at all times, however, on different occasions of setting up the apparatus for a run, the leads from the ammeter were connected differently. Thus, the recording of the bias current's polarity differed. The arrangement is as follows:

- November 30 and earlier: Ammeter red>bias, black>target
- September 5: Ammeter red>target, black>bias

An observation was made with these recent tests. We had already shown there was a cooling effect with the applied bias. These experiments showed a significant heating effect with reversed bias applied to the target. In fact, the plasma/target brightness increased when positively biased in the apparatus, configured as it was these last runs. A more important observation was that the heating or cooling effect was continuous with the application of the bias and was not merely a transient only at the onset of the bias voltage application. While there may have been a transient thermal effect at the onset of biasing, having a shorter duration than the thermal lag of the system, we found that the cooling or heating effect of the bias was continuous. This is very significant to acknowledge for the purposes of protecting the heat shield. An alternative interpretation of the negative bias results (as opposed to the positive bias result which was a net heating effect) is that the plasma itself delivers electrons to the target and it develops a constant static charge even without an applied bias. This is shown by the floating voltage on the target without a bias applied (around –5.7 V). It is a negative voltage and smaller magnitude than the battery bias voltage. However, it may well be that this static charge that develops on the conductive target surface performs as if a bias were applied. This may lead a cooling effect without a bias in the circumstances of this plasma torch and circuit connections. A negative bias to the target did not produce a cooling effect on the November 11 runs, but it did on the September 6 runs. No cooling was found on the November 11 runs where the bias voltage was doubled from the 12 V of the battery to 24 V from two batteries in series. The derivative graphs for September 6 (figs. 194 and 195) show the impact of the negative bias on the temperature was real. One can read from the temperature graphs approximately a 100 degree drop is seen. Unfortunately, this effect was not very reproducible. The November 11 runs showed no significant cooling with negative bias at all. On the other hand, significant heating was found when biasing positive with either voltage. The target heated rapidly over 400 degrees in a few seconds when 24 V positive bias was applied. If only the negative bias could chill equally well!

The bias currents had a high magnitude (0.5 to 1 A) when the target was positively biased. Oddly, and without explanation, there was current (–0.02 A or less) during the application of 24 V negative bias and it resulted in an apparent heating of the target on one thermocouple while the other one beside it showed no upward change. Thus this odd observation of negative bias heating is anomalous and should be ignored. Otherwise, no bias or –12 V bias both resulted in no measurable current. For the September 6 run shown in figures 194 and 195, no segments with zero bias were shown. A bias was always applied whether positive or negative and this created abrupt and clean transitions. In the November 11 runs, shown in figure 196, bias transitions were held for several seconds with a zero-bias voltage period between each bias excursion. Oddly, no cooling was found at zero and negative bias. Other runs from September 6 and November 11 showed only minor or subtle variations due to the application of bias and are not reported here.

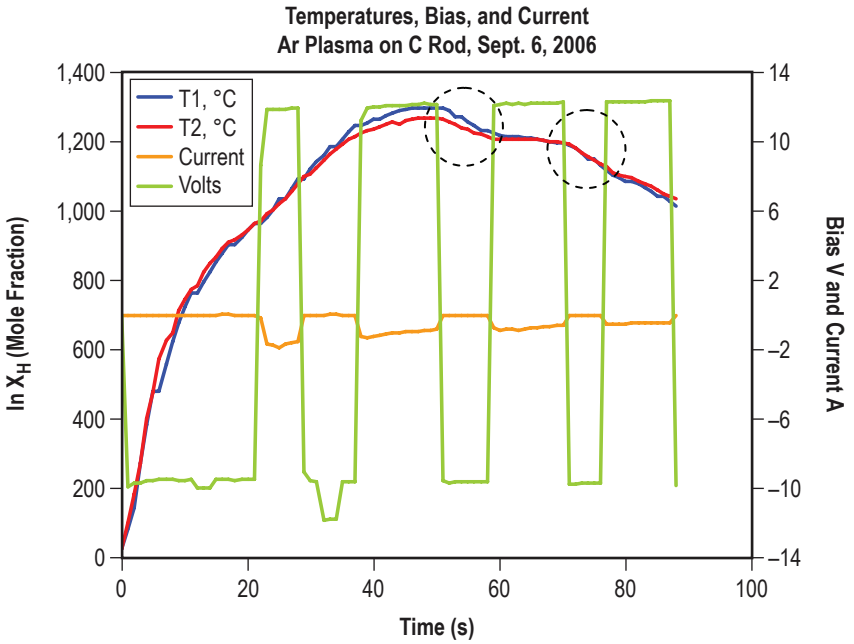

Figure 194. Temperature plots of graphite rod target in plasma torch superposed with bias and current data. K-type thermocouples were used here. Drops in temperature are shown circled as negative bias is applied. Although not very clear here, the influence of the negative bias is clearly shown in the derivative graph in figure 195. Note the current tracks the applied bias. In these runs, the bias current meter was installed with regular polarity where the red/positive lead was at the target as it was with the voltmeter. Negative bias seems to reduce the temperature by about 100 degrees on the latter two cycles where the sample temperature was sufficiently high to be meaningful. Only when the target temperatures are sufficiently high (>1,000 °C based on experience) are the thermal effects from bias observed.

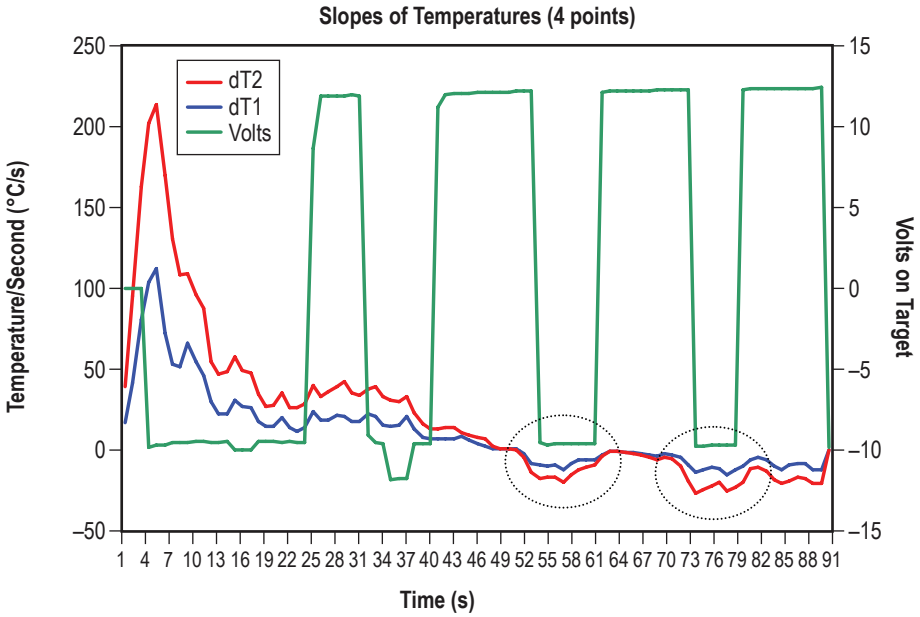

Figure 195. Slopes of temperatures versus data number (≈time) plotted with the bias voltage. This is the same run as figure 194. There are clearly seen places (compare to circled regions on previous graph) where the temperature drops and rises (positive slope=temperature rising, negative slope=cooling, lower slope=cooling, higher slope=heating) as the bias polarity was cycled. The zero bias or equilibrium voltage was –9.7 V due to the plasma impingement. Slopes with four points at a time were calculated for each time increment (data collection point). Derivatives with three or five points did not show the cooling effect as clearly as four points shown in this graph. Interpretation is made more reliable with both thermocouples sharing similar profiles.

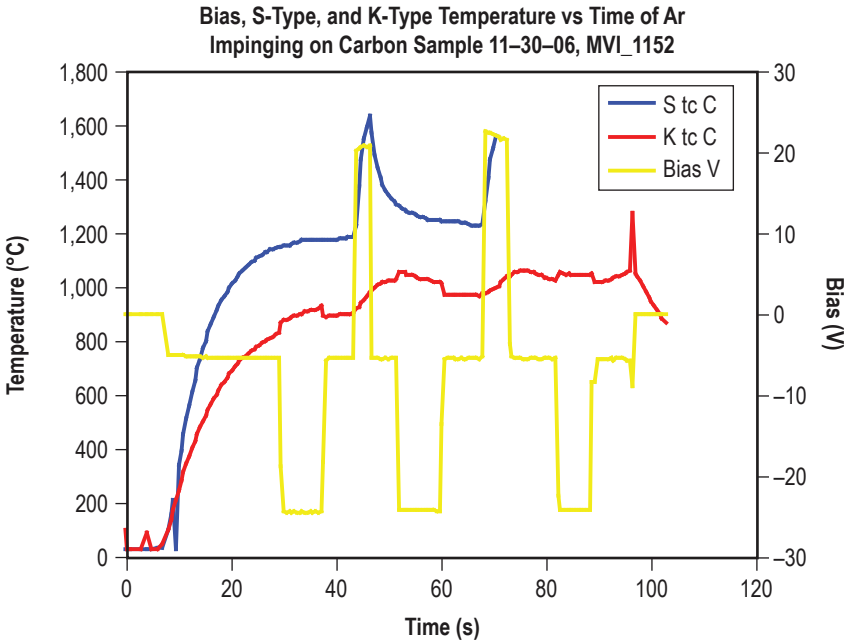

Figure 196. Temperature and bias plots of November 11 run with 24 V bias applied. S-type thermocouple shows enormous heating with positive bias applied. Nearly every run with the welder plasma showed a heating effect, although less severe than this example, when positive bias was applied. The plasma flame grew visibly brighter as well. The poor tracking between the two thermocouples and the anomalous heating with negative bias, seen on only one thermocouple, reduces the value of interpreting the data from this run.

Figure 197 is the electrical schematic and test configuration for the plasma torch EBTPS testing employed for this addendum to the final report. The breadboard diagram shows how the plasma torch, target, electrical bias, and data collection were assembled and connected electrically. The battery supplies the bias voltage and the ammeter measures the current from this bias or when there is no bias applied. The switch allows the bias polarity to be reversed or to completely remove a bias. By design, using the battery ensures that the bias has no electrical ties to ground or to a power supply. Two thermocouples (usually type-K with Inconel sheaths) were placed within a hole drilled axially into the carbon rod target that monitored the heating or cooling effects from the bias. These cannot survive the maximum temperatures encountered at the target nor accurately display these high temperatures. As a result, they were set back an amount (determined experimentally, about 5–8 mm) from the high-temperature zone where the plasma impinged. The high TC of the carbon ensured the response was rapid. As was discovered in earlier experiments, the thermal mass of the target delays the detectable temperature changes introduced by the bias. While greater sensitivity would result from placing the thermocouples close to the plasma source, our concern was to show a cooling effect that would protect the heat shield (target) and this should not be a transient phenomenon. While there may have been a transient thermal effect at the onset of biasing, we found that the cooling or heating effect of the bias was continuous.

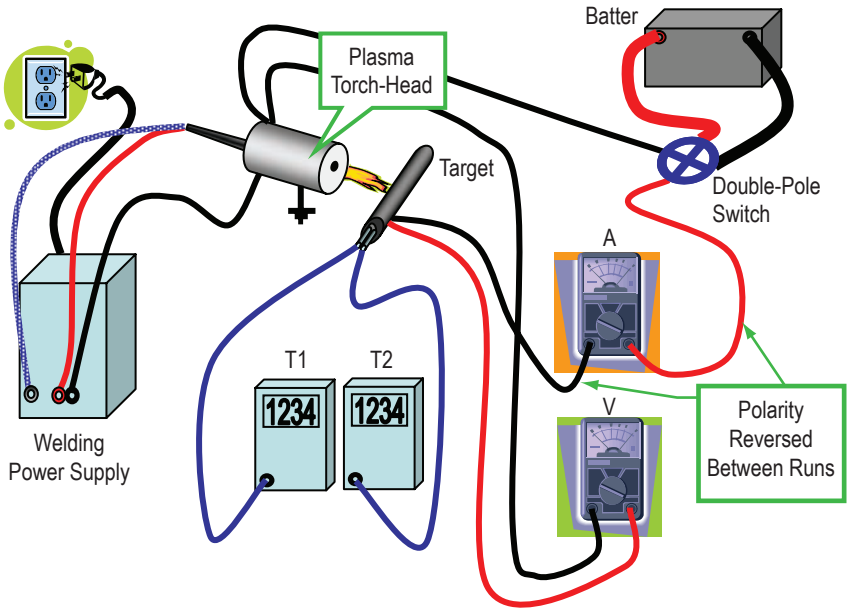

Figure 197. Electrical schematic of the EBTPS test breadboard.

For these experiments the precise temperature of the target under the plasma flame was not required, only the variation over time of the target temperature as the bias was applied or removed was desired. Having two thermocouples provided correlation statistics in these very noisy data sets. For some experiments, alumina sheathed type-S (platinum) thermocouples were used to verify that the target temperatures at the plasma were representative in the trend seen at the type-K thermocouples mounted somewhat more remotely, near but not at the impingement point. In most cases, the longevity of the thermocouples was reduced to a single run. This included the S-type ones that failed almost as quickly as the K-type and showed that the highest temperatures reached on the interior of the carbon rod easily exceeded 2,000 °C. The platinum thermocouple wire melts at 1,760 °C and the alumina sheath melts at 2,010 °C. Dissection of the target after a run showed the thermocouples were melted if placed too close to the plasma flame. The time of melting was known from the open circuit reading of the thermocouple.

Summary of Results

Applying an electrical DC bias to a conductive material exposed to high-temperature plasma can reduce its temperature from 5–100 degrees (if the proper polarity). Little current is needed. An improper polarity will result in significant heating of the material and draw considerable current. Furthermore; the cooling effect is not transitory at the onset of the bias application. Cooling is consistent for the duration of the bias signal. It was not clear if the amount of cooling could be modulated by voltage and current, although different bias voltages and currents were monitored. On the other hand, raising the bias from 12 V to 24 V positive did raise the magnitude of the temperature increase and the current. There was insufficient time to diagnose the source of the asymmetries in these observations.

Helps Advance Exploration

DC bias of several volts did reduce the conductive TPS temperature while exposed to plasma that provides longer TPS material life, improved reliability and potential weight savings of spacecraft. Once the technology is proven in a planetary reentry environment, heat shield design for spacecraft would be revolutionized.

Future Work and Direction

Testing should be continued in a vacuum plasma chamber capable of better simulating the reentry conditions. Need to see how different gasses and pressures influence the quality of cooling and tune for other planetary destinations.

The more complex testing and development of RF biasing should be initiated. Target construction and power distribution are challenges here. Testing an RF bias can only be done in a vacuum chamber; which is why that aspect of the project was not pursued.

Variable control or modulation of the bias may offer further enhancement of the technique and provide power, and thus, weight savings.

Use of supercapacitors for energy storage provides synergistic opportunities to enable the new technology and offer options in spacecraft design. One can slowly charge the capacitor (perhaps with solar energy) as the spacecraft approaches the planet to land on and then dump the power for the brief period of reentry.

References

1. Gehman, Jr., H.W.; et al.: "Columbia Accident Investigation Board, Report Volume 1," U. S. Government Printing Office, August 2003.

2. Joels, K.M.; et al.: *The Space Shuttle Operator's Manual*, Ballantine Books, NY, 1982.

3. *Goodfellow Catalog of Metals—Alloys—Compounds—Ceramics—Polymers—Composites*, Goodfellow Corporation, 800 Lancaster Avenue, Berwyn, PA 19312–1780.

7.4 Polybenzoxazine-Based High-Performance Composites for Ablative Nozzle and Aerocapture Applications

PI—Raj Kaul.

Objective

The objective of the proposed work was to use polybenzoxazine (PBZ) resins to produce preimpregnated PBZ composites and characterize their material properties for use in ablative nozzle applications. Properties such as thermal stability, mechanical strength, and char yield are in the process of being examined. This data will be used to evaluate the potential of PBZ resins to improve quality, ease processing, and enhance performance as compared to traditional nozzle ablative materials. This data may also be used to evaluate PBZ-based materials for use in similar high temperature/high-heat rate environments such as those seen in aerocapture.

Description of Research

PBZ resin was obtained and impregnated onto carbon-fiber substrates (fabric) using standard infiltration techniques. Solvent coating was the method used, which dissolved the resin in a solvent. The resulting solution was then painted or coated onto the fabric reinforcement. The preimpregnated fabric, or prepreg, was then laid up into composite panels and cured. The cure removed the solvent utilized to create the prepreg. Following the cure, the PBZ composite panels were machined into specimens and are being tested. The following properties have been, or are in the process, of being determined:

- Mechanical.
  - Tension.
  - Compression.
  - Shear.
- Thermal.
  - TC.
  - Specific heat.
  - CTE.
  - Ablation/erosion resistance.

The ablation/erosion resistance is being tested using the plasma torch test bed (PTTB) facility. The PTTB uses a plasma torch to simulate the very high temperatures and heating rates seen in the nozzle environment. In addition, Al powder may be entered into the plasma. This allows simulated production of Al oxide fragments that are a byproduct of combustion in solid propellant rocket motors, and one of the primary causes of nozzle component erosion.

The last activity will be fabrication and testing of a subscale motor test at MSFC. This test will validate the initial PTTB erosion resistance testing and evaluate the propensity toward other detrimental

phenomena, such as plylifting. Component fabrication was complete in October 2006 and testing of the components was complete in November 2006.

The rationale behind this approach was to mimic the characterization work to qualify phenolic-based materials that are currently used in man-rated vehicles such as the Space Shuttle. This approach allows a direct comparison between the two material types, making it possible to ascertain not only if PBZs are acceptable, but also, how much improvement they will provide over current materials. Additionally, this approach will provide data required for the design of future components.

PBZ resins have previously been formulated, characterized, and evaluated for use in a couple of applications, placing the CRL of this class of material at 1 or 2. The work currently being performed will increase the CRL to a 3 or 4 by enhancing the previous material characterization data and performing tests specific to the proposed application—ablative nozzles.

Procurement issues have caused approximately 4 mo of delay, relative to the original schedule for this project. The work, otherwise, would have been completed in the proposed time frame.

Results

At this point, two tests have been performed on the PBZ/carbon composite material. The tests related to erosion resistance and thermal property characterization. The erosion resistance test used a 2×2×0.1 PTTB test specimen exposed to 300 Btu/s for 10 s, with a standoff distance of 2 in. The posttest weight loss was 10 percent. Figures 198 and 199 show pretest and posttest photographs of the specimen.

Figure 198. Pretest photograph of carbon/PBZ composite specimen.

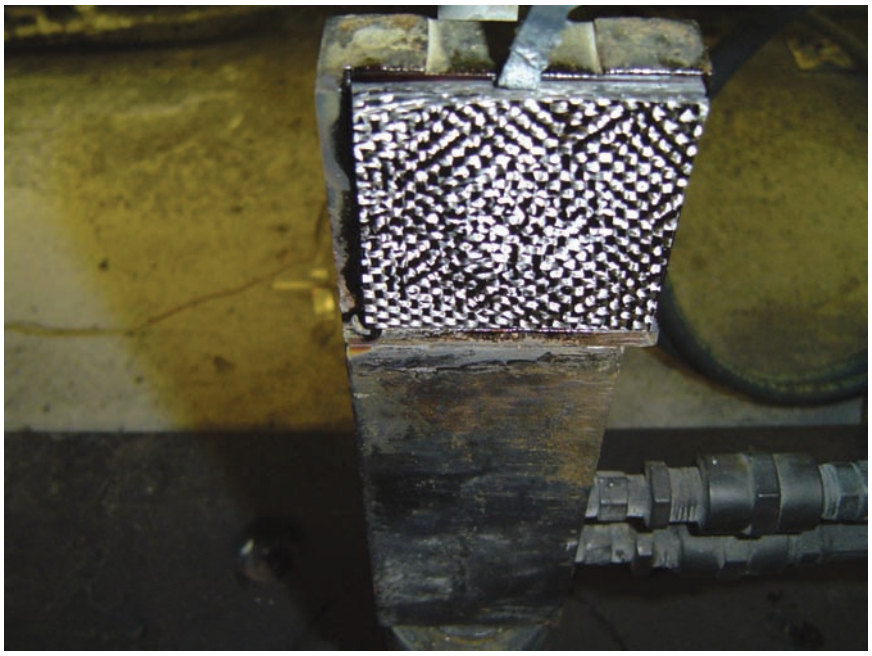

Figure 199. Posttest photograph of the carbon/PBZ specimen.

Thermal property characterization testing consisted of dynamic mechanical analysis (DMA). DMA determined the glass transition temperature of the PBZ-based composite to be 320 °C (608 °F), as shown in figure 200. This data is a measure of the point at which softening occurs in the material.

The results to date continue to support the original hypothesis that PBZ resins have the potential to improve quality, ease processing, and enhance performance as compared to traditional polymer matrix composite (PMC) nozzle ablative materials. The PMCs currently used employ phenolic resins; however, phenolic resins present processing and performance challenges that must be overcome. Phenolics cure by a condensation-type reaction, meaning that a by-product of the reaction—water—must be removed or accommodated through the processing. Processing typically utilizes hot compaction during layup and high pressure (>200 psig) during cures to meet this challenge—both of which add significant cost to the final component. Even with these measures, phenolic PMCs have a propensity toward voids and low-density regions. Performance challenges also relate to the chemistry of the cured phenolic. Erosion of the nozzle throat degrades performance throughout motor firing. As part of thermal decomposition, phenolics form an adherent char that aids the nozzle by reducing this erosion. Significant erosion still occurs, however, limiting both performance and the usable life of the motor.

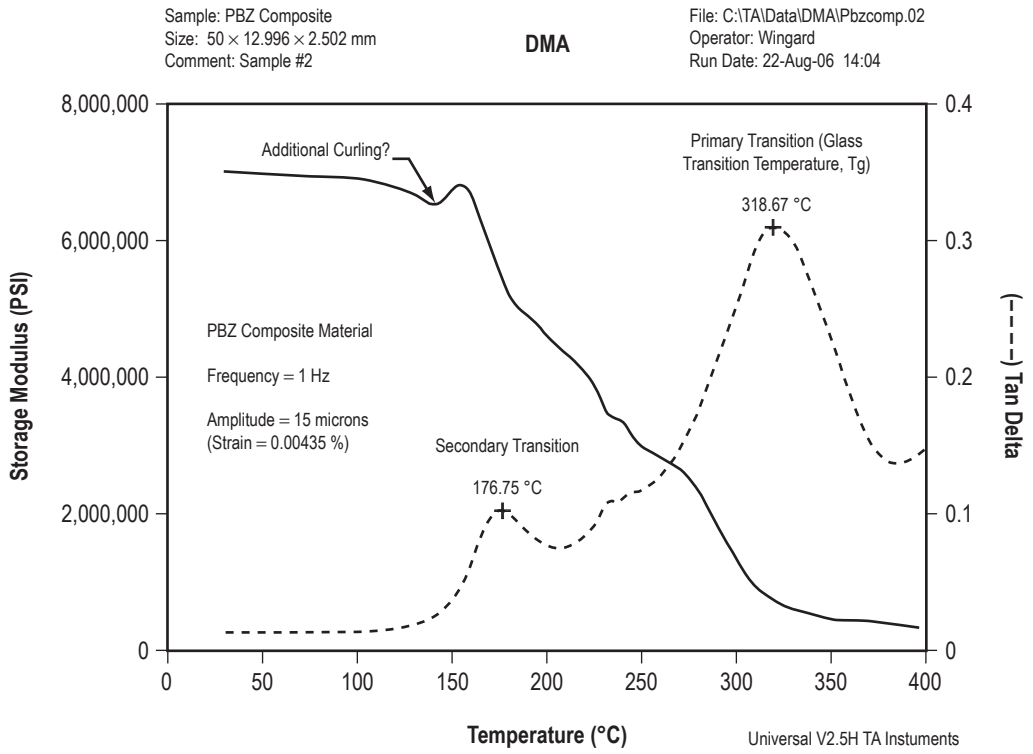

Figure 200. DMA results from carbon/PBZ specimen.

This effort seeks to improve the manufacturing processes of nozzles through the composite resin chemistry by reducing the number of processing steps and decreasing the pressure required for cure. The chemistry and physics of the resin will likewise improve the design of the nozzle by reducing or eliminating component void content and cure shrinkage and improving its resistance to erosion during use. The initial PTTB results indicate that the resin forms an adherent char layer that does resist further erosion of the material. New nozzles designed with PBZ composite could have relevance to the existing RSRM, as well as the new CEV, CLV, and future rocket motors.

Possible Future Research

The next step in evaluating PBZs for nozzle applications is to complete the work that has already been started which includes mechanical and thermal property testing, additional PTTB testing for erosion resistance, subscale motor component fabrication, and subscale motor firing. Most of this work is already in process and will be completed within the next month.

Pending successful results, a follow-on investigation would examine the material through a more in-depth mechanical property characterization and larger solid rocket motor tests. Such work would provide the fidelity needed to look at qualifying this material for use in man-rated vehicles that utilize solid propellant rocket motors (RSRM, CLV, and CEV).

Additional research would put PBZ resins another step closer to use in hardware. In hardware, this resin could improve quality, ease processing, and enhance performance as compared to traditional nozzle ablative materials.

7.5 X-Aerogel Insulated Composite Cryotank Technology Development

PIs—
Mary Ann Meador, Ph.D; Chris Johnston, Ph.D; Lynn Capadona, Ph.D., NASA GRC.
Gweneth Smithers; David Shular; Tom DeLay, NASA MSFC.
James Fesmire; Brekke Scholtens, NASA KSC.

Objective

NASA's exploration of the universe, beginning with a journey back to the Moon with longer duration visits than before, and preparations for a journey to Mars will be possible only through advanced, revolutionary progress in science and engineering. Advanced materials will be integral to many of the avenues that lead to such progress.

Progress in advanced materials comes about through research and development, sometimes beginning serendipitously when an astute scientist or technologist—in the midst of pure research on another topic or in the midst of an ordinary laboratory or manufacturing procedure—notices something surprising and potentially very useful. Other times, progress is made when research is tied to or focused on specific applications, where a strong need dictates how the research is planned. For NASA's exploration to be successful we will need all the above.

The efficient use and storage of cryogenic fuel systems appears to be one of the keys in the early path to exploration of the universe. Two top concerns for these systems are (1) Excess weight and (2) cryogenic boil-off issues that hinder efficient storage. Our approach in addressing these concerns has been to build small experimental units that utilize a lightweight composite material for the cryotank, actually a bottle at this stage, and insulate them with x-aerogel, a material which promises lightweight super insulation.

X-aerogel, an aerogel composite, is the intellectual property of NASA GRC scientists. Aerogel materials—a very broad category—possess a certain type of structural morphology and are well known as superior, lightweight thermal insulators.

Hrubesh and Pekala[1] say it well: "Aerogels are highly porous, open-cell foam materials produced by sol-gel processes and dried by supercritical extraction. The nanosized cells/pores and particles which make up aerogels are primarily responsible for their very low-thermal conduction. The thermal conduction through the solid in aerogels is limited by the extremely small connections between particles making up the conduction path. Similarly, the gaseous conduction is suppressed because the cells/pores are only the size of the mean-free path for molecular collisions. Therefore, molecules collide with the solid network as frequently as they collide with each other. Also, the radiative conductivity through aerogels is low because the aerogels have such low mass fractions and very large surface areas, although the conductivity increases dramatically with rising temperature."

Unfortunately, most aerogels and aerogel composites are very fragile. X-aerogel, however, is a polymer-crosslinked-silica aerogel composite that is strong yet still retains its lightweight and superior insulation property (fig. 201). It requires 300× more force to break but is only 2× more dense than the typical earlier aerogels.

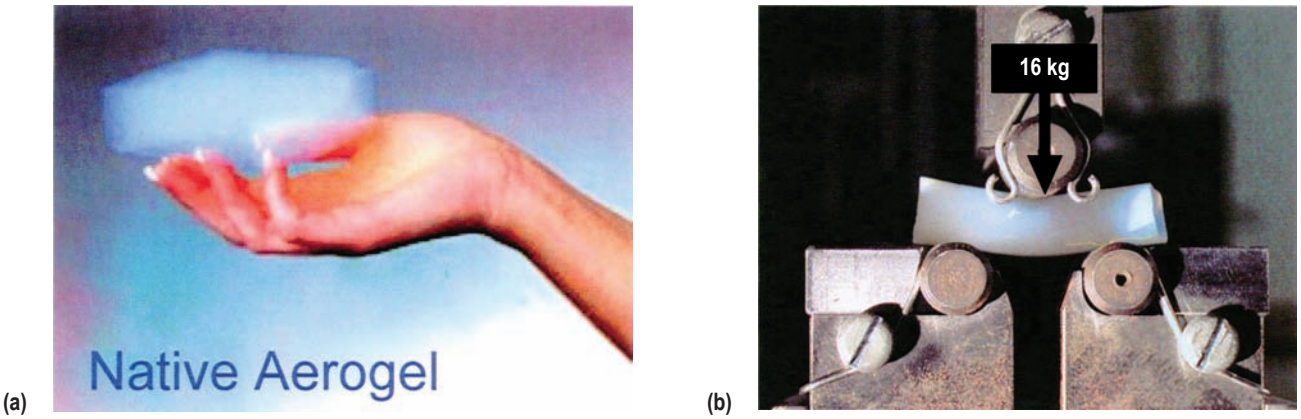

Figure 201. Native aerogel (a) and crosslinked aerogel (b).

Investigators at MSFC and KSC began collaborating with the GRC scientists, developers of the x-aerogel product, to build and test a small cryobottle, with the long-term goal of developing an improved cryotank. While GRC had already invented x-aerogel, they had never produced it in contoured shape before this project.

Description of Research

Early in our collaboration, it was decided that MSFC would fabricate six composite bottles. The bottles would be shipped to GRC to be covered with x-aerogel. GRC would then ship the bottles back to MSFC for composite overwrap. KSC would perform thermal evaluation and MSFC would perform mechanical testing. Producing and testing a small unit was agreed to be the practical way to begin and would indicate the feasibility for a larger scaled-up tank.

The bottles were built according to the configuration provided in ASTM D–2585, Standard Test Method for Preparation and Tension Testing of Filament Wound Pressure Vessels, having a 5.75-in internal diameter. Hexcel IM7 carbon fiber and HEI535 epoxy resin systems were the materials selected. Fiber density was 0.19g/cc, the resin content was 33 percent, and there was no liner. The overwrap sequence was two layers 12° helical (pole to pole) and two layers 90° hoop.

The vessels were wet wound with the fibers having the same 4-lb tension and vacuum bag cured after the winding was completed. The Invar end fittings were grit blasted immediately before use on the wax mandrel assembly. The epoxy matrix resin was allowed to cure at RT for 72 hr before the wax mandrel was melted out by suspending the vessel in an oven at 180 °F for 8 hr while the wax melted (this procedure can also be viewed as a postcure for the epoxy resin). The vessels were leak tested with 100-psi liquid nitrogen before shipment to GRC, as shown in figure 202.

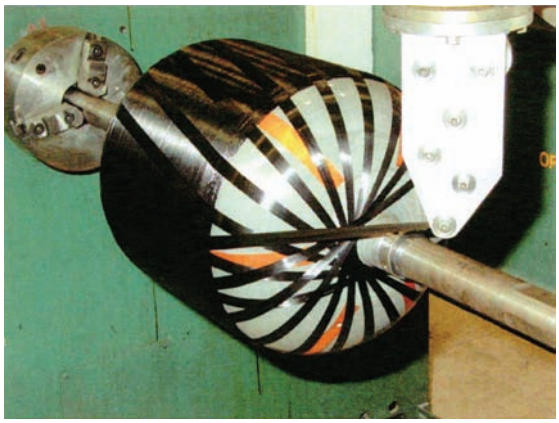

Figure 202. Filament winding a composite bottle.

For x-aerogel formulation, polyisocyanate was used to strengthen the silica aerogel. Isocyanate x-aerogel could possibly have some flammability issues. There was consensus on this decision since we are at an early stage in development, have a low dollar amount, and GRC has the most experience with this formulation. Down the road if feasibility is proven and we start to scale up, we would expect to change the x-aerogel formula. The formula for this phase of the work targets a density of about 200 mg/cc and a 1/2-in thickness of the insulation product.

The advantage that x-aerogel has over conventional aerogels and aerogel composites is the strengthening of the necks around the string of pearls, the term often used to describe the nanostructure of aerogel. The polymer coats the silica all over, but the critical help comes at the neck region, because this is the weak link in an aerogel. So, the thicker necks increase the strength of the material (fig. 203); nanoscale pores are blocked but mesopores remain, retaining low TC; density increases ≈2× while strength increases ≈300×.

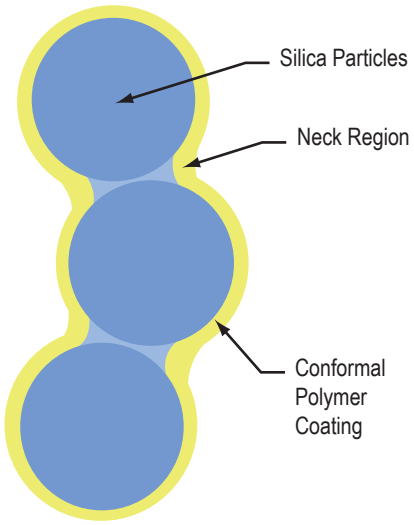

Figure 203. Illustration of x-aerogel structure.

The challenge at GRC for this project was to contour the x-aerogel to conform to the shape of the composite bottle. To solve this challenge, silicone RTV molds were produced to form the x-aerogel insulation. The solution during the timeframe of this phase of the work was to produce 24 sections of insulation for each bottle (fig. 204). Laser scanning of the composite bottle was utilized as a tool to develop accurate molds. The production of x-aerogel involves production of a fragile wet gel, followed by polymer cross-linking, then supercritical extraction to complete the process, producing a dry, strong product. At this writing GRC has produced most of the x-aerogel pieces needed to cover the first unit. When all 24 pieces are completed, they will be adhesively bonded to the bottle.

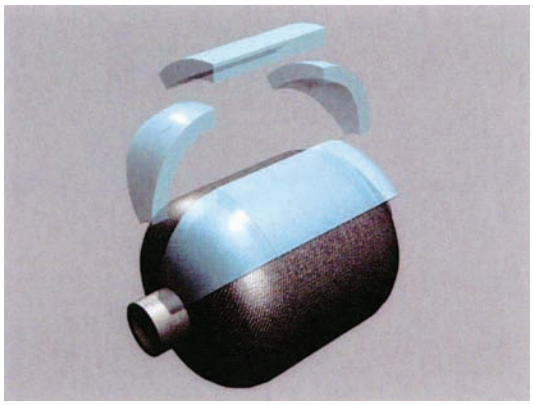

Figure 204. The composite bottle is covered with x-aerogel then overwrapped.

The sectional or pieced approach to x-aerogel insulation cover for the bottles means that we face the risk of creating heat leak paths with the seams. This issue and the learning curve for producing contoured shapes constitute what our team viewed as the two major risks in this phase of the research and development.

As each bottle is covered with insulation at GRC, it will be shipped back to MSFC, where it will be overwrapped with more composite material. We are still discussing a possible soft vacuum packaging for the x-aerogel. We think this is a good thing to try because any degree of vacuum will improve thermal performance of the x-aerogel. So, we will try a soft vacuum when the x-aerogel is overwrapped, and if it doesn't work out the plan will be dropped for the time being.

Once the first unit is completed, the following tests are planned:

- Thermal performance evaluation at KSC.

- NDE, vibration, fill and drain, impact resistance, and burst at MSFC.

With limited funds we must be selective in our testing. For example, there are several points at which we would like to do NDE, but limited funds were available for this activity. We hope to do NDE, specifically thermography, on one bottle before it is covered with insulation, again after the insulation is attached, again after the insulation is overwrapped, and after vibration or impact testing. Also, it would

be informative to do a thermal performance evaluation at various stages of completion, but time, logistics, and funds will determine our final testing plans. KSC is currently in the process of making fitting modifications to enable thermal performance evaluation of the bottle in their test setup (fig. 205).

Figure 205. Thermal performance evaluation will occur at KSC.

We began our collaboration in early 2005 with brief telecons every other week to develop our plans and provide status at each Center. At this time, MSFC has fabricated six composite bottles, plus extras in case any should not pass leak check. Three that passed leak testing were shipped to GRC. MSFC will leak check the remaining bottles then ship three more to GRC.

Even though GRC faced a steep challenge in the development of new techniques for forming x-aerogel into curved sections, they have made real progress in this area. The bigger hurdle for our schedule came in the form of an unexpected delay in the operation of the new larger autoclave, essential for supercritical drying of the x-aerogel product. Final development of safety protocols acceptable to the Safety Office is also taking much longer than expected. As a result, only the older and 10× smaller (1-L capacity) autoclave has been available for use. Hopefully, this situation will soon be resolved, and we will be able to make rapid progress in completing our project.

This collaboration has enabled all of us to benefit from the experience and expertise of our colleagues. Every technical issue that we have faced has been easier because of the collective knowledge sharing among the group. Lockheed-Martin learned of our collaboration and asked to attend our meetings. They have subsequently volunteered to cover a bottle with a spray-on foam insulation, currently used on the Shuttle's ET, to do a test comparison. This direct comparison should provide added benefit to our effort.

Results

The first x-aerogel covered unit is expected to be shipped from GRC in September or October 2006. If the new autoclave comes online soon, the next five bottles should be covered in short order, since the molding learning curve has been conquered to a great extent. Autoclave capacity is now the greater problem. The real results will come only when our completed units are tested. Although our progress to date was described in the Description of Research section it is repeated here. The following tests are planned:

- NDE at MSFC.
- Vibration tests at MSFC.
- Thermal performance evaluation at KSC.
- Fill and drain at MSFC.
- Impact resistance tests at MSFC.
- Burst at MSFC.

Lighter weight, high-performance materials are essential for the realization of Exploration goals. If cryotank weight can be decreased and conservation of cryogenic fuel can be increased—this is a step in the right direction.

Insulation on cryotanks has been a big issue for NASA in recent years. If our feasibility project reveals an alternate insulation candidate for cryotanks, it should be evaluated to see if performance can be significantly improved.

Possible Future Research

Promising test results would lead us to scale-up to a larger tank and to concurrently look at other formulations and processes for x-aerogel production/formation and cryotank attachment. In taking this step, we will probably encounter challenges associated with scale-up and hopefully learn how to solve them. Even though larger pieces of x-aerogel can be made in larger autoclaves, we would never have an autoclave large enough to produce x-aerogel in one piece for a large cryotank application. Therefore, we would need to look at ways to improve the seams. In considering other x-aerogel formulations, we need to look for the optimum density/strength, balance, and nonflammable chemistry.

In addition to cryotanks, the new ability to mold x-aerogel into complex shapes opens a large number of applications. Aerogels are superb not only for thermal insulation and low density, but also for shock absorption, low-sound velocity, and low-dielectric constant. These beneficial properties along with the ability to mold x-aerogel into complex shapes creates numerous space, military, and commercial applications, including the following examples:

- Thermal insulation systems for many types of equipment and structures.
- Infrared invisibility for military vehicles.
- Various types of sensors.
- Supercapacitors.
- Numerous optics applications.
- More efficient ultrasonic devices.
- Shock absorption in protective head gear. Purification filters.
- Hydrogen fuel storage.
- Catalysts for chemical reactions.
- Microwave electronics.
- High-voltage insulators.
- Containers for energetic materials, nonnuclear explosives.

Reference

1. Journal of Material Research, Vol. 9, No. 3, March, 1994.

7.6 Ceramic Reaction Sintered Coatings for Propulsion and Thermal Management Materials

PI—Peter G. Valentine, NASA MSFC, Engineering Directorate, Materials & Processes Laboratory.

Objective

This project was targeted at technology for materials applications such as very high-temperature ceramic coating and joining processes in support of propulsion and thermal management component development—two of the AME Program focused-research areas. To stay within the AME Program funding and schedule constraints of $200k and 10 months, this project dealt strictly with the assembly and checkout of a very high-temperature induction furnace facility at MSFC. No research work was performed. The primary objective was to complete the induction furnace facility so follow-on development work could be performed. The completed facility will enable future development work to be performed in both the very high-temperature coating and joining technology areas. Possible applications for the coating and joining processes include the following:

- Propulsion.
  - Lightweight erosion-resistant nozzles.
  - Thrust chambers.
  - Hot-gas valve components.
- Thermal management.
  - Strong, lightweight, durable, leading edge and heat shield components.

One of the primary technology areas to be further developed using the induction furnace facility is ceramic reaction sintered coatings (CRSC's) for lightweight high-temperature composites, such as C–C and C-SiC. The basic process in fabricating reaction-sintered coatings involves heating components, coated with precursor coating materials, to very high temperatures (2,550 °C (4,622 °F)) to form the desired final ceramic coating microstructures through the mechanisms of particle sintering and eutectic melting/reaction. Prior to joining NASA, the PI had established the techniques for applying such coatings to graphite materials and C–C composites, using facilities at General Atomics (GA), in San Diego, CA.

Description of Research

As this particular project was somewhat different from the other FY 2006 AME-funded tasks, the following information presents an overview of the type of technology that will be the basis for the work to be performed in the very high-temperature induction furnace facility being established at MSFC.

Reaction sintering technology has been successfully demonstrated, by the PI and others, as a technique for applying very high-temperature C–C to high-temperature graphite, ceramic, and CMC materials for a variety of applications and for joining ceramic components to other ceramic or refractory metal components.[1–3] Initially, CRSCs were evaluated by the PI for use in Ford Aerospace divert propulsion systems (fig. 206) and as laser, x-ray, and particle-radiation resistant coatings for Strategic

Defense Initiative (SDI) spacecraft components.[4] The following applications have also been investigated by the PI :

- TPS components.
  - Leading edges for hypersonic vehicles.
- Rocket propulsion components.
  - Liquid, solid, and nuclear thermal systems (fig. 207).
- Nonaerospace components.
  - X-ray anodes.
  - Fusion energy tokamak reactor first-wall materials.[5–7]

Generally, these applications involve very high-temperature, greater than 2,000 °C (3,632 °F), operating environments.

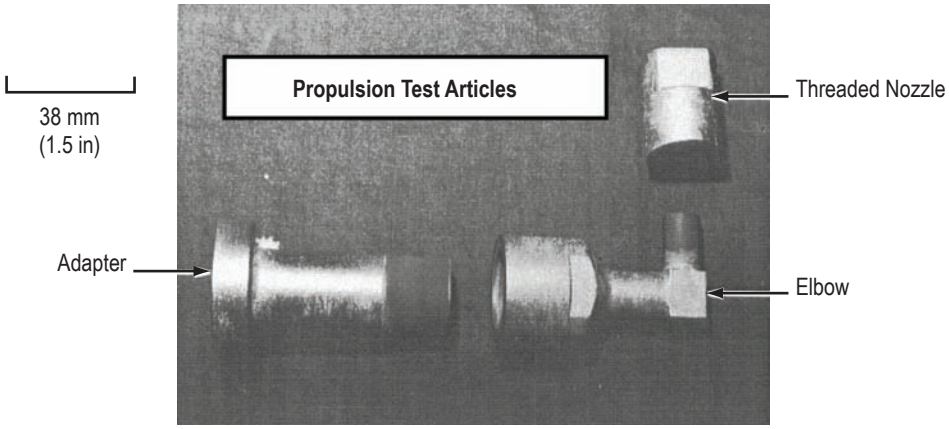

Figure 206. HfB_2-HfC ceramic reaction-sintered coating on Poco Graphite, graphite grade AXF–5Q. The components shown were early developmental test articles for the LEAP Program. Both the internal and external surfaces were coated.

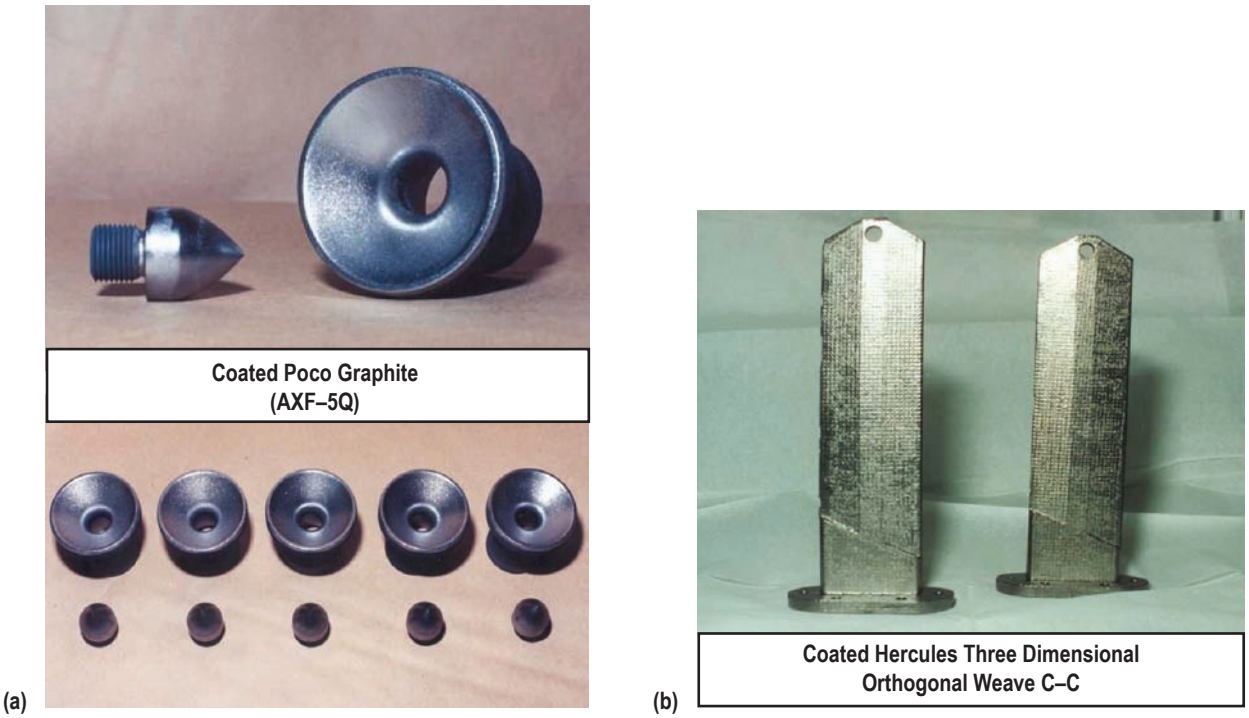

Figure 207. HfB_2-HfC ceramic reaction-sintered coatings on (a) solid-fuel pintles and pintle seats, and (b) struts for a hypersonic air-breathing propulsion system.

The benefits of using CRSCs for these applications, as previously listed, include the following:

- Improved oxidation resistance.
- Improved erosion resistance.
- Decreased H permeability.
- Improved resistance to particle and electromagnetic radiation.
- Ability to use lightweight, low-density (graphite, C–C, etc.) substrate materials.

The same technology has also been used by the PI to fabricate joints between various combinations of graphite, C–C composite, and refractory metal components. Two examples of joining processes demonstrated by the PI include: (1) The assembly of liquid divert propulsion system thrust chamber/nozzle assemblies for kinetic kill vehicles and (2) the assembly of high-temperature computer tomography graphite/refractory metal anode components, a patented process shown in figure 208.[3]

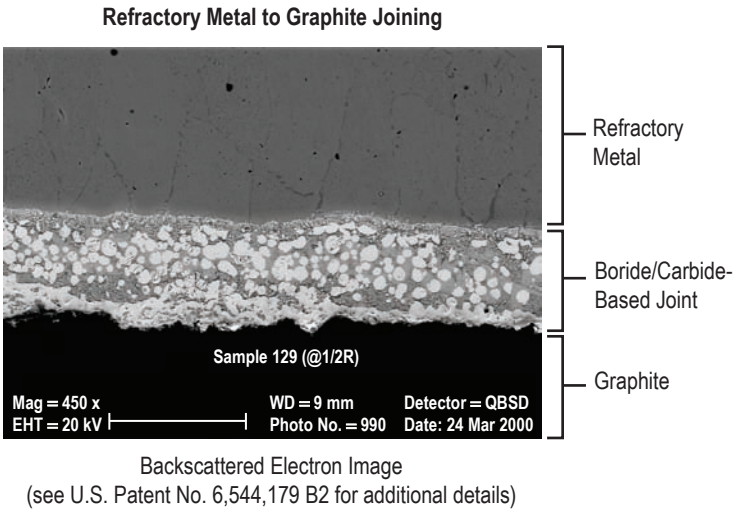

Figure 208. An example of a joint fabricated using a modified version of the basic CRCS application process.

While the coating technique has been successfully used with a fairly extensive number of coating compositions, the composition that has been of greatest interest for short duration very high-temperature exposures has been 30 wt.% hafnium diboride (HfB_2) + 70 wt.-% HfC. Also, various combinations of boron carbide (B_4C) and SiC have been investigated for use as coatings on fusion energy tokamak graphite and C–C components, where low-atomic number elements are of primary interest (fig. 209).

Fabrication of CRSCs involves heating components coated with precursor coating materials to very high temperatures to form the desired final ceramic coatings. The CRSCs investigated by the PI have typically been applied using a three-step process. In the first step, the substrate materials are prepared for application of the coating material. If practical, the substrate surface to be coated is roughened slightly, such as with SiC metallographic grinding paper. The substrate material or component is then ultrasonically cleaned in ethanol. This is followed by a vacuum heat treatment to remove adsorbed/absorbed gases and to vaporize volatile impurities. In the second step of the overall coating process a precursor coating material is applied to the substrate material. The substrate surface is brush coated with a slurry consisting of an organic binder, ethanol, and ceramic powder particles. After the precursor coating material is applied, the coated specimen is heated to 125 °C (257 °F) to cure the binder and evaporate any residual alcohol. The third and final step in the coating process involves high-temperature thermal processing to create the desired final coating. This is accomplished by heat treating the precursor coated specimen, at ≈2,550 °C (4,622 °F) for HfB_2-HfC coatings (in the boron-carbon-hafnium system), to consolidate the coating powder particles by reaction-sintering, as shown in figure 210. Other coating systems have different processing temperatures. The final coating microstructure, that develops during high-temperature processing, forms by a combination of several mechanisms. The two primary mechanisms involved are: (1) Eutectic reaction and (2) solid-particle sintering. Thus, the coating process has been termed reaction sintering.

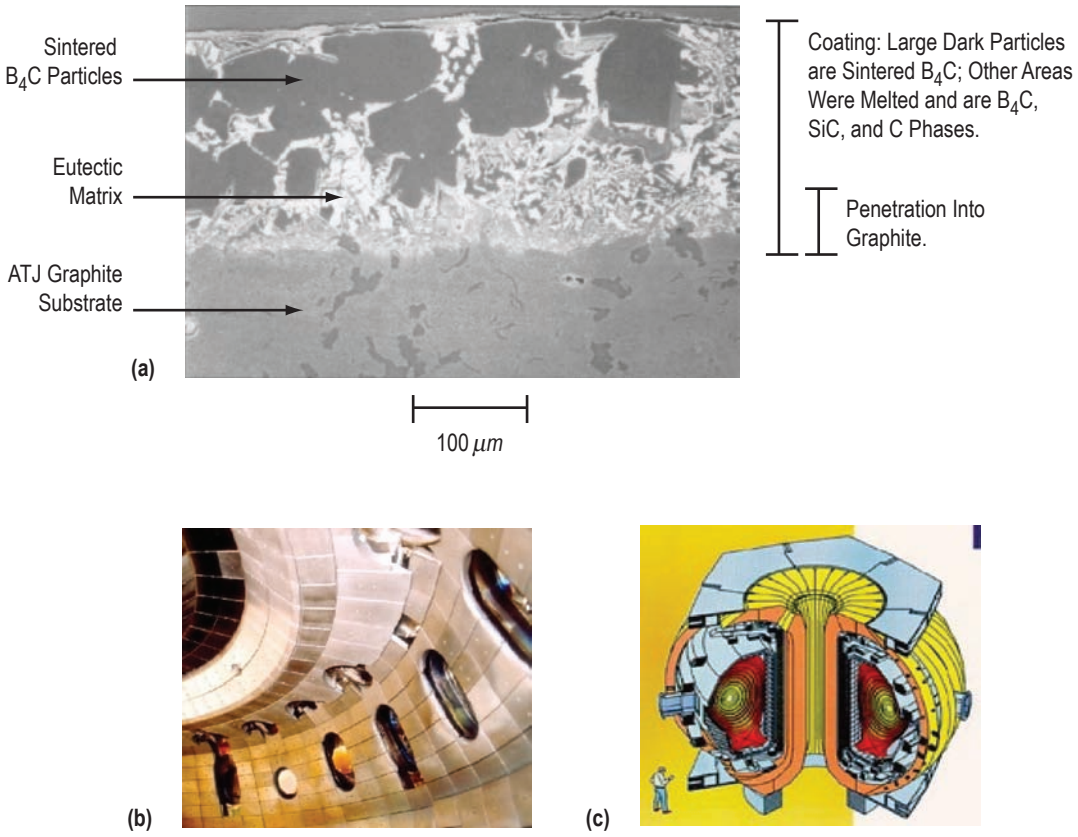

Figure 209. (a) Coating fabricated using a nominal powder particle composition of $7B_4C + 2SiC$. Note: Low atomic number constituents were required. The objectives for applying coatings to fusion energy tokamak plasma-facing components included the following: Reduce erosion of graphite tiles, provide mechanism for releasing boron into plasma for oxygen gettering, and investigate effect of silicon on tokamak's plasma. (b) Upper divertor in DIII–D tokamak at GA (San Diego, CA), note graphite tiles. (c) Sketch of DIII–D tokamak at the National Fusion Facility at GA.

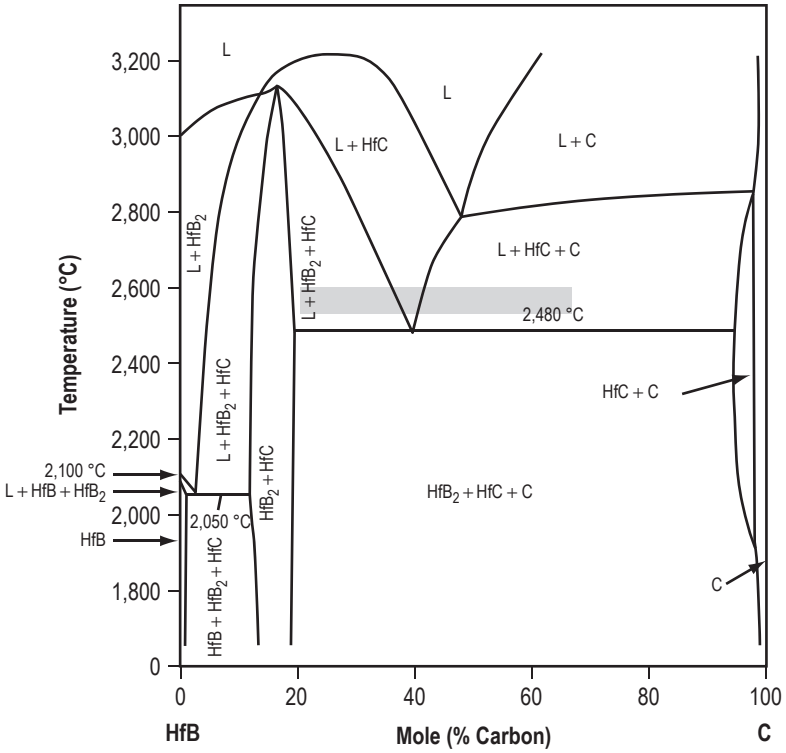

Figure 210. Hf0.5B0.5–C isopleth phase diagram. A section of the ternary Hf-B-C phase diagram is shown. The shaded region shows the portion of the diagram that is of primary interest for the fabrication of HfB_2-HfC CRSCs.

In the area of CRSCs for TPS components, one of the PI's more significant results to date has been the performance of CRSCs on hyper-x leading-edge test specimens. NASA LaRC conducted a series of evaluations for hyper-x leading-edge materials a few years ago. In three series of simulated Mach-10 flight environment tests, the CRSC specimens performed very well with minimal evidence of degradation, as shown in figure 211, primarily a color change at the leading edge caused by the formation of a very thin oxide layer of hafnium dioxide (HfO_2). The reaction sintered coated C–C was one of the three best performing materials in the hyper-x tests and was a candidate for the Mach-10 flight vehicle.

A typical CRSC microstructure consists of two layers. The surface layer is the layer of coating material above the original substrate surface, as shown in figure 212. A second penetration layer is located below the surface layer and is formed by reaction of the coating material with the outermost 50 μm (2 mils) of the substrate material. The CRSC forms a nonporous graded structure on the coated substrate. This type of microstructure enhances the adherence of the coating to the substrate material.

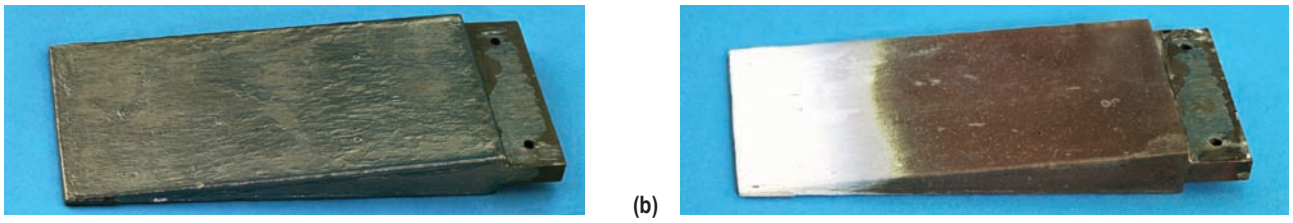

Figure 211. HfB_2-HfC CRSC on a Goodrich C–C hyper-x (X–43) leading-edge test specimen (a) before and (b) after Mach 10, 105,000-ft simulated altitude test exposure. The only visible change noted was a change in color. No weight change occurred.

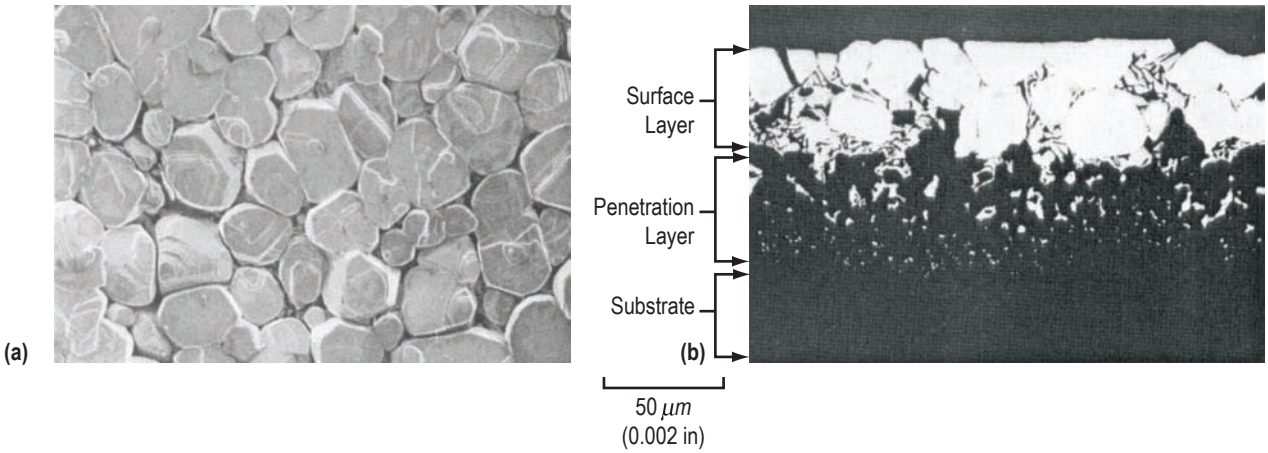

Figure 212. Typical CRSC microstructure. The coating shown was fabricated using a powder mixture of 40-wt% HfB_2 + 60-wt% HfC; the substrate material used was a Hitco carbon composite two-dimensional C–C. (a) Secondary electron image of the surface of a coated specimen, note the flat faces of large HfC particles which have grown during the coating formation process. (b) Backscattered electron image showing the cross-section of the CRSC, note the large white HfC particles (≈25 μm (0.001 in)) in the matrix of eutectic material (HfB_2, HfC, and C). The penetration layer of the coating is approximately equal in thickness (in this example) to that of the surface layer.

Results

This was a 9.5 mo effort, funded by AME, to establish the induction furnace facility in Building 4612, Room 1105, of the Materials and Processes Laboratory at MSFC. At present, it is anticipated that setup and checkout of the induction furnace laboratory will be completed in the October/November 2006 timeframe. The furnace system is scheduled to be operated for the first time on October 17th.

Goals/Status Prior to AME-Funded Effort/Relevance

The primary objective of this effort was to assemble and checkout an induction furnace facility designed specifically for performing very high-temperature coating and joining development work, as previously described. A large portion of the hardware required for this system was purchased prior to the AME-funded task with the support of other MSFC projects. A list of the hardware purchased prior to FY 2006 is included in appendix A, while appendix B contains the list of hardware purchased in FY 2006 with AME funds. This facility will be highly relevant to AME's goals and objectives, as it was designed for performing propulsion and thermal management materials development work. While no materials development work was scheduled to be performed in FY 2006, follow-on development projects and feasibility studies in FY 2007 and beyond should be possible for as little as $25k.

Approach/Work Performed

The intention of this AME-funded effort was to complete the establishment of a very high-temperature induction furnace facility at MSFC, bringing the coating and joining laboratory online in FY 2006. While this was not quite achieved, considerable progress was made and it is currently anticipated that the laboratory will be ready for performing true research and/or development work in the October/November 2006 timeframe. As previously noted, October 17th is scheduled for the furnace system checkout run.

The MSFC induction furnace facility, to conduct coating and joining materials and processes development, is nearing completion. The centerpiece of this facility is an inductively heated vertical water-cooled quartz tube furnace, capable of operating at temperatures as high as 2,800 °C (5,072 °F). Materials and processes development work can be performed in either vacuum or inert (typically argon) atmospheres. Due to the design approach used, very rapid heating and cooling of test specimens is possible—a specimen can be taken from RT to over 2,000 °C (3,632,°F) in approximately 10 min. Temperature control is accomplished using a two-color optical pyrometer sited directly on the surface of the test specimen. Vacuum is maintained, when desired, through the use of both mechanical and diffusion pump systems. The facility also contains the following laboratory equipment:

- Lindberg/Blue-M oven for the drying and curing processes.
- Vacuum desiccator cabinet.
- Fume hood.

- Miscellaneous lab equipment.

  – Top loading analytical balance.
  – Magnetic stirrer/hot plate.

The specific system design, used for laboratory hardware/equipment purchases and furnace system setup, was detailed in a 100+ page document prepared for the PI in 2002–2003 by GA personnel.[9] The nearly complete MSFC system is a duplicate of the unique one-of-a-kind system developed by GA, shown in figure 213. The FY 2006 AME Program support and previous support by a number of different organizations and programs, listed in table 25, along with the design work performed by GA in 2002–2003 and by the MSFC Facilities Management Office in 2005–2006, as well as the purchase of the hardware and equipment needed to establish the laboratory, was funded by a number of different organizations and programs as listed in table 25.

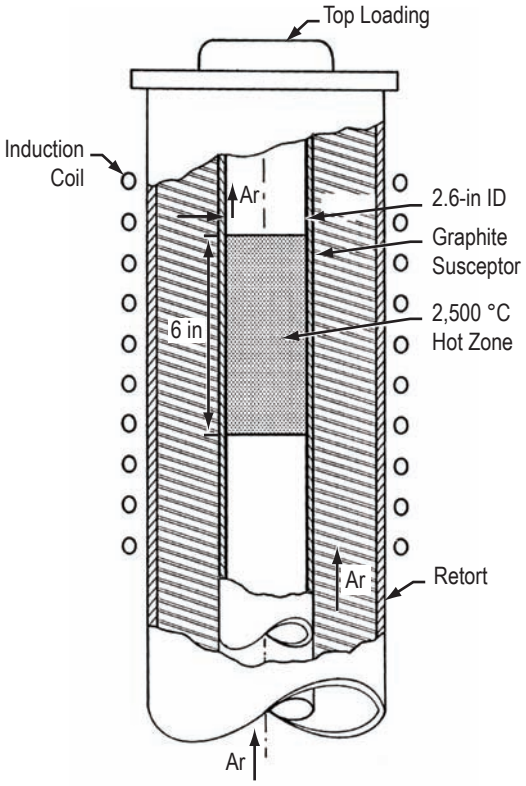

Figure 213. Basic design of the furnace facility being established. An induction furnace with a graphite susceptor, contained within a water-cooled quartz retort, allows vacuum and inert atmosphere thermal processing.

Table 25. Funding sources for laboratory project.

FY	Project or Organization
2002	Center Director's Discretionary Fund (CDDF) Program 3rd Generation Reusable Launch Vehicle Program
2003	Expendable Launch Vehicle Program Office Next Generation Launch Technology Program
2004	Engineering Directorate (ED01)
2006	Advanced Materials for Exploration Program Exploration Systems Mission Directorate (via EM40)

Schedule for the AME-Funded Task

Table 26 lists the specific events and milestones associated with completing this AME-funded effort. The original estimated completion dates, actual completion dates, or anticipated completion dates, are shown.

Table 26. Project schedule.

Task No.	Description	Estimated Completion Date	Actual Completion Date
1	Modification of laboratory to accommodate furnace hardware completed.	February 2006	January 2006
2	Setup water, power, air, etc. Furnace interfaces in lab completed.	April 2006	September 2006
3	Fabrication (machining) of graphite fixtures and components. Metallic connectors and supports completed.	May 2006	August 2006
4	Assembly of furnace system completed.	July 2006	TBD October(?) 2006
5	Furnace system checkout completed.	August 2006	TBD November(?) 2006

Organizations and Personnel Responsible for Accomplishment of this AME Project. The following organizations and personnel were directly responsible for the accomplishment of this laboratory setup task:

- Task Lead—Peter G. Valentine, Ceramics and Ablatives Engineering Team. Mr. Valentine was the PI and was also responsible for project management.

- Consultant Support—Robert F. Stetson, retired GA staff technician and induction furnace expert. Consulting support was provided by Mr. Stetson, an expert in the design and fabrication of induction furnaces for use in conducting coating and brazing (joining) research and development work. Mr. Stetson was the technician at GA who designed and built the coatings system used by the PI when the PI was employed at GA. Additionally, under a small contract in 2002–2003, Mr. Stetson prepared the design report and documentation for the system being completed under this AME effort.

- Technician Support—Allen L. Kinworthy (lead) and several others, Jacobs Sverdrup and associated subcontractors. Mr. Kinworthy (and others) was responsible for performing major portions of the coating/joining facility hardware setup, installation, and checkout.

- MSFC Facilities Support—Felix Aguinaga (lead) and several others, Facilities Management Office and SEI Group, Inc. (and various contractors and subcontractors). Mr. Aguinaga was the lead for the facilities interface installation tasks to enable the setup and operation of the new coating and joining facility.

Possible Future Research

Once the MSFC EM40 induction furnace system and associated laboratory equipment/facilities are completed, which should happen in the October/November 2006 timeframe, this coating/joining facility will provide the means to develop specific materials systems and processing techniques for propulsion and thermal management materials and components—Coatings and/or joint compositions for specific substrates and components. The coating and joining development work will be targeted at components fabricated using graphite, C–C, and C/SiC materials.

The attributes or characteristics of the CRSCs to be fabricated or applied using the facility are summarized in table 27. The materials used by the PI, to date, for fabricating coatings and/or joints have included refractory borides and carbides of metals such as the following: Hf, Mo, Nb, Ta, Ti, V, W, Zr, and Si.

Table 27. Summary of CRSC technology.

Description:
• Coatings capable of withstanding very high temperatures. • Based upon the use of boride and carbide compounds of refractory metals. • Emphasis has been placed on HfB_2-HfC system, to date. • Coating formation involves simultaneous eutectic melting and powder particle sintering. • Precursor coating material reacts with outer portion of substrate material—generally, to a depth of about 50 μm (2 mils).
Applied Successfully to the Following Types of Substrates:
• Graphite materials. • C–C composites.
General Observations:
• Adherence maintained during extreme thermal cycling. • Hard surface layers established. • Reaction-sintered coatings may be used as transition layers for other coatings, such as plasma-sprayed metals and ceramics.
Various Coating Substrate Combinations Have Demonstrated Significant Potential in One or More of the Following Environments:
• Extreme elevated temperatures and rapid thermal cycling; Laser irradiation; x-ray irradiation; oxidizing environments (i.e., arc-jet tests); erosive environments.
Applications Considered to Date Include:
• Propulsion system components. • Leading edges/heat shields. • Fusion energy tokamak first-wall tiles. • Military spacecraft shielding.

Initial and final technology readiness levels (TRL's) of the materials and technology to be developed using this facility will be application specific, as significant work has already been accomplished by the PI with specific materials compositions and components. The basic technology metrics that apply to CRSC technology, for coatings fabricated using this facility, deal primarily with the uniformity of the coating; i.e., the variation in thickness (generally less than ± 25mm), the distribution of microstructural phases, and the percentage and distribution of porosity (percent porosity must be less than 5 percent). The substrate needs to be fully (100 percent) covered with coating material—there can be no bare or uncoated regions. The coating performance characteristics will depend upon the specific application or component utilized.

Finally, as test specimens and components coated or joined in the MSFC coating and joining induction furnace facility are limited in size by the current facility's capabilities (a 6-in long, 2.6-in diameter hot zone), either a larger facility or alternative processing methods must be employed if/when larger test articles are coated or joined. While a larger facility would require a significant need and commitment, other methods of supplying the heat needed to fabricate CRSCs have been considered. Alternative heating methods/sources include lasers, microwaves, and EBs. A small project was conducted by the PI a number of years ago that demonstrated that lasers could be used to apply CRSCs to graphite and C–C substrates without the need for a furnace facility, as shown in figure 214.[10] More work would be needed in the area of alternative processing methods to make methods, such as laser processing, truly viable alternatives to using the induction heating method.

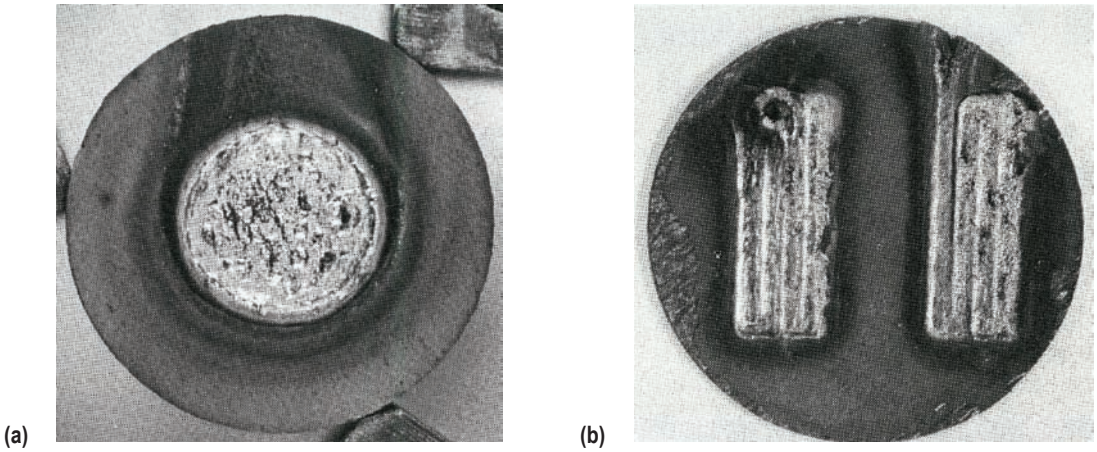

Figure 214. Laser processing has been demonstrated as feasible, but additional development work is still needed to fully make use of this method of fabricating CRSCs. (a) A 1-in diameter precursor coated C–C disk after exposure to a 1.4-cm diameter 4-kw/cm^2 CO_2 laser beam for ≈15 s—the LHMEL I laser at WPAFB was used. (b) A 1-in diameter precursor coated C–C disk after exposure to a 4-mm diameter 3.75-kw/cm^2 (left) and 3.25-kw/cm^2 (right) CO_2 laser beam translating at 6-mm/min—a small machining/cutting laser at WPAFB was used. The coatings in (a) and (b) both made use of HfB_2 and HfC powders. The substrates used were Hitco C composites two-dimensional C–C disks.

References

1. Valentine, P.G.; and Trester, P.W.: "Reaction Sintering: A Method For Achieving Adherent High-Temperature Coatings On Carbon-Carbon Composites," *15th Conference on Metal Matrix*, *Carbon*, *and Ceramic Matrix Composites*, J.D. Buckley, ed., NASA Conference Publication No. 3133, Part 2, pp. 811–827, December 1991.

2. Valentine, P.G.; and Trester, P.W.: "Development Of Brazed Joints In Carbon-Carbon, Graphite, and Refractory Metal Components For Rocket Propulsion And Spacecraft Applications," *15th Conference on Metal Matrix*, *Carbon*, *and Ceramic Matrix Composites*, J.D. Buckley, ed., NASA Conference Publication No. 3133, Part 1, pp. 39–55, December 1991.

3. Horner, M.H.; Trester, P.W.; and Valentine, P.G.: U.S. Patent No. 6,544,179 B2; April 29, 2003.

4. Trester, P.W.; and Valentine, P.G.: "Intrinsically Hardened Materials/High Temperature Radiator Coatings," Wright Laboratories, Air Force Systems Command, Wright-Patterson AFB, OH Final Report Prepared By General Atomics Under Contract No. F33615–87–C–5230; Report No. *WL–TR–91–4081* (GA Report No. GA91–104); Report Security Classification: Secret; May 1991.

5. Trester, P.W.; Valentine, P.G.; and Harrington, R.O.: "Tungsten and Ceramic Coatings for Carbon-Carbon Components," Contract Final Report for General Electric Medical Systems, GA Project No. 2943–078 Milwaukee, WI, December 19, 1995.

6. Valentine, P.G.; Trester, P.W.; Winter, J.; and et. al: "Boron Carbide Based Coatings on Graphite for Plasma-Facing Components," *Journal of Nuclear Materials*, Vol. 212–215, pp. 1146–1152, 1994.

7. Valentine, P.G.; Trester, P.W.; Winter, J.; and et. al.: "B4C-SiC Reaction-Sintered Coatings on Graphite for Plasma Facing Components," *Journal of Nuclear Materials*, Vol. 220–222, pp. 756–761, 1995.

8. Rudy, E.: "Ternary Phase Equilibria in Transition Metal-Boron-Carbon-Silicon Systems," Part V, Compendium of Phase Diagram Data, USAF Wright Laboratories Technical Report No. *AFML–TR–65–2, 1965*.

9. Trester, P.W.; and Stetson, R.F.: "Design Information for Fabrication of a Very High-Temperature Furnace Facility at the NASA Marshall Space Flight Center," General Atomics Report No. *GA–C24282*, GA Project 39110, NASA Contract H34399D, February 2003.

10. Valentine, P.G.; and Trester, P.W.: "Reaction-Sintered Coatings Fabricated at the Laser Hardened Materials Evaluation Laboratory (LHMEL), Test Plan: Laser-Assisted Processing at LHMEL," Contractor Report for Wright Research and Development Center/LHMEL Group and Acurex Corporation, General Atomics Report No. *GA–C20483*, March 1991.

11. Valentine, P.G.; and Trester, P.W.: "A Laser Heating Method for Producing Reaction-Sintered Coatings on Carbon Substrates," *16th Annual Conference on Composites*, *Materials*, *and Structures*, Cocoa Beach, FL, Restricted Sessions, Paper No. 134, January 16, 1992.

Addendum A: Hardware Purchased Prior to the AME-Funded Task

1. Tocco, Inc.: $99,340.00 actual price for all components purchased through Tocco.
   – 50 kW, 3/10 kHz, Inductron II solid-state power supply.
   – High-frequency load matching components.
   – 6-in I.D. × 8-in long, water-cooled multiturn inductor.
   – 30-in long, water-cooled rigid copper bus.
   – Distilled water-cooling recirculating system.
   – Two-color Ircon, Inc. optical pyrometer and swivel mounting base.
   – Two-pen strip chart recorder.

2. Davis Inotek Instruments: $1,499.00 prepurchase quote.
   – A & D Company, Limited HF–300G top-loading analytical balance, item No. AD638812.

3. Kendro Laboratory Products/Furnace Concepts, Inc.: $1,544.00 prepurchase quote.
   – Lindberg/Blue M low-temperature 260 °C mechanical convection oven.

4. Voigt Global Distribution LLC: $402.00 actual price.
   – Lab-Line magnetic stirrer hot plate combination, item No. 1170.

5. BOC Edwards—Purchase No. 1: $1,295.00 prepurchase quote.
   – E2M0.7 two-stage rotary vacuum pump.

6. BOC Edwards—Purchase No. 2: $14,853.81 actual price for all components purchased.
   – Edwards Difstak combined outfit with various accessory hardware.

7. F.E. Burkett: $9,912.76.
   – Quartz furnace retort.
   – Quartz sight glass monocle.
   – Quartz oil bubbler.

8. GrafTech: $1,111.30.
   – Four rolls (0.005 in × 6 in × 100 ft) Grafoil grade GTA, catalog No. G3546.
   – Three sheets Grafoil grade GHA cured laminate (0.125 in × 24 in × 24 in) catalog No. G1503.

** Note: The three GHA Grafoil sheets will need a high-temperature curing operation (see quote).

9. SGL Carbon: $2,485.00.
   – Grade HLM85 graphite rod, SGL material No. 606335 6-in dia × 72-in long nominal dimensions as-is.
   – Grade 31G porous block, SGL material No. 707766 10 × 14 × 14 nominal dimensions.

10. Labconco Corp.: $6,686.05.
    – Vacuum desiccator cabinet, Cat. No. 5530000.
    – 4-ft protector Premier Laboratory hood, Cat. No. 4880400.
    – 48-in solvent storage cabinet, Cat. No. 9902000.
    – Spillstopper work surface, Cat. No. 9847100.

Total of equipment and material purchases = $139,128.92.

Addendum B: Hardware Purchased in FY 2006 Using AME Funds

The following does not include contract/subcontract labor used for the various construction and facilities tasks. Only laboratory equipment, hardware, and tools are listed:

1. Poco Graphite, Inc.: $565.04 w/shipping.
   – Seven AXF–5Q graphite rods (1D × 18), item No. 23852.

2. Labconco Corp.: $1,822.94 w/tax ($0.00) + shipping ($0.00) = $1,822.94.
   – One fiberglass blower (12 in, ¼ hp), item No. 7181000.
   – One filler panel (8-in deep), item No. 9920306.

3. Tokentools Pty. Ltd.: AU $107.45 ($82.09)—includes shipping and Australian tax.
   – One Unimig Ar flow meter and regulator TIG MIG welder for use with bottled Ar gas.

4. W. W. Grainger, Inc.: $151.20 + tax ($12.10) + shipping ($8.50) = $171.80.
   – Eight compact two-speed 4-in fans, item No. 4C800.

5. McMaster-Carr Supply Co.: $701.22 w/tax ($0.00) + shipping ($53.83) = $755.05.
   – One Al rolling platform ladder w/3 steps, platform height 3 ft 4 in, item No. 7993T45.
   – One Masterkleer PVC tubing, 3/8 in ID, ½ in OD, 1/16-in wall thickness, 50 ft, item No. 5233K63.
   – One Masterkleer PVC tubing, 3/8 in ID, 9/16 in OD, 3/32-in wall thickness, 50 ft, item No. 5233K64.
   – One Masterkleer PVC tubing, 3/8-in ID, 5/8-in OD, 1/8-in wall thickness, 50 ft, item No. 5233K65.
   – One Teflon PFA tubing, 1/8-in ID, ¼-in OD, 1/16-in wall, semiclear white, delivered in two pieces—25 ft and 15 ft, item No. 51805K72.

6. VWR International: $693.34 w/tax ($0.00) + shipping ($0.00) = $693.34.
   – One magnetic hot-plate stirrer, MR3001 series, Heidolph, item No. 82005–039.
   – Two VWR spinbar Teflon resin coated stir bars, polygon shaped, item No. 58948–988.
   – One VWR digital calipers, 6 in, item No. 62379–531.

7. Branson Ultrasonic Corporation: $1,301.00 w/tax ($0.00) + shipping ($0.00) = $1,301.00.
   – One Branson 5510DTH ultrasonic cleaner with digital timer, heater, degas, and temperature monitor, item No. 952–518.
   – One A52–2 solid tray (11 × 9 × 6), item No. 410–176.
   – One A52–4 beaker cover (for four 600 ml beakers), item No. 246–013 (d) Four A600–1 600-ml glass beakers, item No. 140–004.

8. VWR International: $19.44 w/tax ($0.00) + shipping ($0.00) = $19.44.
   – One VWR powder-free nitrile examination gloves, large, 100 per pack, item No. 82026–428.

9. Lowe's: $379.63 + tax ($30.37) + shipping ($0.00) = $410.00.

- One GE 6-c/ft Spacemaker compact refrigerator (white), model No. GMR06AAPWW, item No. 180050.
- One Kobalt 20-piece screwdriver set, model No. 324GC20K, item No. 189990.
- One Irwin 10-in curve jaw vise-grip locking pliers with built-in wire cutter, model No. 10WR–3, item No. 97480.
- One Klein Tools 9-1/4-in high leverage side-cutting plier w/New England head, model No. D213–9NE, item No. 35553.
- One Kobalt 7-in needlenose pliers, model No. SP001, item No. 84079.
- One Crescent 10-in chrome adjustable wrench, model No. AC110V, item No. 98101.
- One Crescent 6-in chrome adjustable wrench, model No. AC16V, item No. 90629.

10. McMaster-Carr Supply Co.: $220.71 w/tax ($0.00) + shipping ($12.25) = $232.96.
    - One adhesive-backed silicone rubber sheet, 1/16-in thick, 12 in × 12 in, 60A durometer, item No. 8977K32.
    - One adhesive-backed silicone rubber sheet, 3/16-in thick, 24 in × 24 in, 60A durometer, item No. 8977K75.
    - One pack silicone O-ring AS568A Dash Number 223, pack of 10, item No. 9396K6.
    - Five FEP encapsulated silicone O-rings AS568A Dash Number 223, item No. 9319K99.
    - Fifteen 3M Scotch Brand electrical tape ¾-in W × 66-ft L, black, Super 33+, item No. 76455A12.
    - One pack brass round-head slotted machine screws 6–32 thread, ¾-in length, 100 per pack, item No. 92453A151.

11. The Home Depot: $175.72 w/tax ($0.00) + shipping ($0.00) – discount ($2.20) = $173.52.
    - One WorkForce steel storage rack, 5-shelf unit, Item No. 035441188437.
    - Three SurgeMaster surge protectors, 8-ft power cord, 6 outlets, Item No. 722868475447.
    - One Behr premium transparent weatherproofing wood sealer and finish, No. 500 natural, item No. 082474500019.
    - One DeWalt 14-piece Ti pilot-point drill bit set, item No. 028877525068.
    - One 3-in WorkForce brush, SKU No. 243–269, item No. 6927732910138.
    - One 25-ft Stanley MaxSteel tape measure, item No. 076174337990.
    - One Master Lock padlock, item No. 071649059124.

12. McMaster-Carr Supply Co.: $66.71 w/tax ($0.00) + shipping ($4.00) = $70.71.
    - One type-316 SS wire 0.02-in diameter, 1/4-lb coil, 233 ft/coil, part No. 89045K32.
    - One SS general purpose tweezers, round blunt tip, serrated inside, 10-in length, part No. 7379A23.
    - One SS general purpose tweezers, offset round blunt tip, serrated inside, 4-1/2-in length, part No. 5516A18.
    - One SS general purpose tweezers, pointed blunt tip, serrated inside, 5-11/16-in length, part No. 5516A14.
    - One SS general purpose tweezers, round blunt tip, serrated inside, 12-in length, part No. 7379A24.
    - Five impact-resistant welding filter lens, 2 in × 4-1/4 in, shade No. 12, part No. 5424T42 (same as 5424T1).

- Five impact-resistant welding filter lens, 2 in × 4-1/4 in, shade No. 9, part No. 5424T38 (same as 5424T1).
- One box clear lens cover plastic, 2 in × 4-1/4 in, packs of 12, part No. 5426T5.

13. Swagelok Company: $204.40—w/tax ($?) + shipping ($?) = $204.40.
    - Two SS integral bonnet needle valves, 0.37 Cv, 1/4-in Swagelok tube fitting, regulating stem, part No. SS–1RS4.
    - Four SS Swagelok tube fittings, male connector, 1/4-in tube OD × 1/8-in male NPT, part No. SS–400–1–2.
    - Two SS Swagelok tube fittings, union tee, 1/4-in tube OD, part No. SS–400–3.
    - Four SS Swagelok tube fittings, union, 1/4-in tube OD, Part No. SS–400–6.

14. Alabama Fluid System Technologies Inc.: $137.60—w/tax ($0.00) + shipping ($0.00) = $137.60.
    - Two SS Swagelok tube fittings, bored-through male connector, 1-in tube OD × 1-in male pipe weld, part No. SS–1610–1–16WBT.
    - Four PTFE front ferrules for 1-in Swagelok tube fitting, part No. T–1613–1.
    - Four PTFE back ferrules for 1-in Swagelok tube fitting, part No. T–1614–1.

Total of equipment and material purchases = $6,645.85

7.7 Development of Advanced Deep-Space Heat Rejection System

PI—Robert J. Naumann.

Co-PIs
Leonard E. Adcock and Joel E. Ellis, University of Alabama in Huntsville.

Objective

We were told at an Advanced Propulsion workshop that "if you ain't working the heat rejection problem, you ain't working the problem." Indeed, in considering the Brayton cycle requirements for the JIMO mission, which calls for rejecting some 364 KW of waste heat at temperatures ranging from 300–550 K, the mass of the radiating panels can be a significant fraction of the entire spacecraft.[1] Waste heat is to be transferred from the power converters to the radiator panels by a sodium-potassium (NaK) pumped loop, where the evaporator portion of the heat pipe/radiator elements are inserted into the NaK duct. Since the heat pipes under consideration can carry ≈0.1–1KW (depending on their diameter and operating temperature), several hundred heat pipe/radiator elements will be required. Such an arrangement has the advantage of redundancy since the loss of a few elements does not seriously degrade the performance of the system. Also, each individual radiating element can be optimized for the temperature at which it is sup-posed to operate. An advanced radiator design, proposed by Anderson and Stern, uses Ti-H_2O heat pipes imbedded in an Al honeycomb structure.[2] Thin sheets of high-TC graphite reinforced composite (GFRC) along the top and bottom of the Al honeycomb form the radiating surfaces, as seen in figure 215. These thin sheets of GFRC touch only the outer perimeter of the heat pipe and thermally conductive graphite foam is added to improve the conductive heat transport between the heat pipe and the radiating surface. One advantage of this concept is the added stiffness by the Al honeycomb that supports the thin fragile GFRC sheets; however, it also adds nonradiating mass to the fins.

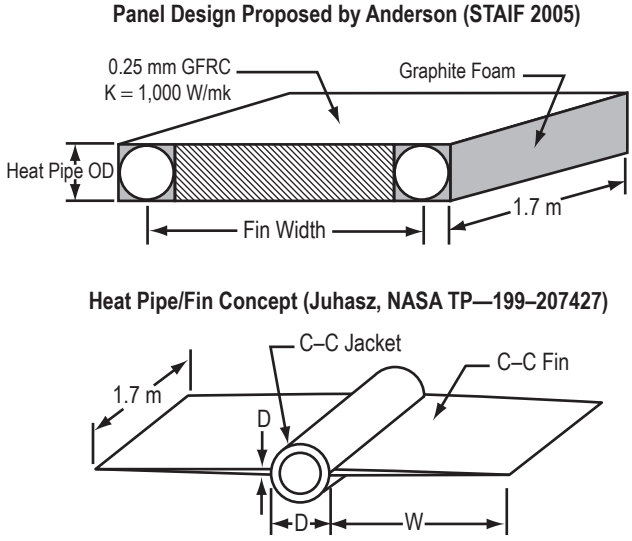

Figure 215. Panel concept versus fin concept. Fin should be more efficient because there is no nonradiating mass and the fins can be tapered to maximize heat radiated per mass.

A novel composite heat pipe/fin radiator concept was developed by Juhasz in support of the SP–100 project.[3] A very thin (0.076 mm) Nb1%Zr liner was brazed to the inside of a 25-mm ID, 1-mm thick C–C shell with integral fins on either side. The 1-m long K-filled heat pipe with a perforated Mo-foil wick was designed to operate in the 700-K regime. Using the C–C jacket as the pressure shell, the linear density of the heat pipe was only 0.250 kg/m^3. Unfortunately when the SP–100 project was cancelled, no further work has been done on composite heat pipes with integral fins, even though the prototype unit was successfully built and tested.[4]

The Juhasz composite heat pipe/fin radiator concept would appear to be more efficient than the panel concept of Anderson because it eliminates nonradiating mass, and the fins could be tapered to increase their radiating efficiency. The objective of this effort was to develop and test a prototype composite heat pipe/fin radiating element that would outperform the panel design proposed by Anderson and Stern in the 350–550 K regime.

Description of the Research

Anderson and Stern considered heat pipes ranging from 3/8 in to 1-in diameter in their panel design. The specific power of a heat pipe/fin can be shown to be inversely proportional to the linear density of the heat pipe, so the smaller diameter heat pipes would be favored if this was the only consideration.[5] However, the power that the heat pipe can deliver also decreases with diameter, so using the smaller diameter would require many more heat pipes. Also, the required thickness of the fin at the root to optimize the fin geometry becomes very thin (much less than 1 mm) for the smaller diameter heat pipes. For this reason we chose to base the design of the prototype heat pipe/fin on the 1-in diameter heat pipe described by Andersen and Stern in reference 2. The linear density of the 1-in heat pipe was estimated to be 0.511 kg/m by extrapolating the masses of the smaller heat pipes derived from data given in tables 1, 2, and 3 of reference 2. Adding a 1-mm thick C–C jacket, assuming a density of 1,500 kg/m^3, would add 0.126 kg/m which would result in a overall linear density of 0.637 kg/m. Assuming a TC of 300 W/m-K, an emissivity of 0.9 and optimizing the fin geometry using the method described in, the specific power was estimated to be 770 W/kg at 425 K—almost twice the estimated specific power of 395 for the 1-in heat pipe panels described in reference 2.[5] The 425 K represents the area weighted average of the heat rejection range of the Brayton cycle, so this temperature was chosen as the comparison base.

The optimized fin geometry called for fins 173-mm wide that taper from 1 mm at the root to a knife-edge at the tip. Use of higher conductivity material would require a root thickness of much less than 1 mm to achieve optimal performance, and it was felt that a root thickness of 1 mm was about the minimum if the panel was to survive the launch environment. The length of the fin is determined by the power the heat pipe can deliver. It was assumed that the 1-in diameter heat pipes, described by Anderson and Stern, could deliver sufficient power to make the condenser/fin 1.9-m long, as shown in figure 216. The following technical issues are to be addressed:

- Can a fin of such a geometry be fabricated?
- Can it withstand thermal cycling without debonding?
- Can it deliver the estimated thermal performance?
- Will it stand up to launch vibrations?

An RFP was released in July 2005 for a prototype heat pipe/fin radiating element based on the geometry shown in figure 216. It soon became clear that the available budget would not support an actual heat pipe/fin prototype so a revised RFP was released in November 2005 for a composite fin and jacket surrounding a 1-in diameter Ti tube, with the idea of installing a heater later to simulate the Ti-H2O heat pipe. The proposal from ATK Space Systems in San Diego, CA was selected in December 2005 and the test article was delivered in March 2006.

GFRC became the material of choice for the fin and jacket based on its combination of conductivity (along the fiber direction), density, strength, and fracture toughness. The fin and jacket over the Ti tube was fabricated with multiple layers of K13D2U graphite fibers in EX1551 cyanate ester polymer prepregs with a rating of 300 W/m-K. Higher conductivity graphite fibers are available, but it was felt that the fin thickness required for structure integrity would not allow us to take full advantage of the higher thermal performance for the reasons mentioned previously (also the higher conductive GFRC was considerably more expensive and required a long lead time). The prepregs were laid with a crossing pattern that was designed to minimize the difference in thermal expansion between the composite and the Ti tube and to increase mechanical stability. The finished test article is shown in figure 217. The end view shows the GFRC wrapped around the Ti tube to capture its heat and feed it into the fins. The taper of the fins was achieved by varying the widths of the prepreg and sanding the finished fin smooth, tapering it to a knife edge.

The 1-in OD Ti tube has an 0.75-in ID and extends some 30 cm beyond the fin to simulate the heat pipe evaporator and to facilitate handling of the fin. Its mass is 1.595 kg. The GFRC used for the shell and fin has a density of 1,750 kg/m^3, somewhat higher than the density estimated for the C–C shell and fins. The jacket, which consists of the 1-mm GFRC wrapped around the Ti tube, has a mass of 0.291 kg. The fairing from the shell to the roots of the fins is thicker at the roots than the specified 1 mm, but was deemed necessary to improve the strength of the joint and prevent a high-stress point. This increased thickness, together with the higher than anticipated density, increased the mass of the fin to 1.034 kg—roughly twice the original estimate for the fin mass. The total mass of the test article, before the heater assembly was installed, was 2.92 kg.

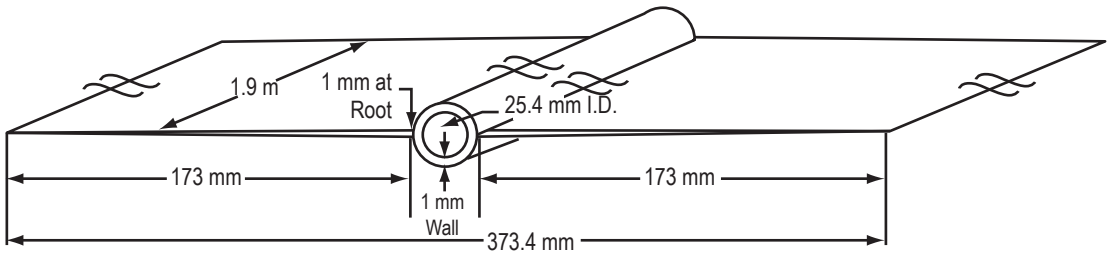

Figure 216. Specified configuration of the jacket and fin assembly for the prototype composite heat pipe/fin radiating element. This jacket will surround a 25.4-mm OD × 2.5-mm wall thickness × 220-cm length welded Ti tube that serves as a simulated heat pipe.

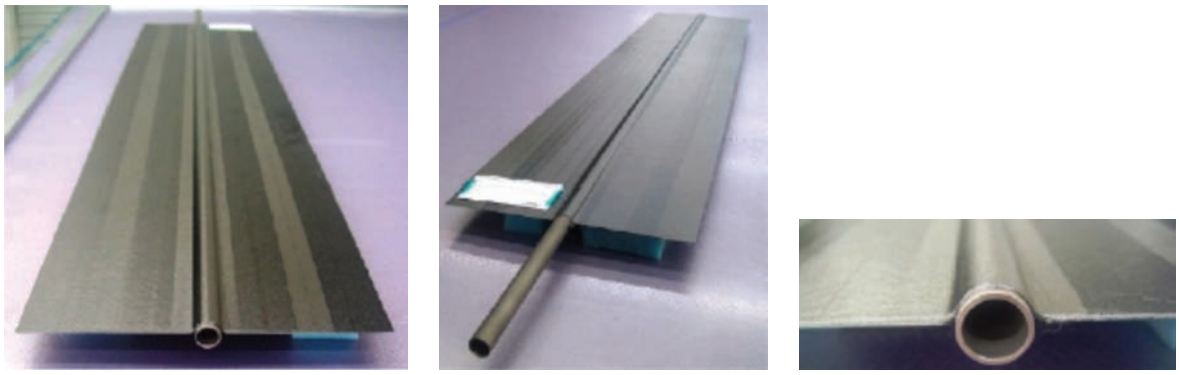

Figure 217. Prototype heat pipe/fin test article as delivered from ATK Space Systems.

GFRC emissivity was measured in situ using an AZ Technology TEMP–2000 to measure normal as well as total hemispherical emissivity. The normal incidence emissivity of the untreated GFRC was found to be 0.85 and the hemispherical emissivity 0.77, somewhat less than the 0.9 that was assumed in the optimization procedure.

A custom-made tube heater capable of supplying 3,500 W was fabricated by Durex Industries. The 0.375-in diameter Incoloy tube heater is the length of the Ti tube and the heater element is the length of the radiating fin. The heater tube was supported inside the Ti tube by Macor spacers, shown in figure 218, which also served as supports for Omega type-K thermocouples to monitor the heater tube temperature. Other Omega type-K thermocouples were fixed to the outside of the Macor spacers to monitor the Ti tube temperature. The space between the tube heater and the Ti tube was stuffed with Cu wool to aid in heat transfer from the heater to the Ti tube. The heater tube was supported at the ends of the Ti tube by Macor cylinders which protruded ≈2 in beyond the ends of the tube. To minimize heat loss to the test chamber floor, these Macor cylinders rested on thin V-notch Al supports that were isolated from the Al support stands by polyethylene blocks.

An array of type-T thermocouples were attached to the GFRC surfaces on one side of the test article to monitor the surface temperatures along the top of the GFRC jacket, the root, the middle of the fins, and the tips of the fins. Additional thermocouples were mounted in holes drilled through the GFRC so as to be in contact with the Ti tube and others were embedded into the GFRC at the root to monitor the heat flow from the shell to the fin. The other side of the radiator was thermally mapped using a Mikron M7500 thermal imager. Several reference thermocouples were located on this for side for comparison.

Thermal vacuum tests were run in the Sunspot vacuum chamber at MSFC. Power to the heater was supplied by two 100 VDC PowerTen power supplies wired in series. Current was measured using a calibrated shunt. The tests were conducted in the high 10^{-5} torr range with a LN_2 cooled shroud that was kept at a nominal 98 K temperature.

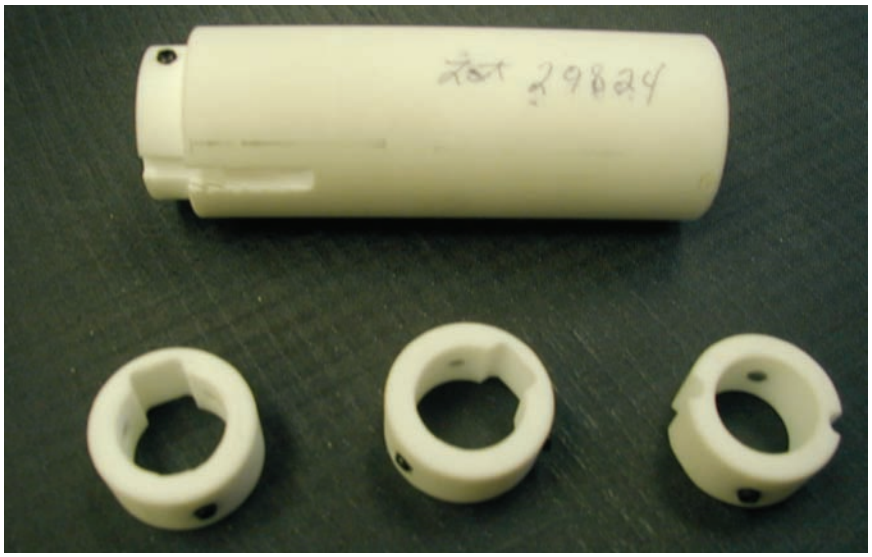

Figure 218. Macor end piece and spacers to locate the rod heater in the center of the Ti tube. The spacers are attached to the heater rod using the small-set screws. The inside notches accommodate the thermocouples that measure the heater temperature. The outside grooves allow passage of the thermocouple wires.

The voltage levels were set to provide the estimated power level at prescribed temperatures beginning at 350 K and data sets were taken after the system equilibrated at the prescribed temperatures. Thermal images were also recorded at each temperature step. After bringing the radiator to ≈550 K, the power was reduced to the power level of each of the previous temperatures to check for reproducibility. After this initial thermal cycle, the power was shut off and the test article was allowed to cold-soak overnight at 130 K. Some of the previous thermal cycles were repeated the next day to determine if any thermal properties had changed as a result of the cold soak.

Test Results

The primary temperature data was taken from the array of type-T thermocouples located along the top of the jacket at 50, 500, 725, 950, 1,175, 1,400, and 1,850 mm from the top edge of the radiator. The thermocouples at 725 and 1,175 mm were epoxied to the top of the shell while the others were embedded in holes drilled through the GFRC composite to make contact with the Ti tube. The readings taken at various power levels are shown in figure 219. There is some variation in the measured temperatures which is probably caused by nonuniformities in the density of the Cu wool that was stuffed between the heater rod and the Ti tube.

It was hoped that we might determine the temperature drop across the GFRC composite by comparing the observed temperatures of the thermocouples mounted on the surface against those embedded in the Ti tube. However, the estimated drop is only ≈2–3 °C and the variation along the axis of tube, as seen in figure 5, precluded this possibility. However, we did find an unexpected ΔT of 5–20 °C (depending on temperature) between the root and the Ti tube.

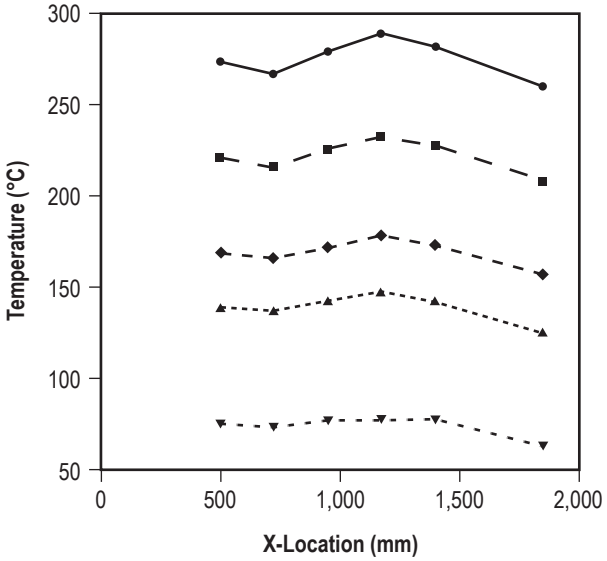

Figure 219. Measured temperatures taken at various locations along the top of the radiator jacket. The power levels were chosen to produce tube temperatures ranging from 550 K (top), 500 K, 440 K, 425 K, and 350 K in descending order.

The thermal imager viewed the top surface of the radiator from about 700–1,200 mm panel, a typical thermal profile is shown as in figure 220. Some variation in temperature can be seen along the middle heated portion, probably due to variations in the density of the Cu wool used as the heat transfer medium, as was discussed previously. Two thermocouple wires can be seen as well as the Kapton tape holding them in place. Transverse scans across the fins showed almost perfect symmetry, as would be expected.

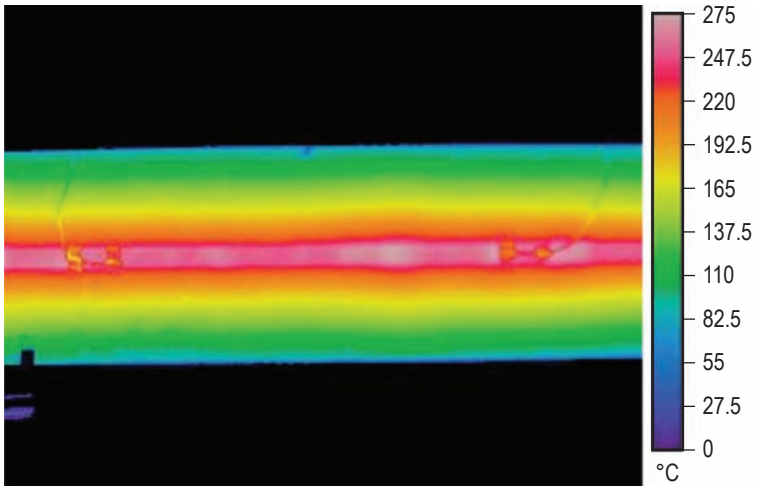

Figure 220. Thermal image of test article at 550 K. Top thermocouples and leads are visible. Temperature variations along the heated core are due to the nonuniformities of the Cu-wool between the heater rod and the Ti tube.

The temperatures indicated by the radiometer along the central curved jacket region were generally 10–15 °C lower than the thermocouple data, while the indicated temperatures along the fins were generally in close agreement with the measured fin temperature at the root and tip. Since the radiometer is not viewing normal to this curved surface, the lower readings on the curved jacket portion are probably due to the fact that the hemispherical emissivity is lower than the normal emissivity.

A simple radiation transport model was developed to predict the power settings at each temperature. The model assumes the GFRC jacket temperature is the same as the tube temperature and radiates into the cold wall as a two-sided flat plate with the measured hemispherical emissivity. The roots of the fin are assumed to be at the same temperature as the jacket and the fin temperature is computed numerically assuming one-dimensional conductive heat flow through the tapered fin together with radiation from both sides of the fin into the chamber cold walls.

A transverse plot of predicted and measured temperatures at 550 K is shown in figure 221. The open squares are the predicted temperatures across the fin, which assumes that the temperature at the root of the fins is the same as the tube temperature. The thermocouples that were mounted to the flat portions of the GFRC did not stick to the surface very well. Several came loose and the ones that did not consistently read colder than expected, presumably because of poor thermal contact. The temperatures from the thermal imager, shown as the solid line in figure 221, agreed with the thermocouple temperatures at the tip and at the root and are therefore considered the more reliable.

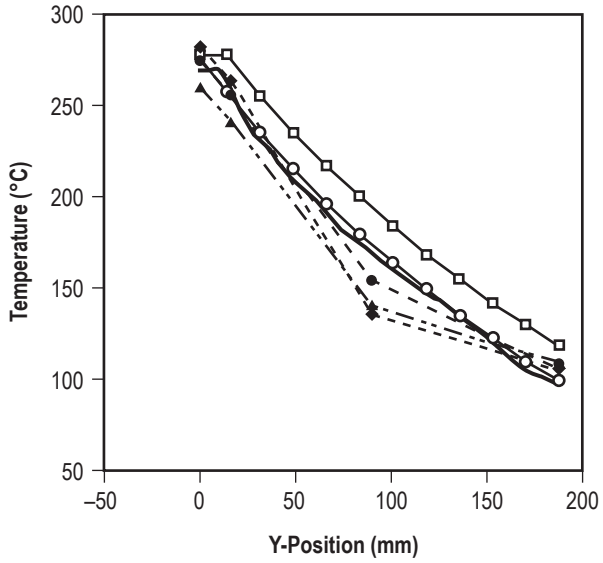

Figure 221. Transverse temperature distribution across the fin at 550 K. The heavy lines are the IR measurements and solid dots are the thermocouple temperatures. The open squares are the ideal fin temperatures and the open circles are the fin temperatures computed from the corrected model.

The average of the temperatures taken along the tube in figure 219 is plotted against the power being supplied in figure 222 (a) along with the power predicted from the simple radiation transport model. At first glance, the close agreement between the measured versus calculated temperatures at the various power levels is very encouraging. However, the measured tip temperatures fall consistently below the predicted temperatures, as may be seen in figure 222 (b).

The lower than expected tip temperatures could be at least partially explained by the fact that the observed root temperatures were ≈5–20 °C lower than the tube temperature over the range 350–550 K, as seen in figure 221. Lowering the RT in the 550 K case by 20 °C in the radiation transport model only reduces the tip temperature by ≈6 °C. To match the observed tip temperature at 550 K, it was necessary to reduce the effective TC of the GFRC from 300 W/m-K to 250 W/m-K. This lower effective TC should have been anticipated as a result of crisscrossing the GFRC fibers.

The revised model calculations, shown as the open circles in figure 221, closely match the transverse temperature profile obtained from the thermal imager. The tip temperatures calculated from the revised model also closely match the observed values, as seen in figure 222 (b). Therefore, we are confident that the radiated power computed from the revised model in figure 222 (a) describes the actual power radiated from the test article and that the difference between the measured power supplied and the calculated power radiated are losses in the system, which will be discussed in the Posttest Inspection section.

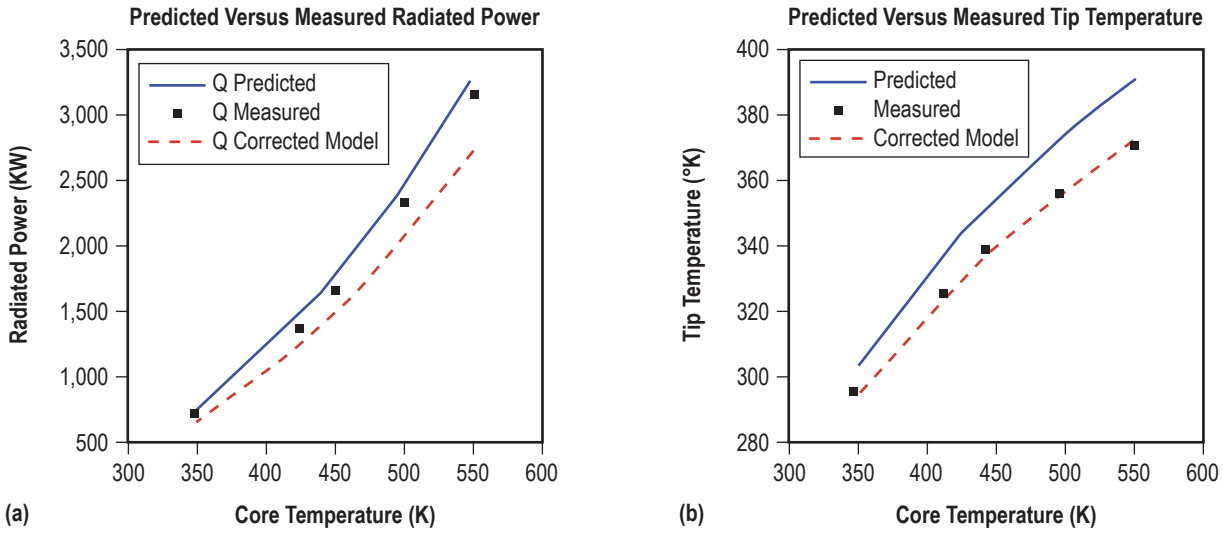

Figure 222. The predicted and measured radiated power is shown in (a). However, the lower than predicted tip temperature, shown in (b), indicates the TC of the GFRC was less than expected, which caused a revision in the estimate of the actual heat radiated, as shown by the dashed curve in (a).

Effect of Thermal Cycling. After raising the temperature of the Ti tube to 550 K, the power settings were reduced to the same levels used during the initial heating sequence to test for repeatability and to see if the high-temperature thermal stresses had in anyway changed the thermal properties. After the data set at 350 K had been taken, the heater power was turned off and the panel was allowed to cold

soak overnight. A sequence of reheating to 350 K, 425 K, and 440 K was then performed. The results are shown in figure 223. It may be seen that the thermal profile at 500 K, second set from the top, remained virtually unchanged after exposure to 550 K. A slight drop in the profile of the third set, 440 K, a slight increase in the fourth (425 K) set, and a more significant drop in the bottom (350 K) set. The slight increase in the 425 K set can be explained by the fact that the power setting was 14 W higher than on the previous run.

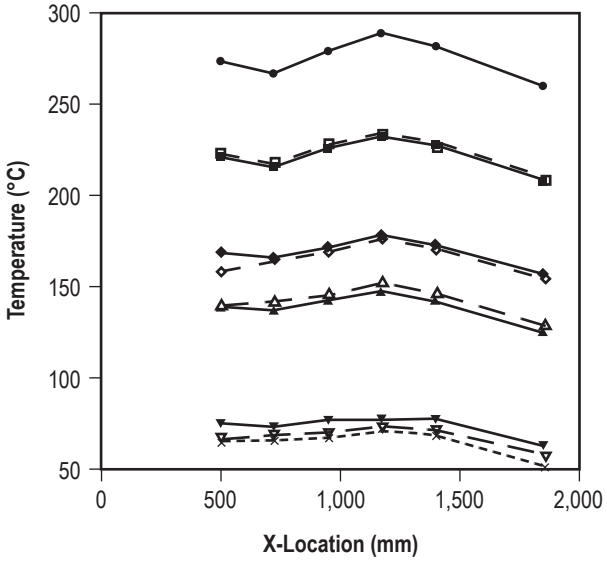

Figure 223. Horizontal profiles of the Ti tube temperature as a result of thermal cycling. The solid lines represent the temperatures at the first heating, the dashed lines are the temperatures after exposure to 550 K, and the dotted line is the temperature after the cold soak.

Posttest Inspection. The most obvious damage observed when the test article was taken from the chamber was the cracks in the Macor support rod at the top of the radiator shown in figure 224. This support rod is directly attached to the end of the heater rod by three small-set screws only an inch from the heated region and was also attached to the Ti tube by two small screws. The intent was to pin this end of the heater rod to the Ti tube and allow the thermal expansion of the heater rod to be taken up by expanding into the extension of the tube at the lower end. During assembly, the heater assembly was inserted through the top end of the Ti tube while packing the Cu wool between the heater and the Ti tube. It became increasingly difficult to move the heater assembly over the last few inches because of the friction due to the packing of the Cu wool. Apparently this friction from the Cu wool was greater than the strength of the Macor and the heater tube expanded from the top end, exposing a portion of the heater rod that ran at 975 K when the tube was at 550 K. The radiation from this exposed heater rod could account for at least some of the difference between the measured power and the calculated power radiated from the panel. There was probably some conductive heat loss through the Macor supports and through the thermally isolated V-notch supports to the cold floor of the chamber. Unfortunately, these supports were not instrumented, so the amount of conducted heat loss is not known.

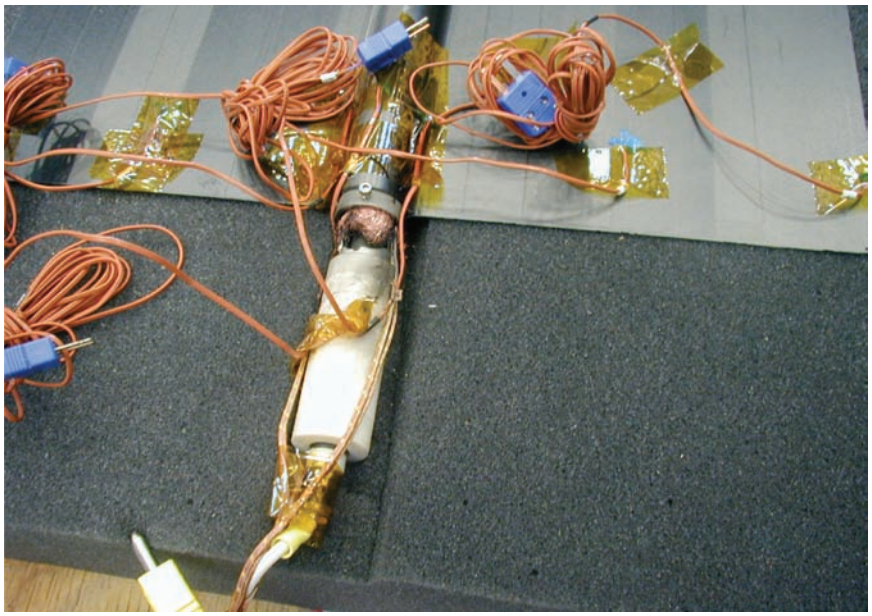

Figure 224. Posttest photo showing cracked ceramic fitting. The heater rod was attached to this ceramic tube, which in turn was pinned to the Ti tube. Thermal expansion of the heater rod was supposed to force the other free end farther into the extended portion of the Ti tube. Apparently, the friction from the Cu wool prevented this from occurring, causing the heater rod to break the top ceramic fitting and extend beyond the Ti tube.

From the thermocouple data, it appears the crack in the Macor support occurred as the temperature was initially being raised from 425 K to 440 K. If so, then all subsequent data sets were taken by a radiator with a slightly degraded coupling between the heater and the Ti tube. Therefore, the first data set at 325 K and 425 K, shown in figure 222, would be expected to be slightly higher than the subsequent data sets taken at the same power settings. This would explain why the initial data set, taken at 350 K, was higher that the subsequent sets, but it doesn't explain why the third data set, taken at 425 °C, almost identically matches the first data set that was taken before the Macor break occurred.

Additional inspection revealed the fin had slight wrinkling that was more pronounced on one side than the other, as seen in figure 225. There were also some small (≈mm) squares missing from the knife-edge of the tapered fins, figure 226, that must have spalled off during thermal cycling. No doubt, these slight mechanical defects were due to thermal stress from the extreme range of temperatures the system was subjected to. However, no debonding was noticed and the thermal properties appeared to remain unaffected.

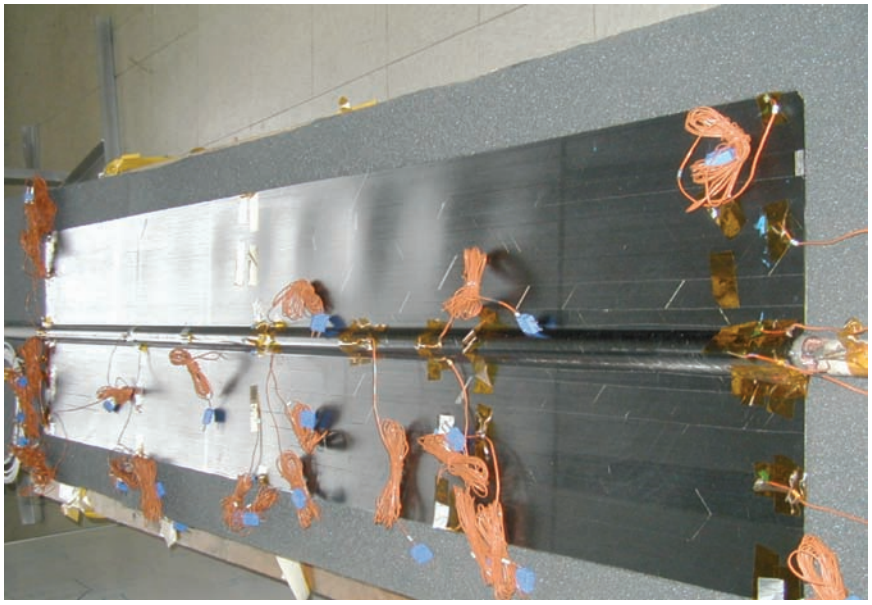

Figure 225. Test article after removal from the chamber. Note a slight wrinkling in the right panel due to extreme thermal gradients during the thermal cycle. In spite of this distortion, no debonding was evident.

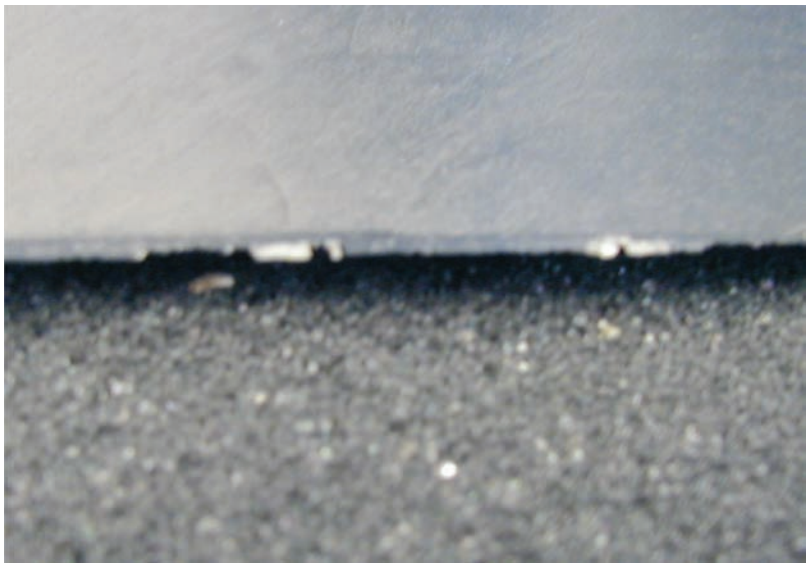

Figure 226. Posttest appearance of the tapered edge of the radiator panel. Small chips, ≈1-mm sq, apparently spalled off the razor edge due to stresses during the thermal cycling.

Conclusions

GFRC composites seem to be an ideal choice for a composite heat pipe/fin space radiator. It is tough and flexible and is neither frangible nor fragile. No evidence of any outgassing products from the material were seen on the vacuum chamber's mass spectrometer. We have demonstrated the ability to fabricate an integral jacket and thin tapered fins that can withstand large temperature excursions without debonding or showing any change in thermal properties. The crisscrossing of the fibers adds strength and stability to the structure was successful in matching the thermal expansion of the Ti tube. The loss of effective TC due to this patterning can easily be compensated for by using higher conductive fibers that are available, but more costly.

The measured emissivity of the GFRC composite is slightly lower than expected. Methods for improving the emissivity of this material without adding weight need to be investigated.

The heat transfer from the Ti tube simulating a Ti-H_2O heat pipe was not as good as was hoped for, resulting in a 5–20 °C drop, depending on the tube temperature, between the tube temperature and the fin temperature at the root. This could probably be improved by changing the way the GFRC is laid up.

Using the modified model that takes into account the observed temperature drop between the Ti tube and the root and the lower effective TC of the crisscrossed GFRC, it appears that the radiator was actually radiating several hundred W less than the power being supplied to it. It is assumed that the cracked Macor heater support, that allowed the heater to protrude from the end of the test article and radiate at high temperature, together with the unknown heat leaks through the isolated V-notched supports can account for this discrepancy.

Even so, from the corrected radiation model, the estimated power radiated at 425 K to the chamber cold wall is 1,259 W versus the 1,376 W supplied. The estimated power radiated to 0 K would then be 1,264 W. If the Ti tube had been replaced with the Ti-H_2O heat pipe as assumed in the optimized model, the mass of the panel would be 2.294 kg and the Q/M would be 551 W/kg, considerably more than the 395 W/Kg estimated for the Anderson panel radiator. Therefore, we have demonstrated that it should be possible to construct a heat pipe radiator/fin with a Ti shell that is more efficient than the same Ti shell heat pipe used in a panel arrangement.

Fixing the heat loss from the heat pipe to the fin root, raising the effective conductivity to 300 W/m-K, and increasing the emissivity to 0.9 would increase the radiated power to 1,578 W and raise the Q/M to 688 W/kg, approaching the optimum value of 771 W/kg. The difference of 83 W/kg is primarily due to the slightly higher than estimated density of the GFRC and the additional material added to the root of the fin for mechanical stability.

Outlook For Composite Heat Pipe/Fin Radiators. Since the specific power of a heat pipe/fin radiator element is inversely proportional to the linear density of the heat pipe and jacket, the real advance in specific power comes from reducing the linear density without reducing the area, hence the power the heat pipe can deliver. Therefore, the major effort should be to make the heat pipe as light as possible by having the C–C or GFRC jacket, lined with thin metallic foils, serve as the pressure shell, as demonstrated by Juhasz.[3] The 2.54-cm diameter × 91-cm Nb-1Zr lined C–C heat pipe developed by

Juhasz had a total mass of 0.291 kg, of which 0.169 kg was the C–C shell. The remaining 0.122 kg included the foil liner, end caps, fill tube, wick, and working fluid. If a similar Ti foil heat pipe could be constructed inside a 2.54-cm diameter × 1-mm thick GFRC jacket, the linear density could be reduced from 0.637kg/m to 0.279kg/m. Using the optimization formulas given in reference 5, the specific power could, in theory, be increased to 1,330 W/kg at 425 K; but this would require an unrealistic fin thickness of 0.5 mm at the root. A different optimization procedure to assume a realistic root thickness will have to be developed, which obtaining the specific powers in excess of 1,200 W/kg at 425 K it is reasonable to assume the specific powers in excess of 1,200 W/kg at 425 K could be obtained.

To put this in perspective, a mission such as JIMO which must radiate ≈364 kW would have to devote 921 kg to the radiator panels, whose specific power averaged 395 W/kg. This could be reduced to 529 kg by using composite heat pipe/fins with a specific power of 688 W/kg, and further reduced to 303 kg by using the foil-lined composite heat pipe/fins.

Acknowledgements

The authors wish to thank each of the following for their support of this effort: Mary Beth Cook, the Deputy Project Manager, New Projects and Partnerships Development at MSFC, who funded this work through Cooperative Agreement NNM05AA2A; National Space Science and Technology Center; and Twila Schneider, AME Task Coordinator at Marshall, who served as the COTR. We are especially grateful to Randy Powers and other members of the MSFC Environmental Test Facility, for their supporting effort during the thermal vacuum testing.

References

1. Mason, L.S.: "A Power Concept for the Jupiter Icy Moons Mission," *NASA/TM—2003–212596,* 2003.

2. Anderson, W.G.; and Stern, T.: "Water Heat Pipe Radiator Trade Study for the 300–550 K Temperature Range," *Proceedings of Space Technology and Applications Forum* (STAIF 2005) edited by M. S. El-Genk) AIP Conference Proceedings CP764, 2005.

3. Juhasz, A.J.: "Design Considerations for a Lightweight Space Radiators Based on Fabrication and Test Experience With a Carbon-Carbon Composite Prototype Heat Pipe," *NASA/TP—1998–207427/ Rev 1*, September, 2002.

4. Juhasz, A.J.; and Rovang, R.D.: "Carbon-Carbon Heat Pipe Testing and Evaluation," *NASA TM—1994–106630*, July, 1994.

5. Naumann, R.J.: "Optimizing The Design Of Space Radiators," *Int. J. Thermophys*. Vol. 25, pp. 1929–1941, 2004.

7.8 Aerocapture Advanced Ablative Thermal Protection System Development

PI—William Congdon, Applied Research Associates, Centennial, CO.

Aerocapture is an advanced propulsion technology currently under development at NASA. Aerocapture is an in-space propulsive maneuver that utilizes drag with an atmosphere to slow an incoming spacecraft and place it into final orbit, in lieu of propulsive fuel. Utilizing aerocapture for orbit capture at the destination saves fuel, saves mass, allows for reduced trip time, and saves overall mission costs.

A number of planetary aerocapture missions of interest to NASA pose entry heating environments with moderately severe radiation levels from 100 to 150 W/cm^2. Candidate ablative TPS materials for these missions are light to medium-weight materials with densities from .22 to .32 g/cm^2 (14–20 lb/ft^3). Of high interest is their response to the radiative heating that would be experienced during the atmospheric entry phase of the aerocapture mission.

To evaluate performance, a comprehensive test program was established. A key facility that was used was the Sandia Solar Tower Facility at the Kirtland Air Force base in Albuquerque, NM. The Sandia Solar Tower, shown in figure 227, was selected for thermal radiation characterization testing of candidate charring ablators for future aerocapture missions. By use of solar collectors, the facility is able to generate a radiation flux of up to approximately 300 W/cm^2 over a sufficiently large sample surface. The collectors are individually computer controlled, allowing radiation to be a shaped pulse as well as a square wave in terms of intensity versus time. Test samples, shown in figure 228, are mounted high in the receiver tower.

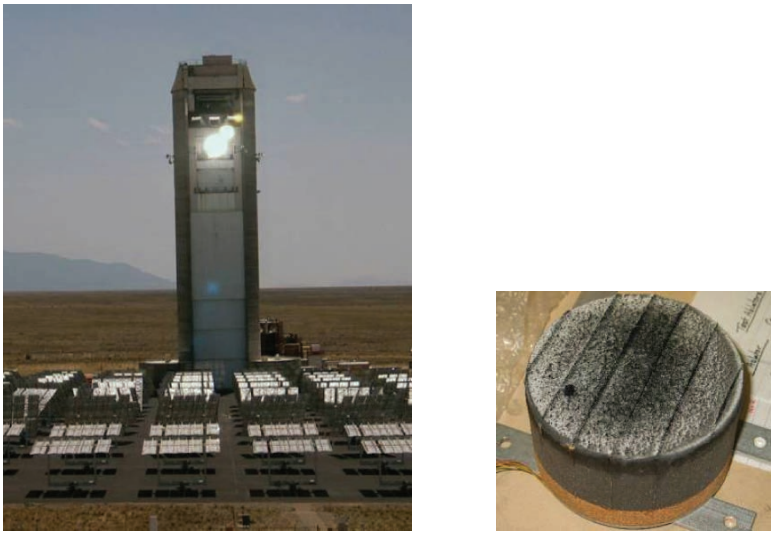

Figure 227. Solar tower test of ablator coupons

Figure 228. Solar tower test of ablator panel.

Under this task, 5-in diameter TPS test samples have been tested, as well as 12-in panels and 24-in panels of TPS and supporting structure. A wide range of exposure times were used to test and characterize the ablative materials. All of the ablators showed good performance against the radiative heating environment. Thermal response models for each ablative candidate are being refined to provide critical design data that can be utilized for future aerocapture missions.

APPENDIX A—SPECIAL STUDIES

A.1 Lightweight Materials Trade Study

A.2 Survey of Radiation Issues and Materials Development

A.3 Environment Stress Cracking of Nonmetals

A.4 Long-Term Use Effects of Lubricants and Seals

A.5 Lunar Environment Materials Exposure Test-Bed—Report and Presentation

A.6 Aerocapture Instrumentation Shortfall Assessment

Study 1
Lightweight Materials

OBJECTIVES

- Identify current radiator coatings and structural materials used on space hardware
- Identify cutting edge materials in these areas
- Identify tests and simulations needed to increase the CRL of newer materials
- Support work needed with documented references and contacts

FOCUS AREAS

- Structural Materials
  - Metals
  - Metallic based composites
  - Polymer / carbon based composites
  - Carbon nanotube composites
- Radiator Coatings
  - Low temperature coatings
  - High temperature coatings

CONCLUSIONS

- Structural Materials
  - Moving steadily from metals to composites
  - ~15 years from cradle to flight for new materials
  - A defined application ⇒ best chance of success for of new material
  - Significant weight savings available in secondary structures – lower requirement hurdles
  - Decrease prototype & manufacturing costs key for greater composite use
  - Metal Matrix Composites are underutilized
  - Carbon nanotube composites show great promise
- Radiator Materials
  - Dust management is key to Lunar applications

RECOMMENDATIONS

1. Use Al-Be alloys in manned environment by resolving health issues
2. Identify candidate hardware for MMCs
3. Assess potential development of Al laminate using XRF1
4. Assess application of ALONtm for surface suit face shields
5. Assess improved FRPC matrix behavior through small % addition of carbon nanotubes
6. Develop new radiator coating
7. Develop Lunar/Mars dust removal device compatible with coating

Study 2
Survey of Radiation Issues & Materials Development

OBJECTIVES

- Identify materials radiation issues for Exploration Missions
- Identify what is being done in response to these issues
- Recommend materials for an evaluation test plan
- Identify gaps in materials development

FOCUS AREAS

- Exploration Mission environments
- Materials flight heritage
- High payoff materials
  - Mission enabling/enhancement
  - Multifunctional
  - High radiation resistance potential
- CEV/CLR/Cargo vehicle applications
- In-situ resource utilization

CONCLUSIONS

- **Long duration Exploration Missions present new materials challenges**
  - **Different environments than LEO**
  - **Repairs/Replacement impracticable/cost prohibitative**
  - **Long life/ high reliability mandatory**
- **Long term effects of deep space environments on materials performance not known**
- **Lunar Test Bed needed to provide design data**
- **Radiation induced outgassing not being addressed**
- **Materials development needed for high priority radiation protection, thermal management, and lunar resource utlization applications**

RECOMMENDATIONS

A. Develop following materials (CRL 3 or above)
1. MSFC RXF1 Composite
2. RF Aerogel Composite Insulation
3. X Aerogel Composite Insulation
4. Carbon-Polymer Composite
5. Sulfur Binder for Lunar Regolith
6. Ceramer Protective Coating
7. Tailorable Conductive Coating

B. Investigate radiation induced outgassing of habitable environment materials

Study 3
Environmental Stress Cracking of Non-Metals

OBJECTIVES

1. Document non-metals uses and failures in space hardware
2. Document critical gaps in existing materials databases
3. Identify ground-based ESC test capabilities
4. Recommend materials for further characterization
5. Develop a test plan

FOCUS AREAS

- Polymers
- Extended Missions
- Spacesuits
  - Multi-layer insulations
  - Other films
  - Fiber fabrics
  - Bulk polymers
- Spacecraft structures
  - Composite matrices
  - Fiber reinforcement
- Habitats
- Rovers

CONCLUSIONS

1. Future space **missions are at risk**
   Multiple ESC and suspected ESC failures of space hardware are documented
2. **Data are sparse**
3. While test capabilities abound, there is **no NASA validated test method**
4. A list of materials has been provided
   These were chosen for likelihood of use, not ESC resistance
5. A test plan is recommended

RECOMMENDATIONS

1. Develop or validate a standard NASA ESC test method
2. Test target materials in single component environments
3. Write NASA ESC materials selection Design Specification
4. Test target materials in multi-component environments
5. Test target materials in *in-situ* environments
6. Develop or validate accelerated ESC testing

Study 4: Long-Term Use Effects of Lubricants and Seals

Objectives:

1. Document state-of-the-art for lubricants and seals
2. Identify gaps between current material capabilities and requirements of materials in space applications
3. Identify ground-based Lubricant and Seals test capabilities
4. Develop a test plan

Focus Areas:

- Space Applications
  - Spacesuit
  - Vehicles
  - Structures
- Liquid and Solid Lubricants
- Seals and Sealing Mechanisms

Conclusions:

- Current lubricants and seals are inadequate for long duration space missions.
- Evaluation is needed on Materials in Primary Areas:
  - Liquid Lubricants
  - Solid Lubricants
  - Hard composite Coatings and Solid Bodies
  - Rolling Element Bearings
  - Spacesuit Sealing and Lubrication
- Earth-based test capabilities are dispersed.

Recommendations:

1. Develop a long-term development plan for lubricants.
2. Develop a long-term development plan for seals.
3. Identify near-term alternatives to new materials for space applications.
4. Determine a near-term testing plan for existing lubricants and seals.
5. Develop a lunar test bed for lubricants and seals.

Study 5
Lunar Environment Materials Exposure Testbed (LEMET)

OBJECTIVES

1. Address the design, development, and performance of a long term materials test bed on the lunar surface
2. Identify the testing and simulations needed to demonstrate the materials' suitability for lunar and Mars missions
3. List rationale for testing on the lunar surface versus earth-based testing
4. Plan for sufficient exposure time to gain a realistic assessment of lunar missions
5. Recommend materials for testing
6. Design and package experiments using inputs from Advanced Materials for Exploration (AME) teams

GUIDELINES AND ASSUMPTIONS

1. Launched along with Robotic Lunar Exploration Program (RLEP) mission
2. Landing on moon accomplished using RLEP Lander
3. Test bed deployed and activated autonomously
4. Test data taken for two years, periodically sending status to earth
5. Provisions for crew-return of test panels, if opportunity arises following testing

STATUS

1. Design Requirements document has been generated and is included in final report as appendix A. Includes all requirements from buildup thru launch, ascent and descent, deployment and return. Includes a listing of all tests and their individual requirements.
2. Conceptual designs have been formulated, including all subsystems, sensors, and instrumentation with requirements for each.

Study 6: Aerocapture Instrumentation Shortfall Assessment

Objectives:

1. Research and identify currently available instrumentation, such as pressure, thermal, and stress sensors, for aerocapture/ballutes and regression rate measurements for ablatives in aeroshells.
2. Assess available instrumentation capabilities/applicability for aerocapture requirements.
3. Identify and document current instrumentation materials related shortfalls in order to provide insight into areas where advancement in materials and/or processes might significantly improve utility of the instrument for the aerocapture mission.

Focus Areas:

- Aerocapture/ballutes
- Aeroshells
- Sensor Technology
  - Thermal
  - Pressure
  - Stress/Strain

Conclusions:

- Non-usable sensor technologies for ballutes:
  - Optical fiber technology
  - Most standard pressure-measuring techniques
  - Thermocouples and thermistors
- Usable sensor technologies for ballutes:
  - RTDs
  - Strain gage and capacitance techniques for pressure
  - Thin film, bonded metallic wire, and semiconductor techniques for strain
- Enhancements to MEMS production:
  - Simplification of the photolithographic masking steps and/or process geometries to enhance throughput, availability, delivery, and cost
  - Improved sensitivity for transducers
  - Improved etching to provide better diaphragm thickness control
  - Reduced conflict between the fabrication requirements of microelectronics and of optimal sensing

Recommendations:

1. Two of the most significant improvements needed in materials science are developing materials to
   - Minimize the thermal coefficient of resistance by design or compensation and
   - Reduce the thermal coefficient of expansion of the substrate to match the CTE of the die and the die attached materials.
2. Explore silicon carbide and silicon nitride and other materials.
3. Test use of conductive threads for electrostatic charge dissipation, and measuring pressure, stress, and temperature.
4. Research battery manufacture to help with power management.
5. Develop high temperature materials for MEMS components.
6. Study thin films of materials such as indium-tin-oxide (ITO) for strain measurements on ballutes.
7. Develop robust adhesives for use with ballute sensor technologies.

APPENDIX B—TASK FACT SHEETS

Materials Characterization

Stardust Materials Analysis

NASA Marshall Space Flight Center

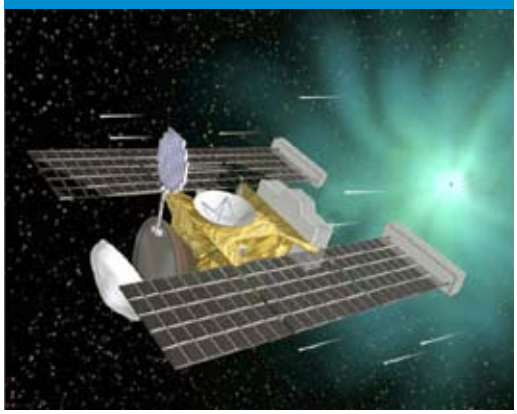

In January 2006, after a nearly 7-year-long voyage through space to and from a rendezvous with Comet Wild 2, the Stardust spacecraft released a sample return capsule that reentered Earth's atmosphere and parachuted to a soft landing in the Utah desert. While the mission's primary science goal was to capture and return cometary and interstellar dust particles, the capsule and science hardware themselves also returned critical information about how materials weathered the harsh space environment. During the mission, the capsule's components (heat shield and back shell, drogue and main parachute, parachute cords, thermal control surfaces, fasteners, lubricants, adhesives, seals, and electronics) were exposed to the combined effects of ultraviolet radiation, charged particle radiation, high vacuum, and extreme temperatures; these conditions cannot be fully simulated on Earth. This is a unique opportunity for materials engineers to analyze hardware returned from space; what they learn about material behavior and property changes during long-term operation and exposure in space will be applied directly to the materials selection and design of future robotic and human missions.

Task Description

At Johnson Space Center's Stardust curation site, the Principal Investigator will make non-destructive measurements of non-primary science hardware items to assess their durability in the space environment. Of special interest are:

- Ablative materials that protected the blunt body capsule and its payload from the heat of reentry
- Other flight components (avionics box, thermal control surfaces, and deployment/retraction mechanisms).

Data from these non-destructive tests will be compared to existing data for the materials, and a lessons-learned report will be published. Postflight materials data will be archived in the NASA Materials and Processes Technical Information System (MAPTIS) databases. This 10-month study was initiated in December 2005 and will be completed in August 2006.

The Stardust sample return capsule lies in the Utah desert, having traveled 2.88 billion miles before its return to Earth. The gray-blue material covering the left half of the capsule is Phenolic Impregnated Carbon Ablator (PICA), the thermal protection system that shielded the capsule and its contents from the extreme temperatures experienced during travel through Earth's atmosphere. In the artist's concept (above, left), the Stardust spacecraft approaches Comet Wild 2. The sample return capsule is on the left of the spacecraft, with its cosmic dust collector extended.

STARDUST MATERIALS ANALYSIS

Anticipated Results

Non-destructive measurement techniques applied to the Stardust non-primary science hardware will yield data on solar absorptance and infrared emittance. Increases in absorptance may indicate damage related to radiation, while changes in emittance, along with absorptance, affect thermal properties and may indicate degradation of performance beyond desired end-of-life properties. Torque measurements on fasteners may expose galling or reveal other mechanism failures and will be used to evaluate breakaway and running torque values to compare with preflight values. (These measurements may be obtained from the Stardust disassembly team.) Visual and photographic observations of material conditions, particularly of the aeroshell, will show how well the spacecraft's trajectory and its aeroshell heatshield protected the sample return canister.

Postflight analyses may also help determine the source of contamination that affected the spacecraft's navigation camera early in the mission. Black light illumination will reveal particulate and molecular contamination, samples of which will be identified using Fourier Transform Infrared diffuse reflectance measurements. Identification of venting patterns and contaminant deposition on the sample return capsule will assist the Stardust team in determining where this contamination originated. The Principal Investigator will publish a NASA technical paper detailing the spacecraft materials' conditions, measurements performed, evaluation of durability in the space environment, and recommendations for further testing.

Potential Future Activities

The techniques and data used for this non-destructive postflight assessment of materials properties can be used in the future for the analysis of hardware returned from the Moon and other planets. While each returned mission will have its own lessons and opportunities for future experiments, comparing data from several missions will reveal how the harsh environmental conditions in space erode material, component, and system performance. In addition, researchers will gain insight into new uses for the analysis techniques and develop new protocols that may improve their sensitivity. Marshall Space Flight Center has the facilities, equipment, and materials properties expertise to perform this and future returned flight hardware assessments.

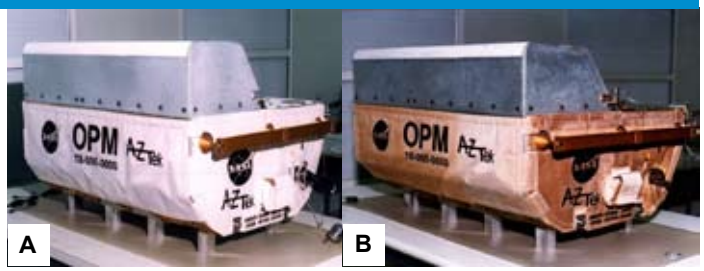

Multi-layer insulation (MLI) blankets covering the sides of the Optical Properties Monitor darkened unexpectedly [preflight (A); postflight (B)] during its 9-month exposure aboard the Mir space station. Postflight analyses showed that exposure to solar ultraviolet radiation in the vacuum of space degraded the thermal performance of one component of the MLI, causing the color change. Analyses of the Stardust capsule are expected to identify materials changes related to space exposure that will improve the ability of designers to select long-lived materials for future spacecraft.

Capability Readiness Level (CRL)

This Advanced Materials for Exploration (AME) task will analyze subsytem-level flight hardware, confirming the CRL of 7 for these materials and adding safety and reliability data that prove the materials' performance. This knowledge will assist scientists, materials engineers, and designers in developing improved materials or material protection systems for future spacecraft, including those that carry humans far from Earth.

Principal Investigator
Miria Finckenor, NASA/MSFC, Miria.M.Finckenor@nasa.gov, (256) 544-9244

AME Contact/Project Lead
Beth Cook, NASA/MSFC, Beth.Cook@nasa.gov, (256) 544-2545

National Aeronautics and Space Administration

Marshall Space Flight Center
Huntsville, AL 35812

www.nasa.gov

FS-2006-06-68-MSFC

Materials Characterization

MISSE-6 Materials Selection

NASA Marshall Space Flight Center

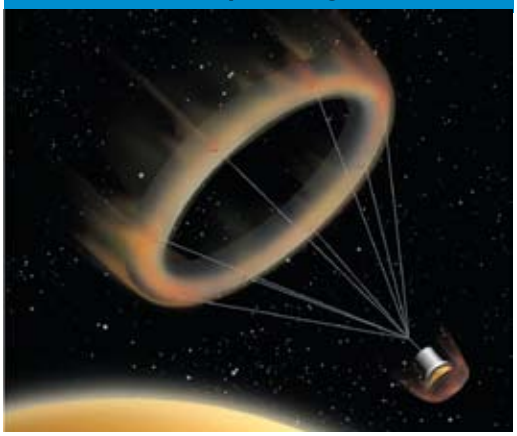

It is important to understand materials' behaviors in the environments where they will operate. No simulator on Earth can duplicate the combined effects of the space environment: radiation, micrometeoroids, space vacuum, and thermal cycling. The Materials on International Space Station Experiment (MISSE) allows researchers to place materials in suitcase-size containers outside the International Space Station (ISS) and to study their response to space environment exposure. Spacecraft designers use these data to select materials that are durable. To provide access to information on numerous materials, industry, academia, and government agencies collaborate to develop the MISSE experiments. For past MISSE experiments, researchers at NASA's Marshall Space Flight Center (MSFC) have selected materials that will be useful for diverse applications such as launch vehicles, lunar spacecraft, and space telescopes.

Task Description

Based on the results from previous experiments (MISSE-1 and -2) recently returned to Earth in August 2005, MSFC materials scientists are designing a module for the sixth mission (MISSE-6) to carry samples that will be useful for advanced exploration craft.

Tasks include

1. Identifying and fabricating candidate materials
2. Testing materials in simulated space environments and for flight qualification
3. Designing a sample carrier and loading samples
4. Performing thermal vacuum bakeout of loaded samples
5. Delivering flight hardware for integration into the MISSE-6 payload.

This 10-month task will be completed in September 2006.

Anticipated Results

Inflatable ballutes – large structures that combine the traits of balloons and parachutes – are being designed to slow down payloads returning to Earth from the Moon and for missions landing on other planets and their moons. (See artist concept, top left.) Based on MISSE-1 and -2 materials performance, this Advanced Materials for Exploration (AME)

Astronauts attached the suitcase-size Materials International Space Station Experiments (upper left) to the ISS Quest airlock and exposed 750 material samples to the space environment for 4 years. In August 2005, the STS-114 mission returned MISSE-1 and -2. MISSE-5 has been deployed on the ISS since August 2005, and MISSE-3 and -4 are slated for delivery to the ISS during the STS-121 mission scheduled for July 2006.

advanced materials for exploration

MISSE-6 MATERIALS SELECTION

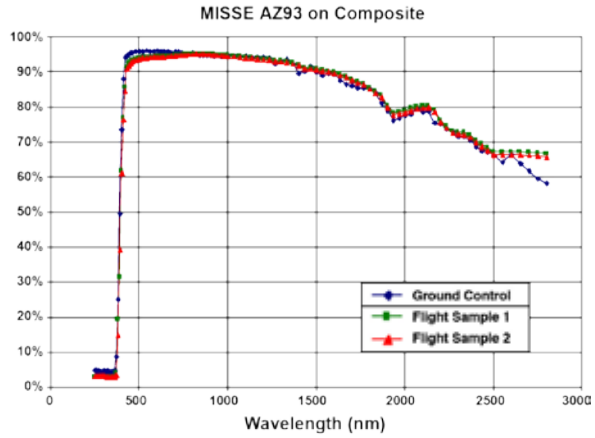

This reflectance data was collected by testing a materials sample composed of a white thermal control coating (AZ93) applied to a high-temperature cyanate ester composite substrate. The data show that even after 4 years in space, the thermal coating was stable. The coated composite, which was part of the MISSE experiment attached to the outside of the International Space Station, could be used to coat space vehicle radiators. Most thermal coatings have been tested on aluminum substrates. This was one of the first experiments to demonstrate that a coating would adhere to a composite substrate and not degrade substantially when exposed to the harsh space environment.

team recommends flying scale models of ballutes made of lightweight yet strong, high-temperature, flexible polymer films. The ballute models will be packed as if for deployment in a 15.24-cm x 15.24-cm x 3.18-cm (6-in. x 6-in. x 1.25-in.) module being designed and flight qualified by the team. The module will be thin enough to allow maximum radiation, hard vacuum exposure, and temperature variation.

The top of this module will be loaded with rip-stop fabrics and wire materials used to tow spacecraft and equipment and tethers that can propel spacecraft by harnessing electrodynamic energy. Based on prior tests and experience working with tether manufacturers, the Principal Investigator selected Spectra® and Zylon® tether materials for MISSE-6. Since tests have shown Zylon® to be very sensitive to ultraviolet (UV) radiation, a protective coating will be applied to some Zylon® tether samples so that environmental responses of coated and uncoated samples can be compared.

Solar sails use the Sun to power spacecraft and may allow more efficient deep space travel. MSFC scientists have exposed thin film sail materials to simulated space environments, including electrons, UV radiation, and meteoroid/debris impact. Based on these tests and recommendations from thin film manufacturers, materials will be selected and loaded into special compartments outfitted with UV-grade windows that prevent exposure to atomic oxygen. Atomic oxygen is abundant in low-Earth orbit where the ISS is located and can erode these materials, but it will not be present in deep space where the sails will mostly operate.

Relevant to the Crew Exploration Vehicle development is the testing of candidate thermal protection materials. These materials include ceramic matrix composites and ablatives that may be used in heat shields. Multipurpose materials also may provide shielding from harmful radiation. Some of these materials have been exposed to space environment conditions in simulators at the MSFC Materials and Processes Laboratory; these test results will be compared with effects observed during MISSE-6.

Potential Future Activities

These MISSE experiments give MSFC the opportunity to flight test materials needed for exploration programs, such as the Crew Launch Vehicle, the Crew Exploration Vehicle, the Robotic Lunar Exploration Program, and the James Webb Space Telescope. Postflight activities will focus on analyzing the MISSE-6 samples; data on materials performance will be placed in the Materials and Processes Technical Information System (MAPTIS) databases, which are accessible to spacecraft designers.

Capability Readiness Level (CRL)

This AME flight experiment will increase the CRL level of all the tested materials to CRL 7.

Principal Investigator
Miria Finckenor, NASA/MSFC, Miria.M.Finckenor@nasa.gov, (256) 544-9244

AME Contact/Project Lead
Beth Cook, NASA/MSFC, Beth.Cook@nasa.gov, (256) 544-2545

National Aeronautics and Space Administration

Marshall Space Flight Center
Huntsville, AL 35812

www.nasa.gov

FS-2006-06-64-MSFC

Materials Characterization

High-Temperature Creep Measurements

NASA Marshall Space Flight Center

At elevated temperatures, such as those inside combustion chambers for advanced rockets, many materials deform (creep) at a slow rate, even though loads and stresses remain constant. After a certain amount of deformation, the rate of creep increases, resulting in fracture. Creep causes materials to change shape, inducing failures in the hot stages of aircraft turbines, and it causes materials to rupture in steam turbines used for power generation. Creep becomes even more important for systems operated at high temperatures. Most conventional methods for measuring creep resistance are limited to temperatures below 1700 °C (3092 °F), but advanced propulsion systems may operate at temperatures as high as 3400 °C (6152 °F).

The Electrostatic Levitator (ESL) at NASA's Marshall Space Flight Center (MSFC) can be used to study materials at these high temperatures. This facility levitates 2- to 3-mm (0.08- to 0.1-in.) diameter spherical samples so that they do not contact a container and thus are not contaminated by it or react with it. This is important because the platinum group of metals, currently being developed for advanced propulsion, often react with test containers, making it difficult to obtain good creep data. Inside the ESL, only the sample is heated, not the instrument and instrumentation, and pyrometry (a non-contact temperature measurement) accesses higher temperatures than possible with traditional thermocouples. Measurements currently available or under development include creep strength, thermal expansion, emissivity, specific heat, conductivity, and phase diagrams.

Task Description

This Advanced Materials for Exploration (AME) effort focuses on developing, validating, and using the ESL to study creep resistance at high temperatures. Tasks include

1. Using centrifugal acceleration (from photon pressure and electromagnetic fields) to induce creep in levitated samples
2. Producing images of sample deformation at specified temperatures and run times
3. Providing a predictive model of stress/strain in samples.

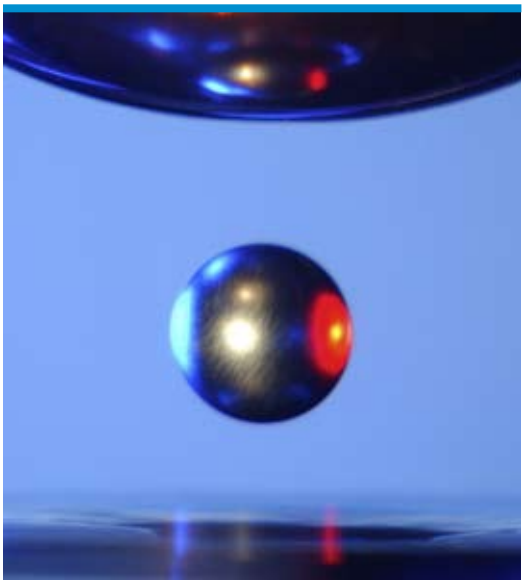

A solid metal sample is suspended by static energy from six electrodes inside the Electrostatic Levitator. The facility is being outfitted with new instrumentation for measuring creep in advanced propulsion materials at higher temperatures than those measured by most conventional creep measurement systems.

advanced materials for exploration

HIGH-TEMPERATURE CREEP MEASUREMENTS

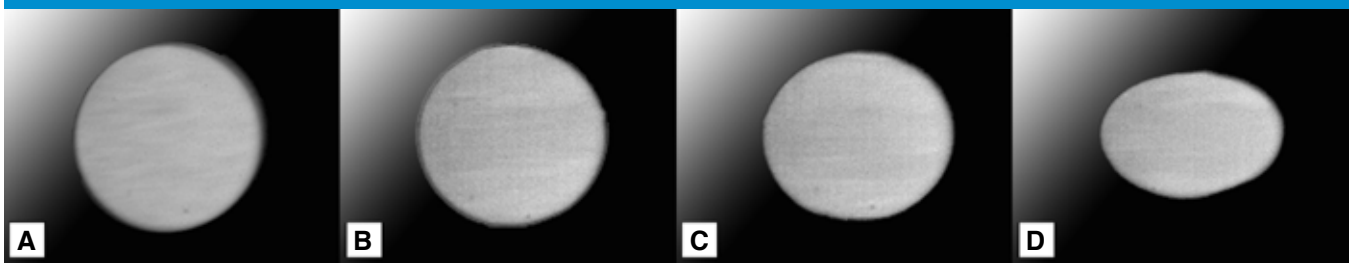

This image (A) of a 2 mm (0.08 in.) niobium sample was made after 30 minutes at 450 Hz inside the Electrostatic Levitator. The beginning of creep occurs (B) after 300 minutes at 4130 Hz. After 350 minutes at 4634 Hz, creep is accelerating, and the sample (C) is deforming. By 430 minutes at 4819 Hz, creep deforms and flattens the sample (D).

4. Supplying samples and performing validation tests using conventional test methods
5. Performing structural analysis of ESL samples to examine deformation behavior and texture development.

This 2-year effort was initiated in FY04 and will be completed in FY06.

Anticipated Results

Investigators upgraded the ESL optics to produce improved images of sample deformation. For initial system tests, samples of tungsten were melted at 3410 °C (6180 °F), and images were recorded. An integrated laser backlighting system supported creep and density measurements. This illumination system allowed images of very bright radiant samples that were being heated to high temperatures, making it easier to analyze video data. The facility has a magnetic rotation system that permits independent control of temperature and rotation.

Partners for this effort included a University of Massachusetts, Amherst, team that developed software tools for reduction and analysis of creep data and a creep model based on past experiment data. Vehicle designers can take data from the ESL measurements, put these in the model, and determine how materials might perform under various operational scenarios. A University of Tennessee, Knoxville, team fabricated and prepared samples for ESL testing, validated ESL testing, and performed microstructure analysis of samples after creep testing.

Potential Future Activities

When this system is completed, it will be the only U.S. test system capable of using a high-quality optical system to measure creep at temperatures higher than 1800 °C (3272 °F). The MSFC system can provide data for temperatures up to 3410 °C (6170 °F). It will be available to NASA for testing propulsion materials and other high-temperature materials sensitive to creep. Moreover, this testing capability can provide data for industry and other government agencies, especially for applications that require operations at high temperatures, such as nuclear power and aircraft design. (For more information on the ESL, visit: http://esl.msfc.nasa.gov)

Capability Readiness Level (CRL)

This AME task is enhancing an existing NASA facility so that valuable materials characterization data can be obtained. It elevates testing technology to CRL 5, helping designers characterize material creep for high-temperature systems used in the Crew Launch Vehicle, the Crew Exploration Vehicle, and future nuclear propulsion systems.

Principal Investigator
Dr. Jan Rogers, NASA/MSFC, Jan.R.Rogers@nasa.gov, (256) 544-1081

AME Contact/Project Lead
Beth Cook, NASA/MSFC, Beth.Cook@nasa.gov, (256) 544-2545

National Aeronautics and Space Administration

Marshall Space Flight Center
Huntsville, AL 35812

www.nasa.gov

FS-2006-09-155-MSFC

Materials Characterization

High Temperature Emissivity Measurement System (HiTEMS)

NASA Marshall Space Flight Center

Spacecraft engine nozzles, radiator panels, habitat surfaces, and other space hardware remove unwanted heat by radiating it into the ambient vacuum environment. Two properties–temperature and emissivity–affect spacecraft materials as they transfer heat energy to the space vacuum. A material's emissivity is dependent not only on its composition but also on its surface finish and temperature. To maximize thermal efficiency of space-based and ground-based components operating in a vacuum environment, it is critical to measure emissivity of finished components over the entire range of the components' operating temperatures. Precise emissivity measurements over a range of temperatures and for a variety of materials are crucial for spacecraft design (especially radiators and rocket nozzles), thermal modeling (spacecraft and habitats), and vacuum processing (metal heating and casting, coating, and semiconductor processing).

Task Description

The Advanced Materials for Exploration (AME) program is developing a High Temperature Emissivity Measurement System (HiTEMS): a one-of-a-kind capability for measuring material emissivity at temperatures from 300 K (27 °C) to 3000 K (2700 °C). Tasks include

1. Designing and building two test systems
2. Developing a multi-wavelength, state-of-the-art optical diagnostic system for measuring emissivity
3. Calibrating and verifying both test systems on a variety of materials.

This 16-month effort was initiated in FY05, and the final design, fabrication, and verification testing of both new test systems will be completed in 2006. The test systems will be ready to conduct tests for customers in early 2007. HiTEMS will provide a unique capability for obtaining materials emissivity data over a broad range of operating temperatures. This information will be critical for design and development of the Crew Launch Vehicle, the Crew Exploration Vehicle and other spacecraft.

An existing vacuum chamber in the Marshall Space Flight Center (MSFC) Space Environmental Effects Laboratory is being outfitted with new instrumentation for making emissivity measurements on a variety of samples (homogeneous materials, composites, and painted or coated materials) at temperatures up to 1600 K (1327 °C).

HIGH TEMPERATURE EMISSIVITY MEASUREMENT SYSTEM (HiTEMS)

A solid metal sample is suspended by static energy from six electrodes inside the Electrostatic Levitator (ESL). The facility is being outfitted with new instrumentation for measuring the emissivity of small samples at temperatures ranging from 1600 to 3000 K (1327 to 2700 °C). Materials created as a result of the ESL tests include new optical materials, new metal alloys, special metallic glasses, and spacecraft components.

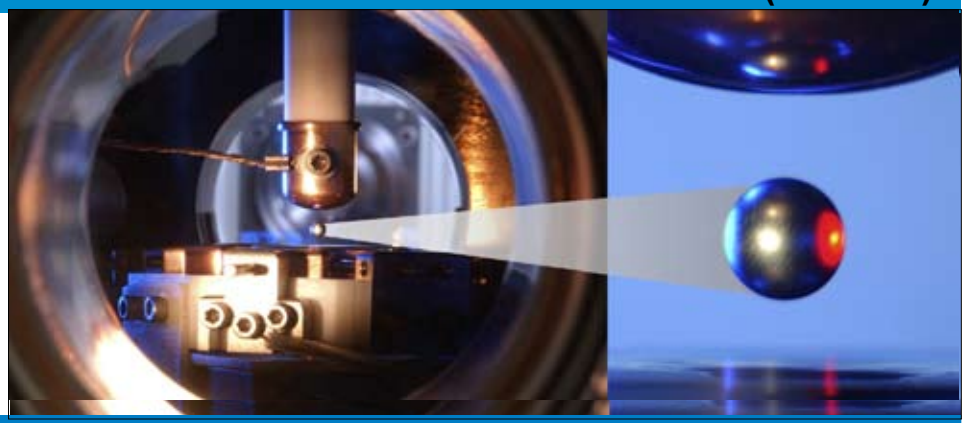

Anticipated Results

To cover this broad temperature range, HiTEMS comprises two test systems at NASA's Marshall Space Flight Center (MSFC). The first system uses contact heating in an existing vacuum chamber in the MSFC Space Environmental Effects Laboratory. It will provide emissivity information from 300 K (27 °C) to 1600 K (1327 °C) and will incorporate an integrated sample holder and heater system that accommodates any solid material (homogeneous materials, composites, and painted or coated materials) up to 3 cm (1.2 in.) in diameter. Sample temperature will be measured using a combination of thermocouples and a multi-wavelength optical pyrometer. (For more information on the Space Environmental Effects Laboratory, visit: http://ed.msfc.nasa.gov/em/em50.html.)

The second test system will provide emissivity measurements from 1600 K (1327 °C) to 3000 K (2700 °C). It uses MSFC's unique Electrostatic Levitator (ESL) system, which heats samples without a crucible. An electrostatic field will levitate each sample to prevent it from contacting contaminating containers, and a laser will heat the sample. This system accommodates spherical samples from 2 to 3 mm (0.08 to 0.12 in.) in diameter. (For more information on the ESL, visit: http://esl.msfc.nasa.gov.) New optical detection technology for both systems is being supplied by industry partner AZ Technology Inc., in Huntsville, Alabama.

Potential Future Activities

When HiTEMS is completed, it will be the only U.S. test system capable of using a high-quality optical system to measure emissivity in a vacuum over such a broad range of temperatures. As materials are tested for emissivity, these data can be entered into NASA's Materials and Processes Technical Information System (MAPTIS) databases where they will be accessible to spacecraft designers, thermal engineers, and others. Moreover, this testing capability can provide data for industry and other government agencies, especially for applications that require operations at high temperatures, such as nuclear power.

Capability Readiness Level (CRL)

This AME task is creating a new laboratory capability for measuring thermal performance of high temperature materials under thermal vacuum conditions that simulate space and lunar surface environments. The creation of this facility elevates this type of testing technology to CRL 5. HiTEMS will help designers characterize material emissivity for high temperature systems used in the Crew Launch Vehicle, the Crew Exploration Vehicle, and in future nuclear-powered and nuclear-propelled spacecraft.

Principal Investigators

Todd Schneider, NASA/MSFC, Todd.A.Schneider@nasa.gov, 246-544-2595

Dr. Jan Rogers, NASA/MSFC, Jan.R.Rogers@nasa.gov, 256-544-1081

AME Contact/Project Lead

Beth Cook, NASA/MSFC, Beth.Cook@nasa.gov, (256) 544-2545

National Aeronautics and Space Administration

Marshall Space Flight Center
Huntsville, AL 35812

www.nasa.gov

FS-2006-05-061-MSFC

Materials Characterization

Phase Contrast X-Ray Imaging

NASA Marshall Space Flight Center

Lightweight, high-performance materials, such as insulating foam and leading edge composites used for space vehicles, require nondestructive evaluation (NDE) techniques for quality inspection and control. Foam debris generation led to the loss of the Space Shuttle *Columbia* and its crew in 2003 and highlighted the critical need to better inspect and control foam quality. However, low-density foam, such as that used to insulate the Space Shuttle External Tank, is hard to adequately inspect using traditional NDE tools. The foam's cellular structure does not absorb X-rays well, resulting in low contrast images that do not accurately reveal flaws. This investigation tested the feasibility of using coherence of X-rays for phase imaging (instead of absorption-based imaging) to better identify foam flaws. Adding the phase information of X-rays into image formation significantly enhanced image contrast and sensitivity, revealing material flaws that were not apparent in images produced by absorption-based X-ray radiography and computed tomography. Detailed information on the intrinsic quality of the foam, including its defects and behavior when stressed with loads, was provided to the Engineering Directorate at NASA's Marshall Space Flight Center where the data are being used to improve foam quality and processing for future Space Shuttle missions as well as for materials and materials processing that support the Vision for Space Exploration.

Task Description

The Advanced Materials for Exploration (AME) study tested a new NDE technique. The following tasks were completed:

1. Developed and tested phase contrast two-dimensional (2D) and three-dimensional (3D) imaging capability for NDE of foams
2. Used NDE to analyze the variations of defects in foam insulation samples with different depths from the outer layers to inner layers
3. Evaluated the suitability of the imaging technique for broad application with other advanced materials
4. Developed capability to load samples and make *in-situ* imaging observations showing how the loads affected the sample.

This 18-month effort was initiated in FY04 and completed in April 2006.

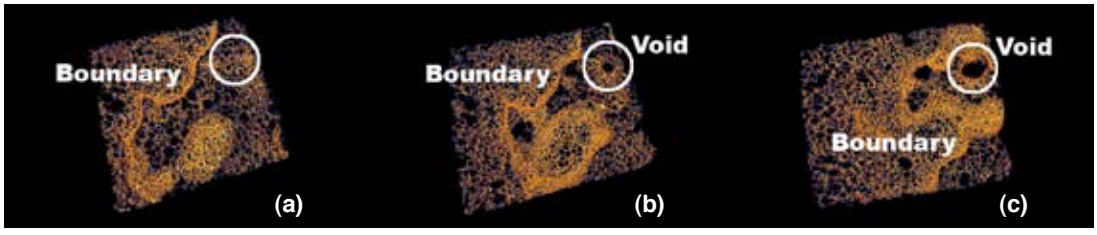

Phase contrast 3D images (a), (b), and (c) show a zigzag boundary and defects inside the foam corresponding to internal foam regions at different depths with (c) being the deepest. The circled void has a dimension of more than 1.5 mm (0.6 in.) along the foam rise direction.

PHASE CONTRAST X-RAY IMAGING

Results

This study tested Shuttle foam insulation BX-250, a polyurethane foam applied by hand to the domes, ramps, and a few other areas of the External Tank. The Principal Investigator successfully competed for synchrotron beamtime at the Department of Energy's Advanced Photon Source in Chicago, IL, one of the few places in the world capable of producing high-energy X-rays required for phase contrast imaging. To create each tomographic (3D) image, samples were bombarded with X-rays, and about 800 projection images were taken over a 180-degree angular range and recorded by a high-resolution CCD camera.

The resultant images from this study provided reliable and detailed data about the foam structure and its flaw formation that was previously impossible to obtain. Images revealed a great variation and high anisotropy in foam structure in terms of cell size, shape, and wall and strut thickness. By analyzing a series of photos taken at different depths inside the foam sample, investigators found the foam is made up layers of cells that are separated by complicated zigzag boundaries characterized by highly irregular cells with wall thicknesses several times that of the regular cells in the layers. These marked differences in the layers and boundaries impact the foam's properties and behavior, in particular how the foam stands up to loading, such as that experienced during a Shuttle launch. The images reveal voids (major defects) throughout the foam. The voids vary considerably in size, but they tend to form more readily along the boundaries and the interfaces between the foam and aluminum substrates.

Investigators conducted pressure tests that showed the foam's strength varied considerably from one region to another as a result of variations in the foam's quality and density. To further test the foam's response to stress, the investigator developed and tested an *in-situ* loading method. Preliminary loading experiments confirmed that the phase contrast images accurately revealed the defects inside the foam and showed how these flaws could result in foam failure. For example, when pressure was exerted, the foam cracked at the boundary knit-lines.

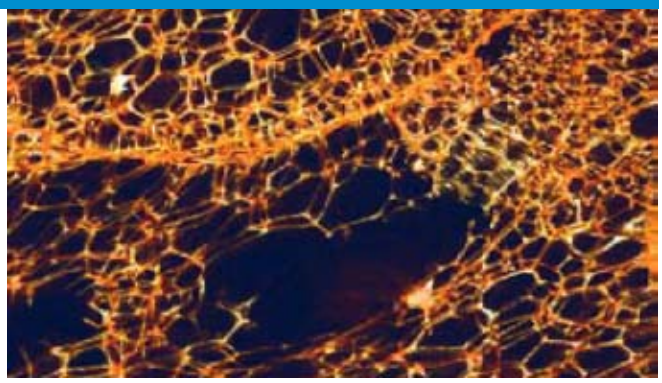

Phase contrast 3D imaging reveals how pressure loading induced internal foam cracking and/or spalling at a knit line.

Experiments also examined lightweight composites, including carbonized foam and composites of polyethylene-epoxy and carbon-carbon. Phase contrast images revealed structural non-uniformity that would affect on the materials' physical properties, reliability and performance.

Potential Future Activities

This feasibility study demonstrated the great potential of phase contrast X-ray imaging to non-destructively characterize advanced lightweight materials and/or structures. Combined *in-situ* loading and image visualization methods offer a powerful way to better understand how foam behaves when stressed. The next step is to develop an in-house phase contrast X-ray imaging tool that would enable low-density material structures to be non-invasively visualized with sufficient sensitivity and resolution to identify flaws.

Capability Readiness Level (CRL)

This AME task tested a new technique for non-destructive evaluation of foam (CRL-3). This insight into the foam structure and response to loading will help result in better foam insulation and safer space exploration vehicles.

Principal Investigator

Dr. Zhengwei Hu, BAE Systems, Zhengwei.Hu-1@nasa.gov, (256) 544-3805

AME Contact/Project Lead

Beth Cook, NASA/MSFC, Beth.Cook@nasa.gov, (256) 544-2545

National Aeronautics and Space Administration

Marshall Space Flight Center
Huntsville, AL 35812

www.nasa.gov

FS-2006-06-86-MSFC

Propulsion Materials

Thrust Chamber Liners

NASA Marshall Space Flight Center

Advanced materials research for thrust chamber assemblies will enable engines to perform at higher temperatures with improved operating margins. These advancements can be applied to nuclear propulsion, as well as to the engines being considered for the Crew Launch Vehicle. Some engine operating conditions are severe enough to erode thrust chambers' throat sections, but new material systems produced with the Vacuum Plasma Spray (VPS) process have demonstrated the ability to reduce or eliminate such erosion. Using VPS to form the thrust chamber liner with a Functional Gradient Material (FGM) has produced a highly effective and durable protective layer on the hot wall. A small thrust chamber liner 5-K lbf (5,000 lbf thrust) was successfully fabricated and has survived over 200 hot-fire tests with no erosion and no degradation to the hot wall protection. Current efforts are addressing the fabrication issues associated with scaling up the process to make larger thrust chamber liners for specific engine systems. The small demonstration liner was successfully fabricated using a mild steel mandrel, but attempts to make larger units were unsuccessful because of larger stresses from the differences in Coefficients of Thermal Expansion (CTEs) between the liner and mandrel materials. An alternate mandrel design is being investigated to eliminate these CTE concerns for larger liners.

Task Description

For this Advanced Materials for Exploration (AME) task, investigators are designing and building a 40-K lbf (40,000 lbf) thrust chamber liner using an alternate mandrel design. Tasks include

1. Demonstrating processes and new mandrel design with large diameter pipe sections
2. Designing and machining a mandrel made of an alternative material to create a CTE compatible with that of the liner material
3. Using the new mandrel and VPS to manufacture a thrust chamber liner made of an FGM formed with GRCop-84 and a protective layer of an oxidation-resistant material
4. Joining the liner with an existing thrust chamber support jacket and manifolds to form a completed assembly for hot-fire testing
5. Conducting hydrostatic proof tests at NASA's Marshall Space Flight Center (MSFC), Huntsville, Alabama
6. Characterizing materials properties of VPS-formed materials.

This 3-year effort was initiated in FY04 and will conclude with a completed 40-K lbf thrust chamber assembly in FY06.

Anticipated Results

The first year, 12-in. diameter pipe sections were used to test the process and demonstrated that matching CTE of the mandrel with that of the copper alloy eliminated stress so that no cracks were experienced during manufacturing. The second year, the 40-K lbf mandrel and liner were manufactured by Plasma Process, Inc. (PPI), a Huntsville company that shares the patent for VPS processing to form FGMs. In the third year

THRUST CHAMBER LINERS

Vacuum Plasma Spray GRCop-84 Liner	NARloy-Z Liner (Current Space Shuttle Main Engine Liner)
2003: Technology Evaluation	1976: SSME Qualification Testing
211 Cycles (1100 sec)	118 Cycles (353 sec)
Maximum Temperature = 1250 °F (950 K)	Maximum Temperature = 1100 °F (866 K)
No hot wall cracks or surface roughening initiated; no liner degradation	Cycles: <30, hot wall cracks and surface roughening initiated
Cycles: ~55, heat load decreased 30%, less coolant required	Cycles: ~70, heat load increased; surface polishing required

Vacuum Plasma Spray was used to form a 5-K lbf thrust chamber liner that has shown no wear after 211 hot fire tests and performed very well compared to previous testing on a NARloy-Z liner, which is currently used in the Space Shuttle Main Engine combustion chamber.

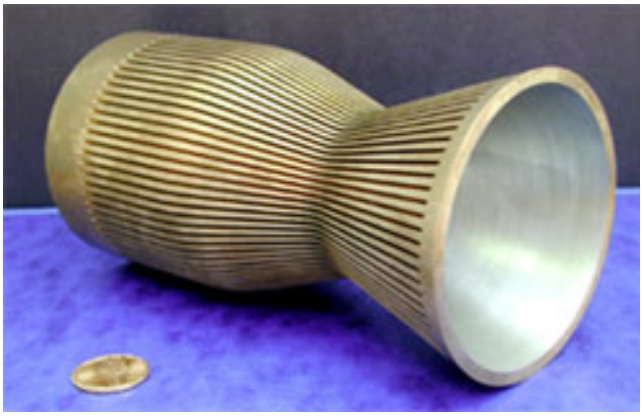

A subscale 5-K lbf thrust chamber liner was successfully fabricated with VPS using GRCop-84 and a protective layer of NiCrAlY on the hot wall.

of the project, Marshall Center investigators are working with PPI to complete the thrust chamber liner assembly. When additional funding becomes available, investigators plan to hot-fire test the 40-K lbf thrust chamber to demonstrate the durability and performance of this liner material system in an appropriate high-temperature environment.

Potential Future Activities

The next step is to manufacture and test thrust chambers with FGM liners in simulated environments and evaluate and characterize the material systems for design and life prediction. The new liner can be scaled up and tested on a full-size engine system, and results can be compared to traditional materials. MSFC has the facilities and expertise to perform analysis and mechanical tests (up to 1500 °F, 1089 K). Thermal spray, hot isostatic pressing, heat treatment furnaces, metallography, electron microscopy, failure analysis, and mechanical testing can be performed under a variety of environmental conditions.

The process has been expanded to provide durable, high-temperature protective coatings to injector faceplates. These faceplates were successfully hot-fire tested and demonstrated similar performance to the thrust chamber liner with no erosion and no degradation to the protective layers applied with VPS. This process might also be used to apply coatings with maximum bond strength to a variety of space vehicle surfaces, such as leading edges and turbine blades. Efforts for the thrust chamber liner were focused on an oxidation protective layer, which endured temperatures up to 2600 °F (1700 K). Higher temperature capability may be possible by adding zirconia (ZrO_2) to the FGM. Zirconia coatings are expected to handle temperatures up to 4000 °F (2478 K), which may be attractive for nuclear propulsion applications.

Capability Readiness Level (CRL)

Hot-fire testing on a small thrust chamber liner provided a CRL 5 for the technology at this time. Successful fabrication of the 40-K lbf thrust chamber liner will further increase the CRL. Testing in a simulated environment with a full-size thrust chamber assembly would elevate the CRL to 7. Elevation of this materials technology will create robust, long-life, reusable thrust chambers for exploration rocket engines.

Principal Investigators

Sandy Elam, NASA/MSFC, Sandra.K.Elam@nasa.gov, (256) 544-8902

Dick Holmes, NASA/MSFC, Richard.R.Holmes@nasa.gov, (256) 544-2722

AME Contact/Project Lead

Beth Cook, NASA/MSFC, Beth.Cook@nasa.gov, (256) 544-2545

National Aeronautics and Space Administration

Marshall Space Flight Center
Huntsville, AL 35812

www.nasa.gov

FS-2006-04-44-MSFC

Propulsion Materials

Hot Hydrogen Materials

NASA Marshall Space Flight Center

The hot hydrogen environment of a high-performance, solid-core nuclear thermal rocket (NTR) presents substantial challenges for designers tasked with selecting materials that can operate in the high-temperature and highly corrosive environment. To advance NTR technology into the operating temperature regime approaching ~3000 K (~4940 °F), new hydrogen-resistant materials must be developed, and their development depends upon having advanced test facilities that can expose potential candidate materials to severely corrosive hot hydrogen environments [above 2200 K (3500 °F)] for extended periods of time.

The arc-heater test facility at Marshall Space Flight Center (MSFC) in Huntsville, Alabama, is being modified to establish such special material processing capabilities and to baseline hot hydrogen testing under non-nuclear conditions. By producing small candidate material specimens through innovative processing and manufacturing techniques and then exposing them to environments that mimic actual NTR firing conditions (with the exception of radiation), researchers have a cost-effective strategy for selecting optimal materials for actual nuclear furnace testing.

Task Description

This Advanced Materials for Exploration (AME) task will develop an electrically heated module for testing and characterizing non-nuclear hydrogen-resistant materials to a maximum surface temperature of 3000 K (4940 °F). This heater will be installed in an attachable test fixture developed under an MSFC Independent Research and Development project to expand the accessible temperature range to 3000 K (4940 °F). Researchers will

1. Conduct a coupled thermal-fluid analysis of the test module to establish basic requirements and specifications
2. Develop an integrated systems design, resulting in a basic configuration
3. Produce a detailed mechanical design
4. Certify final design with thermal and stress analyses
5. Develop complete manufacturing drawings
6. Establish final specifications
7. Transition effort to the build/test phase, which will be funded through MSFC's Nuclear Systems Project Office.

This 10-month AME task will culminate in September 2006.

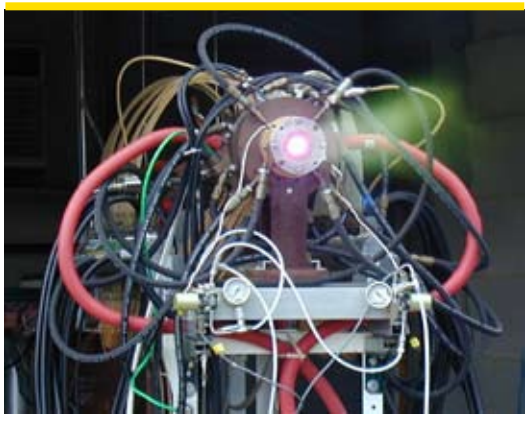

A 770-kW arc-heater performance validation firing at a hydrogen flow rate of 7 g/sec through a sacrificial graphite nozzle. The inferred gas temperature was 2980 K (4904 °F) with a measured efficiency of 47%.

advanced materials for exploration

HOT HYDROGEN MATERIALS

Anticipated Results

This task will advance NASA's capabilities to characterize high-temperature propulsion materials by enhancing an existing hot hydrogen hyper-thermal environment simulator at MSFC. Researchers will develop a tester for non-irradiated screening of candidate hydrogen-resistant materials, *e.g.*, coated graphite, carbides, and cermets, with the added ability to accommodate depleted uranium within the samples. When completed, the tester will enable turbulent convective flow of hydrogen through small, tubular material specimens with core gas temperatures up to 3500 K (5840 °F), sustained specimen temperatures up to 3000 K (4940 °F), real-time measurement of the exposed surface temperature, and simulation of a complete NTR cycle. Precise control of hydrogen temperature, pressure, and flow rate, combined with power deposition in the specimen through a backside resistive heater, will recreate thermal-hydraulic conditions that closely simulate reactor core environments, excluding radiation effects. Comprehensive physical modeling will correlate test results to practical applications. Furthermore, by standardizing specimen geometry, low-cost and rapid testing of candidate materials will accelerate material development. The final deliverable is the complete design of either a coated or uncoated resistive heating element module for the hot hydrogen test facility. Exploratory tests will assess the degree of chemical compatibility of glossy carbon and coated graphite with hydrogen at temperatures up to 3200 K (5300 °F).

MSFC will perform detailed modeling efforts, supported by BAE Systems (Huntsville, Alabama) and the University of Florida (Gainesville). BAE Systems will provide configuration management, interface control, and design certification. Using its Innovative Nuclear Space Power and Propulsion Institute, the University of Florida will conduct thermal-fluid analysis, integrated system design, special test equipment specification, detailed mechanical design, and development of manufacturing drawings.

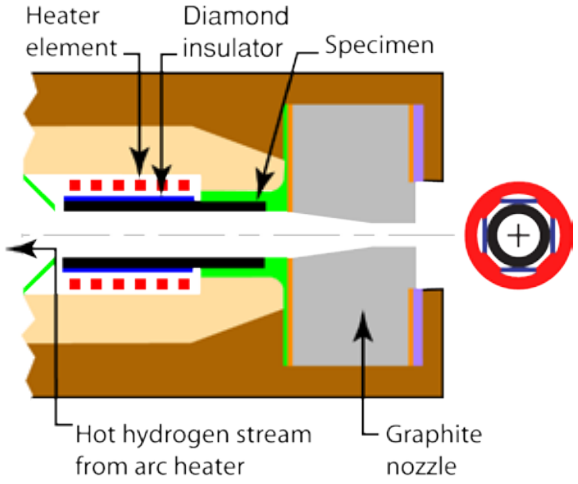

Resistively heated specimen module for the hot hydrogen test facility. Pre-heated hydrogen from the arc-heater is forced through the tubular specimen in which additional electrical power is deposited from a backside resistive heating element. This configuration permits accurate thermal hydraulic simulations that are directly traceable to reactor core environments.

Potential Future Activities

Beginning in FY07, MSFC's Nuclear Systems Project will fund follow-on efforts to build and conduct preliminary tests of the electrically heated test module. After the module has been certified and activated, the unique test capability of this nuclear rocket environment simulator will be available to NASA, other government sectors, commercial, and academic communities for the conduct of research into the development of hot hydrogen-resistant materials. This capability is currently unavailable elsewhere.

Capability Readiness Level (CRL)

When modification of the MSFC arc-heater test facility with the electrically heated test module is complete, the facility will support materials development efforts ranging from CRL 1 to CRL 5.

Principal Investigator

Ron Litchford, NASA/MSFC, Ron.Litchford@nasa.gov, (256) 544-1740

AME Contact/Project Lead

Beth Cook, NASA/MSFC, Beth.Cook@nasa.gov, (256) 544-2545

National Aeronautics and Space Administration

Marshall Space Flight Center
Huntsville, AL 35812

www.nasa.gov

FS-2006-09-151-MSFC

Propulsion Materials

Molybdenum-Rhenium Process Comparison

NASA Marshall Space Flight Center

Nuclear power and propulsion generation require materials that are stable at high temperatures, structurally sound, and compatible with diverse environments. No single material has been identified that is ideal for all applications: power generation equipment and supporting components needed for thermal management, shielding, controls, and structures. Multiple materials will have to be merged to transition from one environment to another within a single piece of hardware, usually from one side of a containment vessel to the other. Materials failures are often the result of bonding problems created by differences in the physical properties of materials that result in mechanical strain or metallurgical instability. Materials processing techniques that use graded transitions can reduce or eliminate these distinct bond lines that are usually the cause of failures.

Task Description

Investigators are comparing two materials application processes–diffusion bonding and plasma spray–that can bond or form layers of two refractory materials: molybdenum-40rhenium (Mo-Re) alloy and 100 percent rhenium (Re). These processes were selected because they are flexible, scale up well to larger samples, and are documented in scientific literature. This allows the study to focus more on materials development and less on process development. Tasks include

1. Evaluating diffusion bonding and plasma spray uses in the scientific literature and for practical applications
2. Demonstrating two processes by bonding Re and Mo-Re
3. Comparing performance of these two bonding methods with traditional techniques such as welding and brazing.

This 2-year effort was initiated in FY05 and is being completed in FY06.

Anticipated Results

Rhenium and molybdenum were selected because of their potential for high-temperature applications, which makes them useful for rocket engine nozzles needed for high-temperature chemical fuels and nuclear fuels. The literature survey revealed the most common use of Re and Mo-Re is in small, uncooled thrusters, with some use in leading edge and heat pipe applications. Little information existed on bonding the materials, except for some electron beam welding analysis.

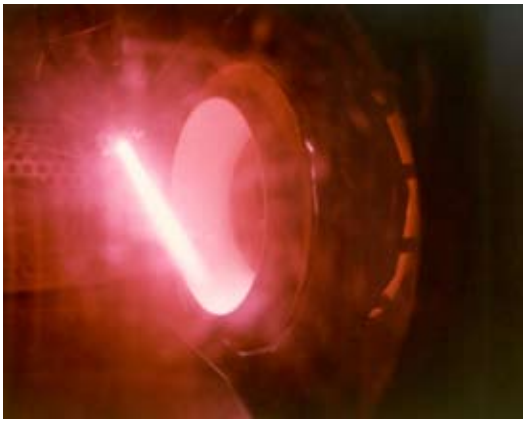

Materials failures can be the result of mechanical strain created when two materials do not bond well. Vacuum plasma spray may improve materials bonding. Here, a copper alloy is sprayed on a casting that replicates the throat section of the Space Shuttle Main Engine combustion chamber.

MOLYBDENUM-RHENIUM PROCESS COMPARISON

In FY05, investigators identified and evaluated methods (powder placement, foil, electroplate, thermal spray) for preparing the diffusion bond. As a precursor for evaluating the plasma spray method, they tested the method with tungsten, a less exotic refractory material. They prepared and analyzed the Re and Mo-Re samples and identified problems with the rhenium powder flow. In addition, the high energy required to spray these refractory alloys caused turntable overheating during the spraying process. Investigators are working to improve the flow by processing the powder, and they are adding shielding to isolate the turntable from samples during vacuum plasma spraying.

In FY06, investigators will continue to develop the plasma spray and diffusion bonding processes. At the end of this effort, investigators will have developed the application processes and compared results for the two materials. These results, along with the study of the technical literature, will provide a more complete set of data with which to select materials and their applications for propulsion components. The study will lay the groundwork for evaluating and comparing the many other candidate processes for forming gradient materials: chemical and physical vapor deposition, powder metallurgy, laser sintering, and other direct metal fabrication processes.

Potential Future Activities

The next steps are to refine processing, fabricate test specimens of each material, and conduct mechanical testing and failure analysis of the samples. The results of these more detailed studies would provide first-order mechanical properties, test data, and failure analysis, as well as more concrete data for design and trade studies examining materials needed for propulsion and nuclear power systems.

Marshall Space Flight Center (MSFC) has the facilities and expertise to perform this materials processing analysis and mechanical testing (up to ~1500 °F): plasma spray, hot isostatic pressing (HIP), metallography, electron microscopy, failure analysis, and mechanical testing in a variety of environmental conditions that simulate space flight and launch conditions. Experts in these processes, as well as welding, brazing, and electroplating, can develop processes and applications and compare them, providing meaningful trade studies and materials selection data.

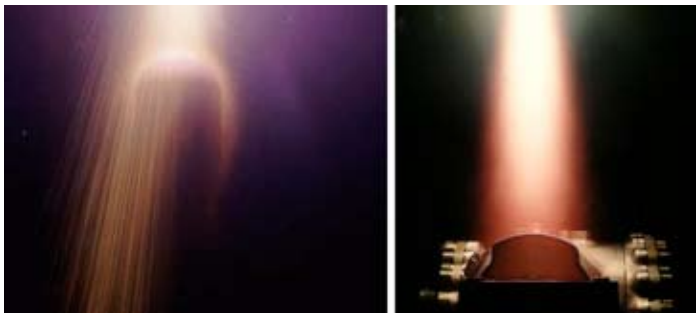

Left: The Vacuum Plasma Spray system at NASA's Marshall Space Flight Center is used to spray tungsten on an 18-in. long graphite mandrel that forms part of a solar thermal absorber cavity.

Right: Copper is sprayed on a titanium fuel valve housing. A similar process will be used to bond layers of refractory materials: molybdenum-40rhenium and 100 percent rhenium. Plasma spraying will be compared to diffusion bonding of the same materials.

Capability Readiness Level (CRL)

This Advanced Materials for Exploration (AME) task develops two materials processes applications and compares them (CRL 2). More extensive laboratory testing and materials evaluation would elevate this propulsion materials technology to CRL 3 and provide data for trade studies and materials selection criteria needed to amalgamate different refractory materials into propulsion components for thermal management, fuel containment, and fusion reaction applications.

Principal Investigator

Frank Zimmerman, NASA/MSFC, Frank.R.Zimmerman@nasa.gov, (256) 544-4958

AME Contact/Project Lead

Beth Cook, NASA/MSFC, Beth.Cook@nasa.gov, (256) 544-2545

National Aeronautics and Space Administration

Marshall Space Flight Center
Huntsville, AL 35812

www.nasa.gov

FS-2006-04-40-MSFC

Propulsion Materials

Advanced Magnets

NASA Marshall Space Flight Center

Innovations in magnet design and use of magnetic materials will enable advanced propulsion systems for exploration vehicles and hardware. Propulsion mechanisms that use or generate magnetic fields are critical for many promising space propulsion systems. Strong static magnetic fields can be used to control exhaust velocities in nozzles, and dynamic systems can provide thrust. Advanced propulsion systems require magnets that produce fields with higher specific energies and magnets made of materials that can survive extreme operating environments, including interactions with harsh propellants, radiation exposure, and vacuum exposure. Strong magnetic fields can be produced by low-temperature binary metal alloys or high-temperature ceramic oxide superconducting windings.

Task Description

As part of tests completed on a high-temperature superconducting (HTS) magnet, these parameters relevant to NASA propulsion were measured:

1. Specific energy (W_m)
2. Critical current
3. Magnetic field profile.

This 7-month study was completed in September 2005.

Results

As a first step, investigators performed tests on an available magnet developed for a space experiment under a previous NASA Small Business Innovation Research (SBIR) by Intermagnetics General Corporation, in Latham, New York, a leading developer of custom HTS magnet systems. Although this magnet was not developed for use in a propulsion system, it gave materials scientists the opportunity to set up an experiment and measure parameters of interest to propulsion researchers.

The magnet, a powder-in-tube HTS conductor composed of $(Bi, Pb)_2Sr_2Ca_2Cu_2O_x$ BSCCO 2223, was cooled to liquid nitrogen temperatures, and current was applied to the magnet windings to create a magnetic field. A magnetic profile was created to show the three-dimensional profile of the magnetic field inside the magnet when 5.1 A and 10.1 A of current were applied to the magnet.

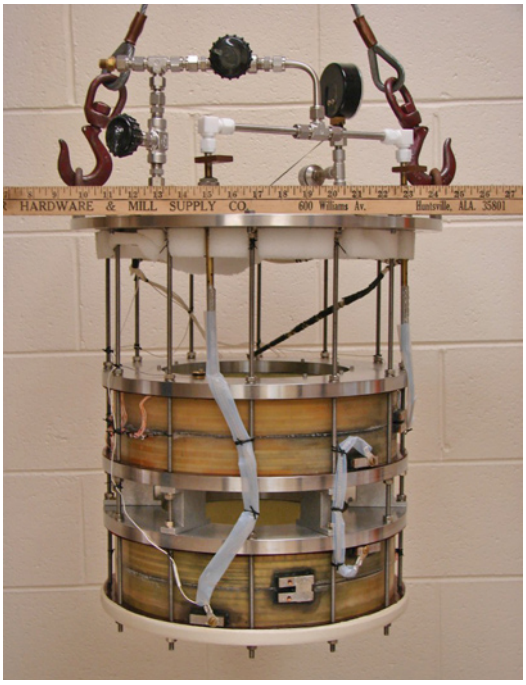

This system consisted of two sets of high-temperature superconducting coils that were donut-shaped and stacked on top of each other with a space between them. In the laboratory, the magnet was cooled to 77 K, and a current was applied.

advanced materials for exploration

ADVANCED MAGNETS

Parameters	Value/Description	Parameters	Value/Description
Coil Type	Split Pair Helmholz	Coil Section Width	82.0 mm
Coil Construction	Pancake	Gap Between Coil Sections	70.0 mm
Field Modification	Fe End Plates	Conductor Required	2800 m (nominal)
Winding Inner Diameter	235.0 mm	Operating Temperature	64 K (min)
Winding Outer Diameter	325.0 mm (nominal)	Cooling Option	Pumped LN_2

Parameters of interest for the High-Temperature Superconducting Magnet that was tested

This revealed how the magnetic field varied over the magnet's structure and how it changed with varying current levels. Researchers determined that the magnetic critical current was 270 V at 12.9 A at 1 μV/cm, which is a measure of increased heat and thus increased resistance in the magnet windings; this indicates how much current the system can tolerate before the magnetic field becomes unstable. The measurement is affected by the materials comprising the magnet, as well as how the materials are treated and constructed.

The magnetic energy density at 65 K was 0.47 kJ/kg and 0.13 kJ/kg at 77 K. This magnet was not designed to maximize the specific energy, which can reach 5 kJ/kg in optimized magnet systems and up to 30 kJ/kg for the most advanced laboratory terrestrial magnets. A tremendous gain in technology is needed to meet the specific energy requirements for the most advanced propulsion systems, which require orders of magnitude increase in magnetic energy density.

Potential Future Activities

Magnet requirements need to be developed for promising propulsion systems, such as the Variable Specific Impulse Magnetoplasma Rocket (VASIMR) and the Plasmoid Thruster. The next step would be to complete a thorough trade study that identifies magnet requirements for these and other potential propulsion systems. Once the requirements are identified, researchers could evaluate and select magnet materials and systems for magnetic specific energy, materials compatibility with propellant, temperature, radiation environment, and overall system weight. Candidate materials should be procured and tested in their anticipated operating environments. As a final step, the best materials identified by the study would be used to design and build a prototype propulsion system with an advanced magnet that could undergo proof-of-concept testing.

To identify magnet requirements, Marshall Space Flight Center materials experts can work on site with propulsion engineers who are designing spacecraft that require advanced magnets. Center laboratories and the Propulsion Research Laboratory have facilities that are ideal for magnet tests and characterization, as well as for further testing of a prototype propulsion system.

Capability Readiness Level (CRL)

This Advanced Materials for Exploration (AME) task performed laboratory tests and characterization of a high-temperature superconducting magnet (CRL 3). Designing and building a prototype propulsion system with an advanced magnet developed on the basis of trade study results and materials requirements and testing in a simulated space environment would raise the CRL to 7. Elevation of this magnet technology is essential to the development of propulsion systems that require advanced magnets.

Principal Investigator

Dr. Martin Volz, NASA/MSFC, Martin.P.Volz@nasa.gov, (256) 544-5078

AME Contact/Project Lead

Beth Cook, NASA/MSFC, Beth.Cook@nasa.gov, (256) 544-2545

National Aeronautics and Space Administration

Marshall Space Flight Center
Huntsville, AL 35812

www.nasa.gov

FS-2006-04-39-MSFC

Vehicle Health

Radiation-Resistant Electronics

NASA Marshall Space Flight Center

Most current spacecraft use silicon-(Si-)based electronics that must be protected from the high-temperature and radiation-filled space environment. Long-duration exploration missions—especially those that have increased exposure to high-energy galactic radiation (in particular, solar flares) and those that use nuclear systems—will require electronic and optical devices that are both radiation resistant and capable of operating at higher temperatures. Current electronic systems are kept in a cooled, centralized area, so advanced electronic systems can reduce weight and power demands by eliminating cooling systems and enhancing reliability. These electronic sensors could also be embedded in spacecraft heat-shielding materials to monitor conditions and effectiveness. Radiation-resistant electronics would be more durable and reliable for operating in natural space environments and for monitoring and controlling nuclear reactors used for space power and propulsion. A new class of materials has properties that are ideal for advanced electronics: wide electronic bandgap, high thermal conductivity, high breakdown electrical field, high current density, high thermal stability, and chemical inertness.

Task Description

The objective of this Advanced Materials for Exploration (AME) research is to use new materials to develop the technology for producing high-temperature and radiation-resistant electronics. Tasks include

1. Studying novel semiconductor materials (SiC, ZnO, GaN, AIN, BN, diamond, *etc.*) and identifying the best materials for space applications
2. Using an in-house high-temperature facility to test candidate materials before and after annealing
3. Acquiring and testing electronic and optical [light emitting diodes (LEDs)] devices
4. Building a high-temperature, radio frequency (RF) crystal growth facility and using it to grow SiC crystals
5. Using the crystals to fabricate simple SiC-based diodes.

This 2-year effort was initiated in FY05 and will be completed in FY06.

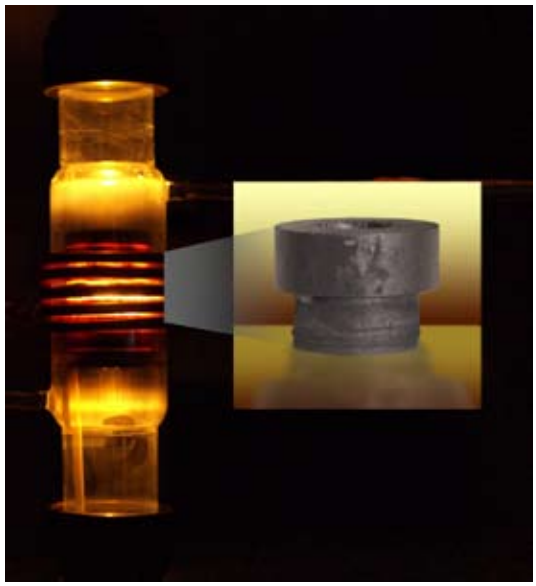

This SiC crystal (inset) was grown by physical vapor transport inside a radio frequency (RF) growth chamber at a temperature range of 2100 to 2350 °C (3812 to 4262 °F). This preliminary test took place inside the new RF facility at the Marshall Space Flight Center. Growth conditions are being improved by using seed crystals and a sample translation system.

advanced materials for exploration

RADIATION-RESISTANT ELECTRONICS

Anticipated Results

By the end of FY05, the team had completed a literature study on radiation-hardened electronic devices and surveyed 212 companies that build high-temperature, radiation-resistance devices. They obtained LEDs that operate at temperatures above 100 °C and some GaN LEDS; the emitting spectra and intensity and the current-voltage (I-V) characteristics were measured for these devices. An annealing furnace was used to harden 12 different types of LEDs, and they were tested at the following temperatures: 150, 175, 200, 250, 300, and 325 °C (302, 347, 392, 482, 572, and 617 °F).

Investigators measured the emitting spectra and intensity and the I-V characteristics of the LEDs and compared these to the measurements made before annealing. After 1 week at a temperature of 200 °C (392 °F) and lower, the intensity of the LEDs remained within 10% of their original values. After 8 weeks at 250 °C (482 °F), the LED intensity dropped up to 50%. After 7 weeks at nearly 300 °C (572 °F), nearly all the LEDs dropped no lower than 50%. After 7 weeks at 325 °C (617 °F), the intensity usually remained at 50%. The fastest decrease in intensity usually occurred in the first few days of annealing.

In FY06, the team will continue the annealing tests on commercial LEDs and extend the tests up to 600 °C (1112 °F). The team developed and constructed a high-temperature RF crystal growth facility, with capability up to 3000 °C (5432 °F). Preliminary growth of SiC materials show promising results. This year, the team will optimize the growth process and produce SiC crystals with controlled electrical properties. They will use a high-end sputtering system to fabricate simple SiC-based diodes.

Potential Future Activities

To fully develop these devices, more comprehensive experiments with *in-situ* monitoring of electronic devices exposed to radiation will be required.

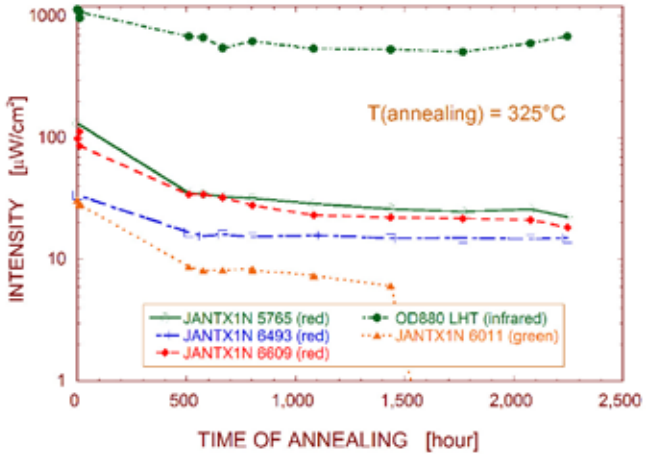

Annealing at 325 °C (617 °F). Representative performance: Initial drop in the emitting power in the first days of annealing, followed by a relatively stable or slightly declining total emission in the next few months, except for one complete failure.

These tests could be balloon-borne experiments, ground-based experiments, or space-based experiments. Although numerous studies have characterized the new materials, the technology for making devices is in its infancy (Technology Readiness Level 2 or 3). The team recommends building on the SiC fabrication processes developed by this study to manufacture more sophisticated devices, such as high-temperature connectors or simple sensors that could be tested in environments that simulate space radiation.

Capability Readiness Level (CRL)

This AME task constructs simple SiC devices with improved properties and studies electronic and optical components under simulated space conditions. The data are essential for predicting how these devices might perform on spacecraft (CRL 5). Flight experiments with more complex components would elevate the CRL to 7. This information could be used to develop more novel electronic and optical devices that would perform better on advanced spacecraft like the Crew Launch Vehicle and the Crew Exploration Vehicle.

Principal Investigator

Dr. Ching-Hua Su, NASA/MSFC, Ching.H.Su@nasa.gov, (256) 544-7776

AME Contact/Project Lead

Beth Cook, NASA/MSFC, Beth.Cook@nasa.gov, (256) 544-2545

National Aeronautics and Space Administration

Marshall Space Flight Center
Huntsville, AL 35812

www.nasa.gov

FS-2006-06-67-MSFC

Vehicle Health

Solar Sail Contouring

NASA Marshall Space Flight Center

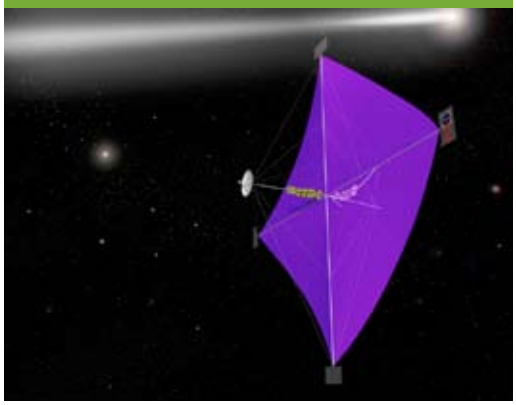

Solar sails are low-cost, efficient, in-space propulsion systems that use photons from the Sun to transport spacecraft on interplanetary journeys. Monitoring solar sail health during deployment and operations is critical to the integrity of the mission. Digital imaging systems must be able to observe different parts of a solar sail and identify wrinkles, folds, or other problems that reduce the sail's ability to optimally reflect sunlight and produce thrust. Creating contrasting visual location indicators on a sail is difficult because blinding sunlight bounces off the sail's mirror-like surface, making indicators hard to discern. Previously tested adhesive disks were observable but added unwanted mass and damaged thin sail material.

Task Description

This investigation tested three processes —**anodizing, coating, and embossing**—for applying visual location indicators on sail-like material while

1. Minimizing added mass
2. Bonding strongly to the sail
3. Providing adequate contrast to the sail material over appreciable viewing angles
4. Preventing alterations to the sail material that would affect its ability to produce thrust.

This Advanced Materials for Exploration (AME) 3-month feasibility study was completed in December 2004.

Results

The application methods were tested on 3-micron-thick multilayer insulation samples made of aluminum on Mylar™, a material similar to sail material. Marking techniques and materials were evaluated for their ability to make observable images that showed contrast between the original material and the marked areas, and researchers noted alterations created by the application process.

Spectral reflectance tests were performed on some samples by researchers from the Marshall Space Flight Center (MSFC) Space Environmental Effects Team. Measurements indicated that it may be possible to produce selective interference effects by anodizing or embossing the film and modifying its thickness so that it strongly reflects degrading ultraviolet light and transmits visible light. Viewing such transmitted light areas against a darker background, such as the back side of the sail, may be the best solution.

All three techniques added identification locators that contrasted with the material and were observable by a digital camera. The embossing technique showed the most promise for marking a sail without causing negative changes to material properties—with the bonus of adding no weight and no new material to a sail. However, it

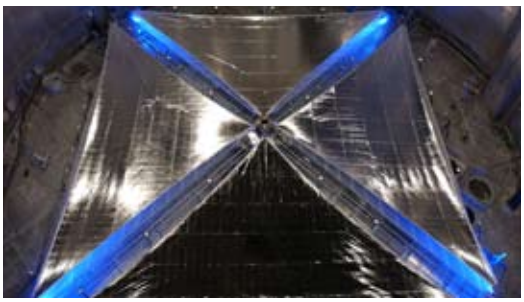

The mirror-like solar sail material maximizes reflection of solar photons but also reflects bright, blinding light that makes it difficult to monitor the sail's shape and condition. Location indicators that either reflect or transmit light and can be imaged by digital systems may solve this problem.

SOLAR SAIL CONTOURING

Method	Advantages	Disadvantages	Rating
Embossing: physically changed material by producing arrays of impressions and depressions	• Adds no mass or new materials that could alter sail properties • Easily applied • Provides partial spectral reflection	• Strained material beyond elastic limits	1
Anodizing: chemically changed material by adding film of aluminum oxide and adjusting thickness to produce interference colors	• Transparent, tough, thin, low mass • Appears black on shiny surface • Easily applied • Strongly bonded	• No strong interference patterns • Transparent windows transmit damaging ultraviolet light	2
Coating: added coating of highly reflective silicon nitride to aluminized polymer similar to back side of sail	• Strong, protective layer of film with low mass • Strongly bonded • Reduced reflectance • Increased emissivity	• Permanently altered sail material • Some mass added • Not all interference effects necessarily good	3

locally strained the study material beyond its elastic limit, so application refinements and strength testing would be required to more thoroughly characterize this process on real sail material.

Potential Future Activities

All three application methods should be tested on actual sail materials being developed by NASA (3-micron Al-CP-1 and 2-micron Al-Mylar™-Cr films). Optical measurements should be made to compare the reflectivity of the location indicator markings and the sail material as a function of wavelength. The Marshall Center has test facilities and experts for producing the samples, making the spectral measurements, performing tensile testing, and creating a simulated space environment. This task identified embossing as the highest priority for future studies that should

1. Identify the optimum pattern and size for the embossed hemispheres, by rapidly producing a variety of embossed samples using a new laser-etching machine (delivered to the Marshall Center in 2005) that can produce locator hemispheres smaller than 5 microns in diameter; measure reflectivity and spectral intensity of samples
2. Ensure embossing does not affect sail material by testing tensile strength of samples and thermal properties
3. Test the embossed samples in a simulated space environment with a collimated light source that mimics the Sun
4. Test and compare embossing on the front and back of sail material.

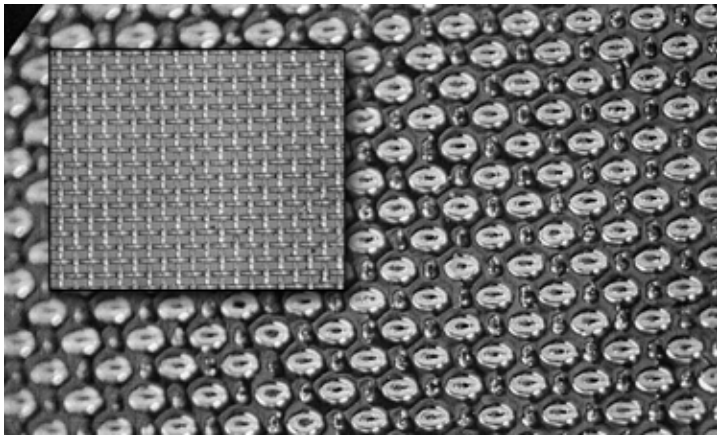

Photomicrograph of a 250 x 250 mesh screen (inset) used as a die to produce embossing patterns, which show a shape imaged in the center of each embossed bump. Machined dies were used, with less success, to emboss patterns in sail-like material. Laser etching machines could be used on future experiments to produce smaller, more precise patterns.

Capability Readiness Level (CRL)

This AME task, using small coupons of solar sail-like material, tested three possible techniques for marking solar sails, with embossing showing clear advantages (CRL 2). Further testing with real solar sail material in the laboratory and later in a simulated environment would elevate this materials process to a CRL of 4 or 5. Elevation of this sail health monitoring capability is crucial to the success of solar sail missions.

Principal Investigator

Palmer Peters, retired NASA/MSFC

AME Contact/Project Lead

Beth Cook, NASA/MSFC, Beth.Cook@nasa.gov, (256) 544-2545

National Aeronautics and Space Administration

Marshall Space Flight Center
Huntsville, AL 35812

www.nasa.gov

NP-2006-03-32-MSFC

Structural Materials

Macroscopic Tether Materials

NASA Marshall Space Flight Center

Cables, stringers, and tethers have great potential for NASA and Department of Defense (DoD) terrestrial and space applications. For example, electrodynamic tethers can be used as propellantless propulsion systems to lower or boost spacecraft and payloads from their orbits and as a low-cost means for generating power. The materials for these applications require further development.

Task Description

The Advanced Materials for Exploration (AME) project is funding six tasks to expedite the advancement of tether materials and to investigate new emerging materials. The science team is investigating:

1. Aluminum/alumina coatings for tether yarns
2. Aluminum wire embedded into a single-strand tether braid
3. Effective methods for electrical shunting
4. Manufacture of an all-metal tether
5. New tether materials with atomic oxygen (AO) resistance and/or high strength
6. Coating/pigment technologies to protect tether materials from ultraviolet (UV) radiation damage.

The effort began in October 2005 and will conclude in September 2006.

Anticipated Results

Task 1: The science team is conducting a review of coating technology to determine what is missing in the testing, limitations of particular coatings, particularly innovative and promising aspects of coating technologies, and next steps for promising technologies.

Task 2: Aluminum electrical conducting wire will be embedded into various braid constructions to address premature tensile failure of the wire. Testing of these braids will include visual and tactile sensing for broken aluminum wires, tensile testing to failure, and electrical resistance.

Task 3: If Task 2 is successful, two designs will be investigated. (1) Spooling a strand from Task 2 into a regular braid: designs that expose aluminum wire on their outer surfaces will be interlaced into a Hoytether™ configuration to accomplish shunting. (2) Creating a Hoytether™ from spools of strength members and of aluminum wire. After a leg of the tether is cut to simulate micrometeoroid damage, tests will include tensile loading and electrical resistance.

The tether braiding machine at Marshall Space Flight Center plaits lengths of fibers and metals into strong, electrically conductive cables, such as those to be used on lunar crater science missions. These cables will be tested for their ability to withstand the rigors of the space environment.

advanced materials for exploration

MACROSCOPIC TETHER MATERIALS

Task 4: A simple, low-cost, maximum-strength, prototype metal tether will be designed for a NASA mission specification.

Task 5: Several new fiber materials will be studied for their technological readiness, including Zylon®, M5, and carbon nanotubes. If these materials are available in sufficient quantities, the team will procure yarns for tensile, abrasion, scanning electron microscopic, UV, AO, and other tests.

Task 6: The team will determine the effectiveness of a sunscreen material for high-performance fibers, including Zylon®, by:

- Coating the tether fibers with thin layers of gold, aluminum, and gold/aluminum by electroless and electroplating of the fibers
- Coating the fibers with amorphous titania sol binder containing small particles of alumina or other oxides.

These coatings will be examined microscopically for uniformity of application on fibers and for cracking after deflection/folding and abrasion and will be tested for both UV and AO resistance.

The team will also metallize a poly(ethyl-ethylketone) (PEEK), a tough thermoplastic that exhibits desirable thermal shock and fatigue resistance in aerospace applications.

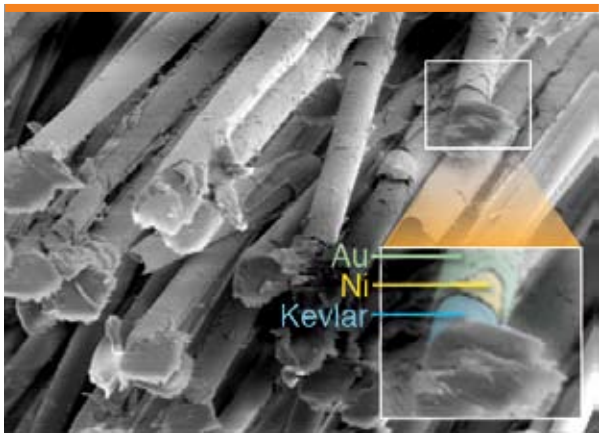

This scanning electron microscope image shows the results of coating Kevlar®, a fiber often used in tether manufacture, with nanometer-thick films of nickel and gold. The gold film protects the fiber from AO degradation; the nickel layer enhances uniformity of the gold coating.

A tether braid of eight 278 dtex Zylon® fibers, six 3270 dtex Zylons®, and two aluminum wire braids forms a high-strength and conductive construction because of the high Zylon® content.

This task is a joint effort between Auburn University in Auburn, Alabama, and Marshall Space Flight Center's (MSFC's) In-Space Propulsion Technology Project (Huntsville, Alabama). Tethers Unlimited, Inc., in Bothell, Washington, will assist with Hoytether™ manufacture, and Steeger-USA, in Inman, South Carolina, will build a takeup system for MSFC's tether braining machine. Tether braiding and testing will be performed in Auburn's Mechanical Engineering Department and at MSFC's Space Environmental Effects Laboratory, Atomic Oxygen Beam Facility, and Propulsion Research Laboratory.

Future Potential Activities

The data from this task are critical to the realization of in-space cable, stringer, and tether applications. Next steps include understanding the electrochemical metalization mechanism at a molecular level to improve its efficiency, exposing a promising coating technology (painting of damaged tethers) for in-space repair, modifying the MSFC braiders for construction of Hoytether™ configurations, design/construction of machinery to build long-length tethers at high rates of production under strict quality control standards, and construction of long-length tethers and in-flight testing for NASA DoD, and aerospace applications.

Capability Readiness Level (CRL)

The CRL for tether coating technology is expected to advance from 1 to 3; macroscopic tether construction and design technology will advance from CRL 2 to 5.

Principal Investigator

Dr. David Beale, Auburn University, dbeale@eng.auburn.edu, (334) 844-3336

AME Contact/Project Lead

Beth Cook, NASA/MSFC, Beth.Cook@nasa.gov, (256) 544-2545

National Aeronautics and Space Administration

Marshall Space Flight Center
Huntsville, AL 35812

www.nasa.gov

FS-2006-09-148-MSFC

Structural Materials

Titanium- and Zirconium-Based Wires

NASA Marshall Space Flight Center

Wire is a mainstay of spacecraft components such as umbilical tethers, and it may well enable novel space transportation systems such as space elevators, solar sails, and tether propulsion. Exploration spacecraft will need wires that are light, strong, and serve multiple purposes. Wire and other materials will be exposed to the harsh thermal, radiation, and vacuum environments of space for longer periods and may even need to operate near a nuclear fuel source. Titanium and zirconium materials are commonly used in aerospace applications and appropriate alloys/microstructures may provide candidate wires due to their strength-weight ratio, corrosion resistance, and wide range of temperature applicability.

An earlier study by this principal investigator resulted in the first known fabrication and evaluation of pearlitic-type titanium- and zirconium-based alloy compositions for potential wire applications. The research began with the postulation that a unique group of titanium- and zirconium-based alloy wires could be fabricated based on the process used to make high-strength cords for tire manufacturing. In this process, the iron-carbon alloy isothermally transforms via a solid-state eutectoid reaction to form two new compositions, or phases. The spacing between the two phases is often fine enough to break up light and give the material a pearl-like appearance, hence the name pearlite. Interactions between the phases contribute to the strength, which is further increased by drawing the wire to a thinner diameter. Examination of titanium and zirconium phase diagrams showed when these base metals were properly alloyed and heat treated, they exhibited a pearlitic-like microstructure, which would be useful for producing novel composite wires.

Task Description

This Advanced Materials for Exploration (AME) research builds on the prior study. Investigators will fabricate wires made of titanium and zirconium alloys and test the wires to see if they have the properties required for operation in the harsh space environment. Tasks include

1. Completing studies of relevant scientific and technical data
2. Applying previous knowledge to facilitate fabrication processes
3. Fabricating and heat treating wires
4. Characterizing wire microstructures
5. Testing, modeling, and evaluating wire mechanical properties.

This 10-month effort was initiated and will be completed in FY06.

Anticipated Results

In the prior study, the following series of alloys, among others, were cast, heat-treated, and slowly cooled through the appropriate eutectoid-type reaction to yield a pearlitic microstructure: titanium-silver, titanium-platinum, titanium-palladium, zirconium-silver, zirconium-platinum, and zirconium-palladium. Under the current study, the alloy

TITANIUM- AND ZIRCONIUM-BASED WIRES

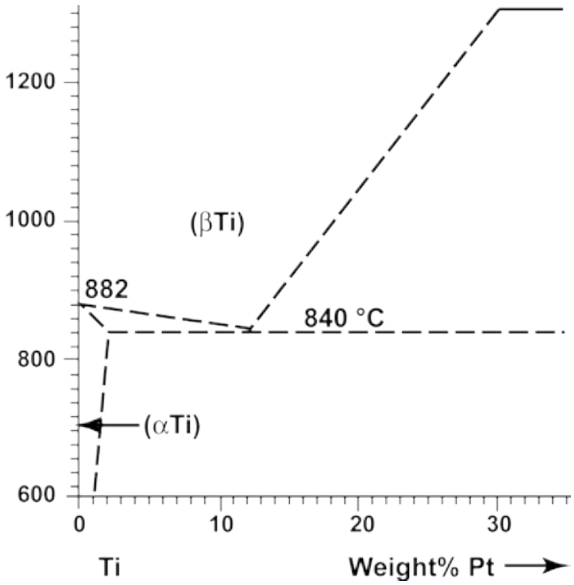

This partial titanium-platinum phase diagram shows a eutectoid reaction at Ti-12wt.%Pt. The principal investigator has produced several pearlitic-type microstructures based on titanium and zirconium alloys exhibiting eutectoid reactions.

compositions will be fine-tuned based on previous results, cast samples will be vacuum heat treated, and samples will be prepared for mechanical testing. Microstructural characteristics/development of the alloys will be examined and recorded throughout the fabrication and testing steps. The resultant mechanical properties of each alloy will be compared with established commercial products, and steps will also be taken to determine the material's potential use in spacecraft components needed for deep space exploration missions.

The wires will be fully fabricated, tested, and evaluated within Marshall Space Flight Center (MSFC) laboratories, including alloy development, heat treatment, and mechanical deformation (rolling and drawing). Diagnostic facilities include a complete metallographic preparation laboratory, diagnostic X-ray equipment, optical microscopes, microprobes, and electron microscopes.

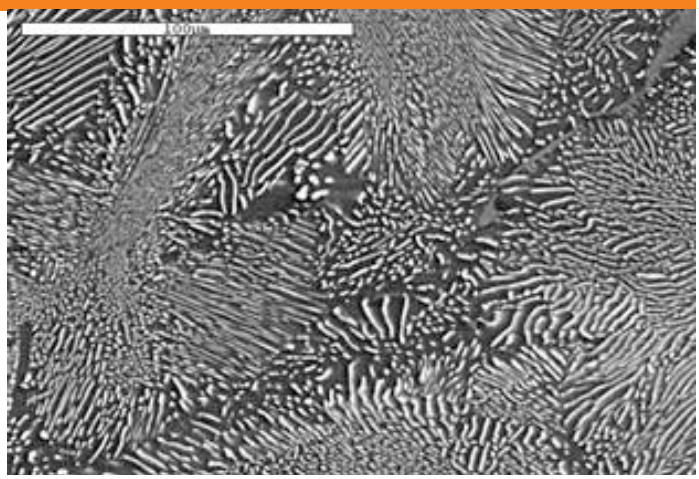

This micrograph shows the Ti-12wt.%Pt microstructure after processing at ~1373 K for ~24 hours and then cooling at 0.1 K/s. A lamellar eutectoid structure consisting of alternate sheets of Ti and Ti3Pt, an intermetallic compound, is seen.

Potential Future Activities

The next steps are to test these novel wire samples in a simulated space environment (vacuum, radiation exposure, extreme temperatures) and to use them in prototype components for structural and propulsion elements. MSFC has the resident materials experts and facilities to produce the wires, test them in simulated space environments, and evaluate their performance.

Capability Readiness Level (CRL)

This AME task will fabricate and test titanium- and zirconium-based wires, among others, in the laboratory (CRL 4). Subsequent testing under simulated space environment conditions would elevate this technology to CRL 7 and provide materials selection criteria for designers of spacecraft structural components and propulsion systems. Development of these materials will contribute to the efficiency and reliability of future spacecraft.

Principal Investigator

Dr. Richard Grugel, NASA/MSFC, Richard.N.Grugel@nasa.gov, (256) 544-9165

AME Contact/Project Lead

Beth Cook, NASA/MSFC, Beth.Cook@nasa.gov, (256) 544-2545

National Aeronautics and Space Administration

Marshall Space Flight Center
Huntsville, AL 35812

www.nasa.gov

FS-2006-06-62-MSFC

Structural Materials

Ionic Liquid Adhesives for Aerocapture

NASA Marshall Space Flight Center

Spacecraft that rely on aerocapture or aerobraking techniques to enter and travel through planetary atmospheres require thermal protection systems (TPSs) that can withstand the extremely high temperatures experienced during these stages of their missions. In addition, these TPSs must be lightweight to reduce payload lifting requirements and must adhere strongly to the aeroshell during atmospheric entry. At the 2004 Advanced Materials for Exploration (AME) Advanced Space Propulsion Materials Workshop: Aerocapture, the maximum temperature and duration challenges for such adhesives during planetary entry were determined to be 500 °C (932 °F) for a 30-minute duration. Current TPS bonding systems have service temperatures between 250 and 300 °C (482 to 572 °F), requiring that the outer TPS be thick enough so that this range is not exceeded. Increasing adhesive service temperatures to at least 500 °C (932 °F) would significantly reduce the thickness and mass required for the outer TPS for future exploration spacecraft, particularly those designed to return samples to Earth.

Ionic liquids (ILs) and their polymers show great promise as stable high-temperature adhesives. ILs are a distinctive class of environmentally friendly organic materials whose high-temperature and chemical stabilities often exceed those of conventional organic materials; many ILs can maintain their integrity at 400 to 500 °C (752 to 932 °F) for several hours. In addition, ILs can be designed for specific applications; the ability to synthesize substrate-specific, adhesion-capable, contamination-tolerant IL adhesives constitutes a significant development in TPS bonding technology. Because ILs can act as solvents, little or no surface preparation of the aeroshell or the TPS may be required, thus reducing manufacturing time and environmental impact.

Task Description

The goal of this AME task is to design ILs based on the "blueprints" of high-temperature, high-strength polymers to create adhesives and bonding agents with higher service temperatures, lower cure temperatures, and better surface adhesion. To accomplish this objective, researchers will:

1. Synthesize IL monomers that adhere to candidate structural material (aluminums, ceramics, and composites) with strengths equivalent to existing structural polymer adhesives and that can cure at ambient temperatures

2. Polymerize the ILs and test the resulting materials in high-temperature and vacuum conditions

3. Document critical behaviors, characteristics, and process chemistry that promote the desired ILs performance with each candidate material.

This 10-month AME will culminate in September 2006.

IONIC LIQUID ADHESIVES FOR AEROCAPTURE

Anticipated Results

This AME task will demonstrate that ILs can replace current adhesives, which are deficient in high-temperature designs. Researchers at Marshall Space Flight Center (MSFC) will synthesize IL monomers based on the chemistry of known high-temperature, high-strength polyimides, *e.g.,* fluorinated and aromatic polyimides and bis-maleimides. After curing, the mechanical and adhesive properties of the resultant candidate resins will be determined by baseline tests and processing methods. Curing processes will also be assessed.

By investigating alternate polymerization techniques, researchers hope to define a 500-°C (932-°F) IL adhesive that can be cured at low temperatures for each structural material. The adhesives' temperature performance data and process sensitivity will lay the groundwork for continued development of environmentally friendly high-temperature bonding systems.

Left: Button tensile testing was used to determine tensile properties of adhesive bonds between various ionic liquids and aluminum. Preliminary results suggest that some IL-based polyimides (ILPI-1) can exhibit adhesive strengths comparable to—even slightly greater than—conventional polyimides. Work is ongoing at MSFC to determine optimum curing conditions so that the inherent strength of IL polyimides for adhesives, bonding agents, and structural composites can be maximized.

Right: Two polyimide films, CP2, a conventional material (top) and ILPI-1, an IL-based material, (bottom) show that the IL polyimide contains fewer bubbles/voids that can reduce mechanical strength.

Potential Future Activities

Future work would include continuing the development of IL adhesives/bonding agents that would be stronger and possibly withstand even higher temperatures, based on the current rapid advances in the state of the art of IL technology. For example, recent articles in the scientific literature indicate that impurities such as halide ions can decrease the chemical and thermal stability of ILs. Since halogenated compounds are commonly used in IL syntheses, finding ways to remove halogens from the final product, or even circumvent their use altogether, is an active area of research. Additionally, research into the development of IL-based bis-maleimides, which can be cured at low temperatures and do not off-gas, should be promoted. Research could also broaden to include improvement of material properties such as radiation resistance and electrical conductivity (static charge build-up mitigation). Field tests of the adhesives developed in this task, possibly conducted during robotic lunar lander missions, would pave the way for their use on later NASA missions to the Moon, Mars, and other planets. Industrial applications include adhesives, composites, and structural materials that not only have superior performance over conventional materials but are also "green."

Capability Readiness Level (CRL)

This task will advance the CRL of high-temperature adhesive materials development from 1 to 3.

Principal Investigator

Rhonda Libb, NASA/MSFC, Rhonda.S.Libb@nasa.gov, (256) 961-1479

AME Contact/Project Lead

Beth Cook, NASA/MSFC, Beth.Cook@nasa.gov, (256) 544-2545

National Aeronautics and Space Administration

Marshall Space Flight Center
Huntsville, AL 35812

www.nasa.gov

NP-2006-09-136-MSFC

Structural Materials/
Thermal Materials

Novel Nanolaminates

NASA Marshall Space Flight Center

Materials constructed of extremely thin (on the order of nanometers) alternating layers of different materials often exhibit novel qualities that are far different from the bulk properties of the contributing materials. While the behavior of composite materials is usually governed by the "rule of mixtures," in which their properties are an average of those of the contributing materials, the properties of nanolaminates are determined by the layer thicknesses and detailed structures of the interfaces between layers. This attribute makes it possible for researchers to tailor materials with specific property values, such as strength, oxidation resistance, and reduced hydrogen embrittlement.

The aerospace industry has shown great interest in the potential of nickel/aluminum oxide (Ni/Al_2O_3) metal-matrix composites (MMCs) as an advanced propulsion material, such as those used in rocket engine preburners (above). The focus of this task is the engineering of a Ni/Al_2O_3 nanolaminate that is expected to have better strength, creep and fatigue resistance, oxygen compatibility, and corrosion resistance than traditional MMCs.

Task Description

To demonstrate the distinctive properties of a Ni/Al_2O_3 nanolaminate, this Advanced Materials for Exploration (AME) task will:

(1) Modify an existing Chemical Vapor Deposition (CVD) facility at the University of Alabama in Huntsville to include computer control of alternating vapor sources

(2) Use CVD to manufacture Ni/Al_2O_3 nanolaminates of several thicknesses, alternating nanolayers of Ni and Al_2O_3

(3) Characterize the material structures and determine intra-lamellae spacing with X-ray Diffraction (XRD), Scanning Electron Microscopy (SEM), and optical microscopy techniques

(4) Manufacture thicker bilayered materials to test for mechanical strength at elevated temperatures [up to 800 °C (1472 °F)]

(5) Compare resulting nanomaterials properties to Ni-based MMCs and Ni-based superalloys.

This 10-month task began in December 2005 and will culminate in September 2006.

Anticipated Results

The manufacturing process is a critical factor in nano-engineering. Investigators selected CVD because it is less expensive than physical vapor disposition techniques, often yields better microstructures, and can be used to manufacture complex shapes. The research team has developed a CVD technique and processing equipment

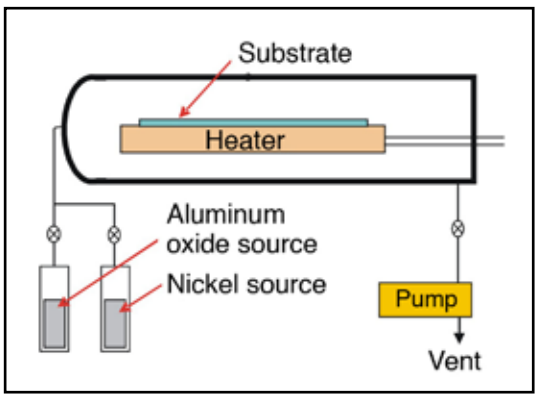

Chemical Vapor Diffusion process

advanced materials for exploration

NOVEL NANOLAMINATES

Credit: Media Fusion, Inc./NASA

Nanolaminate materials are expected to improve the performance of ballute materials by increasing their strength and ability to function at the high temperatures associated with aerocapture in planetary atmospheres.

to deposit films of Al_2O_3 and Ni and will use this technique to engineer Ni/Al_2O_3 laminate structures comprised of up to thousands of alternating layers. The resulting material is expected to exhibit significant resistance to hydrogen embrittlement, be 30% lighter than Ni, and possess heretofore unequaled strength from ambient temperatures to 1000 °C (1832 °F).

First, investigators will deposit single or just a few layers to establish the optimal CVD parameters. Using facilities in the Materials and Processes Laboratory and the National Center for Advanced Manufacturing at Marshall Space Flight Center, the team will characterize these materials by SEM (surface characteristics and lamellae spacing), XRD (orientation and size of the grains and intra-lamellae space), optical microscopy (microstructure quality), and profilometry (total layer thickness). When they have determined the best deposition conditions, researchers will fabricate thicker samples [0.5 x 4 mm and >1 mm thick (0.02 x 0.16 in. and >0.04 in.)] with hundreds of nanolayers in several bilayer thicknesses (10, 20, 50, and 100 nm). These samples will be characterized mechanically and metallographically using tensile pull and hardness indentation tests to evaluate strength at elevated temperatures [>800 °C (1472 °F)]. The thermo-mechanical properties of the Ni/Al_2O_3 nanolaminates then will be compared with those of Ni alloys and Ni/Al_2O_3 MMCs.

Potential Future Activities

Successful demonstration of the advanced properties of Ni/Al_2O_3 nanolaminates will be of interest to developers of improved rocket engine components, such as injector faceplates and bodies and preburners. Another potential application is in ballute structures. A thin nanolaminate coating no thicker than a few micrometers could enhance the polyimide thin films currently used for ballute structures, improving strength and operations at temperatures above 500 °C (932 °F). The nanolaminate may also have a desirable thermal anisotropy. Heat conduction through the layers will be far less than heat conduction along the layers. CVD fabrication of rolls of a nanolaminate-coated polyimide foil and of free-standing foil structures [0.05 to 0.2 mm thick (0.002 to 0.008 in.)] is possible. The potential for metal alloys with protective alumina coatings to show increased resistance to hydrogen embrittlement is another future potential investigation.

Capability Readiness Level (CRL)

At the completion of this task, the CRL of Ni/Al_2O_3 nanolaminates will have increased from 1 to 3.

Principal Investigator

Dr. Martin P. Volz, NASA/MSFC, Martin.P.Volz@nasa.gov, (256) 544-5078

AME Contact/Project Lead

Beth Cook, NASA/MSFC, Beth.Cook@nasa.gov, (256) 544-2545

National Aeronautics and Space Administration

Marshall Space Flight Center
Huntsville, AL 35812

www.nasa.gov

FS-2006-06-65-MSFC

Thermal Management

Heat Pipe Degradation

NASA Marshall Space Flight Center

Heat pipes are highly efficient at transferring thermal energy generated by high-powered spacecraft and habitat support systems. Nuclear reactors and energy conversion devices require heat pipes designed to operate at temperatures in excess of 600 °C (1112 °F) to transfer energy both to engines for the production of surface power and to radiators for the dispelling of heat. Heat pipes used for exploration missions must operate for long periods in hostile space and planetary environments with high radiation, low gravity, vacuum, sharp temperature gradients, and contaminating dust. Currently, there are not enough high-temperature data to characterize heat pipe performance degradation over long-duration space missions in harsh environments.

Contamination (poisoning) of the heat pipe transfer fluid will degrade the efficiency of the heat pipe by modifying the thermophysical characteristics of the transfer liquid. Penetration of lunar or Martian soil and dust (regolith) can cause contamination particularly if they are built up around heat pipes to provide insulation and radiation protection. Chemical reaction between the containment metal and the regolith over long periods of time could lead to corrosion of welds and escape of the heat pipe active vapor.

Task Description

The objective of this Advanced Materials for Exploration (AME) research is to obtain data and access potential mechanisms that may lead to degradation of heat pipe performance, with special emphasis on the reactivity of the candidate material with the environment. Tasks include

1. Designing and fabricating thermosyphons (gravity-driven devices which do not require wick structures)
2. Measuring the diffusivity of gases through a heat pipe material, specifically Inconel 625™
3. Measuring reactivity of Inconel 625™ with lunar and Martian soil simulants
4. Measuring reactivity of heat pipe materials with sodium
5. Modeling behavior of thermosyphons.

This 16-month effort was initiated in FY05 and will be completed in FY06.

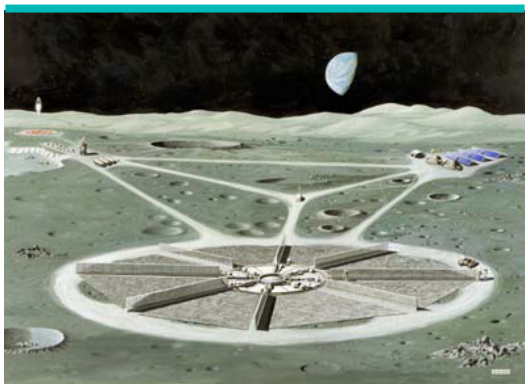

Lunar-based nuclear power reactors (above) will require heat pipes that are designed to operate at high temperatures in harsh environments for long periods. Marshall Space Flight Center researchers have designed a furnace to study how gas diffuses through the metal wall of a heat pipe. The furnace is equipped with gas pressure and flow controllers and pressure measuring gauges. This data can be used to design improved space power reactors.

HEAT PIPE DEGRADATION

Anticipated Results

Researchers are designing and testing heat pipes made of thick-walled outer tubes and thin-walled inner tubes through which gases (hydrogen, helium, and carbon dioxide) can penetrate. The heat pipes are constructed of traditional materials (Inconel 625™, stainless steel, and refractory metals). Gas diffusion is being measured over a range of temperatures and times. In early 2006, the first test was well underway and was assessing the diffusion of helium through Inconel 625™.

In a separate experiment, investigators are measuring the reactivity of the heat pipe materials with lunar soil simulant (JSC-1), and Martian simulant. Lunar simulant was ball-milled and sized to below 150 mesh and heated. These powders are then loaded under vacuum into Inconel 625™ tubes and heated for 500 hours and longer. Following testing, the tubes are opened and the powder retrieved for reactivity tests. Electron microscopy and X-ray diffraction are used to determine whether reaction has taken place and has modified the simulant phases or corroded the metal. For comparison, tubes have also been loaded with sodium.

For another assessment, six gravity-assisted heat pipes (thermosyphons) are built, will be filled with sodium, and will be operated at high temperatures for 2 months. Investigators will compile data on the reactivity of the sodium with the heat pipe materials. Temperature profiling will be done during the thermal tests to ascertain if there is any degradation of heat transfer over time. Marshall Space Flight Center (MSFC) laboratory facilities are being used for all heat pipe manufacturing, testing, and modeling. MSFC has fluid physicists and materials scientists with experience developing similar experiments for Earth and spacebased experiments.

Potential Future Activities

These tests were carried out over a short time frame. To simulate longer operating times, future tests should be continued for a year or longer. Cycling of the temperature is also important as the "start-up" characteristics may change after long periods of operation. The use of thermosyphons simplified the design, but future experiments should be carried out with a wick structure. Finally, controlled amounts of a contaminating gas could be introduced into the tubes.

This illustrates the condition of Inconel tubes and powder following reaction at 1000 °C (1832 °F) for 500 hours. Note the "clinkering" of the powder.

Capability Readiness Level (CRL)

This AME task tested heat pipes in the laboratory and simulated chemical conditions on the lunar surface to obtain data essential to predicting heat pipe performance under specific, simulated environments (CRL 4) for lunar surface applications. Experiments in space with real heat pipes and fluids would elevate this to CRL 8 for in-space transportation. Designers could use the experiment data to predict heat pipe performance and operations under various conditions. A detailed understanding of various environmental effects on heat pipe performance is essential for assuring optimized, long-duration performance and prediction of heat pipe reliability for specific environments (space, Moon, Mars) and applications (habitats, propulsion systems, nuclear power generators).

Principal Investigator

Dr. Don Gillies, NASA/MSFC, Donald.C.Gillies@nasa.gov, (256) 544-9302

AME Contact/Project Lead

Beth Cook, NASA/MSFC, Beth.Cook@nasa.gov, (256) 544-2545

National Aeronautics and Space Administration

Marshall Space Flight Center
Huntsville, AL 35812

www.nasa.gov

FS-2006-09-154-MSFC

Thermal Management

Carbon Fiber Thermal Conductivity

NASA Marshall Space Flight Center

NASA uses low thermal conductivity carbon fibers to reduce the erosion rate for rocket nozzles during engine firings. Low thermal conductivity carbon fibers are also used to insulate hot structures inside Thermal Protection Systems (TPSs) that shield spacecraft reentering Earth's atmosphere. Nearly all other instances where carbon fiber technology is employed use the types having high strength, stiffness, and conductivity. Carbon fibers are selected for use in insulation because their coefficient of thermal expansion (CTE) matches the CTE for the carbon-carbon TPS, reducing material stress at high temperatures. Carbon fiber also is one of the few materials that retains some strength at the temperatures experienced by the carbon-carbon (C-C) TPS.

Task Description

This Advanced Materials for Exploration (AME) research is the first to perform thermal conductivity testing of existing low conductivity fibers at incandescent temperatures. Experiments will demonstrate the insulative capability of carbon-based fibers and assess the performance of different fiber types as hot structure insulators. Tasks include

1. Performing a literature study
2. Selecting high-performance carbon fibers for materials characterization
3. Conducting thermal conductivity testing of the selected fibers.

This 1-year effort was initiated in FY05 and will be completed in FY06.

Anticipated Results

The literature survey revealed that very little research has been performed on low-conductivity fibers used mainly for aerospace and military purposes. Most existing research involved fibers used near room temperature, and there was no thermal conductivity research on fibers at highly elevated temperatures, such as those encountered during atmospheric reentry.

Investigators identified two commercially available test materials [one rayon and one Poly Acrylo Nitrile (PAN) precursor type]; these were selected because of availability of materials characterization data, precursor chemistry, and similarity to potential TPS insulations. A test

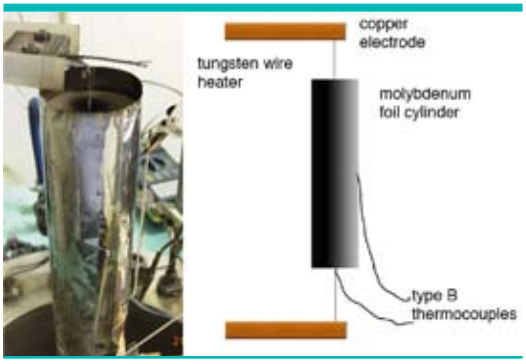

To measure thermal conductivity, carbon fibers are packed in a cylinder, and the core is heated over a range of temperatures to greater than 1400 °C (2552 °F). Thermocouples measure the temperature difference from the core to the outer shell of the cylinder to measure changes in heat transfer through the carbon fiber insulation.

CARBON FIBER THERMAL CONDUCTIVITY

procedure for minimizing carbon fiber conductivity without compromising strength was developed, based on an axial cylinder geometry method developed by the National Institute of Standards and Testing (NIST).

For these preliminary thermal conductivity experiments, carbon fiber insulation (fiber wool or bundles of randomly oriented fibers) was packed into a foot-long molybdenum foil cylinder. Carbon fibers from PAN and from rayon precursors were compared. Copper electrodes provided energy to a tungsten-rhenium wire heater element running axially through the core of the cylinder, and B-type thermocouples measured the temperature at the cylinder's core and outer shell. The whole assembly was mounted in a high vacuum chamber to prevent burning of the carbon fibers, to eliminate convective heat transport, and to simulate the rarified atmosphere during a spacecraft's reentry. Investigators found that the core-to-surface temperature difference scaled linearly with power to the heater, indicating that the ratio of heat transferred by the two conduction paths through the fiber wool did not likely change as a function of heat. This behavior was reproduced with a higher fiber packing density in a separate test.

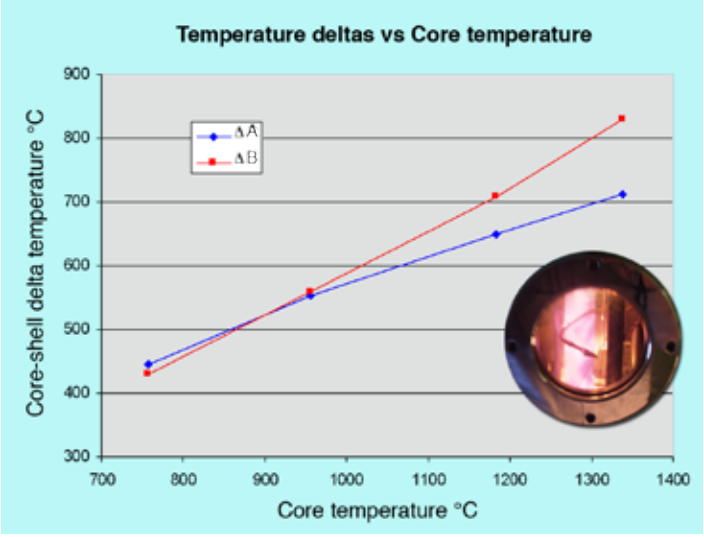

This chart shows the differences between the heater core temperatures and the shell temperatures and is plotted against one heater temperature (of two). These differences are a direct measure of the heat loss through the fiber. Plotted this way, one would expect that as the heater temperature increased, the thermal response would have been a curve upward as the fraction of radiative heat transfer progressively increases over that of conduction. This was not the case as the lines are basically straight. The heater power was increased until the shell became incandescent itself, as shown in this view through the vacuum chamber window (inset).

Potential Future Activities

More tests with different sets of parameters should be completed to corroborate the initial findings of these experiments. These tests should include fibers made from precursors with different molecular alignment(s). To further improve the insulation properties of low-conductivity carbon fibers, various heat treatment processes could be applied to the fibers. Such treatments have been shown to increase thermal conductivity and strength. However, the literature only reports the results that were positive for improving the properties in these directions. This investigation examines the reverse effect. If heat treatment, other processing factors, and the orientation of the fiber can be controlled, it may be possible to engineer improved insulation for TPS hot structures. Samples should be expanded to include other carbon-based materials that might prove valuable for thermal protection.

Capability Readiness Level (CRL)

This AME task tested small samples at temperatures similar to re-entry temperatures experienced by TPS insulation around hot structures (CRL 3). Scaling up, refining these experiments, and testing in a vacuum and simulated space environment would elevate this technology to CRL 5. This technology supports the development of more efficient thermal protection systems for space vehicles.

Principal Investigator

Dr. William Kaukler, University of Alabama in Huntsville (UAH), William.F.Kaukler@nasa.gov, (256) 544-0693

AME Contact/Project Lead

Beth Cook, NASA/MSFC, Beth.Cook@nasa.gov, (256) 544-2545

National Aeronautics and Space Administration

Marshall Space Flight Center
Huntsville, AL 35812

www.nasa.gov

FS-2006-09-153-MSFC

Thermal Management

Electronically Biased Thermal Protection System

NASA Marshall Space Flight Center

Aerocapture uses a planet's atmosphere to create drag and slow the velocity of space vehicles without using propellant. This fuel-free braking system should reduce spacecraft mass, but tremendous heat is generated as drag is created by friction between the vehicle and the planet's atmosphere. The Space Shuttle leading edge reaches approximately 1650 °C (3000 °F) when the Shuttle enters Earth's atmosphere. Spacecraft can be designed with aeroshells by applying heat shielding to external surfaces. These aeroshells must weigh less than propellant-based orbital capture systems. The thermal protection systems (TPSs) for leading edges must be non-ablative, low mass, operated at high temperatures (1900 °C, 3452 °F), and insulated to protect internal vehicle parts. Studies have shown that radio frequencies can reduce the temperature by electrically biasing the surfaces of hypervelocity aircraft. In principle, a low-voltage DC bias to a spacecraft surface should inhibit energetic ions formed during reentry from transferring their energy to the TPS and thus reduce the heat load. Studies suggested electrical biasing could reduce drag and reduce heating. This may increase the life of the TPS, which allows a reduction in TPS design mass.

Task Description

This Advanced Materials for Exploration (AME) study aims to demonstrate that electrical biasing can lower peak heating on TPSs by modifying ion-surface interactions and increasing plasma flow around the spacecraft's leading edge. Tasks include

1. Developing a prototype TPS test sample with an electrically biased coating
2. Testing the coated TPS in a hot gas environment
3. Evaluating the heat flux variance by comparing the electrically biased, coated sample to a sample with no electrical bias.

This 2-year effort was initiated in FY04 and will be completed in FY06.

Anticipated Results

In FY05, investigators made test articles of different forms of carbon with various geometries and used a hydrogen-oxygen torch to produce temperatures and plasma gas. Embedded thermocouples provided temperature data. When the test article was heated, the electrical bias was created by applying a simple DC voltage of 5 to 12 V to the TPS coating. To obtain higher temperatures (1926 °C, 3500 °F), researchers tested different geometries and blowtorch styles. Temperature traces during a test using a flat graphite plate reached 1204 °C (2200 °F) and burned through Grafoil, a flexible paper-like form of graphite (carbon) that conducts electricity and is temperature resistant. These early tests revealed no effects generated by the electrical biasing on the TPS because the temperatures were too low and not enough plasma was generated.

ELECTRONICALLY BIASED THERMAL PROTECTION SYSTEM

Heat produced by a large surface mixing torch eventually burned through the TPS coating, but higher temperatures (1500 ºC, 2732 ºF) and more plasma were generated using another test article with this shape.

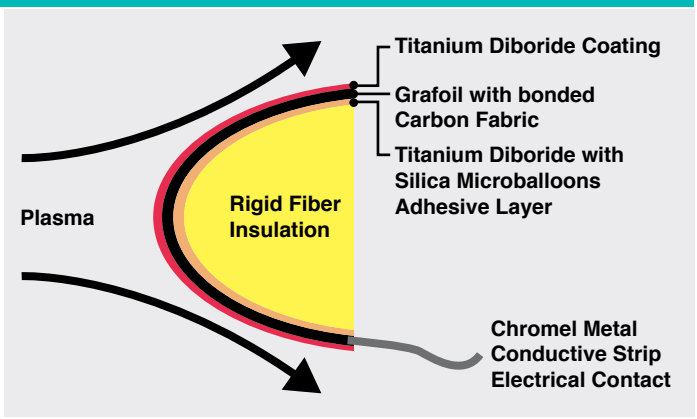

This diagram shows insulation with a titanium diboride coated Grafoil bonded to carbon fabric. When an electic current is applied, it may inhibit ion formation and thus reduce heating.

A smaller, thinner, round-shaped graphite test article provided the best results with temperatures reaching 1500 °C (2732 °F); heat was generated by a large surface mixing torch head. However, the test article showed little response to the applied voltage. Although the temperature was appropriately high and the torch generated plasma, the amount of plasma reaching the target was insufficient to demonstrate the effect. This is being improved by generating plasma more efficiently and reducing or eliminating the mixing of the atmosphere with the plasma stream. Investigators are repeating the test with a smaller target and a shorter distance between the torch and the target.

In FY06, a commercial plasma heating source and a vacuum plasma torch will be used to heat the test articles; these heat sources should produce higher temperatures and more plasmas, which will be a better test of the effectiveness of electrically biasing the TPS. Also in FY06, two ideal conductive outer coating materials were identified for future testing: titanium diboride (TiB_2) and boron carbide (B_4C).

Potential Future Activities

If the present study shows it is feasible to reduce temperature by reducing drag because the charged leading edge electrically rejects plasma, this process could be scaled up. Investigators could build larger test articles with a variety of conductive coatings such as TiB_2 and B_4C, and perform a series of similar tests in Marshall Space Flight Center space simulators. If biasing does effectively cool the TPS, calculations should be made to determine the weight of the support electronics needed to enable biasing. Follow-on studies should compare the weight required to store and deliver power with the weight savings gained by not attaching heavy shielding or fuel-driven propulsion braking systems. This would provide rationale for building more elaborate electrically biased TPSs for future spacecraft.

Capability Readiness Level (CRL)

This AME task built small samples and tested them in a laboratory environment (CRL 3). Scaling up, refining these designs, and testing in a simulated space environment would elevate this technology to CRL 5. This technology supports fuel-free aerocapture, which could reduce the mass of interplanetary spacecraft, resulting in smaller, less expensive vehicles.

Principal Investigator

Dr. William Kaukler, University of Alabama in Huntsville (UAH), William.F.Kaukler@nasa.gov, (256) 544-0693

AME Contact/Project Lead

Beth Cook, NASA/MSFC, Beth.Cook@nasa.gov, (256) 544-2545

National Aeronautics and Space Administration

Marshall Space Flight Center
Huntsville, AL 35812

www.nasa.gov

FS-2006-06-66-MSFC

Thermal Management

High-Performance Ablative Composites

NASA Marshall Space Flight Center

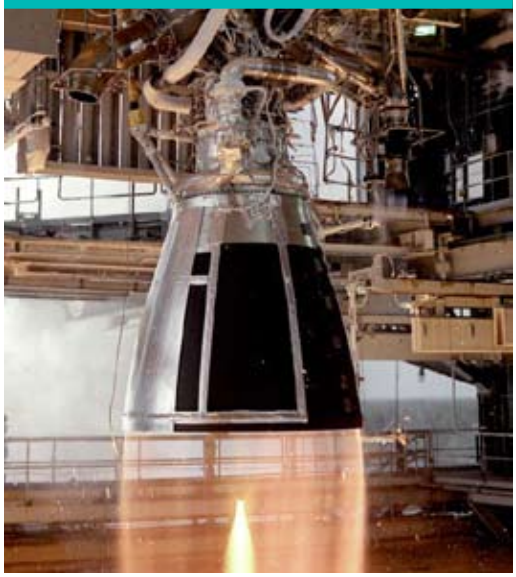

Ablative combustion chambers and nozzles are used throughout the aerospace industry for both liquid and solid propellant motors. The nozzles rely on Polymer Matrix Composites (PMCs), unique combinations of organic resins and inorganic fibers, to provide the ablative and erosion characteristics that will withstand the extremely high temperatures [>2760 °C (>5000 °F)] and supersonic gas flows associated with rocket motor plumes. Currently used phenolic resins present processing and performance challenges – curing by-products, costly processing techniques, voids and low-density regions in the finished product, and pocketing and plylift during operations.

The use of a new class of resins, polybenzoxazines (PBZs), holds the promise of improved nozzle component quality, easier and more cost-effective processing, and enhanced motor performance. Unlike the ablative phenolic resins, PBZs:

- Cure by an addition-type polymerization without reaction by-products, thus reducing or eliminating component voids and shrinkage
- Do not require hot compaction cycles during layup or high-pressure autoclave cures
- Produce an erosion-resistant, adherent char yield in excess of 70%, compared to 30-55% yields for phenolics, to protect nozzle throats from erosion during motor firing, thus enhancing nozzle motor performance.

In addition, PBZ resins exhibit excellent high-temperature mechanical properties and low moisture absorption, assets required of materials used in aerocapture environments.

Task Description

This Advanced Materials for Exploration (AME) task will evaluate the potential of PBZ resins to improve quality, ease processing, and enhance nozzle performance as compared to traditional nozzle ablative materials. Researchers will

- Use PBZ resins to fabricate pre-impregnated PBZ composites
- Characterize the composite's mechanical and thermal properties
- Test the material's ablative/erosion resistance
- Fabricate and test a small-scale motor built using the PBZ composite.

This 10-month AME task will culminate in September 2006.

A PBZ-impregnated composite undergoes the plasma torch test as part of its initial screening. Should the material perform well in this test, it will be used to fabricate the nozzle for a subscale motor.

advanced materials for exploration

HIGH-PERFORMANCE ABLATIVE COMPOSITES

Anticipated Results

This task is the first evaluation of PBZ composites for use in ablative nozzle applications. PBZ-based resins potentially provide processing and performance advantages over conventional aerospace materials, including increased component use life. This effort will improve the manufacturing processes of nozzles through the chemistry of the composite resin by reducing the number of processing steps and decreasing the pressure required for cure. The chemistry and physics of the composite will likewise improve the design of the nozzle by reducing or eliminating ablative component voids and shrinkage during curing and improving its resistance to erosion during use.

Marshall Space Flight Center's (MSFC's) Composites Fabrication and Testing laboratories at NASA's National Center for Advanced Manufacturing (NCAM) will manufacture and cure panels of PBZ resin impregnated onto carbon fiber fabric. ATK Thiokol, Inc., personnel in Huntsville, AL, will assist with specimen and component machining. MSFC's Materials and Processes Laboratory will evaluate the specimens for thermal stability [thermal conductivity, specific heat, coefficient of thermal expansion, and ablation/erosion resistance (char yield)] and mechanical strength (tension, compression, and shear). MSFC's Plasma Torch Test Bed Facility will be used to simulate the very high temperatures and heating rates seen in the nozzle environment. In addition, aluminum powder may be entered into the plasma to simulate the production of solid aluminum oxide fragments output from solid rocket motor nozzles; these fragments are a primary cause of nozzle erosion. The fabrication and test of a subscale motor at MSFC will validate the initial erosion resistance and the propensity of the PBZ composite to exhibit other detrimental phenomena, such as plylifting.

Potential Future Activities

Follow-on work would characterize additional PBZ composites for use in the design and fabrication of new rocket nozzles. These activities would have relevance to the Crew Exploration and Crew Launch Vehicles, and other future rocket motors. In addition, this AME task lays the groundwork for investigations of PBZ composites for use in nozzleless propulsion such as aerocapture applications. All required fabrication and test capabilities and engineering expertise are available at MSFC.

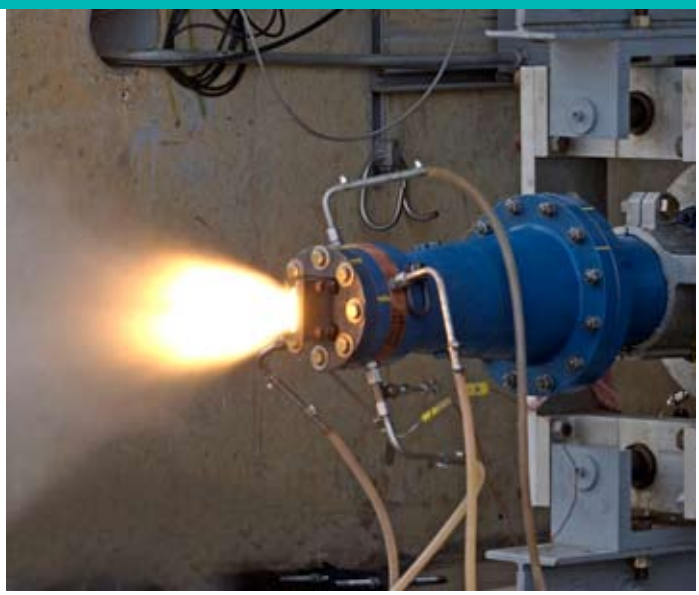

Following plasma torch testing to characterize the PZB material's ablative and erosion resistance, a nozzle built with the PZB-based composite will undergo a subscale motor test firing, similar to the one shown above. This firing will further characterize the material's performance and its potential application as a nozzle component.

Capability Readiness Level (CRL)

PBZ resins have previously been formulated, characterized, and evaluated for use in several applications, placing the CRL of this class of material at 1 or 2. This AME task will advance the CRL to 3 or 4 by enhancing previous material characterization data and performing testing specific to ablative nozzle application.

Principal Investigator
Dr. Raj Kaul, NASA/MSFC, Raj.K.Kaul@nasa.gov, (256) 544-1084

AME Contact/Project Lead
Beth Cook, NASA/MSFC, Beth.Cook@nasa.gov, (256) 544-2545

National Aeronautics and Space Administration

Marshall Space Flight Center
Huntsville, AL 35812

www.nasa.gov

FS-2006-09-150-MSFC

Thermal Management

Aerogel-Insulated Cryogenic Tanks

NASA Marshall Space Flight Center

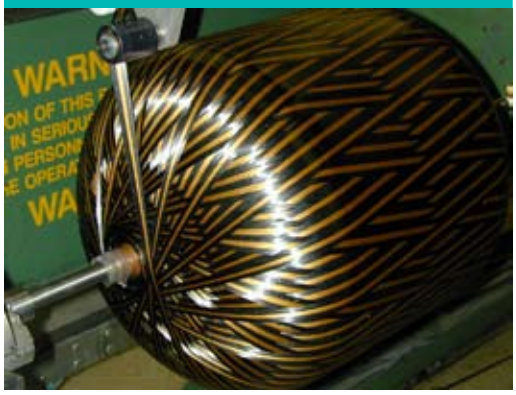

Insulation protects spacecraft from the very low and high temperatures experienced during loading of cryogenic propellants, launch, orbital or interspace travel, and atmospheric reentry. Insulation must also minimize heat flow to the cryogenic fuel tanks while a spacecraft waits on the launch pad in ambient atmospheric temperatures. A promising family of advanced materials—aerogels and aerogel composites—exhibits excellent insulation properties at extreme temperatures and at vacuum or atmospheric pressure. These materials are also exceedingly lightweight and thus cost-efficient. Conventional aerogels, however, are very fragile. Scientists at Glenn Research Center (GRC) have developed a polymer-crosslinked silica aerogel composite, called X-aerogel, that requires 300 times more force to break, has 10 times the specific compression strength of steel, but is only 2 times more dense than earlier aerogels. This quantum technology leap in robustness allows X-aerogel, unlike its predecessors, to be used in applications in which other aerogels would crumble or turn to dust. Monoliths of X-aerogel can also be molded into complex shapes to insulate, for example, the curved shape of a cryotank. In addition, by using the right type and amount of polymer crosslink, flexible X-aerogel monoliths can be manufactured.

Task Description

Three NASA Centers—GRC, Kennedy Space Center (KSC), and Marshall Space Flight Center (MSFC)—are combining their expertise in aerogel and X-aerogel production, composite cryotank manufacture, and testing to advance spacecraft insulation technology by insulating small cryotanks with X-aerogel. Tasks include:

- Manufacture of small composite bottles (cryotanks): MSFC
- Production of enough X-aerogel to insulate several small composite bottles: GRC
- Cryogenic thermal performance testing of the X-aerogel/cryotank system: GRC, KSC
- Evaluation of the thermal conductivity of the insulation: KSC
- Mechanical test and non-destructive evaluation of the insulated cryotanks: MSFC.

This work is part of a series of collaborations between GRC, MSFC, and KSC that began in 2005; the current task should be completed before 2007. This effort has been funded by multiple sources, and the Advanced Materials for Exploration (AME) program is supporting the MSFC-led tasks.

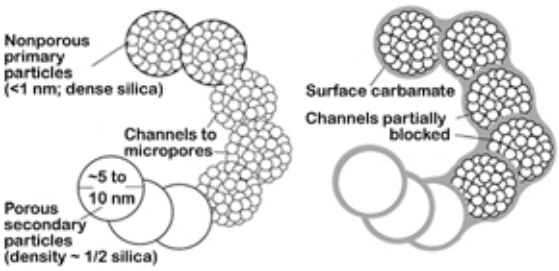

When the primary particles of this aerogel react with an isocyanate monomer, a conformal polyurethane/polyurea coating forms around the nanoparticles, making them stronger, breathable, and hydrophilic.

AEROGEL-INSULATED CRYOGENIC TANKS

Anticipated Results

Results of tests on the X-aerogel-insulated subscale composite cryotanks will enable scaling up to larger insulated composite tanks, which are considered strategic to NASA's Vision for Space Exploration. In addition, findings from thermal performance tests may advance zero boil-off (ZBO) technologies; ZBO systems include active cooling devices. Active systems, combined with passive insulation systems, will make it possible to store cryogenic propellants for long periods without the need for venting. This capability will allow a reduction in the size and weight of propellant tanks.

Researchers at GRC will produce X-aerogel to cover six small [5.75-in. (14.6-cm) internal diameter] composite bottles made of carbon fiber/epoxy resin. The bottles will be manufactured by MSFC's Non-Metals Engineering Branch, where advanced techniques, such as fiber wrapping, are routinely used to build cryotanks of all sizes. After being insulated at GRC, the bottles will return to MSFC for overwrapping with more composite material. When the first of the miniature cryotanks is complete, it will undergo cryogenic thermal performance testing at KSC and MSFC. If the first unit performs well, the remaining five bottles will be completed and will undergo a battery of tests at MSFC and KSC.

Future Potential Activities

The data resulting from this task will be critical to the manufacture and insulation of full-scale cryogenic composite tanks. Future experiments that focus on successful scaling up will be necessary to increase Capability Readiness Level (CRL). In addition, the ability to mold X-aerogel into complex shapes makes the other beneficial aerogel properties available to numerous space, military, and commercial applications: as thermal insulation systems for many types of equipment and structures, to provide infrared invisibility for military vehicles, as various types of sensors, as supercapacitors, in numerous optics applications, for more efficient ultrasonic devices, as shock absorption in protective head gear, as purification filters, for hydrogen fuel storage, as catalysts for chemical reactions, in microwave electronics, as high-voltage insulators, and as containers for energetic materials (non-nuclear explosives).

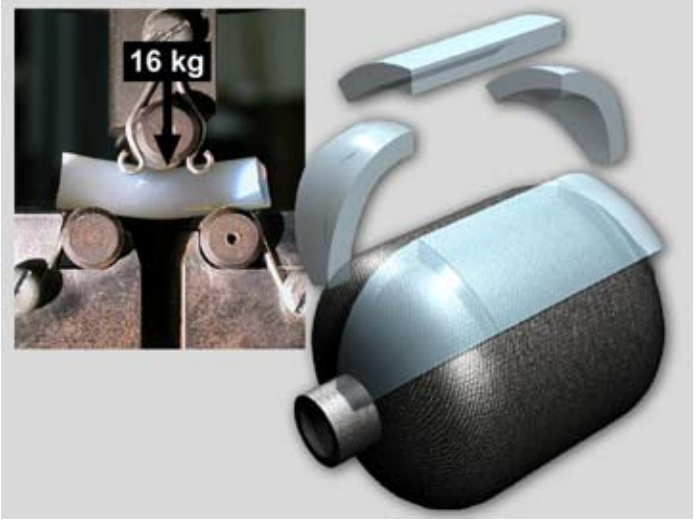

Upper left: A crosslinked silica aerogel undergoing a three-point flexural bending test. The density of the monolith is ~0.55 g/cm^3 (0.3 oz/in.^{3}). The density of the underlying silica is ~0.18 g/cm^3 (0.1 oz/in.^{3}), and the silica has been crosslinked with polyhexamethylene diisocyanate.

Right: The ability to cast X-aerogel into curved shapes creates the possibility of using this extremely lightweight but tough material as insulation for cryogenic tanks, resulting in significant weight reduction.

Capability Readiness Level

The CRL for subscale cryotanks is 3. Completion of this task is anticipated to elevate the CRL to 4, provide the basis for thermal insulation system development, and increase the CRL of full-scale cryotanks.

Principal Investigators

Dr. Mary Ann Meador, NASA/GRC, Maryann.Meador@nasa.gov, (216) 433-3221

James Fesmire, NASA/KSC, James.E.Fesmire@nasa.gov, (321) 867-7557

Gweneth Smithers, NASA/MSFC, Gweneth.A.Smithers@nasa.gov, (256) 544-0282

AME Contact/Project Lead

Beth Cook, NASA/MSFC, Beth.Cook@nasa.gov, (256) 544-2545

National Aeronautics and Space Administration

Marshall Space Flight Center
Huntsville, AL 35812

www.nasa.gov

FS-2006-08-115-MSFC

Thermal Management

Reaction-Sintered Materials

NASA Marshall Space Flight Center

Reaction sintering is a proven technology for applying high-temperature ceramic reaction-sintered coatings (CRSCs) to graphite and ceramic matrix composite materials that will be used at very high temperatures. These coatings have been evaluated for use in propulsion and thermal protection system applications, which typically involve operating environments greater than 2000 °C (3632 °F). In these applications and environments, reaction-sintered coatings have improved oxidation and erosion resistance, decreased hydrogen permeability, and improved resistance to particle and electromagnetic radiation. They also make possible the use of low-density substrate materials, such as graphite and carbon-carbon. Reaction sintering has also been used to fabricate joints between various combinations of graphite, carbon-carbon composites, and refractory metal components. Facilities that support CRSC and joining technology development are critical for both thermal management applications (strong, lightweight, durable, leading edge and heat shield components) and propulsion applications (lightweight erosion-resistant nozzles, thrust chambers, and hot-gas valve components) required for tomorrow's spacecraft.

Task Description

Funding for this Advanced Materials for Exploration (AME) project enables the completion of a 5-year effort financed by multiple projects to create an ultra-high-temperature furnace facility at Marshall Space Flight Center (MSFC), only the second such facility in existence. Tasks include

1. Modification of an existing laboratory to accommodate new furnace hardware
2. Installation of furnace interfaces in the laboratory (water, power, air, *etc.*)
3. Fabrication (machining) of graphite fixtures and components and metallic connectors and supports
4. Assembly and checkout of the furnace system.

This 10-month AME project will culminate in September 2006.

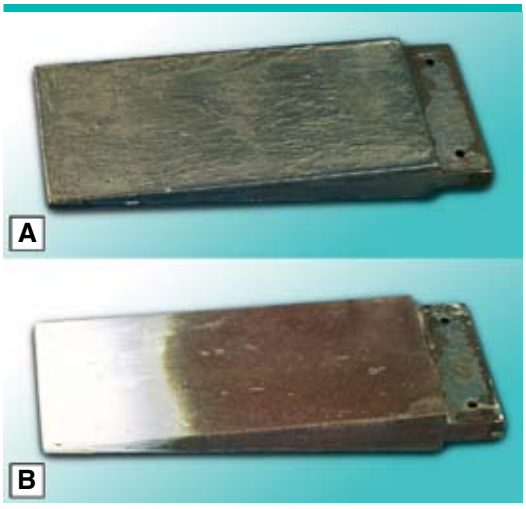

The coating composition of greatest interest for short duration ultra-high temperature exposures is a boron-carbon-hafnium system (70 wt.-% HfC + 30 wt.-% HfB_2). This coating on a carbon-carbon Hyper-X leading edge test specimen [(A) before and (B) after] Mach 10, 105,000-ft test exposure only changed in color and experienced no weight loss. (Weight loss would signify degradation of thermal protection system components.)

REACTION-SINTERED MATERIALS

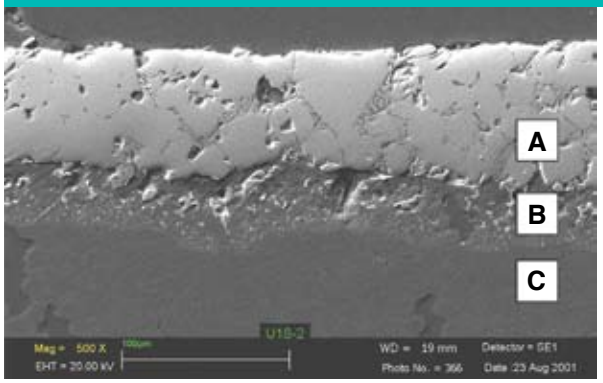

This micrograph of a hafnium carbide, hafnium diboride, and silicone carbide coating (A) on a carbon-carbon composite substrate shows how a reaction-sintered structure forms a non-porous graded microstructure (B) that enhances adherence of the coating to the substrate (C).

Anticipated Results

Completion of this task will provide NASA the capability for conducting in-house CRSC and joining processes and with the unique resources for applying coatings to lightweight high-temperature composites such as carbon-carbon and carbon/silicon-carbide, both of which are of particular interest for use in many NASA applications. The completed induction furnace system will allow scientists and engineers to fashion ceramic coating microstructures that are compatible with specific materials and environments. The furnace will heat components coated with precursor coating materials to very high temperatures, *e.g.*, 2550 °C (4622 °F), to form the desired final microstructures.

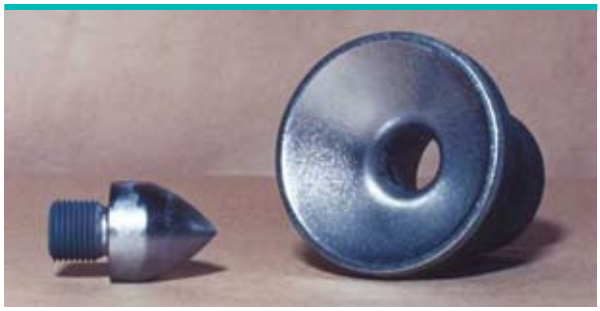

This graphite pintle (left) and its seat (right) have been ceramic reaction-sintered coated with HfB_2-HfC to better protect the components from the extremely erosive, high-temperature, solid rocket motor environment in which they operate.

The reaction-sintering process provides uniformity of coating thickness (variation of ±25 µm), uniform distribution of microstructural phases, low percentage of porosity (% porosity <5%), and 100% substrate coverage. The process consists of three steps:

1. Ultrasonically cleaning and then heating substrate materials in a vacuum furnace to remove adsorbed/absorbed gases and to vaporize volatile impurities
2. Brush coating the substrate surfaces with a slurry of an organic binder, alcohol, and ceramic powder particles; then heating the precursor-coated specimen in an oven to cure the binder and to evaporate the alcohol
3. Heat treating the cured, precursor-coated specimen in a very high-temperature induction furnace to consolidate the coating powder particles by reaction sintering.

The final microstructure of the coating, developed during high-temperature processing, forms primarily by chemical reaction and solid particle sintering.

Potential Future Activities

When complete, the very high-temperature furnace and laboratory will support a variety of thermal management and propulsion materials development projects and feasibility studies for a reasonable investment per task. Anticipated uses include development of ceramic reaction-sintered coatings for use in hot gas valves, thermal protection system components (leading edges for hypersonic vehicles), and rocket propulsion systems (including liquid, solid, and nuclear thermal systems). Using this facility, NASA will be able to develop specific materials systems and processing techniques (coatings and/or joint compositions) for particular substrates and components.

Capability Readiness Level (CRL)

Initial and final CRL levels of the materials and technology to be developed using this facility will be application specific.

Principal Investigator

Peter G. Valentine, NASA/MSFC, Peter.G.Valentine@nasa.gov, (256) 544-2837

AME Contact/Project Lead

Beth Cook, NASA/MSFC, Beth.Cook@nasa.gov, (256) 544-2545

National Aeronautics and Space Administration

Marshall Space Flight Center
Huntsville, AL 35812

www.nasa.gov

FS-2006-09-149-MSFC

Thermal Management

Heat Pipe/ Radiator Design

NASA Marshall Space Flight Center

Some International Space Station radiators are housed in trusses (above) weighing in at 12,476 kg (27,506 lb) and measuring 13.7 m (45 ft) long, 4.6 m (15 ft) wide, and 4 m (13 ft) high. Future missions to the Moon and Mars will require even more efficient and durable thermal management systems to dissipate waste energy generated by high-powered spacecraft and habitat life support systems. Generally, for greater heat rejection, the radiators and heat pipes must be larger. Since spacecraft need to be as light as possible to carry more payload and people, it is crucial that designers optimize radiator designs to provide maximum heat rejection with minimum mass.

The latest radiator designs are segmented and consist of many parallel, finned heat pipes. Each pipe has an evaporator section that is immersed in a manifold or duct containing fluid to be cooled while the condenser section is equipped with fins that radiate to space. The width, thickness, and emissivity of the fins drive this modular radiator design.

Task Description

This Advanced Materials for Exploration (AME) research team built and is testing a heat pipe fin prototype based on a design the team developed for a modular heat rejection system that used heat pipe fin elements optimized for low weight, higher heat rejection, and durability. Tasks include

1. Development of a heat pipe model
2. Selection of optimal fin material and evaluation of surface coatings to increase emissivity
3. Design and fabrication of heat pipe fin prototype
4. Testing and evaluation of the prototype's heat rejection capacity, emissivity, and durability when exposed to vacuum conditions.

This 2-year effort was initiated in FY04 and will be completed in FY06.

Anticipated Results

A heat pipe fin model was developed to calculate the heat rejected in terms of the operating temperature, the mass per unit length of heat pipe, the width and thickness of the fin geometry, and the properties of the fin material (conductivity, density, and emissivity). The model showed fin geometry must be optimized relative to the heat pipe to

Investigators prepare the 1.9-m (6.23-ft) long high thermal conductivity heat pipe fin for testing in a vacuum chamber at NASA's Marshall Space Flight Center (MSFC). A graphite fiber reinforced polymer covers a 2.5-cm (0.98-in.) diameter titanium (Ti) tube.

HEAT PIPE/RADIATOR DESIGN

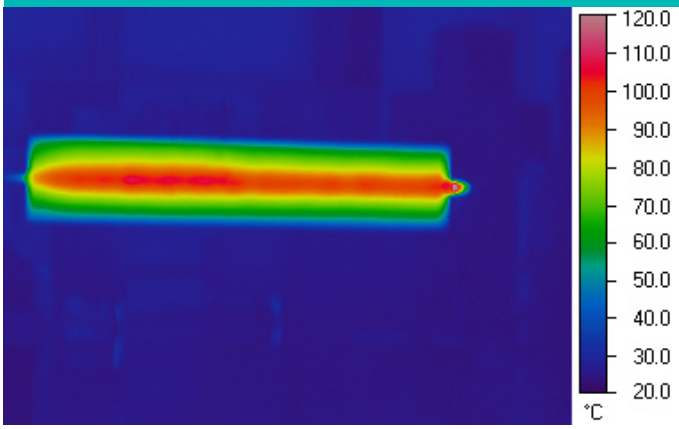

This infrared image of the heat pipe fin made during testing shows the temperature profile across the fin.

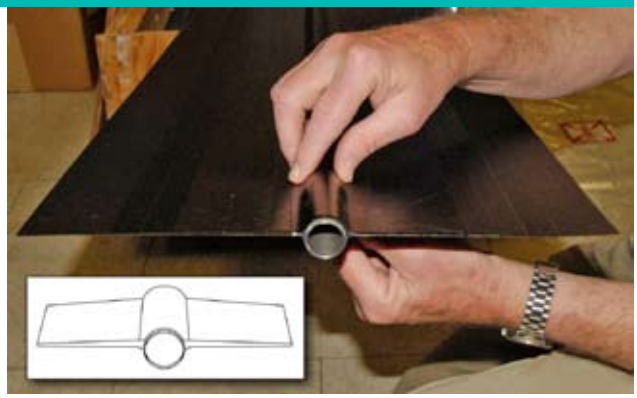

Models showed that heat pipes with tapered, wafer-thin, coated fins would provide greater heat rejection and would result in a decrease in radiator weight and size.

maximize heat radiated for minimum mass. An algorithm was then used to optimize the geometry of the fin design; this revealed that tapering the fins should maximize heat radiation and minimize mass.

The model compared existing radiator designs made with various materials. After consultations with several companies, investigators determined that fins tapered to a knife-edge thickness could best be made with a composite material. ATK Composites in San Diego, California, fabricated a high thermal conductivity graphite fiber reinforced polymer fin. The graphite fibers are patterned to match the thermal expansion of the titanium tube, which should ensure good heat transfer from the pipe to the fin during thermal cycling and reduce the possibility of delamination.

The team installed electric tube heaters in the Ti tube to simulate a heat pipe, placed the prototype fin in a vacuum chamber, and heated it to 550 K (530°F) to measure its heat rejection capacity. Thermocouples and infrared radiometers mapped heat flow around the heat pipe and the temperature profile in the fins. Researchers also recorded the surface material's emissivity. After testing, investigators examined the fin to determine the condition of the material, checking for delamination of the composite or other materials defects resulting from heating and cooling during the tests. The heat pipe fin design could become the basic element for new lightweight radiators.

Potential Future Activities

To validate this design, strength and vibration tests should be conducted. If emissivity needs to be optimized, the fins could be coated with various materials and tested. The fin prototype could be tested further for survivability and emissivity in Marshall Space Flight Center (MSFC) vibration and space environments chambers. Positive results would provide the foundation for building an optimized heat pipe/radiator using this fin design.

Capability Readiness Level (CRL)

This AME task built a prototype for a heat pipe fin and tested its performance in a vacuum environment (CRL-5). Refinement of this heat pipe/radiator design and fabrication and testing of a prototype radiator in space simulators would elevate this technology to CRL 7.

Principal Investigator

Dr. Robert Naumann, University of Alabama in Huntsville, naumannr@email.uah.edu, (256) 824-6846

AME Contact/Project Lead

Beth Cook, NASA/MSFC, Beth.Cook@nasa.gov, (256) 544-2545

National Aeronautics and Space Administration

Marshall Space Flight Center
Huntsville, AL 35812

www.nasa.gov

FS-2006-09-152-MSFC

REPORT DOCUMENTATION PAGE

Form Approved
OMB No. 0704-0188

1. AGENCY USE ONLY *(Leave Blank)*	2. REPORT DATE	3. REPORT TYPE AND DATES COVERED
	July 2008	Technical Memorandum

4. TITLE AND SUBTITLE

Advanced Materials for Exploration Task Research Results

5. FUNDING NUMBERS

6. AUTHORS

Compilers: M.B. Cook, K.L. Murphy,* and T. Schneider**

7. PERFORMING ORGANIZATION NAME(S) AND ADDRESS(ES)

George C. Marshall Space Flight Center
Marshall Space Flight Center, AL 35812

8. PERFORMING ORGANIZATION REPORT NUMBER

M–1234

9. SPONSORING/MONITORING AGENCY NAME(S) AND ADDRESS(ES)

National Aeronautics and Space Administration
Washington, DC 20546–0001

10. SPONSORING/MONITORING AGENCY REPORT NUMBER

NASA/TM—2008–215465

11. SUPPLEMENTARY NOTES

Marshall Space Flight Center, Science and Mission Systems Office
*Jacobs Engineering Group, Inc., 1525 Perimeter Parkway Suite 330 Huntsville, AL 35806
**Integrated Concepts and Research Corporation, MSFC, Building 4623, Marshall Space Flight Center, Al 35812

12a. DISTRIBUTION/AVAILABILITY STATEMENT

Unclassified-Unlimited
Subject Category 23
Availability: NASA CASI 301–621–0390

12b. DISTRIBUTION CODE

13. ABSTRACT *(Maximum 200 words)*

The Advanced Materials for Exploration (AME) Activity in Marshall Space Flight Center's (MSFC's) Exploration Science and Technology Directorate coordinated activities from 2001 to 2006 to support in-space propulsion technologies for future missions. Working together, materials scientists and mission planners identified materials shortfalls that are limiting the performance of long-term missions. The goal of the AME project was to deliver improved materials in targeted areas to meet technology development milestones of NASA's exploration-dedicated activities. Materials research tasks were targeted in five areas: (1) Thermal management materials, (2) propulsion materials, (3) materials characterization, (4) vehicle health monitoring materials, and (5) structural materials. Selected tasks were scheduled for completion such that these new materials could be incorporated into customer development plans.

14. SUBJECT TERMS

advanced materials, thermal management, propulsion materials, vehicle health monitoring, structural materials, heat pipes, radiators, functionally gradient material, thermal protection system, tether materials, solar sail, superconducting magnets, radiation-resistant electrons, composite aerogel, aerocapture, nanolaminates, ablative composites

15. NUMBER OF PAGES

328

16. PRICE CODE

17. SECURITY CLASSIFICATION OF REPORT	18. SECURITY CLASSIFICATION OF THIS PAGE	19. SECURITY CLASSIFICATION OF ABSTRACT	20. LIMITATION OF ABSTRACT
Unclassified	Unclassified	Unclassified	Unlimited

National Aeronautics and
Space Administration
IS20
George C. Marshall Space Flight Center
Marshall Space Flight Center, Alabama
35812